Improved analysis of brain connectivity using high angular resolution diffusion MRI

Proefschrift voorgelegd tot het behalen van de graad van doctor in de Wetenschappen aan de Universiteit Antwerpen te verdedigen door

Ben Jeurissen

Faculteit Wetenschappen
Departement Fysica

Antwerpen 2012

PROMOTOREN
prof. dr. J. Sijbers
prof. dr. A. Leemans
dr. J.D. Tournier

Universiteit Antwerpen

Faculteit Wetenschappen

Improved analysis of brain connectivity using high angular resolution diffusion MRI

Verbeterde analyse van hersenconnectiviteit met behulp van diffusie MRI met hoge hoekresolutie

Proefschrift voorgelegd tot het behalen van de graad van

Doctor in de Wetenschappen

aan de Universiteit Antwerpen, te verdedigen door

Ben JEURISSEN

Promotoren:
Prof. Dr. Jan Sijbers
Prof. Dr. Alexander Leemans
Dr. Jacques-Donald Tournier

Antwerpen, 2012

Doctoral committee:

Prof. Dr. Jan Naudts
Prof. Dr. Jan Sijbers
Prof. Dr. Marleen Verhoye

Prof. Dr. Daniel C. Alexander
Prof. Dr. Stefan Sunaert
Dr. Jacques-Donald Tournier
Prof. Dr. Floris Wuyts

Contact information:

✉ **Ben Jeurissen**
Vision Lab, Dept. of Physics
University of Antwerp (CDE)
Universiteitsplein 1, Building N1.16
B-2610 Wilrijk, Antwerpen, Belgium
☎ +32 3 265 24 58
+32 3 265 22 45
ben.jeurissen@ua.ac.be
http://visielab.ua.ac.be/people/ben-jeurissen

All rights reserved. No part of the material protected by this copyright notice may be reproduced or utilized in any form or by any means, electronic or mechanical, including photocopying, recording, broadcasting or by any other information storage and retrieval system without written permission from the copyright owner.

Acknowledgments

It is a pleasure to thank the many people who made this thesis possible, to only some of whom it is possible to give particular mention here. I would especially like to thank:

Jan Sijbers, my supervisor. Thank you for giving me the opportunity to pursue a PhD degree at the Vision Lab and for your trust and excellent guidance from start to finish. I am also very grateful for your continuous support to participate in international scientific conferences, workshops and courses, which has definitely given an added value to this work.

Alexander Leemans, my co-supervisor. I could not have imagined a better mentor, both on a scientific and a personal level. You convinced me that doing research is the most exciting job in the world. Although you left the country as soon as I started my PhD, countless hours of VoIP-conversations and many ISMRM conferences have allowed us to collaborate closely over the years. You were always ready to provide me with a fresh perspective when I needed one. Your contribution to this dissertation is paramount.

Donald Tournier, my co-supervisor at the other end of the world. Even though we have been very far apart most of the time, you have certainly not taken your job as a co-supervisor lightly. I thank you for the many hours spent proofreading my work, improving my manuscripts and providing me with new insights, often at impossible hours due to the large time difference. I feel honored to have been able to learn from such a talented scientist, distinguished for his high impact contributions within the field of high angular resolution diffusion imaging.

I would also like to thank *all* my colleagues from the Vision Lab for providing a nice working climate and for their scientific input. I would especially like to mention Toon Huysmans and Dirk Poot, who I have 'bugged' repeatedly with 'small' technical and scientific questions and were always ready to help instantly, regardless of the topic. I truly admire their scientific capabilities. I would also like to mention Guy Thoonen and Wim Van Aarle, with whom I originally shared an office. Thanks for all the lighthearted interdisciplinary chats we had, back in the good old days when CT, MRI and remote sensing researchers were still allowed to work within the same office. My more recent office mate, Jelle Veraart, also deserves a special mention. Through our daily discussions, my knowledge of MRI in general and diffusion MRI in particular has increased markedly during the last two years. I think there is now more about MRI that you can teach me than the other way around. I also enjoyed our occasional late night excursions in Antwerp and other cities of the world. Last but not least there is Steve de Backer, who helped me a lot with technical issues during my first months at the Vision Lab.

Much of the work in this dissertation would not have been possible without the

diffusion-weighted MRI data sets that were kindly provided to me. Many thanks goes to Els Fieremans, then at the University of Ghent, for providing HARDI data of her excellent fiber crossing phantom. I'm also grateful to Donald Tournier and colleagues at the Brain Research Institute in Melbourne for providing me with human HARDI data sets. I'm much in debt to Derek Jones and colleagues at the Cardiff University Brain Research Imaging Centre for providing me several high quality HARDI data sets, that were used in several of our collaborative publications. Special thanks also to Derek for providing valuable feedback on my papers. It has been an honor collaborating with one of the leading scientists in diffusion MRI. I'm also grateful to Paul Parizel and colleagues at the University Hospital of Antwerp and to the Annemie Van der Linden, Marleen Verhoye, Johan Van Audekerke, Geert De Groof and Ines Blockx of the Bio Imaging Lab for their input of data.

Much thanks goes to Pièrre Fillard and the other co-authors of our collaborative NeuroImage paper for the fruitful collaboration. Also, many thanks to Wim Van Hecke, Jeny Rajan, Dirk Poot, Jelle Veraart, Yannick Bastiaensen, Maarten Naeyaert, Sjoerd Vos, Yael Reijmer and Martijn Froeling for their scientific collaboration.

Many thanks to Matthan Caan, Jonathan Clayden, Shahrum Nedjati-Gilani, Maxime Descoteaux, Flavio Dell'Acqua, David Raffelt, Tom Close, Robert Smith, Shawna Farquharson, Richard Masterton, Fernando Calamante and Allan Connelly for the many interesting discussions about both MRI and life in general during several conferences. I also have to mention my Belgian conference buddies: Wim Van Hecke, Jelle Veraart, Stefan Sunaert, Thijs Dhollander, Sabine Deprez and Judith Verhoeven with whom I have enjoyed plenty of dinners and drinks during the ISMRM conference.

I am grateful to the Institute for the Promotion of Innovation through Science and Technology in Flanders - Belgium (IWT) and the Interdisciplinary institute for Broadband Technology (IBBT) for financially supporting this research.

I never would have been able to complete this work were it not for the dedicated support and love of my friends and family. In particular, I would like to thank my non-disciplinary friends, who have kept my mind sane during the past years (you know who you are). I have enjoyed our badminton sessions, skiing trips, café visits, board game sessions, dancing lessons, camping trips, concerts, festivals, weddings, family events... I am also very grateful to my parents for their support and unconditional trust and love since the beginning of my career. Finally, a huge thanks goes to Nathalie for her support and understanding during the entire course of my PhD research, especially in the last stretch of writing my PhD thesis. She raised my spirits when necessary and was always there for me.

I sincerely thank you all,

Ben Jeurissen
Antwerpen, March 2012

Contents

Summary

This dissertation deals with the use of constrained spherical deconvolution (CSD) of diffusion weighted (DW) MRI data for the purpose of improved fiber tractography. The manuscript is divided into two large parts. **Part I**, provides the necessary **background material** on diffusion MRI, multi-fiber reconstruction algorithms and fiber tractography. **Part II** provides an overview of the main **contributions** of this thesis.

Background

Diffusion-weighted (DW) MRI is a magnetic resonance imaging (MRI) technique that indirectly measures the local mobility of water molecules. It is unique in its ability to measure diffusion non-invasively, making it the method of choice for *in vivo* diffusion measurements. A key feature of diffusion MRI is that it can provide information about the geometry of the underlying tissue microstructure, at scales much smaller than the imaging resolution. In fibrous tissue, such as in the brain white matter (WM), water molecules tend to diffuse more along the fibers, enabling researchers to obtain information about the orientation and 'integrity' of the underlying tissue. Currently, **diffusion tensor imaging (DTI)** is the most widely used method for assessing WM orientation and integrity, owing to its modest acquisition requirements. The ability to assess WM orientation and integrity from a single *in vivo* scan raises huge possibilities for neuroscientific research and there has been a rapid increase in clinical studies using DTI in the last decade. For a detailed review of the principles of diffusion, diffusion MRI and DTI the reader is referred to **Chapter 1**.

Despite its popularity, DTI has an important limitation in that it can only model a single fiber population per voxel. However, due to partial volume effects between adjacent WM fiber bundles, many voxels contain contributions from several differently oriented fiber populations. In such voxels, DTI orientation and DTI integrity metrics are unreliable. Recently, a number of methods have been proposed that are able to **extract multiple fiber orientations from the DW signal**, overcoming the limitation of DTI. One particularly promising method is **constrained spherical deconvolution (CSD)**, which recovers the full fiber orientation distribution function (fODF) within each voxel directly from the diffusion data using the concept of spherical deconvolution. By applying a non-negativity constraint on the fODF, CSD allows robust multiple fiber orientation estimation using relatively modest acquisition settings. An in-depth review of the different multi-fiber reconstruction algorithms, CSD in particular, is provided in **Chapter 2**.

Fiber tractography pieces together the local WM orientations derived with DTI or more advanced multiple fiber reconstruction algorithms in order to infer long-range connectivity patterns between distant brain regions. Diffusion MRI based fiber tractography is unique in its ability to delineate the WM fiber pathways in a non-invasive way, raising possibilities for clinical applications and providing new insights in how the brain is wired up. Fiber tractography algorithms can be classified largely into deterministic and probabilistic algorithms. Deterministic tractography algorithms reconstruct the most likely trajectory emanating from a given point, whereas probabilistic algorithms produce a distribution of trajectories, reflecting the degree of uncertainty of the trajectories. The concepts, limitations, and applications of fiber tractography are introduced in **Chapter 3**.

Contributions

As DTI based fiber tractography becomes unreliable in regions of complex fiber configurations, we developed a **new deterministic tractography algorithm based on CSD**. As CSD is capable of resolving multiple fiber orientations within each voxel, it is expected to improve tractography results in regions of complex fiber architecture. By means of a simple crossing fiber phantom, we showed that the algorithm is able to track through regions containing crossing fibers where DTI tractography fails. In addition, our method was evaluated quantitatively on a more complex fiber phantom, as part of the MICCAI 2009 fiber cup contest. Analysis of the results revealed our solution was characterized by the lowest average error for both the spatial and directional metric and our method was the only one tracing the correct fiber bundles from start to end. In **Chapter 4**, our algorithm, as well as the quantitative and qualitative evaluation using different MR phantoms is explained in detail. In addition we briefly discuss some applications of the proposed CSD tractography method.

While CSD offers an improved estimate of the fiber orientations in the presence of partial volume effects, diffusion MRI is inherently a noisy technique, resulting in uncertainty associated with each fiber orientation estimate. In **Chapter 5**, we introduce the use of **bootstrapping techniques to quantify the uncertainty of CSD estimated fiber orientations**. The performance of bootstrapping was measured in terms of accuracy and precision using Monte Carlo simulations. We looked at both the 'classic repetition bootstrap' approach which estimates the fiber orientation uncertainty by randomly selecting individual measurements from a set of repeated measurements, and the 'residual bootstrap' approach, which estimates the fiber orientation by randomly selecting model residuals, requiring only a single measurement and thus being more clinically feasible. Our simulations showed that the 'classic repetition bootstrap' significantly underestimates the uncertainty when only a few repeated acquisitions are available, which is typically the case. We showed that this large downward bias can be removed by using the bootknife approach, allowing accurate CSD fiber orientation uncertainty estimates with only a limited set of repeated measurements and without making assumptions about the sources of uncertainty in the data. However, in a clinical setting, even a few repeated measurements can render acquisition time unacceptably long. For this reason

we also investigated the residual bootstrap, which performs the bootstrapping procedure on the residuals of a model fit, requiring only a single acquisition. Our simulations showed that the combination of the residual bootstrap with the modified spherical harmonics model allows accurate estimates of the CSD fiber orientation uncertainty, bringing it into the clinical realm.

In **Chapter 6**, we build on the findings of Chapters 4 & 5 to formulate a **new probabilistic tractography algorithm based on CSD and the residual bootstrap**, overcoming the limitations of DTI tractography and at the same time providing uncertainty measures of the fiber trajectories, using only a single acquisition. Using Monte Carlo simulations, we measured the accuracy and precision of the residual bootstrap method when estimating CSD fiber pathway uncertainty. We also applied our algorithm to clinical DW data and compared our method to state-of-the-art DTI residual bootstrap tractography and to an established probabilistic multi-fiber CSD tractography algorithm which draws samples directly from the fODF. CSD residual bootstrap probabilistic tractography showed advantageous over DTI residual bootstrap probabilistic tractography: in regions of multiple fiber orientations, CSD was much less prone to fiber dispersion, false positives, and false negatives. We also showed the advantages of our method over CSD fODF sampling tractography: in regions of well ordered and sharp peak orientations, our method does not suffer from unrealistically high dispersion and our method has a higher specificity in general.

In **Chapter 7**, we set out to assess the **prevalence of voxels containing multiple fiber orientations**, as these are the voxels where multi-fiber reconstruction algorithms would result in improved tractography results. For this purpose, we acquired large, high quality DW data sets and extracted the fiber orientations using both CSD and the bedpostx algorithm. Our results indicated that multiple fiber orientations can be found in a much higher percentage of WM voxels than previously reported, with CSD providing much higher estimates than bedpostx. These findings have obvious and profound implications for both tractography and integrity analyses, and strengthen the growing awareness that fiber tractography and 'WM integrity' metrics derived from DTI need to be interpreted with extreme caution, underlining the importance of the methods developed in the previous chapters.

Part I

Background

1 Diffusion MRI

Contents

1.1 Introduction

Diffusion MRI is a magnetic resonance imaging (MRI) method that measures the local mobility profile of water molecules. It is unique in its ability to measure diffusion non-invasively, making it the method of choice for *in vivo* diffusion measurements. The success of diffusion MRI stems from the fact that it can describe the geometry of the underlying tissue microstructure. This is achieved by measuring the average diffusion of water molecules, which can act as a probe for the structure of the biological tissue at scales much smaller than the imaging resolution. In an environment without any hindrances, e.g. a glass of water, the diffusion of water molecules is the same regardless of the direction in which it is measured. However, in fibrous tissue, such as the brain white matter, water molecules tend to diffuse more along the fibers, enabling researchers to obtain information about the neural architecture.

In this chapter, we will first review the basic physical principles of diffusion. Next, we will briefly introduce the properties of diffusion in the brain white matter. Then, we will explain how diffusion can be measured *in vivo* using diffusion MRI. Finally, we will briefly discuss the applications of diffusion MRI and its challenges and limitations.

1.2 Diffusion

At the microscopic scale, individual water molecules are constantly in motion as a result of their thermal energy (Fig. 1.1). This phenomenon, referred to as 'Brownian motion', was first described in 1828 by the Scottish botanist Robert Brown, who observed a perpetual random motion of pollen grains suspended in water while studying them under a microscope [Brown, 1828].

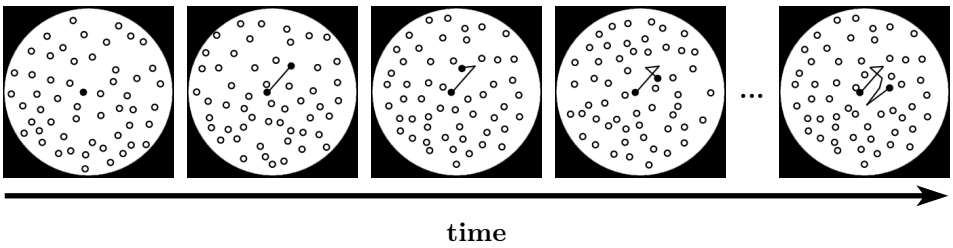

Fig. 1.1: Brownian motion at the microscopic scale: a single water molecule exhibits a 'random walk' due to its thermal energy.

Diffusion, or the process in which particles move from a region of higher to one of lower concentration, can be considered the macroscopically observable effect of the microscopic Brownian motion of particles. The physical law describing this process is called Fick's first law [Fick, 1855]:

$$\boldsymbol{J} = \quad D\nabla\boldsymbol{C} \tag{1.1}$$

where $\boldsymbol{J}$ is the net particle flux (units: $\mathrm{mol}/(\mathrm{m}^2\,\mathrm{s})$), $\boldsymbol{C}$ is the particle concentration (units: $\mathrm{mol}/\mathrm{m}^3$), and D is the diffusion coefficient (units: m^2/s). The minus sign

in Fick's first law embodies the notion that particles move from regions of high concentration to regions of low concentration. The rate of this flux is proportional to the concentration gradient and to the diffusion coefficient. Unlike the flux vector or the concentration gradient, the diffusion coefficient is an intrinsic property of the medium, and its value is determined by the size of the diffusing molecules and the temperature and microstructural features of the environment. Imagine introducing a drop of red wine into a glass of water. Initially, the wine appears to remain concentrated at the point of release, but over time it spreads radially into a spherically symmetric profile (Fig. 1.2). Notice that this process takes place without

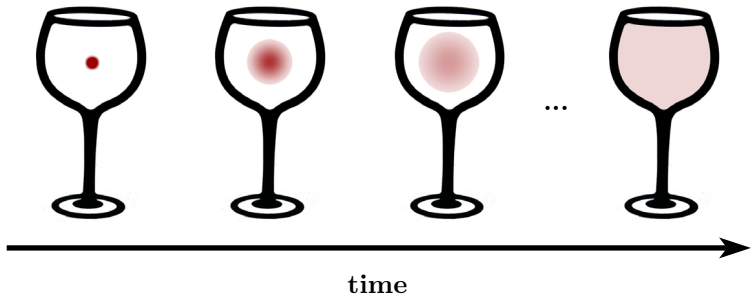

Fig. 1.2: Diffusion at the macroscopic scale: net flux of wine molecules from a region of high concentration to a region of low concentration.

stirring or other bulk fluid motion. Note also that if one waits long enough, the concentration of wine particles will become uniform throughout the glass. Although the net flux of particles stops at this point in time, microscopic motions of the molecules still persist; it is just that on average, there is no net molecular flux.

While the random nature of Brownian motion prevents us from predicting the behavior of a single water molecule (Fig. 1.3a-d), it is possible to predict the behavior for a large collection of water molecules (Fig. 1.3e-f). The study of such a large ensemble of randomly moving particles is facilitated by the introduction of a probabilistic framework. In 1905, Einstein introduced the 'displacement distribution' or 'diffusion probability density function', $p(\boldsymbol{r})$, which quantifies the fraction of particles that will have been displaced by $\boldsymbol{r}$ within a certain 'diffusion time' t, or equivalently, the likelihood that a single particle will undergo that displacement. Using this framework, Einstein showed that, provided that the number of particles is sufficiently large and provided that they are free to diffuse $p(\boldsymbol{r})$, takes the form of a Gaussian distribution (Fig. 1.4) [Einstein, 1905]:

$$p(\boldsymbol{r}) = \frac{1}{\sqrt{(4\pi t D)^3}} e^{-\frac{\|\boldsymbol{r}\|^2}{4tD}} \tag{1.2}$$

where D is the classical diffusion coefficient appearing in Fick's first law (units: m^2/s), t is the diffusion time (units: s) and $\boldsymbol{r}$ is the displacement vector (units: m). The width of this Gaussian distribution is determined by the diffusion coefficient D and the diffusion time t, with the peak being at zero displacement ($\boldsymbol{r} = \boldsymbol{0}$). The isoprobability surface of p will take the form of a sphere, centered at the origin, with

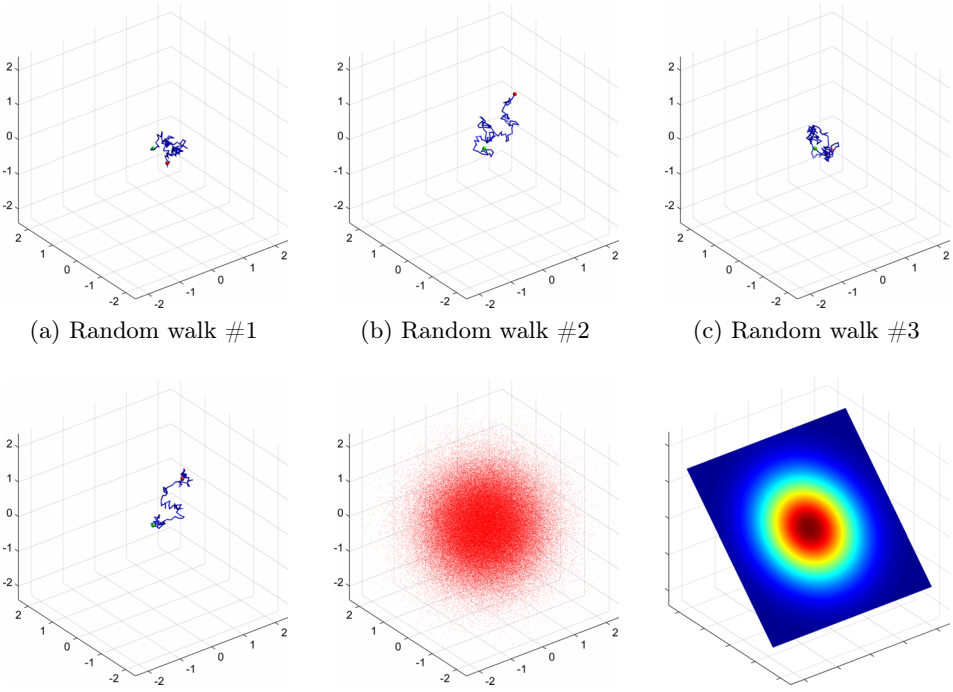

(a) Random walk #1 (b) Random walk #2 (c) Random walk #3

(d) Random walk #4 (e) 2×10^6 endpoints (f) Histogram

Fig. 1.3: Given the same initial position (green dot), different random walks end up in different end positions (red dots). This prevents us from predicting the behavior of a single water molecule (a-d). However, looking at a large collection of end points (e), and calculating a 3D histogram reveals a 3D Gaussian distribution (f).

a radius proportional to the square root of the diffusion coefficient and the diffusion time (Fig. 1.4c). The fact that the isoprobability surface is spherical, embodies the notion that the diffusion is isotropic, i.e. there is an equal probability of displacing a given distance from the origin - no matter in which direction it is measured. From Eq. (1.2), one can derive the well-known Einstein equation, which provides an

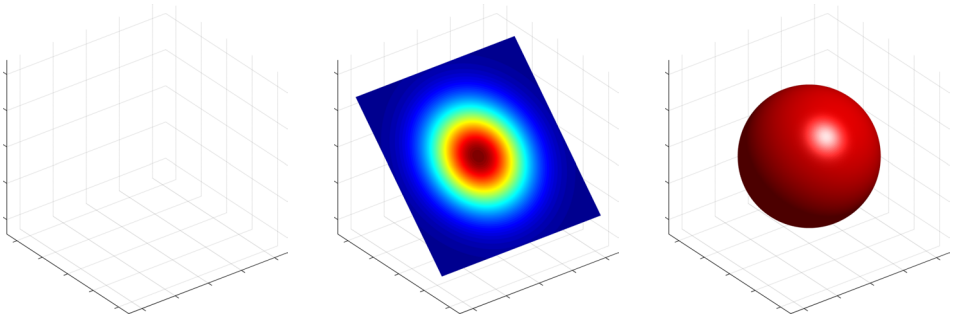

(a) environment (b) PDF (c) isoprobability surface

Fig. 1.4: Free (isotropic) diffusion

explicit relationship between the mean-squared 3D displacement of the ensemble, characterizing its Brownian motion, and the diffusion coefficient [Einstein, 1905]:

$$\langle \|\boldsymbol{r}\|^2 \rangle = 6Dt \tag{1.3}$$

where $\langle \|\boldsymbol{r}\|^2 \rangle$ is the mean-squared displacement of particles (units: m^2). For example, the diffusion coefficient for water at body temperature is $3 \times 10^{-3}\,\mathrm{mm}^2/\mathrm{s}$. Thus, given a diffusion time of 30 ms, the water molecules will have displaced on average 23 µm in all directions.

1.3 Apparent diffusion

If the diffusing water molecules encounter any hindrances along their random walk, the mean squared displacement per unit time will be lower than when observed in 'free' water. Thus, when Eq. (1.3) is used to compute the diffusion coefficient, it will *appear* that the diffusion coefficient is lower. Therefore, the diffusion coefficient that we measure in a biological sample, is usually referred to as the *apparent* diffusion coefficient (ADC) [Le Bihan et al., 1986]. This property of diffusion is key to diffusion MRI and will allow us to acquire information about the microstructural features of biological tissue.

1.3.1 Isotropic diffusion

Unordered tissue microstructure (Fig. 1.5a) typically gives rise to isotropic diffusion, in which the ADC is equal no matter in which direction it is measured (Fig. 1.5b). This type of diffusion can be modeled using a single ADC as in Eq. (1.2). The

isoprobability surface of p is again a sphere, however, due to the hindrances, the radius is reduced compared to that of free diffusion (Fig. 1.5c).

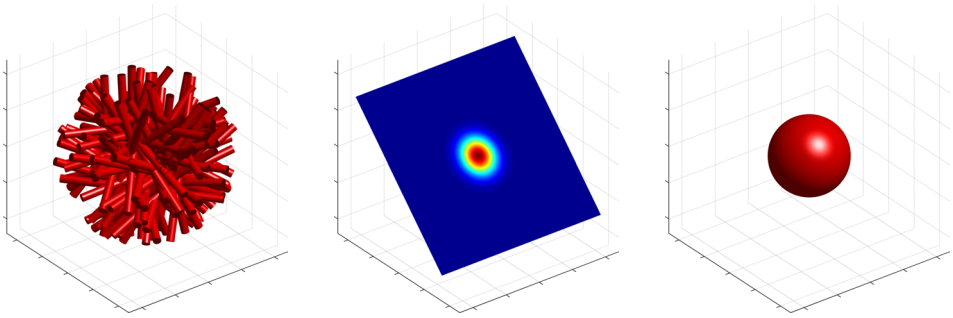

(a) environment (b) PDF (c) isoprobability surface

Fig. 1.5: Hindered, isotropic diffusion (no coherent structure)

1.3.2 Anisotropic diffusion

The introduction of well ordered hindrances (Fig. 1.6a) may cause the diffusion to become anisotropic, i.e. the ADC becomes dependent on the orientation in which it was measured [Moseley et al., 1990, Doran et al., 1990, Chenevert et al., 1990]. One can imagine that water molecules can diffuse more freely parallel to the hindrances, than perpendicular to the hindrances (Fig. 1.6b). The diffusion can now no longer be described with a single diffusion coefficient. For a single bundle consisting of tightly packed cylinders, the isoprobability surface of p typically takes the form of an ellipsoid (Fig. 1.6c).

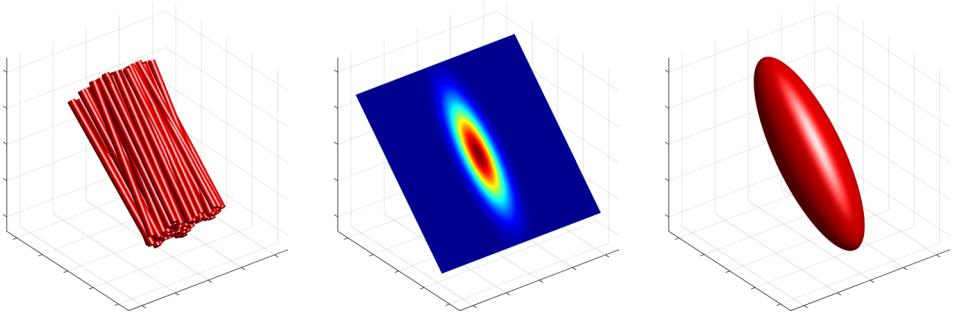

(a) environment (b) PDF (c) isoprobability surface

Fig. 1.6: Hindered, anisotropic diffusion (single coherent fiber bundle)

The next most complex model to characterize Gaussian diffusion in which the displacements per unit time are not the same in all directions is the diffusion tensor model [Basser et al., 1994a,b, Basser and Pierpaoli, 1996, Basser, 2002, Basser and

Jones, 2002]:

$$p(\boldsymbol{r}) = \frac{1}{\sqrt{(4\pi t)^3 \, |\boldsymbol{D}|}} \, e^{\frac{\boldsymbol{r}^{\mathrm{T}} \boldsymbol{D}^{-1} \boldsymbol{r}}{4t}} \tag{1.4}$$

where

$$\boldsymbol{D} = \frac{\langle \boldsymbol{r}\boldsymbol{r}^{\mathrm{T}} \rangle}{6t} = \begin{bmatrix} D_{xx} & D_{xy} & D_{xz} \\ D_{xy} & D_{yy} & D_{yz} \\ D_{xz} & D_{yz} & D_{zz} \end{bmatrix} \tag{1.5}$$

is the diffusion tensor, which is the 3×3 covariance matrix of the molecular displacements along three orthogonal orientations. $\boldsymbol{D}$ is a symmetric and positive definite matrix. Note that, as $\boldsymbol{D}$ is symmetric, it contains only 6 unique elements. In general, the isoprobability surface of p takes the form of an ellipsoid.

1.4 Diffusion in neural tissue

At the cellular level, the neural tissue of brain is built from neurons or nerve cells. A neuron is an electrically excitable cell that processes and transmits information by electrical and chemical signaling. A typical neuron can be divided into three parts: the soma or cell body, the dendrites and the axon (Fig. 1.7). From the soma, many dendrites extend. The soma and dendrites receive chemical signals from other neurons and process the information. The axon, which is a thin and very long extension from the nerve cell, transmits this information from the soma towards other nerve cells by means of electrical conduction. The transmission speed along the axons is increased by a myelin sheet, which acts as an insulator.

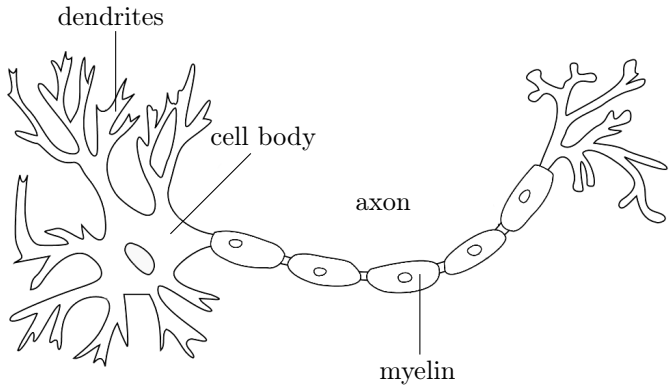

Fig. 1.7: Schematic representation of a typical neuron, consisting of a cell body, dendrites and long myelinated axons. The image is taken from Wikipedia and is licensed under the Creative Commons CC-BY-SA-3.0 License.

At the macroscopic level, the brain is made up of three major components: white matter (WM), grey matter (GM) and cerebrospinal fluid (CSF) (Fig. 1.8). While WM consists mostly of myelinated axons, GM contains the cell bodies. As

such, WM is the tissue through which information passes between different areas of the GM. Conversely, GM is the tissue where the information from the WM is processed. The CSF occupies the ventricular system around and inside the brain. It acts as a cushion for the brain, providing mechanical and immunological protection.

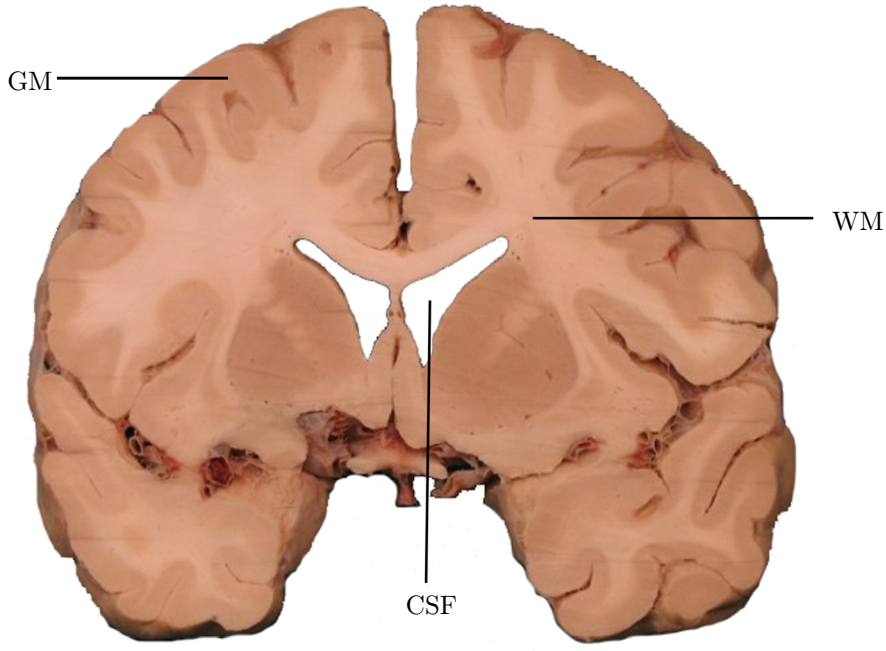

Fig. 1.8: Coronal post mortem brain slice with the three macroscopic components: white matter (WM), grey matter (GM) and cerebrospinal fluid (CSF). Section was made and photographed by Dr. Bruce Crawford and Kurt McBurney at the University of Victoria. The image is licensed under the Creative Commons CC BY-NC-SA 2.5 License.

Apart from the myelin, WM axons contain an axonal membrane, neurofilaments and microtubules, all oriented along the major axis of the axon (Fig. 1.9a). Additionally axons are often organized and tightly packed together into nerve bundles (Fig. 1.9b). All these factors contribute to diffusion anisotropy inside the WM, i.e., diffusion is less restricted parallel to the axon bundles than perpendicular to it. This feature will allow us to extract geometrical information about the WM fiber bundles based on diffusion. Experimental evidence suggests that the tissue component predominantly responsible for the anisotropy of molecular diffusion observed in white matter is not myelin, as was first hypothesized, but rather the cell membrane [Beaulieu, 2002]. The degree of myelination of the individual axons and the density of cellular packing seem merely to modulate anisotropy. Furthermore, microtubules, and neurofilaments appear to play only a minor role.

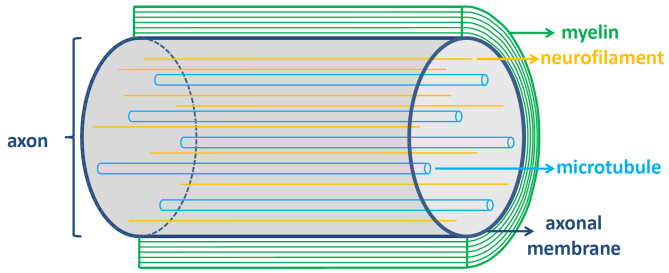

(a) single myelinated axon

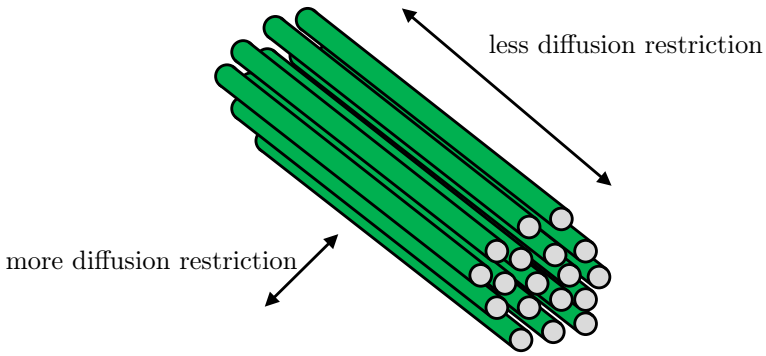

(b) bundle of myelinated axons

Fig. 1.9: Schematic representation of (a) a single axon and (b) a bundle of highly organized, tightly packed axons, typically found in the WM. The axon is surrounded by myelin and the axonal membrane and contains several structures, such as neurofilaments and microtubuli (a). Diffusion can take place more easily parallel to the WM bundles than perpendicular to it (b).

1.5 Measuring diffusion with MRI

Diffusion MRI is an imaging technique that allows one to measure the amount of water diffusion at different positions in a sample. Although a thorough understanding of the principles of nuclear magnetic resonance (NMR) and magnetic resonance imaging (MRI) is a prerequisite to understand diffusion MRI, a general introduction into these principles is considered beyond the scope of this dissertation. An excellent and complete description of the principles of MRI can be found in Liang and Lauterbur [2000].

1.5.1 Spin-echo (SE) sequence

A Spin-echo (SE) sequence [Hahn, 1950] (Fig. 1.10) starts with the excitation of the hydrogen nuclei with a 90° radiofrequency (RF) pulse that tilts the magnetization vector into the plane whose normal is along the main magnetic field $\boldsymbol{B}_0$. The spins precess around the magnetic field - a phenomenon called Larmor precession [Bloch et al., 1946, Purcell et al., 1946]. The Larmor equation states that the precession frequency ω (units: rad/s) of spins in a magnetic field is directly proportional to the strength B_0 of the main magnetic field (units: T):

$$\omega = \gamma B_0 \tag{1.6}$$

where γ is the gyromagnetic ratio - a constant specific to the nucleus under examination (units: rad/(s T)). E. g., the hydrogen nucleus in water has a gyromagnetic ratio value of approximately 2.68×10^8 rad/(s T). Following Faraday's Law, the precessing magnetic fields of the spins will induce a voltage (signal) in the receiver coil. Initially, the spins are coherent, but they immediately start dephasing due to magnetic field inhomogeneities and dipolar interactions, leading to a decay of the induced signal (T_2* decay). This dephasing can be reversed through a subsequent application of a 180° RF pulse, and the signal is refocused. In this 'spin-echo' experiment, the time between the first RF pulse and the echo is called TE and it is twice the time between the two RF pulses. The generated echo is detected by a receiver coil. From this (spatially encoded) raw data MR images are reconstructed.

1.5.2 Magnetic field gradients

The magnetic field can be made to vary in a linear manner over the volume of interest, by the addition of a linear magnetic field gradient G on top of the main magnetic field B_0 [Carr and Purcell, 1954]:

$$B(x) = B_0 + Gx \tag{1.7}$$

where x the position along the gradient direction (see Fig. 1.11). Given Eqs. (1.6)-(1.7), this results in a position-dependent precessional frequency of the spins:

$$\omega(x) = \gamma B(x) = \gamma(B_0 + Gx) \tag{1.8}$$

This position-dependent precessional frequency is the basis of spatial encoding in MRI, but it can also be applied to make MR sequences sensitive to diffusion or diffusion-weighted (DW).

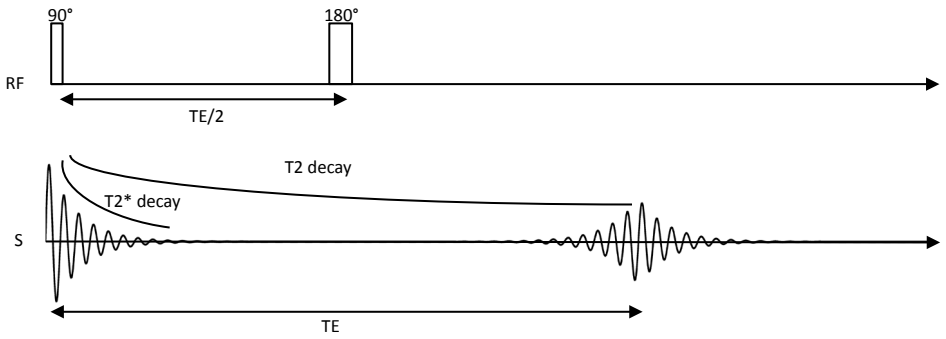

Fig. 1.10: Spin-echo (SE) sequence. The 90° RF pulse tilts the magnetization vector into the plane orthogonal to the main magnetic field. The spins subsequently start to precess around the magnetic field, inducing a voltage (signal) in the receiver. Spins that are initially coherent dephase due to magnetic field inhomogeneities and dipolar interactions, leading to a decay of the signal (T_2* decay). The dephasing due to magnetic field inhomogeneities can be reversed through a subsequent 180° RF pulse at time TE/2, causing a strong echo at time TE.

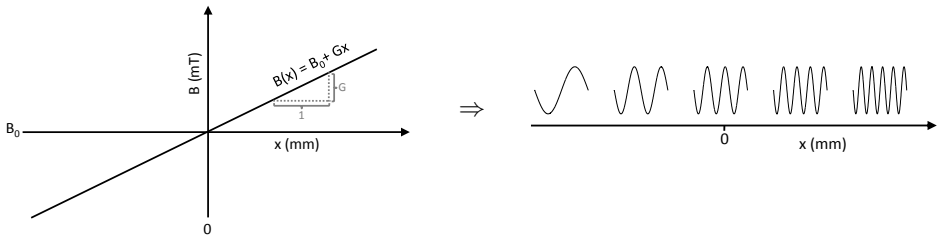

Fig. 1.11: A linear magnetic field gradient results in a position-dependent precession frequency.

1.5.3 Pulsed Gradient Spin-echo (PGSE) sequence

The Spin-echo sequence can be made sensitive to diffusion along a particular orientation by the addition of two linear diffusion-encoding gradients, symmetrically positioned around the 180° refocusing RF pulse [Stejskal and Tanner, 1965]. Consider two rectangular diffusion gradient pulses $\boldsymbol{g}(t)$ along the x-direction ($\|\boldsymbol{g}(t)\| = g_x(t)$) with duration time δ and with time Δ between the gradient pulse onsets (Fig. 1.12). During the pulse $g_x(t) = g_x$ is constant.

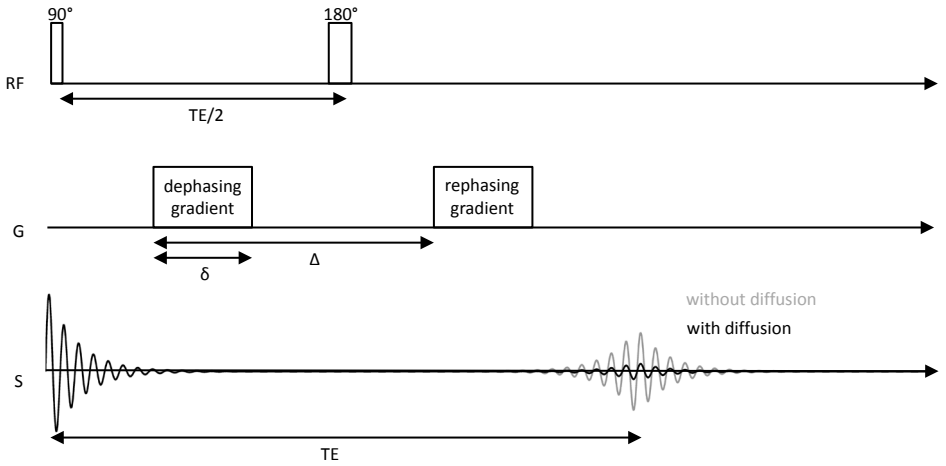

Fig. 1.12: Pulsed Gradient Spin-echo (PGSE) sequence. The first (dephasing) gradient pulse induces a position-dependent phase shift. For static spins, this phase shift is canceled by means of the second (rephasing) gradient pulse. Spins that do move during time Δ will experience a net phase shift proportional to the traveled distance, resulting in signal loss.

The first (dephasing) gradient pulse induces a position-dependent phase shift ϕ_1 of the spin transverse magnetization:

$$\phi_1 = \quad \gamma \int_0^{\delta} g_x(t)x(t)\,\mathrm{d}t = \quad \gamma\delta g_x x_1 \tag{1.9}$$

where γ is the gyromagnetic ratio for hydrogen nuclei and the spin position $x(t) = x_1$ is assumed to be constant during the short pulse duration δ (the so-called 'narrow pulse' regime). Note that the amount of dephasing is proportional to the duration δ and the strength g_x of the gradient. Similarly, the second (rephasing) gradient pulse induces a phase shift ϕ_2:

$$\phi_2 = \gamma \int_{\Delta}^{\Delta+\delta} g_x(t)x(t)\,\mathrm{d}t = -\gamma\delta g_x x_2 \tag{1.10}$$

The application of the 180° RF pulse in between both gradients, reverses the phase change that occurred prior to it. For static spins, i.e. spins not undergoing any

diffusion along the gradient direction ($x_1 = x_2$), the net phase shift ϕ will be zero:

$$\phi = \phi_2 - \phi_1 = \gamma \delta g_x (x_2 - x_1) = 0 \tag{1.11}$$

Spins that *do* undergo diffusion along the gradient direction during the time period Δ will experience a net phase shift, depending on the distance traveled ($x_2 - x_1$):

$$\phi = \gamma \delta g_x (x_2 - x_1) \neq 0 \tag{1.12}$$

These diffusing spins are not completely refocused. In general, the amplitude of the PGSE signal S is given by:

$$S = S_0 \langle e^{i\phi} \rangle \leq S_0 \tag{1.13}$$

where S_0 is the signal intensity in the absence of a diffusion-encoding gradient and $\langle ... \rangle$ represents the ensemble average of the spin population. Given that the displacement distribution of diffusing spins follows a random distribution (see Section 1.2), the phase distribution of the spins also becomes randomly distributed, resulting in a decreased amplitude in the ensemble averaged signal. Stejskal and

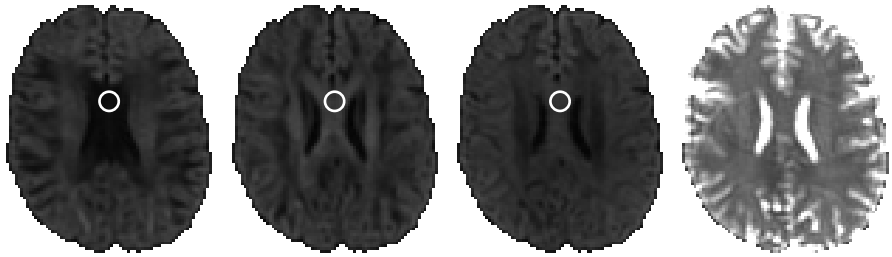

(a) DW ∥ x-axis (b) DW ∥ y-axis (c) DW ∥ z-axis (d) no DW

Fig. 1.13: Axial DW images with gradients orientations along (a) the x-axis, (b) the y-axis, and (c) the z-axis. Note that in the region marked by the white circle, the signal is low when the diffusion gradient is applied along the x-axis and high when the diffusion gradient is applied along the y- and z-axis, implying that the diffusion and the underlying microstructure are left-right oriented. Note also that, due to the dephasing caused by the random motion of water molecules, the intensity in the DW images is much lower than in an image without diffusion weighting (d).

Tanner [1965] demonstrated that the signal attenuation $A(\boldsymbol{q}) = S(\boldsymbol{q})/S(\boldsymbol{0})$ can be expressed as the 3D Fourier transform $\mathcal{F}$ of the diffusion probability density function $p(\boldsymbol{r})$:

$$A(\boldsymbol{q}) = \int_{\mathbb{R}^3} p(\boldsymbol{r}) e^{-i\boldsymbol{q}^{\mathrm{T}}\boldsymbol{r}} d\boldsymbol{r} = \mathcal{F}[p(\boldsymbol{r})] \tag{1.14}$$

with

$$\boldsymbol{q} = \gamma \delta \boldsymbol{g} \tag{1.15}$$

the so-called q-vector and $\boldsymbol{g}$ the applied diffusion gradient vector. The space of all possible 3D q-vectors is called *q-space*. Intuitively, one can reconstruct the diffusion

PDF p by sampling the diffusion signal along many q-vectors and performing an inverse 3D Fourier transform. This is the principle behind q-space imaging [Callaghan et al., 1988].

1.5.4 ADC Imaging

Combining Eqs. (1.2) and (1.14), we can relate the signal attenuation $A(\boldsymbol{q}) = S(\boldsymbol{q})/S(\mathbf{0})$ to the ADC D of the underlying tissue:

$$A(\boldsymbol{q}) = e^{-\|\boldsymbol{q}\|^2 \Delta D} = e^{-\gamma^2 \delta^2 \|\boldsymbol{g}\|^2 \Delta D} \tag{1.16}$$

Eq. (1.16) is a special case of the more general Stejskal-Tanner equation, which takes the duration of the diffusion encoding gradients into consideration as well:

$$A(\boldsymbol{q}) = e^{-\|\boldsymbol{q}\|^2 (\Delta - \delta/3) D} = e^{-\gamma^2 \delta^2 \|\boldsymbol{g}\|^2 (\Delta - \delta/3) D} = e^{-bD} \tag{1.17}$$

where the diffusion weighting factor or b-value, introduced by Le Bihan et al. [1986], is defined as:

$$b = \gamma^2 \delta^2 \|\boldsymbol{g}\|^2 \left(\Delta - \frac{\delta}{3} \right) \tag{1.18}$$

Eq. (1.17) allows one to estimate the apparent diffusion coefficient D, from a single DW image $S(\boldsymbol{q})$, along with a reference image $S(\mathbf{0})$. Note that Eq. (1.17) assumes that diffusion is free and can therefore be modeled by a Gaussian. Note also that the resulting diffusion coefficient D is dependent on the gradient strength $\|\boldsymbol{g}\|$ and the time sequence parameters δ and Δ and that the diffusion of water molecules is measured in a predefined direction, without detecting water diffusion in other directions.

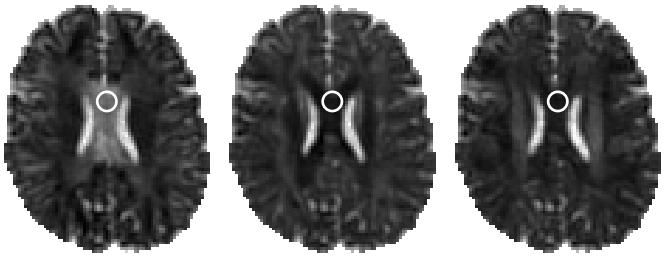

(a) ADC ∥ x-axis (b) ADC ∥ y-axis (c) ADC ∥ z-axis

Fig. 1.14: Axial ADC images along the x-, y- and z-axis. Note that in the region marked by the white circle, ADC ∥ x-axis is much higher than ADC ∥ y-axis and ADC ∥ z-axis, implying that the diffusion and the underlying microstructure are left-right oriented.

1.5.5 Diffusion tensor imaging (DTI)

Combining Eqs. (1.4) and (1.14), the Stejskal-Tanner equation can be modified to estimate the full diffusion tensor [Basser et al., 1994a,b, Basser and Pierpaoli, 1996,

Basser, 2002, Basser and Jones, 2002], resulting in a system of equations:

$$A(\boldsymbol{q}) = e^{-\boldsymbol{q}^{\mathrm{T}}\boldsymbol{D}\boldsymbol{q}(\Delta-\delta/3)} = e^{-\gamma^2\delta^2\|\boldsymbol{g}\|^2(\Delta-\delta/3)\hat{\boldsymbol{g}}^{\mathrm{T}}\boldsymbol{D}\hat{\boldsymbol{g}}} = e^{-b\hat{\boldsymbol{g}}^{\mathrm{T}}\boldsymbol{D}\hat{\boldsymbol{g}}} \tag{1.19}$$

with

$$\hat{\boldsymbol{g}} = \frac{\boldsymbol{g}}{\|\boldsymbol{g}\|} \tag{1.20}$$

Eq. (1.19) allows one to estimate the apparent diffusion tensor $\boldsymbol{D}$ from a collection of DW images $S(\boldsymbol{q})$ along different non-collinear gradient directions, along with a reference image $S(\mathbf{0})$. Given that $\boldsymbol{D}$ contains only 6 unique elements, at least 6 DW images are required to solve the system of equations. On the other hand, overdetermining the solution for $\boldsymbol{D}$ reduces the amount of noise propagating from the DW measurements into the calculated diffusion tensor [Papadakis et al., 1999, 2000]. Moreover, based on Monte Carlo simulations, it has been shown that at least 20 unique gradient directions are necessary for a robust estimation of anisotropy, whereas at least 30 unique sampling orientations are required for a robust estimation of the tensor-orientation [Jones, 2004]. Note that Eq. (1.19) still assumes that diffusion is Gaussian.

$$\boldsymbol{D} = \begin{bmatrix} D_{xx} & D_{xy} & D_{xz} \\ D_{xy} & D_{yy} & D_{yz} \\ D_{xz} & D_{yz} & D_{zz} \end{bmatrix}$$

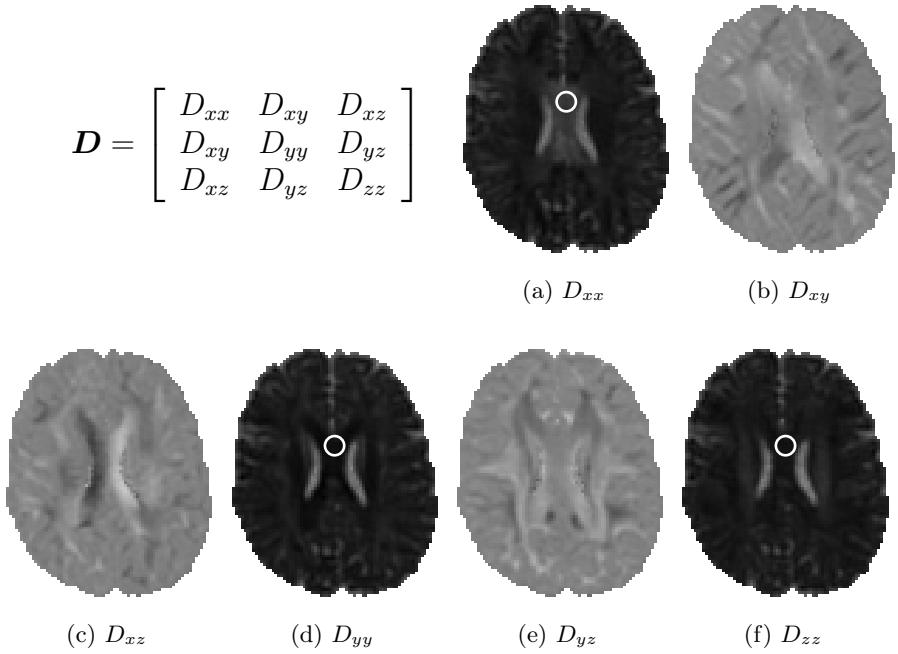

(a) D_{xx} (b) D_{xy}

(c) D_{xz} (d) D_{yy} (e) D_{yz} (f) D_{zz}

Fig. 1.15: Individual DT components (axial slices). Note that in the region marked by the white circle, D_{xx} is much higher than D_{yy} and D_{zz}, implying that the diffusion and the underlying microstructure are left-right oriented.

1.5.5.1 Geometrical interpretation

Since $\boldsymbol{D}$ is a symmetric and positive definite second-rank tensor, it can be decomposed into real eigenvalues and eigenvectors:

$$\boldsymbol{D} = \boldsymbol{E}\boldsymbol{\Lambda}\boldsymbol{E}^{-1} \tag{1.21}$$

with

$$\boldsymbol{E} = \begin{bmatrix} \boldsymbol{e}_1 & \boldsymbol{e}_2 & \boldsymbol{e}_3 \end{bmatrix} \quad \text{and} \quad \boldsymbol{\Lambda} = \begin{bmatrix} \lambda_1 & 0 & 0 \\ 0 & \lambda_2 & 0 \\ 0 & 0 & \lambda_3 \end{bmatrix} \tag{1.22}$$

defining the matrix of orthonormal eigenvectors $\boldsymbol{e}_i$ and the diagonal matrix of eigenvalues λ_i (with $i = 1, 2, 3$), respectively [Hasan et al., 2001]. The three eigenvalues λ_i correspond to the diffusivities along the principle axes of the diffusion tensor. The orientation of the principle axes is given by the three eigenvectors $\boldsymbol{e}_i$, which are mutually orthogonal by definition. Consequently, the principal axes of the ellipsoidal isoprobability surface of the diffusion tensor and their corresponding radii, are given by the eigenvectors $\boldsymbol{e}_i$ and the eigenvalues λ_i, respectively. By convention, the eigenvalues and their corresponding eigenvectors are sorted as follows: $\lambda_1 > \lambda_2 > \lambda_3$. Consequently, the first eigenvector $\boldsymbol{e}_1$ describes the dominant diffusion direction and is also called the principal diffusion vector (PDV).

1.5.5.2 Scalar measures

From the eigenvalues, different scalar measures can be calculated, that characterize the diffusion profile [Bahn, 1999]:

- The mean diffusivity (MD) (Fig. 1.17f) is a measure of the average diffusion:

$$\mathrm{MD} = \frac{\lambda_1 + \lambda_2 + \lambda_3}{3} = \langle\lambda\rangle \tag{1.23}$$

  MD is typically much higher in CSF than in the parenchyma (WM and GM). Inside the CSF and inside the parenchyma MD is typically homogeneous.

- The fractional anisotropy (FA) (Fig. 1.17g) is a measure of the degree of diffusion anisotropy [Pierpaoli and Basser, 1996]:

$$\mathrm{FA} = \sqrt{\frac{3}{2}} \frac{\sqrt{(\lambda_1 - \langle\lambda\rangle)^2 + (\lambda_2 - \langle\lambda\rangle)^2 + (\lambda_3 - \langle\lambda\rangle)^2}}{\sqrt{\lambda_1^2 + \lambda_2^2 + \lambda_3^2}} \tag{1.24}$$

  The FA is appropriately normalized so that it takes values from zero (when diffusion is isotropic) to one (when diffusion is constrained along one axis only). FA is typically much higher in the WM structures than in the CSF and GM, due to the WM's highly organized and tightly packed myelinated axons. Because of this, FA is often used as a surrogate marker for WM 'integrity' [Beaulieu, 2002].

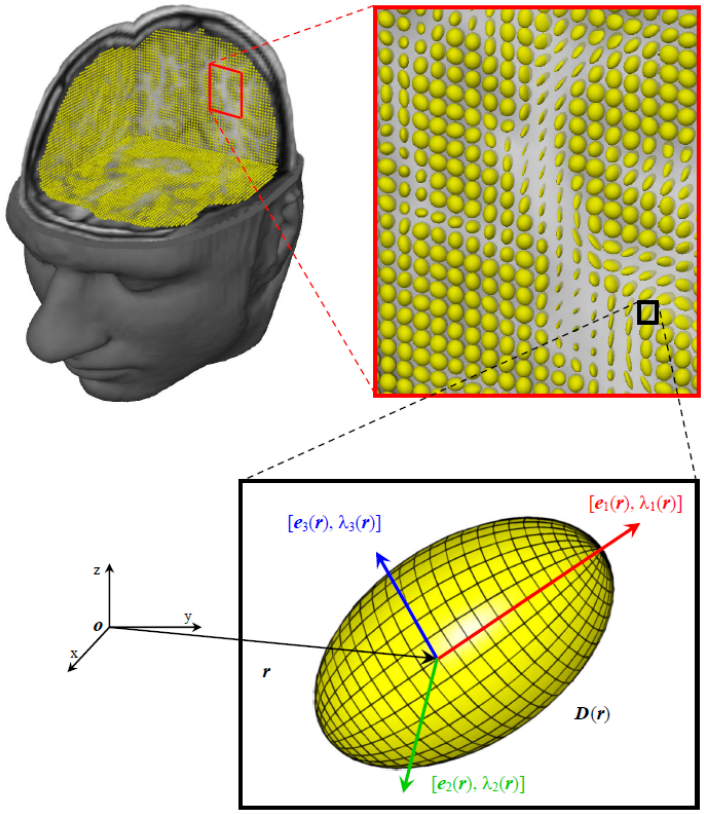

Fig. 1.16: Isoprobability surfaces derived from the diffusion tensor field. Note that in each voxel the isoprobability surface is an ellipsoid which is uniquely defined by the tensors' eigenvectors and eigenvalues. Image courtesy of Alexander Leemans.

- The axial diffusivity (AD) (Fig. 1.17d) is a measure of diffusion along the first eigenvector:

$$\mathrm{AD} = \lambda_1 \tag{1.25}$$

- The radial diffusivity (RD) (Fig. 1.17e) is a measure of the average diffusion perpendicular to the first eigenvector:

$$\mathrm{RD} = \frac{\lambda_2 + \lambda_3}{2} \tag{1.26}$$

  Decreased AD but unchanged RD is typically assumed to indicate a lower axonal density or axonal damage, while increased RD but unchanged AD is typically assumed to indicate demyelination [Beaulieu, 2002]. As such, AD and RD allow a more specific interpretation of the general concept of WM 'integrity' associated with FA.

- The linear coefficient (CL) (Fig. 1.17j) is a measure of the linearity of the diffusion tensor profile [Westin et al., 2002]:

$$\mathrm{CL} = \frac{\lambda_1 - \lambda_2}{\lambda_1} \tag{1.27}$$

  As with the FA, the CL is typically much higher in the highly organized WM structures than in the CSF and GM.

- The planar coefficient (CP) (Fig. 1.17k) is a measure of the planarity of the diffusion tensor profile [Westin et al., 2002]:

$$\mathrm{CP} = \frac{\lambda_2 - \lambda_3}{\lambda_1} \tag{1.28}$$

  The CP is typically high in regions where multiple underlying fiber orientations are lying in the same plane.

- The spherical coefficient (CS) (Fig. 1.17l) is a measure of the sphericity of the diffusion tensor profile [Westin et al., 2002]:

$$\mathrm{CS} = \frac{\lambda_3}{\lambda_1} \tag{1.29}$$

  The CS is typically much higher in the CSF and GM than in the WM. However, it is also high in regions where multiple underlying fiber orientations are known to cross. CL, CP and CS lie in the range from zero to one, and their sum is equal to one.

Note, that since all these parameters are calculated from the eigenvalues, they will be rotationally invariant by definition. For visualization purposes, an FA map (Fig. 1.17g) is often combined with a direction encoding RGB-map (Fig. 1.17h), where the color represents the orientation of the first eigenvector (red: left-right oriented; green: anterior-posterior; blue: superior-inferior) [Pajevic and Pierpaoli, 1999] and the intensity of the map reflects the anisotropy (Fig. 1.17i).

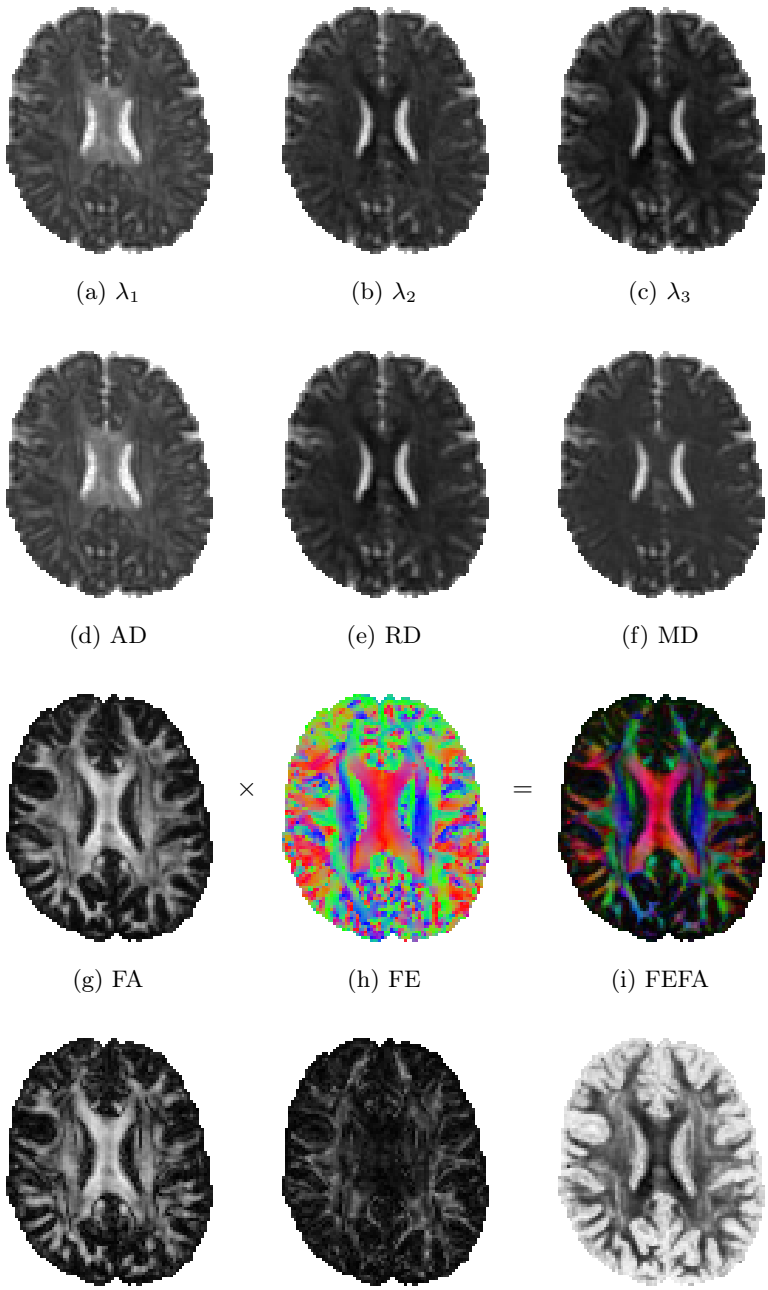

Fig. 1.17: Overview of the common scalar measures derived from the DT eigenvalues.

1.6 Applications

Diffusion MRI is a powerful noninvasive tool to study complex neural tissue architecture. Scalar measures derived with diffusion MRI, such as AD, RD, MD, and FA, have been used to study a broad range of neurological conditions including, but not limited to, stroke [Beauchamp et al., 1998, Keir and Wardlaw, 2000, Sotak, 2002, Kane et al., 2007], tumors [Field and Alexander, 2004], various white matter diseases such as dementia, multiple sclerosis, amyotrophic lateral sclerosis and Alzheimer's disease [Horsfield and Jones, 2002] and psychiatric disorders such as schizophrenia [Kubicki et al., 2007]. In addition, diffusion MRI has been used extensively to study brain development [Neil et al., 2002] and aging [Moseley, 2002, Sullivan and Pfefferbaum, 2006]. Recent reviews describing several applications in brain research are given by Dong et al. [2004] and Assaf and Pasternak [2008]. Although the central nervous system is the focus of most application studies, diffusion MRI has also been applied successfully in other fibrous tissue types such as cardiac muscle [Dou et al., 2002], skeletal muscle [Heemskerk et al., 2009] and plant tissue [Li et al., 1997].

1.7 Challenges and limitations

While the number of applications of diffusion MRI has exploded in recent years, obtaining reliable diffusion data remains a challenging task [Jones and Cercignani, 2010, Tournier et al., 2011]. The most important challenges will be briefly discussed here.

1.7.1 Motion

Diffusion MRI is sensitized to translational motion of water molecules, which is of the order of 5-15 µm assuming typical measurement times. Hence, a small amount of subject motion can lead to a significant amount of signal phase shift or signal loss, which can severely affect image quality [Skare and Andersson, 2001, Pierpaoli et al., 2003, Jones and Pierpaoli, 2005, Nunes et al., 2005]. For the brain, there are two major sources of subject motion: head motion and physiological motion.

Head motion causes global displacement of tissue, resulting in global misregistration of the different DW images. To reduce motion sensitivity, fast acquisition schemes such as single-shot echo-planar imaging (EPI) are commonly used. Additionally, head motion is often corrected for after the acquisition using rigid registration algorithms that realign the different DW images to a baseline scan, typically a non DW image [Netsch and van Muiswinkel, 2004]. However, large differences in contrast between the DW images, low SNR, and low spatial resolution, make such registration a challenging task. Additionally, one has to realize that the diffusion images contain orientational information, so any spatial transformation that is performed on the data must also be applied to the orientational information [Leemans and Jones, 2009].

Physiological motion, such as cardiac pulsation, causes local displacement of tissue, resulting in local misregistrations of the different DW images. Additionally, stretching and shearing of the tissue will cause incoherent motion of spins within

voxels, resulting in signal attenuation [Jones and Cercignani, 2010]. This additional signal attenuation will be perceived as extra diffusion parallel to the direction of the applied encoding gradient. Pulsation artifacts are usually alleviated using cardiac gating [Skare and Andersson, 2001, Nunes et al., 2005, Jones and Cercignani, 2010]. Cardiac gating times the acquisition of MR data to the primary source of physiological motion in order to minimize motion artifacts.

1.7.2 Eddy currents

Although EPI sequences offer improved acquisition times and therefore reduced susceptibility motion artifacts, they are subject to eddy current distortions introduced by the gradients, especially the large diffusion-encoding gradients [Jezzard et al., 1998]. When a magnetic field is time-varying, such as when ramping up a diffusion-encoding gradient, electric currents (eddy currents) will be generated in nearby conductors, generating local magnetic field gradients that will either add to or subtract from the subsequent gradients that are used for spatial encoding. In most imaging acquisitions, eddy currents are not a major problem. Spatial encoding gradients are normally applied for short periods such that the rising and falling edges of the gradient are close together in time, and thus there is a form of self-compensation. Diffusion gradients, however, are much stronger and due to the limited gradient amplitude on clinical systems, need to be applied for much longer than usual. The rising and falling parts of the gradient are now sufficiently temporally separated and the eddy currents are no longer self-compensated. Eddy currents will cause geometrical distortions in the DW images. Typically, eddy currents are compensated for using a twice-refocused EPI sequence [Reese et al., 2003]. In addition, eddy current distortions are often corrected for after the acquisition using affine registration algorithms that realign the different DW images to a non DW image [Netsch and van Muiswinkel, 2004]. However, large differences in contrast between the DW images, low SNR, and low spatial resolution, make such registration a challenging task.

1.7.3 Signal-to-noise ratio (SNR) and Spatial resolution

Given that diffusion MRI measures signal loss, it is inherently a noisy technique [Stejskal and Tanner, 1965]. Signal-to-noise Ratio (SNR) could be increased by increasing scan time, but since this puts additional strain on the patient and increases the likelihood of head motion, this is typically not desired. Diffusion MRI images typically employ large voxels to increase SNR (common voxel sizes for human diffusion MRI are $2 \times 2 \times 2$ mm^3 to $3 \times 3 \times 3$ mm^3). As a consequence, SNR and spatial resolution of diffusion MRI are much lower than that of standard anatomical MRI.

1.7.4 Partial volume effects

Given the large voxel sizes used in diffusion MRI, many voxels consist of a mixture of signals from different anatomical structures. It is known that ambiguous results are obtained when DTI is used to study regions in which WM fibers cross or

multiple fibers merge [Alexander et al., 2001, Tuch et al., 2002, Wheeler-Kingshott and Cercignani, 2009]. In such regions, it can be shown that the second-rank diffusion tensor model is incapable of describing multiple fiber orientations within an individual voxel [Tuch et al., 2002]. The acquired signal of a single voxel can be considered as the average signal of the differently oriented fiber structures. Therefore, it is important to keep in mind that DTI is only valid for unidirectional fiber bundles that are large with respect to the voxel size. Fig. 1.18 shows an example of DTI in a voxel containing crossing fibers. More information on this issue and possible solutions can be found in Chapter 2.

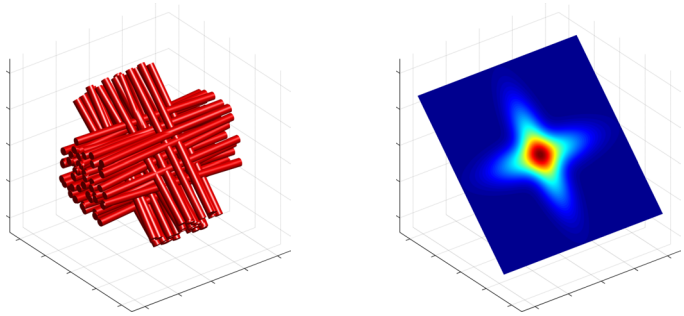

(a) environment

(b) true PDF

(c) true isoprobability surface

(d) DTI isoprobability surface

Fig. 1.18: Diffusion in an environment with multiple fiber populations. Note that while the true diffusion PDF (b) and its isoprobability surface (c) are able to characterize the underlying fiber populations (a), the diffusion tensor model cannot (d).

Bibliography

A. L. Alexander, K. M. Hasan, M. Lazar, J. S. Tsuruda, and D. L. Parker. Analysis of partial volume effects in diffusion-tensor MRI. *Magnetic Resonance in Medicine*, 45(5):770–780, 2001.

Y. Assaf and O. Pasternak. Diffusion tensor imaging (DTI)-based white matter

mapping in brain research: a review. *Journal of Molecular Neuroscience*, 34(1): 51–61, 2008.

M. M. Bahn. Comparison of scalar measures used in magnetic resonance diffusion-tensor imaging. *Journal of Magnetic Resonance*, 139(1):1–7, 1999.

P. J. Basser. Relationships between diffusion tensor and q-space MRI. *Magnetic Resonance in Medicine*, 47(2):392–397, 2002.

P. J. Basser and D. K. Jones. Diffusion-tensor MRI: theory, experimental design and data analysis–a technical review. *NMR in Biomedicine*, 15(7-8):456–467, 2002.

P. J. Basser and C. Pierpaoli. Microstructural and physiological features of tissues elucidated by quantitative-diffusion-tensor MRI. *Journal of Magnetic Resonance Series B*, 111(3):209–219, 1996.

P. J. Basser, J. Mattiello, and D. LeBihan. Estimation of the effective self-diffusion tensor from the NMR spin echo. *Journal of Magnetic Resonance Series B*, 103: 247–247, 1994a.

P. J. Basser, J. Mattiello, and D. LeBihan. MR diffusion tensor spectroscopy and imaging. *Biophysical Journal*, 66(1):259–267, 1994b.

N. J. Beauchamp, A. M. Ulug, T. J. Passe, and P. C. Van Zijl. MR diffusion imaging in stroke: review and controversies. *Radiographics*, 18(5):1269, 1998.

C. Beaulieu. The basis of anisotropic water diffusion in the nervous system–a technical review. *NMR in Biomedicine*, 15(7-8):435–455, 2002.

F. Bloch, W. W. Hansen, and M. Packard. Nuclear induction. *Physical Review*, 70 (7-8):460–474, 1946.

R. Brown. A brief account of microscopical observations made in the month on June, July and August 1828 on the particles contained in the pollen of plants and on the general existence of active molecules in organic and inorganic bodies. *Philosophical Magazine*, 4:161–173, 1828.

P. T. Callaghan, C. D. Eccles, and Y. Xia. NMR microscopy of dynamic displacements: k-space and q-space imaging. *Journal of Physics E: Scientific Instruments*, 21:820, 1988.

H. Y. Carr and E. M. Purcell. Effects of diffusion on free precession in nuclear magnetic resonance experiments. *Physical Review*, 94(3):630, 1954.

T. L. Chenevert, J. A. Brunberg, and J. G. Pipe. Anisotropic diffusion in human white matter: demonstration with MR techniques in vivo. *Radiology*, 177(2):401, 1990.

Q. Dong, R. C. Welsh, T. L. Chenevert, R. C. Carlos, P. Maly-Sundgren, D. M. Gomez-Hassan, and S. K. Mukherji. Clinical applications of diffusion tensor imaging. *Journal of Magnetic Resonance Imaging*, 19(1):6–18, 2004.

M. Doran, J. V. Hajnal, N. V. Bruggen, M. D. King, I. R. Young, and G. M. Bydder. Normal and abnormal white matter tracts shown by MR imaging using directional diffusion weighted sequences. *Journal of Computer Assisted Tomography*, 14(6):865, 1990.

J. Dou, T. G. Reese, W. Y. I. Tseng, and V. J. Wedeen. Cardiac diffusion MRI without motion effects. *Magnetic Resonance in Medicine*, 48(1):105–114, 2002.

A. Einstein. Über die von der molekularkinetischen Theorie der Wärme geforderte Bewegung von in ruhenden Flüssigkeiten suspendierten Teilchen. *Annalen der Physik*, 322(8):549–560, 1905.

A. Fick. On liquid diffusion. *Philosophical Magazine*, 10(63):30–39, 1855.

A. S. Field and A. L. Alexander. Diffusion tensor imaging in cerebral tumor diagnosis and therapy. *Topics in Magnetic Resonance Imaging*, 15(5):315, 2004.

E. L. Hahn. Spin echoes. *Physical Review*, 80(4):580, 1950.

K. M. Hasan, P. J. Basser, D. L. Parker, and A. L. Alexander. Analytical computation of the eigenvalues and eigenvectors in DT-MRI. *Journal of Magnetic Resonance*, 152(1):41–47, 2001.

A. M. Heemskerk, T. K. Sinha, K. J. Wilson, Z. Ding, and B. M. Damon. Quantitative assessment of DTI-based muscle fiber tracking and optimal tracking parameters. *Magnetic Resonance in Medicine*, 61(2):467–472, 2009.

M. A. Horsfield and D. K. Jones. Applications of diffusion-weighted and diffusion tensor MRI to white matter diseases–a review. *NMR in Biomedicine*, 15(7-8): 570–577, 2002.

P. Jezzard, A. S. Barnett, and C. Pierpaoli. Characterization of and correction for eddy current artifacts in echo planar diffusion imaging. *Magnetic Resonance in Medicine*, 39(5):801–812, 1998.

D. K. Jones. The effect of gradient sampling schemes on measures derived from diffusion tensor MRI: a Monte Carlo study. *Magnetic Resonance in Medicine*, 51 (4):807–815, 2004.

D. K. Jones and M. Cercignani. Twenty-five pitfalls in the analysis of diffusion MRI data. *NMR in Biomedicine*, 23(7):803–820, 2010.

D. K. Jones and C. Pierpaoli. Confidence mapping in diffusion tensor magnetic resonance imaging tractography using a bootstrap approach. *Magnetic Resonance in Medicine*, 53(5):1143–1149, 2005.

I. Kane, P. Sandercock, and J. Wardlaw. Magnetic resonance perfusion diffusion mismatch and thrombolysis in acute ischaemic stroke: a systematic review of the evidence to date. *Journal of Neurology, Neurosurgery & Psychiatry*, 78(5): 485, 2007.

S. L. Keir and J. M. Wardlaw. Systematic review of diffusion and perfusion imaging in acute ischemic stroke. *Stroke*, 31(11):2723–2731, 2000.

M. Kubicki, R. McCarley, C. F. Westin, H. J. Park, S. Maier, R. Kikinis, F. A. Jolesz, and M. E. Shenton. A review of diffusion tensor imaging studies in schizophrenia. *Journal of Psychiatric Research*, 41(1-2):15–30, 2007.

D. Le Bihan, E. Breton, D. Lallemand, P. Grenier, E. Cabanis, and M. Laval-Jeantet. MR imaging of intravoxel incoherent motions: application to diffusion and perfusion in neurologic disorders. *Radiology*, 161(2):401, 1986.

A. Leemans and D. K. Jones. The B-matrix must be rotated when correcting for subject motion in DTI data. *Magnetic Resonance in Medicine*, 61(6):1336–1349, 2009.

T. Q. Li, M. Häggkvist, and L. Ödberg. Porous structure of cellulose fibers studied by q-space NMR imaging. *Langmuir*, 13(13):3570–3574, 1997.

Z. P. Liang and P. C. Lauterbur. *Principles of magnetic resonance imaging: a signal processing perspective*, volume 4. Wiley-IEEE press, 2000.

M. E. Moseley. Diffusion tensor imaging and aging–a review. *NMR in Biomedicine*, 15(7-8):553–560, 2002.

M. E. Moseley, Y. Cohen, J. Kucharczyk, J. Mintorovitch, H. S. Asgari, M. F. Wendland, J. Tsuruda, and D. Norman. Diffusion-weighted MR imaging of anisotropic water diffusion in cat central nervous system. *Radiology*, 176(2):439, 1990.

J. Neil, J. Miller, P. Mukherjee, and P. S. Hüppi. Diffusion tensor imaging of normal and injured developing human brain-a technical review. *NMR in Biomedicine*, 15(7-8):543–552, 2002.

T. Netsch and A. van Muiswinkel. Quantitative evaluation of image-based distortion correction in diffusion tensor imaging. *IEEE Transactions on Medical Imaging*, 23(7):789–798, 2004.

R. G. Nunes, P. Jezzard, and S. Clare. Investigations on the efficiency of cardiac-gated methods for the acquisition of diffusion-weighted images. *Journal of Magnetic Resonance*, 177(1):102–110, 2005.

S. Pajevic and C. Pierpaoli. Color schemes to represent the orientation of anisotropic tissues from diffusion tensor data: application to white matter fiber tract mapping in the human brain. *Magnetic Resonance in Medicine*, 42(3):526–540, 1999.

N. G. Papadakis, D. Xing, C. L. H. Huang, L. D. Hall, and T. A. Carpenter. A comparative study of acquisition schemes for diffusion tensor imaging using MRI. *Journal of Magnetic Resonance*, 137(1):67–82, 1999.

N. G. Papadakis, C. D. Murrills, L. D. Hall, C. L. H. Huang, and T. Adrian Carpenter. Minimal gradient encoding for robust estimation of diffusion anisotropy. *Magnetic Resonance Imaging*, 18(6):671–679, 2000.

C. Pierpaoli and P. J. Basser. Toward a quantitative assessment of diffusion anisotropy. *Magnetic Resonance in Medicine*, 36(6):893–906, 1996.

C. Pierpaoli, S. Marenco, G. Rohde, D. K. Jones, and A. S. Barnett. Analyzing the contribution of cardiac pulsation to the variability of quantities derived from the diffusion tensor. In *Proceedings of the International Society for Magnetic Resonance In Medicine*, volume 11, page 70, Toronto, Canada, 2003.

E. M. Purcell, H. C. Torrey, and R. V. Pound. Resonance absorption by nuclear magnetic moments in a solid. *Physical Review*, 69:37–38, 1946.

T. G. Reese, O. Heid, R. M. Weisskoff, and V. J. Wedeen. Reduction of eddy-current-induced distortion in diffusion MRI using a twice-refocused spin echo. *Magnetic Resonance in Medicine*, 49(1):177–182, 2003.

S. Skare and J. L. R. Andersson. On the effects of gating in diffusion imaging of the brain using single shot EPI. *Magnetic Resonance Imaging*, 19(8):1125–1128, 2001.

C. H. Sotak. The role of diffusion tensor imaging in the evaluation of ischemic brain injury–a review. *NMR in Biomedicine*, 15(7-8):561–569, 2002.

E. O. Stejskal and J. E. Tanner. Spin diffusion measurements: spin echoes in the presence of a time-dependent field gradient. *The Journal of Chemical Physics*, 42(1):288, 1965.

E. V. Sullivan and A. Pfefferbaum. Diffusion tensor imaging and aging. *Neuroscience & Biobehavioral Reviews*, 30(6):749–761, 2006.

J. D. Tournier, S. Mori, and A. Leemans. Diffusion tensor imaging and beyond. *Magnetic Resonance in Medicine*, 65(6):1532–1556, 2011.

D. S. Tuch, T. G. Reese, M. R. Wiegell, N. Makris, J. W. Belliveau, and V. J. Wedeen. High angular resolution diffusion imaging reveals intravoxel white matter fiber heterogeneity. *Magnetic Resonance in Medicine*, 48(4):577–582, 2002.

C. F. Westin, S. E. Maier, H. Mamata, A. Nabavi, F. A. Jolesz, and R. Kikinis. Processing and visualization for diffusion tensor MRI. *Medical Image Analysis*, 6 (2):93–108, 2002.

C. A. M. Wheeler-Kingshott and M. Cercignani. About axial and radial diffusivities. *Magnetic Resonance in Medicine*, 61(5):1255–1260, 2009.

2

Multi-fiber reconstruction

Contents

The work in this chapter has been published as:

- **B. Jeurissen**, A. Leemans, J. D. Tournier, and J. Sijbers. HARDI-based methods for fiber orientation estimation. In *Proceedings of the International Society for Magnetic Resonance in Medicine*, volume 20, Melbourne, Australia, 2012

2.1 Introduction

Currently, DTI is the established method for assessing white matter microstructure and connectivity [Basser et al., 1994a,b, Mori and Van Zijl, 2002]. However, in voxels containing multiple fiber orientations (a condition often called 'crossing fibers'), the model has been shown to be inadequate [Alexander et al., 2001, Frank, 2001, Alexander et al., 2002, Frank, 2002, Tuch et al., 2002, Jansons and Alexander, 2003, Tournier et al., 2004, Tuch, 2004, Anderson, 2005, Wedeen et al., 2005]. Note that crossing fibers are inherent to DWI, due to its coarse resolution (in the order of 2 to 3 mm) compared with the radius of a single axon (0.1 to 10 µm).

The problem of DTI in crossing fiber regions, stems from the fact that it can only model Gaussian diffusion. Being a unimodal function, the Gaussian function is simply not equipped to deal with multiple fiber configurations. Fig. 2.1 illustrates this problem by showing various examples of complex fiber architecture and their corresponding diffusion tensor. Note that all of the biophysical properties of the underlying axons were kept constant in this experiment and that all changes are solely the consequence of a change in large-scale spatial organization. From Fig. 2.1, it is clear that there are two obvious consequences when using the tensor model in regions of crossing fibers. Firstly, the large-scale spatial organization will have a large impact on the scalar measures derived from the tensor [Alexander et al., 2001]. It is well known that tensor-derived measures, such as FA, as well of other indices such as axial and radial diffusivity, all of which are currently widely used, become ambiguous in these regions [Alexander et al., 2001, Wheeler-Kingshott and Cercignani, 2009, Jones and Cercignani, 2010]. In the example in Fig. 2.1, FA drops from 0.9 (bundle of straight fibers), over 0.6 (bending, fanning, two crossing fibers at acute angle) to 0.4 (two crossing fibers at a right angle), simply by changing the large-scale spatial organization. Note that introducing a third orthogonal fiber population would further reduce FA down to *zero*. This has important consequences for the interpretation of such measures, as they are commonly regarded as surrogate markers of WM 'integrity' [Beaulieu, 2002].

Secondly, it is clear from Fig. 2.1, that in the case of multiple fiber orientations, the first eigenvector of the diffusion tensor reflects the average fiber orientation, which does not necessarily correspond with any of the true underlying fiber orientations. In some cases, such as two orthogonally crossing fiber populations, the first eigenvector can even become undefined. In such cases, the principal orientation of the diffusion tensor will be completely determined by the noise in the data. This mismatch between the estimated fiber orientation and the true fiber orientation is extremely problematic for tensor-based tractography methods ([Frank, 2001, Tuch et al., 2002, Alexander et al., 2002, 2001, Frank, 2002]). Even if one wrong orientation estimate is encountered, the tracking algorithm may veer off-course, away from the true end-point of the WM tract, causing false negatives [Behrens et al., 2007, **Jeurissen** et al., 2011]; and/or into adjacent yet unrelated WM tracts, resulting in false positives [Pierpaoli et al., 2001, **Jeurissen** et al., 2011].

For these reasons, there is increasing interest in using more complex models than the DT that are able to resolve multiple fiber orientations in a single voxel. In the remainder of this chapter, we provide an overview of the most widely used multi-fiber reconstruction methods [Alexander, 2006, Seunarine and Alexander, 2009,

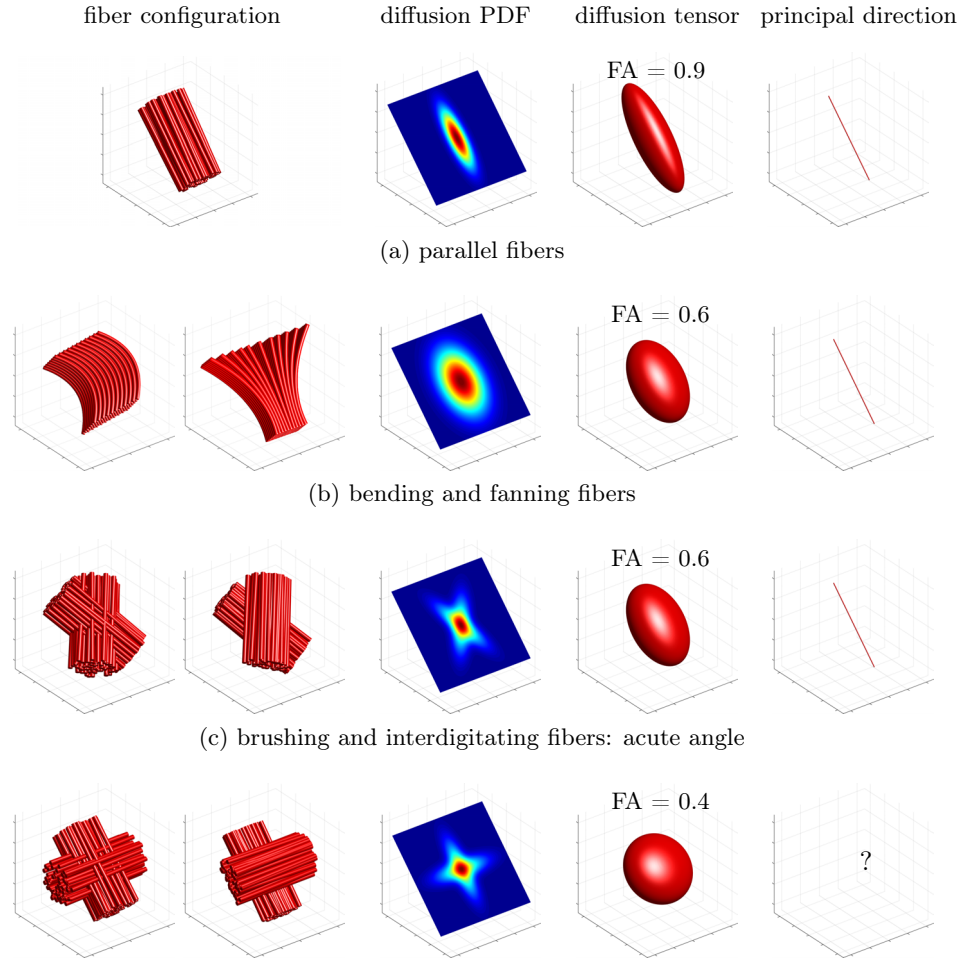

(a) parallel fibers

(b) bending and fanning fibers

(c) brushing and interdigitating fibers: acute angle

(d) brushing and interdigitating fibers: right angle

Fig. 2.1: The 'crossing fiber' problem. The first column shows a schematic representation of various fiber configurations at the length scale of a single voxel. The second column shows the corresponding diffusion PDF. The third and fourth column show the DTI model and its principal orientation. Note that the diffusion tensor model cannot resolve complex fiber configurations and the reported principal orientation can be considered the average fiber orientation. In the case of two orthogonal fiber bundles, the tensor becomes perfectly oblate, rendering the principal orientation undefined. Note further that, even from the perfect diffusion PDF, one cannot distinguish fanning from bending fiber configurations, and brushing from interdigitating fibers.

Tournier et al., 2011, **Jeurissen** et al., 2012]. Because the spherical deconvolution method will be used extensively in this thesis, extra space will be devoted to it. Given that some of these methods make use of spherical harmonics modeling to represent functions on the sphere, we begin with a short introduction to spherical harmonics.

2.2 Spherical harmonics

The spherical harmonics (SH) $Y_l^m(\theta,\phi)$ of order $l = 0, 1, 2, ...$ and degree $m = -l, ..., 0, ..., l$ are defined as:

$$Y_l^m(\theta,\phi) = \sqrt{\frac{(2l+1)}{4\pi}\frac{(l-m)!}{(l+m)!}}P_l^m(\cos\theta)e^{im\phi} \tag{2.1}$$

where (θ,ϕ) are spherical coordinates ($\theta \in [0,\pi], \phi \in [0,2\pi[$), and $P_l^m(\cdot)$ are the associated Legendre polynomials. It can be shown that Y_l^m is an orthonormal basis for complex functions of the unit sphere [Courant and Hilbert, 1953]. As a consequence, any function of the unit sphere $S(\theta,\phi)$ can be expressed by an infinite series of SH:

$$S(\theta,\phi) = \sum_{l=0}^{\infty}\sum_{m=-l}^{l} c_l^m \cdot Y_l^m(\theta,\phi) \tag{2.2}$$

Note that even order Y_l^m are antipodally symmetric, while odd order Y_l^m are antipodally anti-symmetric:

$$Y_l^m(\pi-\theta,\phi+\pi) = \begin{cases} Y_l^m(\theta,\phi) & \text{if } l \text{ is even} \\ -Y_l^m(\theta,\phi) & \text{if } l \text{ is odd} \end{cases} \tag{2.3}$$

Typically, the functions we want to represent using SH are real and antipodally symmetric. Therefore, a modified SH basis is defined that is also real and antipodally symmetric. In order to impose the symmetry constraint, only SH of even order are considered (see Eq. (2.3)). In order to impose the real-valued constraint, the real and imaginary parts of Y_l^m are chosen depending on the degree m. The modified spherical harmonics $Y_l^{'m}(\theta,\phi)$ of order $l = 0, 2, 4, ...$ and degree $m = -l, ..., 0, ..., l$ are then defined as:

$$Y_l^{'m}(\theta,\phi) = \begin{cases} \sqrt{2}\cdot \mathrm{Re}\left[Y_l^m(\theta,\phi)\right] & \text{if } m > 0 \\ Y_l^m(\theta,\phi) & \text{if } m = 0 \\ \sqrt{2}\cdot \mathrm{Im}\left[Y_l^{-m}(\theta,\phi)\right] & \text{if } m < 0 \end{cases} \tag{2.4}$$

or more explicitly as:

$$Y_l^{'m}(\theta,\phi) = \begin{cases} \sqrt{2}\cdot\sqrt{\frac{(2l+1)}{4\pi}\frac{(l-m)!}{(l+m)!}}P_l^m(\cos\theta)\cos(m\phi) & \text{if } m > 0 \\ \sqrt{\frac{(2l+1)}{4\pi}}P_l^0(\cos\theta) & \text{if } m = 0 \\ \sqrt{2}\cdot\sqrt{\frac{(2l+1)}{4\pi}\frac{(l+m)!}{(l-m)!}}P_l^{-m}(\cos\theta)\sin(-m\phi) & \text{if } m < 0 \end{cases} \tag{2.5}$$

It can be shown that $Y_l^{'m}$ forms an orthonormal basis for real and antipodally symmetric functions of the unit sphere [Descoteaux et al., 2007]. As a consequence any real and antipodally symmetric spherical function $S(\theta, \phi)$ can be expressed by an infinite series of modified SH:

$$S(\theta, \phi) = \sum_{l=0}^{\infty} \sum_{m=-l}^{l} c_l^m \cdot Y_l^{'m}(\theta, \phi) \tag{2.6}$$

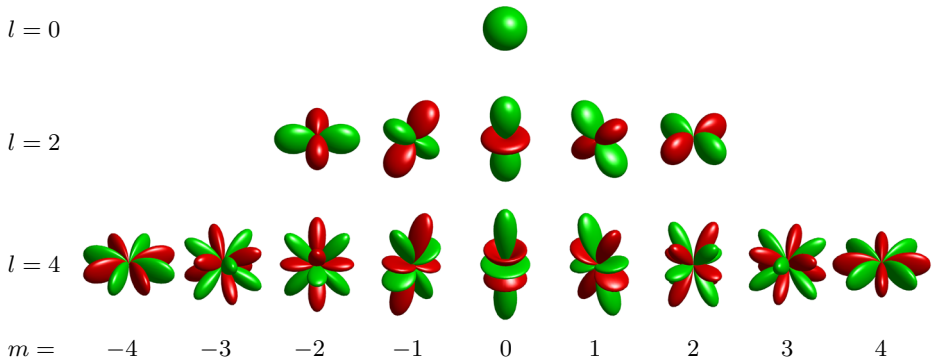

Fig. 2.2: The modified SH basis $Y_l^{'m}(\theta, \phi)$ up to order $l = 4$. The function value is visualized as the distance from the origin to the surface. Green indicates positive function values. Red indicates negative function values. Notice that the angular frequency of the basis functions increases with order l.

Fig. 2.2 shows the modified SH basis functions $Y_l^{'m}$ up to order $l = 4$. The higher order basis functions correspond to the higher angular frequency modes of the unit sphere, and thus relatively smooth functions can be represented concisely using a truncated SH series:

$$S(\theta, \phi) \approx \sum_{l=0}^{l_{\max}} \sum_{m=-l}^{l} c_l^m \cdot Y_l^{'m}(\theta, \phi) \tag{2.7}$$

where $\{c_l^m\}$ denote the SH coefficients and $l_{\max}$ is the SH order at which the series is truncated. Since only even degree coefficients are used, Eq. (2.7) consists of $n_c = (l_{\max} + 1) \times (l_{\max} + 2)/2$ terms. For a set of discrete samples of the unit sphere, Eq. (2.7) can be expressed as a linear system of equations:

$$\boldsymbol{s} = \boldsymbol{Y}\boldsymbol{c} \tag{2.8}$$

where $\boldsymbol{s}$ is the $n_s \times 1$ sample vector, $\boldsymbol{Y}$ is the $n_s \times n_c$ matrix constructed with the modified SH basis, $\boldsymbol{c}$ is the $n_c \times 1$ vector of SH coefficients. The coefficients $\boldsymbol{c}$ can now be estimated using least-squares minimization:

$$\hat{\boldsymbol{c}} = (\boldsymbol{Y}^{\mathrm{T}}\boldsymbol{Y})^{-1}\boldsymbol{Y}^{\mathrm{T}}\boldsymbol{s} \tag{2.9}$$

Note that, the modified SH series truncated at $l_{\max}$ has n_c degrees of freedom, requiring at least n_c spherical samples of the function S in order to solve Eq. (2.8).

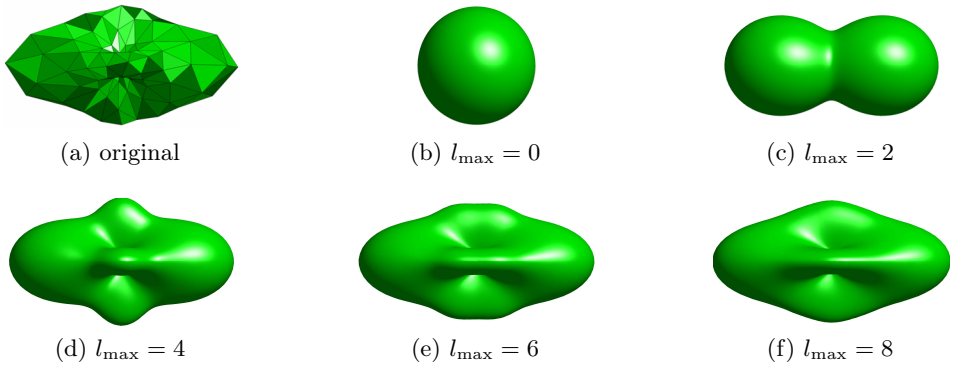

(a) original (b) $l_{\max} = 0$ (c) $l_{\max} = 2$

(d) $l_{\max} = 4$ (e) $l_{\max} = 6$ (f) $l_{\max} = 8$

Fig. 2.3: A DW signal being modeled by a modified SH series with increasing $l_{\max}$. Note that, as $l_{\max}$ increases, the truncated SH series more accurately represents the original signal. At $l_{\max} = 8$, the significant features of the DW signal are captured by the truncated SH series.

For example, to estimate the modified SH coefficients up till $l_{\max} = 8$, at least 45 spherical samples are required. Fig. 2.3 shows a DW signal acquired at a fixed $\boldsymbol{q}$-space radius being modeled by a modified SH series with increasing $l_{\max}$. A recent study has shown that the highest order for which significant terms can be found in *in vivo* DW signal profiles at $b = 3000$ s/mm^2 is 8 [Tournier et al., 2009].

2.3 Model-free approaches

Remember from Eq. (1.14) that the signal attenuation $S(\boldsymbol{q})/S(\boldsymbol{0})$ as a function of the $\boldsymbol{q}$-vector can be expressed as the 3D Fourier transform $\mathcal{F}$ of the diffusion probability density function $p(\boldsymbol{r})$. Methods based on $\boldsymbol{q}$-space will provide an estimate of $p(\boldsymbol{r})$ by directly exploiting this Fourier relationship. As there is no explicit need for a model of the diffusion, these methods are considered to be model-free.

An important concern with the $\boldsymbol{q}$-space approaches is that $p(\boldsymbol{r})$ does not necessarily reflect the true fiber orientation distribution [Tuch et al., 2003]. Fiber orientations are typically extracted from $p(\boldsymbol{r})$ by identifying the directions along which the probability of displacement is highest [Wedeen et al., 2005, 2008, Campbell et al., 2005, Perrin et al., 2005, Berman et al., 2008]. Although water molecules are most likely to move along the fiber orientation, moves along other, even perpendicular orientations are still common. As a consequence, closely aligned fiber orientations will be blurred together and thus be identified as a single fiber orientation [Zhan and Yang, 2006, Tournier et al., 2008]. Additionally, the overlapping of diffusion coming from different fiber populations, can introduce a bias in the estimated fiber orientations [Zhan and Yang, 2006, Tournier et al., 2008]. These issues are illustrated in Fig. 2.10, where we compare the fiber orientations extracted using both a model-free $\boldsymbol{q}$-space approach and a model-based approach. The blurring and the bias can be addressed by the introduction of a suitable model for diffusion

in WM, however these methods can than no longer be deemed model-free [Tuch et al., 2003, Descoteaux et al., 2009].

Another concern is that the Fourier relationship used by the $\boldsymbol{q}$-space approaches relies on infinitesimally short pulses (the narrow pulse regime). In practice, however, this requirement cannot be met, due to the limited gradient power available in clinical systems. As a consequence, p is subject to additional blurring [Bar-Shir et al., 2008, Yeh et al., 2010].

2.3.1 Diffusion spectrum imaging (DSI)

Diffusion spectrum imaging (DSI) attempts to measure the diffusion PDF $p(\boldsymbol{r})$ directly by applying the inverse Fourier transform on the $\boldsymbol{q}$-space samples $A(\boldsymbol{q}) = S(\boldsymbol{q})/S(\boldsymbol{0})$ [Wedeen et al., 2005]:

$$p(\boldsymbol{r}) = \mathcal{F}^{-1}\left[A(\boldsymbol{q})\right](\boldsymbol{r}) \tag{2.10}$$

As such, DSI makes no assumptions about the tissue microstructure or the shape of $p(\boldsymbol{r})$. In practice, DSI acquires measurements $S(\boldsymbol{q})$ for each of a Cartesian grid of $\boldsymbol{q}$-vectors (Fig. 2.4a) and reconstructs a discrete version of $p(\boldsymbol{x})$ by applying the 3D inverse fast Fourier transform (IFFT). The discrete representation of $p(\boldsymbol{r})$ we get from the IFFT is not directly useful for estimating the fiber orientations, since it is a function of 3D space. In practice, one usually calculates the diffusion orientation density function (dODF) $\psi(\hat{\boldsymbol{r}})$. ψ is simply the projection of p onto the unit-sphere [Tuch, 2004]:

$$\psi(\hat{\boldsymbol{r}}) = \int_0^\infty p(\alpha\hat{\boldsymbol{r}})\mathrm{d}\alpha \tag{2.11}$$

where $\hat{\boldsymbol{r}} = \boldsymbol{r}/\|\boldsymbol{r}\|$ is a unit-vector in the direction of $\boldsymbol{r}$. In practice, $\psi(\hat{\boldsymbol{r}})$ is calculated for each of a finite set of directions $\hat{\boldsymbol{r}}$ by taking steps along the line in direction $\hat{\boldsymbol{r}}$, interpolating the discrete p to estimate its value at each step and summing the values over all steps. The major limitation of DSI is the large amount of data required to perform the inverse Fourier transform and the correspondingly long acquisition time. To cover the Cartesian grid points in $\boldsymbol{q}$-space, typically requires 500-1000 measurements, which is an order of magnitude more than the typical spherical acquisition scheme used for DTI. In practice, image resolution is reduced in order to make such an acquisition clinically feasible.

2.3.2 Q-ball imaging (QBI)

Q-ball imaging (QBI) directly estimates the dODF using the significantly shorter and more efficient high-angular resolution diffusion imaging (HARDI) acquisition [Tuch, 2004]. As opposed to a full $\boldsymbol{q}$-space acquisition, a HARDI acquisition samples the $\boldsymbol{q}$-space only at a fixed $\boldsymbol{q}$-space radius, resulting in a high angular density spherical acquisition scheme (Fig. 2.4b). QBI approximates the dODF $\psi(\hat{\boldsymbol{r}})$ by the Funk-Radon transform (FRT) of the HARDI signal $S(\boldsymbol{q})$ [Tuch, 2004]:

$$\psi(\hat{\boldsymbol{r}}) \approx \int_{\substack{\boldsymbol{q}\perp\hat{\boldsymbol{r}} \\ \|\boldsymbol{q}\|=q'}} S(\boldsymbol{q})\ \mathrm{d}\boldsymbol{q} \tag{2.12}$$

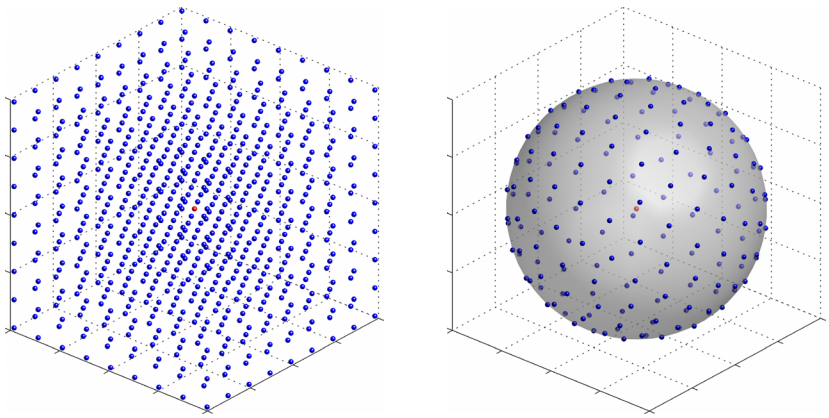

(a) Full Cartesian $\boldsymbol{q}$-space sampling (b) HARDI $\boldsymbol{q}$-space sampling

Fig. 2.4: Full Cartesian vs. HARDI $\boldsymbol{q}$-space sampling. $\boldsymbol{q}$-space sampling vectors are indicated as blue spheres. $\boldsymbol{q}$-space samples without diffusion weighting are situated at the origin and are indicated by a red sphere. $\boldsymbol{q}$-space samples further away from the origin have stronger diffusion weighting. For HARDI $\boldsymbol{q}$-space sampling, all sample points lie on the same sphere in $\boldsymbol{q}$-space, indicated by a transparent gray sphere.

Fig. 2.5 describes all the steps involved in the original q-ball algorithm. While the original implementation uses radial basis functions to interpolate $S(\boldsymbol{q})$ and represent $\psi(\hat{\boldsymbol{r}})$, more recent work has introduced the use of the modified spherical harmonics basis to represent $S(\boldsymbol{q})$ and $\psi(\hat{\boldsymbol{r}})$. This approach has the advantage that the FRT can be performed analytically [Hess et al., 2006, Descoteaux et al., 2007]. First $S(\boldsymbol{q})$ is represented using a finite modified SH series:

$$\hat{S}(\boldsymbol{q}) = \sum_{l=0}^{l_{\max}} \sum_{m=-l}^{l} c_l^m Y_l^{'m}(\boldsymbol{q}) \tag{2.13}$$

Substitution of Eq. (2.13) into Eq. (2.12) yields:

$$\psi(\hat{\boldsymbol{r}}) \approx \int\limits_{\substack{\boldsymbol{q}\perp\hat{\boldsymbol{r}} \\ \|\boldsymbol{q}\|=q'}} \sum_{l=0}^{l_{\max}} \sum_{m=-l}^{l} c_l^m Y_l^{'m}(\boldsymbol{q}) \, \mathrm{d}\boldsymbol{q} \tag{2.14}$$

which can be reordered to:

$$\psi(\hat{\boldsymbol{r}}) \approx \sum_{l=0}^{l_{\max}} \sum_{m=-l}^{l} c_l^m \int\limits_{\substack{\boldsymbol{q}\perp\hat{\boldsymbol{r}} \\ \|\boldsymbol{q}\|=q'}} Y_l^{'m}(\boldsymbol{q}) \, \mathrm{d}\boldsymbol{q} \tag{2.15}$$

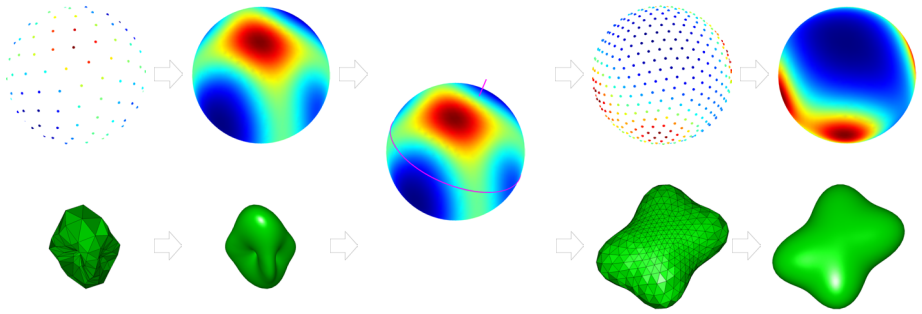

(a) disc. DWI (b) cont. DWI (c) FRT (d) disc. ODF (e) cont. ODF

Fig. 2.5: Overview of the original q-ball algorithm. First, the set of discrete measurements on a sphere in $\boldsymbol{q}$-space (a) are interpolated to a continuous representation (b). On the interpolated measurements the FRT (c) is performed for a set of discrete ODF sample points (d) by taking equal steps along the great circle and summing all the $\boldsymbol{q}$-space samples. Finally, the discrete ODF (d) is interpolated again to yield a continuous representation of the ODF (e).

It can be shown that the FRT can be performed analytically on the modified spherical harmonics basis functions [Hess et al., 2006, Descoteaux et al., 2007]:

$$\int\limits_{\substack{\boldsymbol{q}\perp\hat{\boldsymbol{r}}\\ \|\boldsymbol{q}\|=q'}} Y_l'^m(\boldsymbol{q})\ \mathrm{d}\boldsymbol{q} = 2\pi P_l(0) Y_l'^m(\hat{\boldsymbol{r}}) \tag{2.16}$$

where $P_l(\cdot)$ are the unassociated Legendre polynomials of order l. Hence, the ODF can be computed directly from the spherical harmonics representation of $S(\boldsymbol{q})$:

$$\psi(\hat{\boldsymbol{r}}) \approx \sum_{l=0}^{l_{\max}} \sum_{m=-l}^{l} 2\pi P_l(0) c_l^m Y_l'^m(\hat{\boldsymbol{r}}) \tag{2.17}$$

In other words, if $\boldsymbol{f}$ and $\boldsymbol{s}$ are the $n_c \times 1$ SH coefficient vectors of $\psi(\hat{\boldsymbol{r}})$ and $S(\boldsymbol{q})$, respectively, and $\boldsymbol{Q}$ is the $n_c \times n_c$ diagonal matrix with $\boldsymbol{Q}_{jj} = 2\pi P_{l_j}(0)$ where $l_j = (0, 2, 2, 2, 2, 2, 4, 4, 4, 4, 4, 4, 4, 4, 4, ...)$, the FRT can be performed directly on the SH coefficients as a single matrix multiplication:

$$\boldsymbol{f} = \boldsymbol{Q}\boldsymbol{s} \tag{2.18}$$

allowing very fast q-ball reconstructions.

QBI has been shown to be capable of producing results similar to DSI with substantially reduced acquisition times. In the absence of noise, the approximation of Eq. (2.12) becomes closer as the $\boldsymbol{q}$-radius q' increases. However, to ensure adequate SNR in the DW images, QBI is typically performed using low to intermediate q'-values. This will introduce significant blurring in the dODF, which will reduce the angular resolution and may introduce a bias [Tournier et al., 2008]. These issues are illustrated in Figs. 2.10 and 2.11, where we compare the fiber orientations extracted with QBI to those obtained with a model-based approach. Although

blurring and the bias can be reduced using large q'-values, this will reduce SNR and/or increase scan time.

2.3.3 Persistent angular structure MRI (PAS-MRI)

Persistent angular structure MRI (PAS-MRI) provides an estimate of the persistent angular structure (PAS) of the diffusion PDF [Jansons and Alexander, 2003]. Like QBI, PAS-MRI uses the much faster HARDI acquisition scheme. The underlying principle is that spins are assumed to diffuse by a fixed distance, with an angular distribution given by the PAS. With this definition of the radial dependence of the spin propagator, it becomes possible to perform the 3D Fourier transform required for $\boldsymbol{q}$-space analysis. PAS-MRI is combined with a maximum entropy constraint to improve the stability of the results. The maxima of the PAS correspond well to the underlying fiber orientations and the entropy constraint allows PAS-MRI to operate on low b-value data [Jansons and Alexander, 2003]. Although the first implementation of PAS-MRI was computationally intensive, limiting its practical use, new implementations make the computation time more manageable [Sakaie, 2008, Sweet and Alexander, 2010].

2.4 Model-based approaches

Model-based approaches rely on an explicit model that provides an estimate of the DW signal arising from a number of fiber populations. Typically, they operate on HARDI acquisitions.

2.4.1 Multi-tensor models

The multi-tensor model is a straightforward generalization of the single-tensor model, replacing the Gaussian model for p with a mixture of n Gaussian probability densities:

$$p(\boldsymbol{r}) = \sum_{i=1}^{n} a_i \frac{1}{\sqrt{(4\pi t)^3 \left|\boldsymbol{D}_i\right|}} e^{-\frac{\boldsymbol{r}^{\mathrm{T}} \boldsymbol{D}_i^{-1} \boldsymbol{r}}{4t}} \qquad \text{with} \qquad \sum_{i=1}^{n} a_i = 1 \tag{2.19}$$

The system of equations that relates the signal attenuation $A(\boldsymbol{q}) = S(\boldsymbol{q})/S(\boldsymbol{0})$ to the diffusion tensors of the underlying tissue becomes:

$$A(\boldsymbol{q}) = \sum_{i=1}^{n} a_i e^{-\boldsymbol{q}^{\mathrm{T}} \boldsymbol{D_i} \boldsymbol{q} (\Delta - \delta/3)} = \sum_{i=1}^{n} a_i e^{-b \hat{\boldsymbol{g}}^{\mathrm{T}} \boldsymbol{D_i} \hat{\boldsymbol{g}}} \qquad \text{with} \qquad \sum_{i=1}^{n} a_i = 1 \tag{2.20}$$

Note that the model assumes that the voxels contain n distinct fiber populations and that diffusing molecules stay within one population (no exchange). For $n = 2$, Eq. (2.20) has 13 free parameters: 12 for the six components of each DT and one for the volume fractions (as $a_2 = 1 - a_1$). To reduce the number of unknowns and improve the stability of the fitting procedure, several constraints can be imposed to the composing tensors. Typically, the shape of the tensor is assumed to be axially symmetric [Tuch et al., 2002, Behrens et al., 2007]. The anisotropy is also often

fixed [Tuch et al., 2002, Behrens et al., 2007], although some implementations allow the anisotropy to vary [Hosey et al., 2005]. An additional isotropic compartment is sometimes included to account for CSF or gray matter contamination [Hosey et al., 2005, Behrens et al., 2007]. One of the most widely used models is called the ball-and-sticks model, in which the DW signal is fitted to a combination of sticks, which represent different fiber populations with complete anisotropy; and a ball, which represents the isotropic compartment [Behrens et al., 2007].

One of the most important limitations of the multi-compartment models, is that they require an estimate of the number of fiber populations n to include into the model. Typically, this is achieved by model-selection, comparing the goodness of fit for different n [Alexander et al., 2002, Hosey et al., 2005, Parker and Alexander, 2003]. Other implementations use Bayesian automated relevance determination (ARD) to drive the volume fractions of excess fiber populations to zero [Behrens et al., 2007].

Closely related to the multi-tensor models is the more general family ofl multi-compartment models [Panagiotaki et al., 2012]. In particular, the composite hindered and restricted model of diffusion (CHARMED) models the DW signal attenuation $A(\boldsymbol{q}) = S(\boldsymbol{q})/S(\mathbf{0})$ with one extra-axonal (hindered) compartment $A_h(\boldsymbol{q})$, characterized using a single diffusion tensor, and and a number of intra-axonal (restricted) compartments $A_{r,i}(\boldsymbol{q})$ $(i = 1, ..., n)$, each characterized using a model of restricted diffusion within a cylinder [Assaf et al., 2004, Assaf and Basser, 2005]:

$$A(\boldsymbol{q}) = a_h A_h(\boldsymbol{q}) + \sum_{i=1}^{n} a_{r,i} A_{r,i}(\boldsymbol{q}) \qquad \text{with} \qquad a_h + \sum_{i=1}^{n} a_{r,i} = 1 \tag{2.21}$$

where a_h is the hindered volume fraction and $a_{r,i}$ are the n restricted volume fractions. Note that this approach requires a more demanding and more lengthy acquisition scheme with multiple and high b-values in order to discriminate between the hindered and restricted components of the model.

2.4.2 Spherical deconvolution (SD)

A different approach to overcome the limitation of the multi-tensor models is to use a continuous distribution of fiber orientations instead of a discrete number of fiber populations. Spherical deconvolution (SD) methods model the DW signal $S(\boldsymbol{q})$ as the convolution of the fiber orientation distribution function (fODF) $\phi(\hat{\boldsymbol{r}})$, which gives the fraction of fibers that are aligned along $\hat{\boldsymbol{r}}$, and a response function $R(\boldsymbol{q}; \hat{\boldsymbol{r}})$, which is the signal measured from a single fiber population with orientation $\hat{\boldsymbol{r}}$ [Tournier et al., 2004, Anderson, 2005, Alexander, 2006]:

$$S(\boldsymbol{q}) = \int \phi(\hat{\boldsymbol{r}}) R(\boldsymbol{q}; \hat{\boldsymbol{r}}) \, \mathrm{d}\hat{\boldsymbol{r}} \tag{2.22}$$

Fig. 2.6 explains the concept of spherical convolution by means of a simple fODF consisting of two distinct delta peaks. The response function is rotated to match each peak and the resulting DW signal profiles are summed to form the corresponding DW signal. Fundamentally, spherical convolution can be seen as an extension of the

multi-tensor model, where the number of discrete fiber populations n is increased to infinity. From Eq. (2.22) it is clear that the fODF $\phi(\hat{\boldsymbol{r}})$ can be recovered by

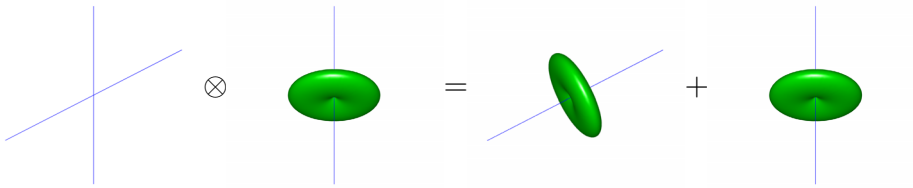

(a) fODF (b) single fiber signal (c) DW signal 1 (d) DW signal 2

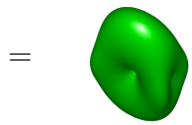

(e) DW signal

Fig. 2.6: Spherical convolution. The DW signal (e) is assumed to be the convolution of the fODF (a) and the single fiber response function (b). For the example of a discrete fODF consisting of two delta peaks (a), the convolution is obtained by rotating the response function to match each peak (c-d) and summing the resulting DW signal profiles (e). In general the fODF is not a discrete, but instead is a continuous orientation distribution function. The summation then becomes a continuous integral.

performing the spherical deconvolution operation [Tournier et al., 2004, Anderson, 2005]. The various implementations differ in the basis functions they use to represent the fODF, with many methods using the modified SH [Tournier et al., 2004, 2007, Anderson, 2005, Alexander, 2005], others using Wishart basis functions [Jian and Vemuri, 2007a,b]; and yet others working directly on the data [Dell'Acqua et al., 2007, Patel et al., 2010]. They also differ in the constraints placed on the solution, with many implementations introducing a non-negativity constraint [Tournier et al., 2007, Jian and Vemuri, 2007a,b, Dell'Acqua et al., 2007, Patel et al., 2010] and others including a maximum entropy term [Alexander, 2005]. Finally, they differ in the assumed response function, with some methods assuming a diffusion tensor model [Anderson, 2005, Dell'Acqua et al., 2007, Kaden et al., 2007, 2008], and others measuring it directly from the data [Tournier et al., 2004, 2007]. In the remainder of this section we will focus on the implementation using the modified SH basis functions as proposed by Tournier et al. [2004].

The deconvolution operation can be performed elegantly using the set of spherical and rotational harmonics [Healy et al., 1998, Tournier et al., 2004, Anderson, 2005]. In this framework, Eq. (2.22) becomes a simple matrix multiplication:

$$\boldsymbol{s} = \boldsymbol{R}\boldsymbol{f} \tag{2.23}$$

where $\boldsymbol{f}$ and $\boldsymbol{s}$ are the $n_c \times 1$ SH coefficient vectors of $\phi(\hat{\boldsymbol{r}})$ and $S(\boldsymbol{q})$, respectively; and $\boldsymbol{R}$ is the $n_c \times n_c$ rotational harmonic matrix of $R(\boldsymbol{q}; \hat{\boldsymbol{r}})$. Under the assumption

that the response function is axially symmetric, it can be shown that $\boldsymbol{R}$ is a diagonal matrix, whose elements can be calculated directly from the SH coefficients of the response function [Tournier et al., 2004, 2007]. From Eq. (2.23) then follows the formula for spherical deconvolution:

$$\boldsymbol{f} = \boldsymbol{R}^{-1}\boldsymbol{s} \tag{2.24}$$

which is a simple linear operation directly on the SH coefficients. However, as can be appreciated from Fig. 2.7, the spherical deconvolution problem is ill-posed and thus susceptible to noise, resulting in spurious high angular frequency fODF lobes and physically impossible high angular frequency negative lobes (Fig. 2.7c).

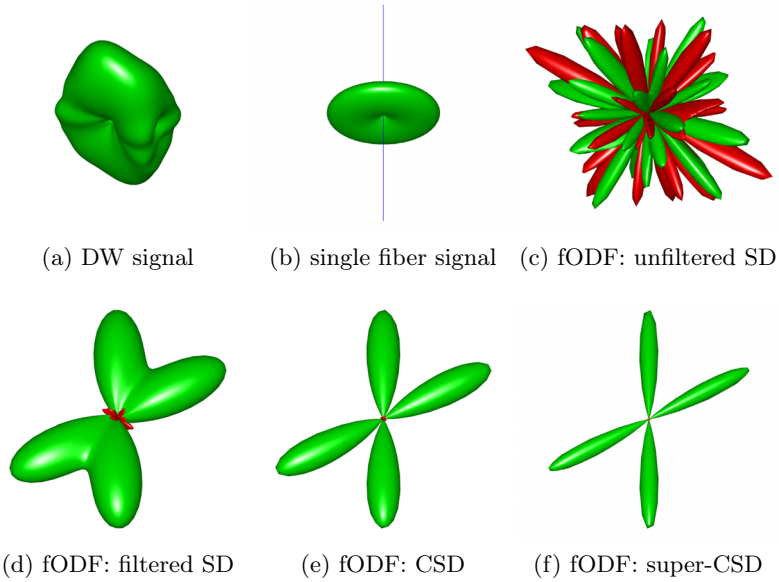

(a) DW signal (b) single fiber signal (c) fODF: unfiltered SD

(d) fODF: filtered SD (e) fODF: CSD (f) fODF: super-CSD

Fig. 2.7: Spherical deconvolution of a noisy DW signal (a) with a single fiber response function (b) using unfiltered (c), filtered (d), constrained (e) and super-resolved constrained deconvolution (f). Green indicates positive amplitude, while red indicates negative amplitude. Note that, by adding noise to the DW data, the unfiltered estimation becomes unstable, resulting in spurious high angular frequency fODF lobes and physically impossible high angular frequency negative lobes (c). Using a low-pass filter, which attenuates the high angular frequency components of the fODF, the negative lobes can be reduced to some extent (d). This, however, comes at the expense of reduced angular resolution (wider, overlapping lobes) (d). By imposing a non-negativity constraint onto the fODF, the physically impossible amplitudes can be avoided without the sacrifice of angular resolution, resulting in a sharp and accurate fODF without negative lobes (e). In addition, the additional information provided by the non-negativity constraint, allows to estimate the even sharper super-resolved fODF (f).

Note that, even for noiseless DW data (Fig. 2.8), the unfiltered fODF (Fig. 2.8c) contains small negative lobes which are physically impossible, resulting from the truncation of the SH series. This truncation artifact is equivalent to the Gibbs

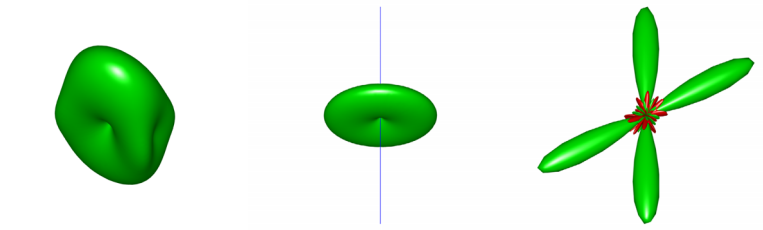

(a) DW signal (b) single fiber signal (c) fODF: unfiltered SD

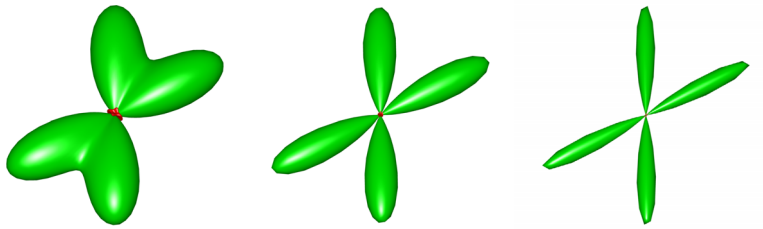

(d) fODF: filtered SD (e) fODF: CSD (f) fODF: super-CSD

Fig. 2.8: Spherical deconvolution of a noiseless DW signal (a) with a single fiber response function (b) using unfiltered (c), filtered (d), constrained (e) and super-resolved constrained deconvolution (f). Green indicates positive amplitude, while red indicates negative amplitude. Note that, even for noiseless DW data, the unfiltered fODF (c) contains lots of negative lobes which are physically impossible, resulting from the truncation of the SH series. This truncation artifact is equivalent to the Gibbs phenomenon seen in the Fourier series. The negative lobes can be reduced by employing a low pass filter on the SH coefficients (d). This, however, comes at the cost of reduced angular resolution (wider, overlapping lobes). By imposing a non-negativity constraint onto the fODF, the physically impossible amplitudes can be avoided without the sacrifice of angular resolution (e), resulting in a sharp and accurate fODF without negative lobes (e). In addition, the additional information provided by the non-negativity constraint, allows to estimate a very sharp super-resolved fODF (f).

phenomenon seen in the Fourier series. Using a low-pass filter, which attenuates the high angular frequency components of the fODF, the negative lobes can be reduced to some extent (Fig. 2.7d, 2.8d) [Tournier et al., 2004]. This, however, comes at the cost of reduced angular resolution (wider, overlapping lobes).

2.4.2.1 Constrained spherical deconvolution (CSD)

Without low-pass filtering, the noise will introduce large spurious negative lobes in the reconstructed fODF, which are physically impossible (Fig. 2.7c,2.8c). This observation provides an alternative way of reducing the ill-conditioning of the technique, by adding a constraint on the presence of these negative values in the fODF, rather than filtering out the high angular frequencies. Most WM voxels are expected to contain contributions from relatively few fiber bundles. Therefore, apart from a few well-defined peaks (corresponding to the fiber orientations), the fODF is expected to be zero over most of its support. As a result, eliminating any negative values in these regions must also strongly reduce the high frequency noise that generated them. This is the basic principle of constrained spherical deconvolution (CSD) [Tournier et al., 2007]. With the non-negativity constraint it becomes possible to perform the spherical deconvolution operation with drastically reduced noise sensitivity while retaining angular resolution, resulting in accurate and precise fiber orientation estimations at relatively low b-values (Figs. 2.7e,2.8e,2.10,2.11) [Tournier et al., 2007, 2008].

CSD is typically carried out as an iterative process. First, an initial estimate of the fODF is obtained using filtered SD. Then, a set of directions is identified, along which the fODF amplitude is negative. This information is then incorporated as a Tikhonov constraint, driving the amplitude of the fODF along those orientations to zero. Finally, an improved estimate of the fODF is obtained by solving the Tikhonov problem, providing a new set of negative amplitude directions. The procedure is repeated until convergence is achieved. Formally, the Tikhonov problem solved at every iteration is:

$$\boldsymbol{f}_{i+1} = \arg\min\{\|\boldsymbol{R}\boldsymbol{f}_i - \boldsymbol{s}\|^2 + \lambda^2\|\boldsymbol{L}\boldsymbol{f}_i\|^2\} \tag{2.25}$$

where $\boldsymbol{f_i}$ and $\boldsymbol{s}$ are the $n_c \times 1$ SH coefficient vectors of the current fODF estimate and the DW signal, respectively; and $\boldsymbol{R}$ is the $n_c \times n_c$ matrix that performs the spherical convolution operation. The first term is the data-driven part and ensures that the convolution of the current fODF estimate with the response function agrees with the DW signal. The second term is the regularization term, with λ the regularization parameter, which controls the relative weighting between the two terms (typically, $\lambda = 0.1$); and $\boldsymbol{L}$ the $n_t \times n_c$ constraint matrix, penalizing negative lobes. $\boldsymbol{L}$ is constructed as follows. At each iteration, the fODF is evaluated along a large set of n_t uniformly distributed orientations (typically, $n_t = 300$, calculated using electrostatic repulsion [Jones et al., 1999]):

$$\boldsymbol{a} = \boldsymbol{P}\boldsymbol{f}_i \tag{2.26}$$

where $\boldsymbol{P}$ is the $n_t \times n_c$ matrix, mapping $\boldsymbol{f}_i$ onto the amplitudes $\boldsymbol{a}$ along the n_t

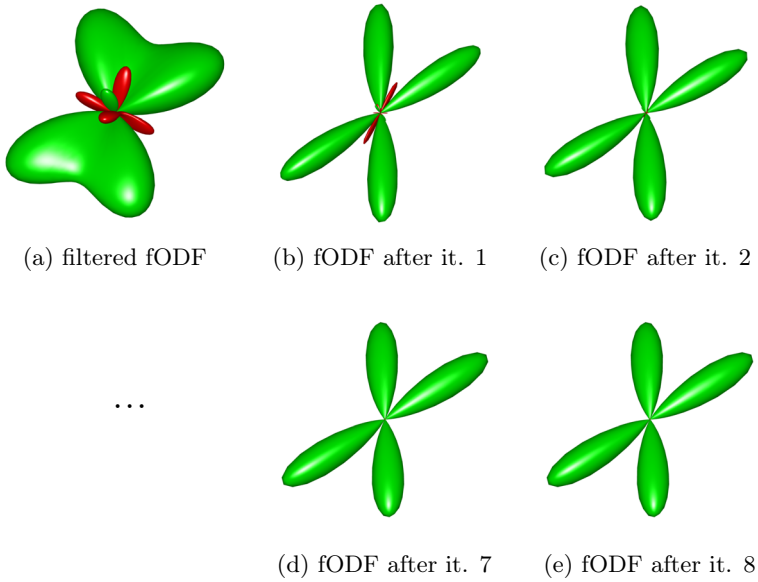

(a) filtered fODF (b) fODF after it. 1 (c) fODF after it. 2

... (d) fODF after it. 7 (e) fODF after it. 8

Fig. 2.9: Constrained spherical deconvolution (CSD). Green indicates positive amplitude, while red indicates negative amplitude. First, an initial estimate of the fODF is obtained using filtered SD (a). From this initial fODF, a set of orientations is identified along which the fODF amplitude is smaller than a user-specified threshold τ, controlling the amplitude below which the corresponding fiber orientation density is assumed to be zero. Using Tikhonov regularization the fODF amplitude along these orientations is constrained to zero (b). This procedure is performed iteratively (b-d) until convergence is achieved (e). Note that the negative lobes are reduced as the algorithm progresses and are almost completely gone after 2 iterations.

orientations. L is then defined as:

$$\boldsymbol{L}_{m,n} = \begin{cases} \boldsymbol{P}_{m,n} & \text{if } \boldsymbol{a}_m < \tau \\ 0 & \text{if } \boldsymbol{a}_m \geq \tau \end{cases} \tag{2.27}$$

where τ is a threshold controlling the amplitude below which the corresponding fiber orientation density is assumed to be zero. Typically, τ this is set to 10% of the mean initial fODF amplitude. It is clear that the regularization term will be minimal, in case there are no fODF amplitudes that fall below the threshold. After solving the Tikhonov problem, the improved fODF $\boldsymbol{f}_{i+1}$ is then used to form a new matrix $\boldsymbol{L}$ and the process is repeated until there is no further change in the matrix $\boldsymbol{L}$; in other words, until the set of directions that can be assumed to have zero fiber density is established. Convergence is typically reached within 5 to 10 iterations, with little or no dependence on SNR. Fig. 2.9 shows an example of an fODF being iteratively improved through CSD.

Apart from improving the stability of the deconvolution process, the additional information provided by the non-negativity constraint also allows the possibility of estimating more parameters than there are actual measurements (a concept known as super-resolution), provided that the amount of prior information is sufficient to constrain the additional degrees of freedom. In practice, this means that using 60 DW directions, it is possible to estimate the 91 modified SH coefficients required for harmonic order $l_{\max} = 12$ provided that the number of directions along which the fiber density can be assumed to be zero never falls below 31. This technique, called super-resolved CSD or super-CSD, allows to robustly resolve narrow inter-fiber angles and reduces the bias of closely aligned fiber orientations, using a limited amount of DW data (Figs. 2.7f, 2.8f, 2.10, 2.11) [Tournier et al., 2007, 2008].

2.4.2.2 Real data example

Fig. 2.12 shows results produced from data obtained from a healthy volunteer, consisting of 60 DW images acquired at $b = 3000$ s/mm^2, analyzed using both DTI (Fig. 2.12a) and CSD (Fig. 2.12b). Clearly, CSD is able to resolve fiber crossings in regions where DTI is not.

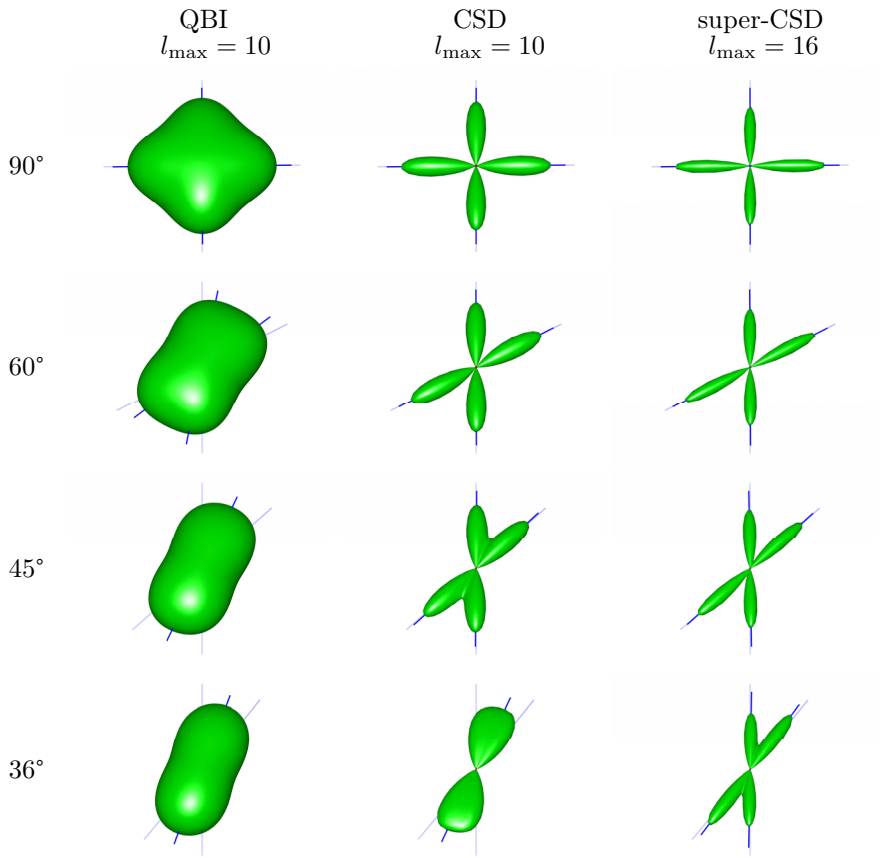

Fig. 2.10: dODF (QBI) vs. fODF (CSD and super-resolved CSD) for inter-fiber angles ranging from 90° to 36°, at a fixed b-value of $b = 4000\,\mathrm{s/mm^2}$. Note that the fODF is much sharper than the dODF. As a consequence, closely aligned fiber orientations (inter-fiber angles 45° and 36°) will be blurred together in the dODF and thus be identified as a single fiber orientation. Additionally, the blurring introduces a bias in the dODF orientations for all inter-fiber angles other than 90°. On the other hand, the fODF derived with CSD, is able to resolve much smaller inter-fiber angles. Additionally, the fiber orientations extracted from the CSD fODF are much less biased than those extracted from the QBI dODF. Using the super-resolved variant increases the angular resolution and reduces the bias even more.

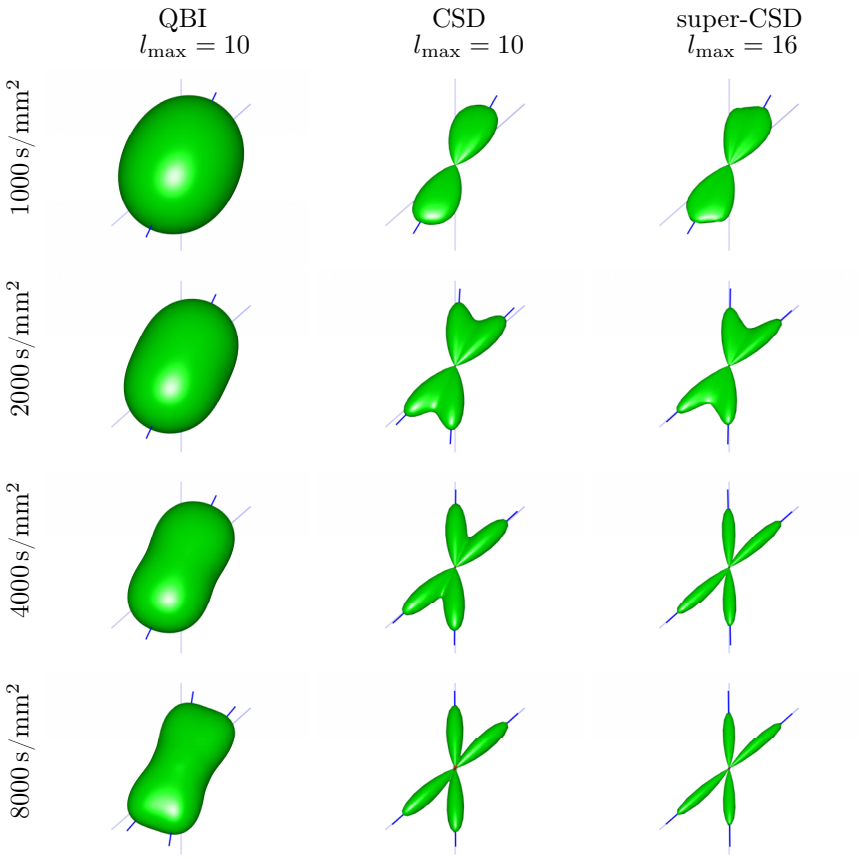

Fig. 2.11: dODF (QBI) vs. fODF (CSD and super-resolved CSD) for a fixed inter-fiber angle of 45°, at b-values ranging from $b = 1000\,\mathrm{s/mm^2}$ to $b = 8000\,\mathrm{s/mm^2}$. Note that the QBI dODF requires high b-values in order to resolve small inter-fiber angles. Note also, that while QBI is able to resolve the fiber orientations at $b = 8000\,\mathrm{s/mm^2}$, the fiber orientations exhibit a significant bias. CSD, on the other hand, is able to resolve small inter-fiber angles at much lower b-values and with much less bias, especially when using the super-resolved variant.

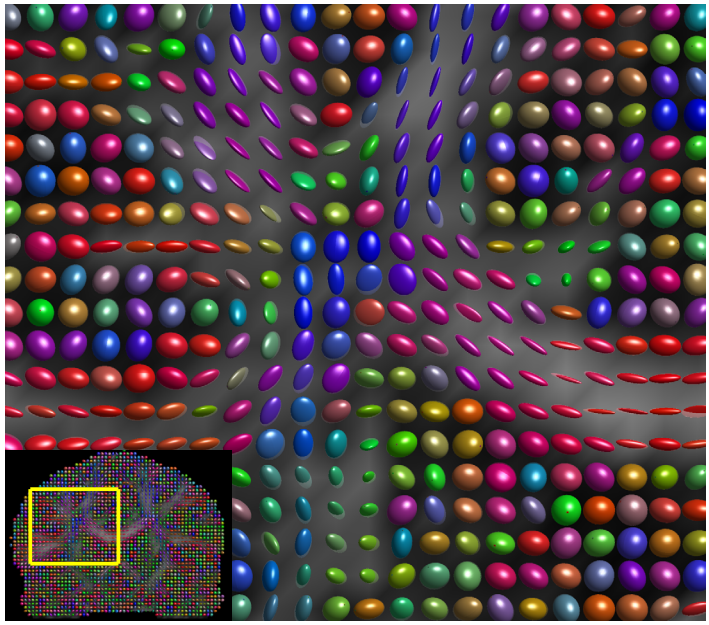

(a) DTI ellipsoids

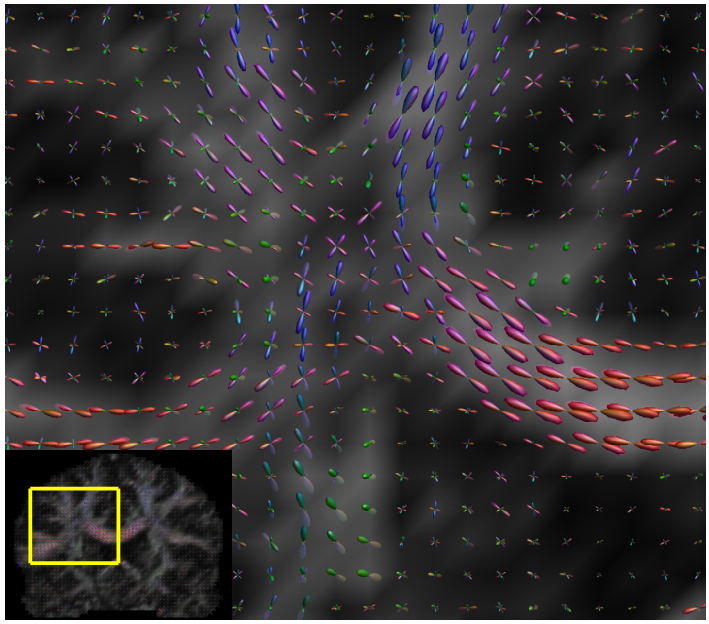

(b) CSD fODFs

Fig. 2.12: DTI ellipsoids (a) and CSD fODFs (b) for a coronal section showing lateral projections of the corpus callosum (left-right: red fODF lobes) crossing through the fibers of the corona radiata (inferior-superior: blue fODF lobes) and the fibers of the superior longitudinal fasciculus (anterior-posterior: green fODF lobes). DTI is unable to resolve these crossings.

2.5 Applications

2.5.1 Orientation information and tractography

Most of the methods described above aim to provide improved estimates of fiber orientations. As such, their primary application is to guide WM fiber tractography [Lazar, 2010, Tournier et al., 2011]. As an example, Fig. 2.13 shows the dominant fiber orientations extracted from CSD fODFs which could be used for the purpose of fiber tracking. WM fiber tractography will be discussed in more detail in Chapter 3.

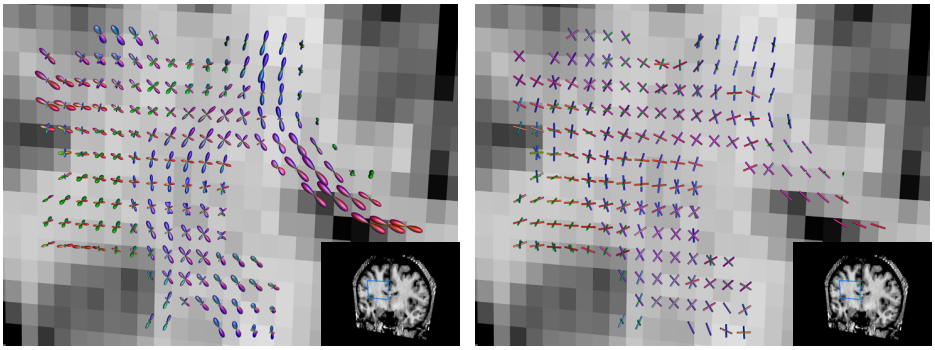

(a) CSD fODFs (b) dominant fiber orientations

Fig. 2.13: CSD fODF being used to extract fiber orientations in a crossing fiber region.

2.5.2 Quantitative information

Measures of diffusion anisotropy based on DTI have been used as surrogate markers of WM integrity in countless studies [Assaf and Pasternak, 2008], but these are profoundly affected by crossing fibers [Alexander et al., 2001, Wheeler-Kingshott and Cercignani, 2009, Jones and Cercignani, 2010]. As such, there is an increasing need to extract quantitative information in the WM that is insensitive to crossing fibers.

2.5.2.1 Generalized fractional anisotropy (GFA)

Analogously to FA in DTI, Tuch [2004] defines the generalized fractional anisotropy (GFA), which is a measure of the variation in the dODF $\psi(\hat{\boldsymbol{r}})$. Mathematically:

$$\mathrm{GFA} = \sqrt{\frac{\int(\psi(\hat{\boldsymbol{r}}) - \bar{\psi})^2 \mathrm{d}\hat{\boldsymbol{r}}}{\int \psi(\hat{\boldsymbol{r}})^2 \mathrm{d}\hat{\boldsymbol{r}}}} \qquad \text{with} \qquad \bar{\psi} = \frac{\int \psi(\hat{\boldsymbol{r}}) \mathrm{d}\hat{\boldsymbol{r}}}{4\pi} \tag{2.28}$$

This definition can be applied to any other function of the unit sphere, such as the fODF [Seunarine and Alexander, 2009]. While the sensitivity of this metric to crossing fiber effects is reduced to some extent compared to FA, GFA measures are still significantly lower in crossing fiber regions and are highly correlated with FA measures, hampering the general uptake of this metric.

2.5.2.2 Apparent fiber density (AFD)

A new approach is to use the volume fractions as identified by mixture model approaches as a quantitative index [Jbabdi et al., 2010, Raffelt et al., 2012]. Jbabdi et al. [2010] make tract-wise comparisons directly on the volume fractions as obtained with the ball-and-sticks model, assuming that increased volume fractions correspond to an increased axonal density along the corresponding fiber orientation. Raffelt et al. [2012] use the fODF derived with spherical deconvolution and make voxel wise comparisons directly on the full fODF. Their measure, dubbed 'apparent fiber density' (AFD) assumes that any differences in the fODF amplitude along a given orientation can be attributed to differences in the relative amount of underlying axons thought to be aligned with this orientation. Recent advances allow non-linear registration of fODF images [Raffelt et al., 2011], including appropriate reorientation and modulation, thus enabling group comparisons or correlations of AFD between patients and controls [Raffelt et al., 2012]. These approaches can potentially provide more reliable and more readily interpretable results than the commonly used DTI-derived anisotropy measures.

Bibliography

A. L. Alexander, K. M. Hasan, M. Lazar, J. S. Tsuruda, and D. L. Parker. Analysis of partial volume effects in diffusion-tensor MRI. *Magnetic Resonance in Medicine*, 45(5):770–780, 2001.

D. C. Alexander. Maximum entropy spherical deconvolution for diffusion MRI. In *Proceedings of the international conference on Information Processing in Medical Imaging*, pages 76–87, Glenwood Springs, Colorado, USA, 2005.

D. C. Alexander. Multiple-fiber reconstruction algorithms for diffusion MRI. *Annals of the New York Academy of Sciences*, 1064:113–133, 2006.

D. C. Alexander, G. J. Barker, and S. R. Arridge. Detection and modeling of non-Gaussian apparent diffusion coefficient profiles in human brain data. *Magnetic Resonance in Medicine*, 48(2):331–340, 2002.

A. W. Anderson. Measurement of fiber orientation distributions using high angular resolution diffusion imaging. *Magnetic Resonance in Medicine*, 54(5):1194–1206, 2005.

Y. Assaf and P. J. Basser. Composite hindered and restricted model of diffusion (CHARMED) MR imaging of the human brain. *NeuroImage*, 27(1):48–58, 2005.

Y. Assaf and O. Pasternak. Diffusion tensor imaging (DTI)-based white matter mapping in brain research: a review. *Journal of Molecular Neuroscience*, 34(1): 51–61, 2008.

Y. Assaf, R. Z. Freidlin, G. K. Rohde, and P. J. Basser. New modeling and experimental framework to characterize hindered and restricted water diffusion in brain white matter. *Magnetic Resonance in Medicine*, 52(5):965–978, 2004.

A. Bar-Shir, L. Avram, E. Özarslan, P. J. Basser, and Y. Cohen. The effect of the diffusion time and pulse gradient duration ratio on the diffraction pattern and the structural information estimated from q-space diffusion MR: experiments and simulations. *Journal of Magnetic Resonance*, 194(2):230–236, 2008.

P. J. Basser, J. Mattiello, and D. LeBihan. Estimation of the effective self-diffusion tensor from the NMR spin echo. *Journal of Magnetic Resonance Series B*, 103: 247–247, 1994a.

P. J. Basser, J. Mattiello, and D. LeBihan. MR diffusion tensor spectroscopy and imaging. *Biophysical Journal*, 66(1):259–267, 1994b.

C. Beaulieu. The basis of anisotropic water diffusion in the nervous system–a technical review. *NMR in Biomedicine*, 15(7-8):435–455, 2002.

T. E. J. Behrens, H. Johansen-Berg, S. Jbabdi, M. F. S. Rushworth, and M. W. Woolrich. Probabilistic diffusion tractography with multiple fibre orientations: what can we gain? *NeuroImage*, 34(1):144–155, 2007.

J. I. Berman, S. W. Chung, P. Mukherjee, C. P. Hess, E. T. Han, and R. G. Henry. Probabilistic streamline q-ball tractography using the residual bootstrap. *NeuroImage*, 39(1):215–222, 2008.

J. S. W. Campbell, K. Siddiqi, V. V. Rymar, A. F. Sadikot, and G. B. Pike. Flow-based fiber tracking with diffusion tensor and q-ball data: validation and comparison to principal diffusion direction techniques. *NeuroImage*, 27(4):725–736, 2005.

R. Courant and D. Hilbert. *Methods of mathematical physics: Vol. 1.* Wiley, 1953.

F. Dell'Acqua, G. Rizzo, P. Scifo, R. A. Clarke, G. Scotti, and F. Fazio. A model-based deconvolution approach to solve fiber crossing in diffusion-weighted MR imaging. *IEEE Transactions on Biomedical Engineering*, 54(3):462–472, 2007.

M. Descoteaux, E. Angelino, S. Fitzgibbons, and R. Deriche. Regularized, fast, and robust analytical Q-ball imaging. *Magnetic Resonance in Medicine*, 58(3): 497–510, 2007.

M. Descoteaux, R. Deriche, TR Knösche, and A. Anwander. Deterministic and probabilistic tractography based on complex fibre orientation distributions. *IEEE Transactions on Medical Imaging*, 28(2):269–286, 2009.

L. R. Frank. Anisotropy in high angular resolution diffusion-weighted MRI. *Magnetic Resonance in Medicine*, 45(6):935–939, 2001.

L. R. Frank. Characterization of anisotropy in high angular resolution diffusion-weighted MRI. *Magnetic Resonance in Medicine*, 47:1083–1099, 2002.

D. M. Healy, H. Hendriks, and Kim P. T. Spherical Deconvolution. *Journal of Multivariate Analysis*, 67(1):1–22, 1998.

C. P. Hess, P. Mukherjee, E. T. Han, D. Xu, and D. B. Vigneron. Q-ball reconstruction of multimodal fiber orientations using the spherical harmonic basis. *Magnetic Resonance in Medicine*, 56(1):104–117, 2006.

T. Hosey, G. Williams, and R. Ansorge. Inference of multiple fiber orientations in high angular resolution diffusion imaging. *Magnetic Resonance in Medicine*, 54 (6):1480–1489, 2005.

K. M. Jansons and D. C. Alexander. Persistent angular structure: new insights from diffusion magnetic resonance imaging data. *Inverse problems*, 19(5):1031–1046, 2003.

S. Jbabdi, T. E. J. Behrens, and S. M. Smith. Crossing fibres in tract-based spatial statistics. *NeuroImage*, 49(1):249–256, 2010.

B. Jeurissen, A. Leemans, D. K. Jones, J. D. Tournier, and J. Sijbers. Probabilistic fiber tracking using the residual bootstrap with constrained spherical deconvolution. *Human Brain Mapping*, 32:461–479, 2011.

B. Jeurissen, A. Leemans, J. D. Tournier, and J. Sijbers. HARDI-based methods for fiber orientation estimation. In *Proceedings of the International Society for Magnetic Resonance in Medicine*, volume 20, Melbourne, Australia, 2012.

B. Jian and B. C. Vemuri. Multi-fiber reconstruction from diffusion MRI using mixture of wisharts and sparse deconvolution. In *Proceedings of the international conference on Information Processing in Medical Imaging*, pages 384–395, Kerkrade, The Netherlands, 2007a.

B. Jian and B. C. Vemuri. A unified computational framework for deconvolution to reconstruct multiple fibers from diffusion weighted MRI. *IEEE Transactions on Medical Imaging*, 26(11):1464–1471, 2007b.

D. K. Jones and M. Cercignani. Twenty-five pitfalls in the analysis of diffusion MRI data. *NMR in Biomedicine*, 23(7):803–820, 2010.

D. K. Jones, M. A. Horsfield, and A. Simmons. Optimal strategies for measuring diffusion in anisotropic systems by magnetic resonance imaging. *Magnetic Resonance in Medicine*, 42(3):515–525, 1999.

E. Kaden, T. R. Knösche, and A. Anwander. Parametric spherical deconvolution: Inferring anatomical connectivity using diffusion MR imaging. *NeuroImage*, 37 (2):474–488, 2007.

E. Kaden, A. Anwander, and T. R. Knösche. Variational inference of the fiber orientation density using diffusion MR imaging. *NeuroImage*, 42(4):1366–1380, 2008.

M. Lazar. Mapping brain anatomical connectivity using white matter tractography. *NMR in Biomedicine*, 23:821–835, 2010.

S. Mori and P. C. M. Van Zijl. Fiber tracking: principles and strategies-a technical review. *NMR in Biomedicine*, 15(7-8):468–480, 2002.

E. Panagiotaki, T. Schneider, B. Siow, M. G. Hall, M. F. Lythgoe, and D. C. Alexander. Compartment models of the diffusion MR signal in brain white matter: a taxonomy and comparison. *NeuroImage*, 59(3):2241–2254, 2012.

G. J. M. Parker and D. C. Alexander. Probabilistic Monte Carlo based mapping of cerebral connections utilising whole-brain crossing fibre information. In *Proceedings of the International Conference on Information Processing in Medical Imaging*, pages 684–695, Lake District, United Kingdom, 2003.

V. Patel, Y. Shi, P. M. Thompson, and A. W. Toga. Mesh-based spherical deconvolution: a flexible approach to reconstruction of non-negative fiber orientation distributions. *NeuroImage*, 51(3):1071–1081, 2010.

M. Perrin, C. Poupon, Y. Cointepas, B. Rieul, N. Golestani, C. Pallier, D. Riviere, A. Constantinesco, D. Le Bihan, and J. F. Mangin. Fiber tracking in q-ball fields using regularized particle trajectories. In *Proceedings of the International Conference on Information Processing in Medical Imaging*, pages 52–63, Glenwood Springs, Colorado, USA, 2005. Springer.

C. Pierpaoli, A. Barnett, S. Pajevic, R. Chen, L. R. Penix, A. Virta, and P. J. Basser. Water diffusion changes in Wallerian degeneration and their dependence on white matter architecture. *NeuroImage*, 13(6):1174–1185, 2001.

D. Raffelt, J. D. Tournier, J. Fripp, S. Crozier, A. Connelly, and O. Salvado. Symmetric diffeomorphic registration of fibre orientation distributions. *NeuroImage*, 56:1171–1180, 2011.

D. Raffelt, J. D. Tournier, S. Rose, G. R. Ridgway, R. Henderson, S. Crozier, O. Salvado, and A. Connelly. Apparent fibre density: a novel measure for the analysis of diffusion-weighted magnetic resonance images. *NeuroImage*, 59: 3976–3994, 2012.

K. Sakaie. Accelerated persistent angular structure. In *Proceedings of the MICCAI'08 Workshop on Computational Diffusion MRI*, pages 138–147, New York, USA, 2008.

K. K. Seunarine and D. C. Alexander. Multiple fibers: beyond the diffusion tensor. In *Diffusion MRI: from quantitative measurement to in vivo neuroanatomy*, pages 55–72. Academic Press, 2009.

A. Sweet and D. C. Alexander. Reduced encoding persistent angular structure. In *Proceedings of the International Society for Magnetic Resonance in Medicine*, volume 18, page 572, Stockholm, Sweden, 2010.

J. D. Tournier, F. Calamante, D. G. Gadian, and A. Connelly. Direct estimation of the fiber orientation density function from diffusion-weighted MRI data using spherical deconvolution. *NeuroImage*, 23(3):1176–1185, 2004.

J. D. Tournier, F. Calamante, and A. Connelly. Robust determination of the fibre orientation distribution in diffusion MRI: non-negativity constrained super-resolved spherical deconvolution. *NeuroImage*, 35(4):1459–1472, 2007.

J. D. Tournier, C. H. Yeh, F. Calamante, K. H. Cho, A. Connelly, and C. P. Lin. Resolving crossing fibres using constrained spherical deconvolution: validation using diffusion-weighted imaging phantom data. *NeuroImage*, 42(2):617–625, 2008.

J. D. Tournier, F. Calamante, and A. Connelly. How many diffusion gradient directions are required for HARDI? In *Proceedings of the International Society for Magnetic Resonance In Medicine*, volume 17, page 358, Honolulu, USA, 2009.

J. D. Tournier, S. Mori, and A. Leemans. Diffusion tensor imaging and beyond. *Magnetic Resonance in Medicine*, 65(6):1532–1556, 2011.

D. S. Tuch. Q-ball imaging. *Magnetic Resonance in Medicine*, 52(6):1358–1372, 2004.

D. S. Tuch, T. G. Reese, M. R. Wiegell, N. Makris, J. W. Belliveau, and V. J. Wedeen. High angular resolution diffusion imaging reveals intravoxel white matter fiber heterogeneity. *Magnetic Resonance in Medicine*, 48(4):577–582, 2002.

D. S. Tuch, T. G. Reese, M. R. Wiegell, and V. J. Wedeen. Diffusion MRI of complex neural architecture. *Neuron*, 40(5):885–895, 2003.

V. J. Wedeen, P. Hagmann, W. Tseng, T. G. Reese, and R. M. Weisskoff. Mapping complex tissue architecture with diffusion spectrum magnetic resonance imaging. *Magnetic Resonance in Medicine*, 54(6):1377–1386, 2005.

V. J. Wedeen, R. P. Wang, J. D. Schmahmann, T. Benner, W. Y. I. Tseng, G. Dai, D. N. Pandya, P. Hagmann, H. D'Arceuil, and A. J. de Crespigny. Diffusion spectrum magnetic resonance imaging (DSI) tractography of crossing fibers. *NeuroImage*, 41(4):1267–1277, 2008.

C. A. M. Wheeler-Kingshott and M. Cercignani. About axial and radial diffusivities. *Magnetic Resonance in Medicine*, 61(5):1255–1260, 2009.

C. H. Yeh, J. D. Tournier, K. H. Cho, C. P. Lin, F. Calamante, and A. Connelly. The effect of finite diffusion gradient pulse duration on fibre orientation estimation in diffusion MRI. *NeuroImage*, 51(2):743–751, 2010.

W. Zhan and Y. Yang. How accurately can the diffusion profiles indicate multiple fiber orientations? A study on general fiber crossings in diffusion MRI. *Journal of Magnetic Resonance*, 183(2):193–202, 2006.

3

Fiber tractography

Contents

3.1 Introduction

Fiber tractography pieces together the local WM orientations derived in Chapter 2 to infer long-range connectivity patterns between distant brain regions. Diffusion MRI based fiber tractography is unique in its ability to delineate the WM fiber pathways in a non-invasive way. This raises possibilities for clinical applications and can provide new insights in neuroscientific research. Fiber tractography algorithms can be classified largely into deterministic, probabilistic, and global algorithms. In this chapter, we will discuss these different approaches and their limitations. We end the chapter with a brief overview of the current applications.

3.2 Deterministic tractography

Deterministic streamline tractography is currently the most common method for fiber tractography [Mori and Van Zijl, 2002]. A streamline through a vector field is any line whose tangent is parallel to the local vector during its entire course. Mathematically, a line can be represented as a 3D space curve $\boldsymbol{r}(s)$, parameterized by its arc length s. In order for a streamline to align with the vector field, the tangent at arc length s, has to be equal to the vector at the corresponding position:

$$\frac{\mathrm{d}\boldsymbol{r}(s)}{\mathrm{d}s} = \boldsymbol{v}\left[\boldsymbol{r}(s)\right] \tag{3.1}$$

where $\boldsymbol{r}(s)$ denotes the 3D position along the streamline and $\boldsymbol{v}$ is the 3D vector field.

In the case of fiber tractography, the vector field $\boldsymbol{v}$ is chosen to reflect the local fiber orientations that are calculated from the diffusion data. For DTI tractography, $\boldsymbol{v}$ is typically the field of first eigenvectors derived from the diffusion tensor [Conturo et al., 1999, Basser et al., 2000] (Fig. 3.1). For tractography methods based on multi-fiber reconstruction algorithms, $\boldsymbol{v}$ typically consists of the dODF [Wedeen et al., 2008, Descoteaux et al., 2009] or fODF orientations along which the probability is highest [**Jeurissen** et al., 2009], as these orientations are most likely to coincide with the underlying WM fibers. However, remember from the previous chapter that, although diffusion is thought to be least hindered along fiber orientations, there is still a significant component of diffusion along other orientations, even perpendicular to the main fiber axis. As a result, the dODF is blurred and potentially provides biased fiber orientation estimates. For this reason, the fODF probably suits the purpose of tractography better.

Note that Eq. (3.1) is a differential equation that can be solved by means of integration:

$$\boldsymbol{r}(s) = \int_{s_0} \boldsymbol{v}\left[\boldsymbol{r}(s)\right] \mathrm{d}s \tag{3.2}$$

where $\boldsymbol{r}(s_0) = \boldsymbol{r}_0$ represents the starting point of the streamline which is often referred to as *seed point*. Formally, streamline tractography can be defined as the process of integrating voxelwise fiber orientations into fiber pathways. In the next subsections, we will discuss the common choices one has to make in developing a streamline tractography algorithm.

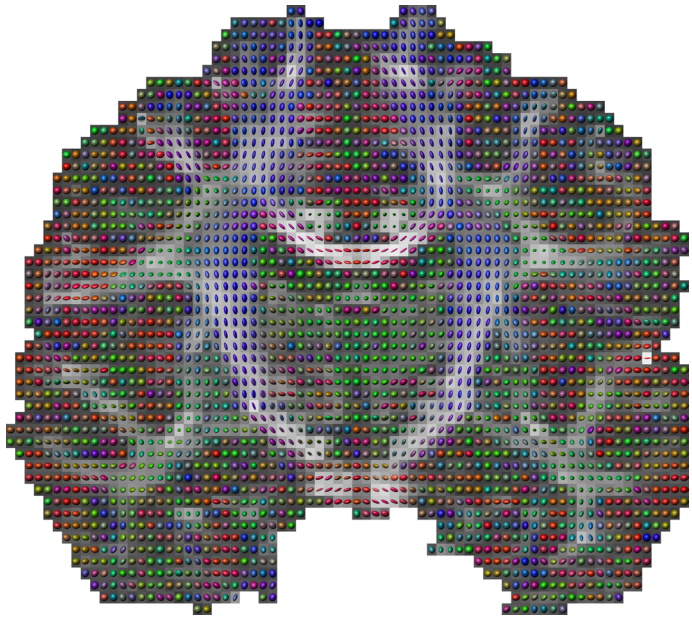

(a) The diffusion tensor field imposed on the FA map

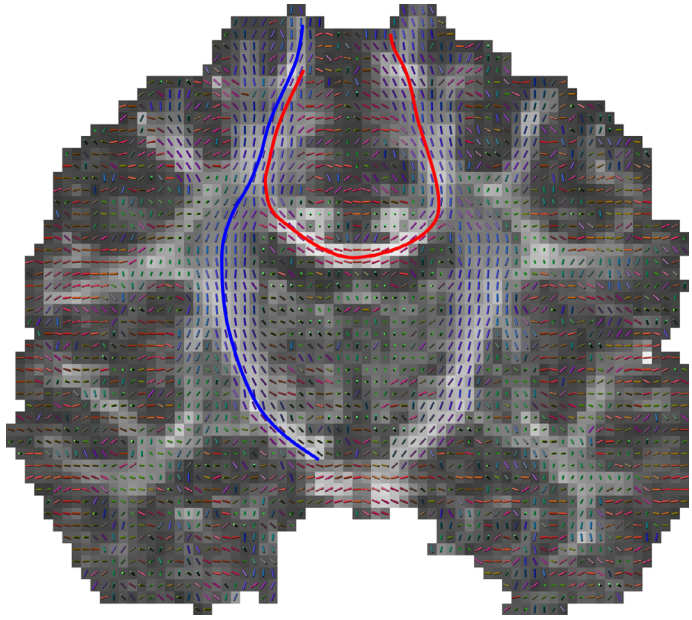

(b) The first eigenvector field imposed on the FA map

Fig. 3.1: Example of DTI streamlines on coronal slices of the human brain. The blue streamline corresponds to the corticospinal tract (CST). The red streamline corresponds to the corpus callosum. Note that each streamline's tangent is parallel to the local vector field during its entire course.

3.2.1 Integration

The most intuitive way to perform the numerical integration of Eq. (3.2) is by starting the procedure at seed point $\boldsymbol{r}_0$, calculating the corresponding fiber orientation $\boldsymbol{v}(\boldsymbol{r}_0)$, and following that direction for a short distance Δ, which is called the 'step size', to obtain the next point $\boldsymbol{r}_1 = \boldsymbol{r}_0 + \boldsymbol{v}(\boldsymbol{r}_0)\Delta$ on the pathway. This method, known as Euler integration, can reconstruct the entire streamline by iteratively performing this procedure:

$$\boldsymbol{r}_{i+1} = \boldsymbol{r}_i + \boldsymbol{v}(\boldsymbol{r}_i)\Delta \tag{3.3}$$

Note that Eq. (3.3) assumes that the value $\boldsymbol{v}(\boldsymbol{r}_i)$ is constant during the step size Δ, which will make this method susceptible to overshoot in highly curved regions, especially for larger step sizes (Fig. 3.2). In order to take into account the variations of $\boldsymbol{v}$ between $\boldsymbol{r}_i$ and $\boldsymbol{r}_{i+1}$, the use of higher order numerical integration schemes has been proposed, such as the second-order Runge-Kutta (RK2) or midpoint integration scheme:

$$\boldsymbol{r}_{i+1} = \boldsymbol{r}_i + \boldsymbol{v}\left(\boldsymbol{r}_i + \boldsymbol{v}(\boldsymbol{r}_i)\frac{\Delta}{2}\right)\Delta \tag{3.4}$$

which has an associated error of order $O(\Delta^3)$ or the fourth-order Runge-Kutta (RK4) scheme:

$$\boldsymbol{r}_{i+1} = \boldsymbol{r}_i + \frac{\boldsymbol{k}_1}{6} + \frac{\boldsymbol{k}_2}{3} + \frac{\boldsymbol{k}_3}{3} + \frac{\boldsymbol{k}_4}{6} \tag{3.5}$$

with

$$\begin{aligned}
\boldsymbol{k}_1 &= \boldsymbol{v}\left(\boldsymbol{r}_i\right)\Delta \\
\boldsymbol{k}_2 &= \boldsymbol{v}\left(\boldsymbol{r}_i + \frac{\boldsymbol{k}_1}{2}\right)\Delta \\
\boldsymbol{k}_3 &= \boldsymbol{v}\left(\boldsymbol{r}_i + \frac{\boldsymbol{k}_2}{2}\right)\Delta \\
\boldsymbol{k}_4 &= \boldsymbol{v}\left(\boldsymbol{r}_i + \boldsymbol{k}_3\right)\Delta
\end{aligned}$$

The RK4 scheme has an associated error of order $O(\Delta^5)$ and is known to be a good candidate for the numerical solution of Eq. (3.2).

3.2.2 Interpolation

From the right hand sides of Eq. (3.2)-(3.5) it is clear that the integration process requires that the fiber orientations are available at arbitrary positions in space. Unfortunately, the diffusion data that the local fiber orientations are derived from are acquired on a rectangular imaging grid. Therefore we need a method for interpolating the discrete measurements into continuous space. The simplest method to obtain an estimate of the local fiber orientation at any location is to use nearest-neighbor interpolation [Mori et al., 1999, Xue et al., 1999]. This method approximates the desired fiber orientation by that of the nearest voxel. However, this approach leads to a much greater propagation of errors than approaches that perform a smooth interpolation between grid points (Fig. 3.3) [Lazar and Alexander,

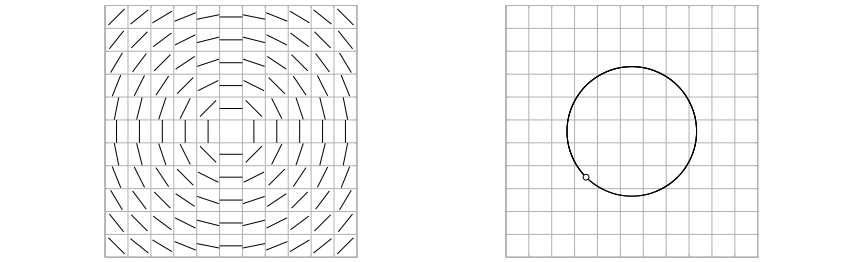

(a) Orientation field (b) Ground truth

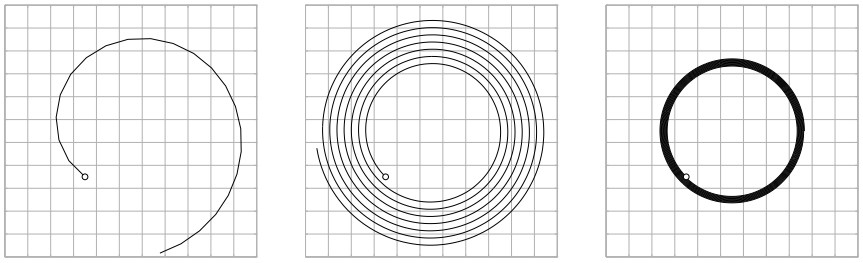

(c) Euler, step size: 1 (d) Euler, step size: 0.1 (e) Euler, step size: 0.01

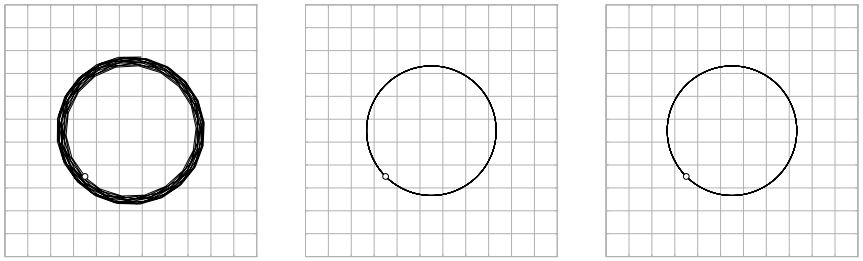

(f) RK2, step size: 1 (g) RK2, step size: 0.1 (h) RK2, step size: 0.01l

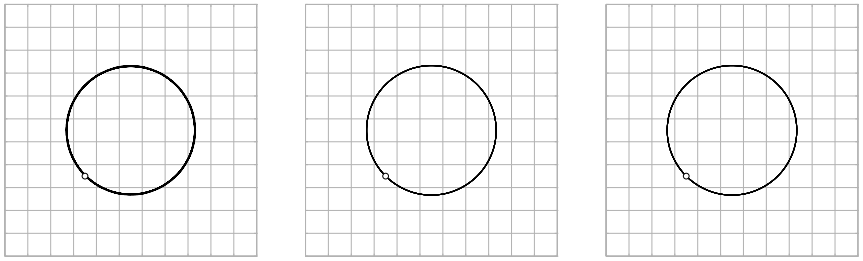

(i) RK4, step size: 1 (j) RK4, step size: 0.1 (k) RK4, step size: 0.01

Fig. 3.2: Euler vs. RK2 vs. RK4 integration for different step sizes. The seed point is indicated as a white dot. Note that, as we move away from the seed point, the integration errors accumulate. For Euler integration the accumulated error can become quite large, especially for large step sizes. Using higher order RK integration schemes, drastically reduces interpolation error made at each step, resulting in a much smaller accumulated error (even for relatively large step sizes).

2003]. Smooth interpolation methods assume that the fiber orientations between grid points contain contributions from each neighboring point. Most algorithms use trilinear interpolation, where the quantity of interest is calculated as a weighted sum from the 8 voxels nearest to the point of interest with the weight of each neighboring voxel determined by their distance to the point of interest. Some implementations perform trilinear interpolation on the raw diffusion weighted data and recompute the DT/dODF/fODF based on the interpolated data [Conturo et al., 1999, **Jeurissen** et al., 2011]. Another approach is to directly interpolate the DT/dODF/fODF profiles. While the latter approach can save a lot of computation time, special care has to be taken when the relationship between the diffusion data and the diffusion profiles is not linear, as is the case for the DT [Pajevic et al., 2002, Batchelor et al., 2005, Arsigny et al., 2006, Mishra et al., 2006].

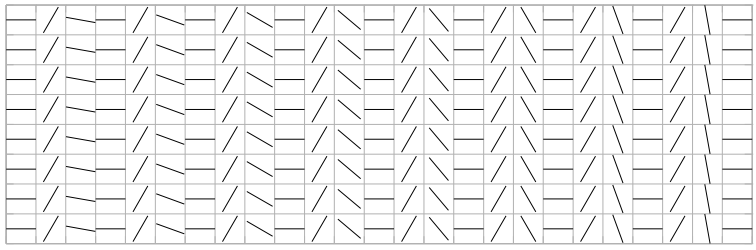

(a) Orientation field

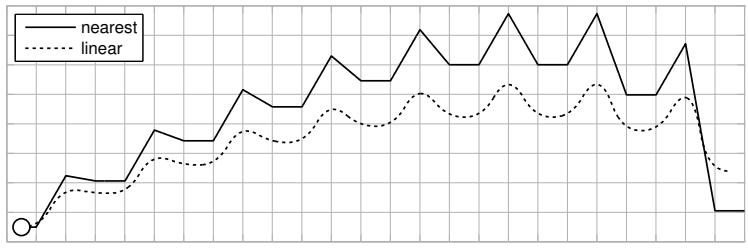

(b) Streamlines

Fig. 3.3: Nearest neighbor vs. linear interpolation. The seed point is indicated as a white dot. Note that, as we move away from the seed point, the errors made by the nearest neighbor interpolation accumulate.

3.2.3 Seed point selection

In general, the integration procedure is performed on a number of seed points $\boldsymbol{r}_0$ that define a specific 'region of interest' (ROI).Typically, these ROIs are defined by the user. This task requires anatomical knowledge and is subject to inter-operator variability. To reduce the operator dependence, ROIs can also be defined from atlas labels, or they can be obtained from cortical activation maps measured with functional MRI (fMRI). This last approach is particularly appealing since it allows for correlation analyses between structural and functional connectivity.

An alternative to ROI-based tractography is the use of 'whole-brain' tractography, where tracking is initiated from all voxels in the brain (Fig. 3.4a). The bundles of interest are then extracted by means of tract-editing techniques.

3.2.4 Tract-editing and clustering

Tract-editing is used to introduce prior anatomical knowledge of the fiber bundles in the brain, in order to refine the fiber-tracking results. In practice, tract-editing is performed by defining ROIs through which the tract is known to pass (also referred to as inclusive ROIs or AND gates). Tracts that enter these regions are considered anatomically plausible, and all other tracts are discarded. It is also possible to define regions through which the tracts are known *not* to pass and discard any tract that enters these regions (also referred to as exclusive ROIs or NOT gates). As an example, Fig. 3.4b shows a successful 3D reconstruction of the cingulum bundle, by means of two AND gates. This technique has been successfully used to isolate and visualize many different WM bundles and as such it is sometimes referred to as '*in vivo* virtual dissection'. While this technique is very powerful, it requires expert anatomical knowledge about the tracts of interest. As manual ROI-based tract-editing can be time consuming, clustering algorithms have emerged, that group fiber trajectories into bundles on the basis of their properties, such as length and curvature profile [O'Donnell et al., 2006, Batchelor et al., 2006, Xu et al., 2009], or by using WM atlases [O'Donnell and Westin, 2007].

3.2.5 Tract termination

A final important aspect of streamline tractography is choosing when a tract should stop. Two criteria are commonly used: a threshold on the diffusion anisotropy and a curvature threshold. For example, in DTI tractography it is common to stop a streamline when the FA falls below a certain threshold value (typically $FA < 0.2$). The rationale behind this criterion is that regions of low FA tend to be associated with high uncertainty in the principal diffusion direction, and therefore a large potential error for the next streamline step. For tractography methods based on multi-fiber reconstruction algorithms, tracking is usually terminated when the dODF or fODF amplitudes along the current tracking orientation fall below a certain threshold [Descoteaux et al., 2009, **Jeurissen** et al., 2011].

The curvature threshold imposes a maximum local curvature of the tract: if the angle between two successive steps is above a predefined threshold, the tract is terminated. Since it is unusual to find bends in the white matter bundles that have radii of curvature on the scale of an imaging voxel, any sudden change in trajectory is likely to be caused by artifacts such as noise.

3.2.6 Limitations

Deterministic streamline tractography is susceptible to three main sources of errors [Behrens and Jbabdi, 2009]. First, as seen in Chapter 1, DWI is susceptible to imaging noise, which may cause a poor estimation of the dominant diffusion directions used in streamline tractography. As an example, Fig. 3.5 shows the

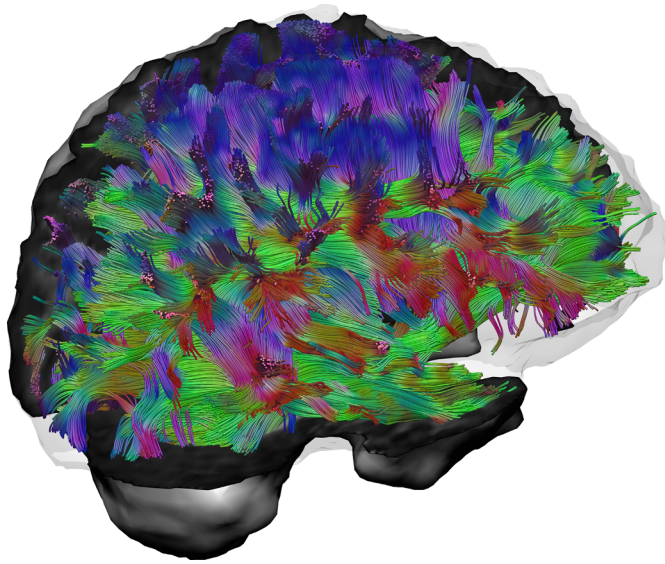

(a) Whole brain tractography

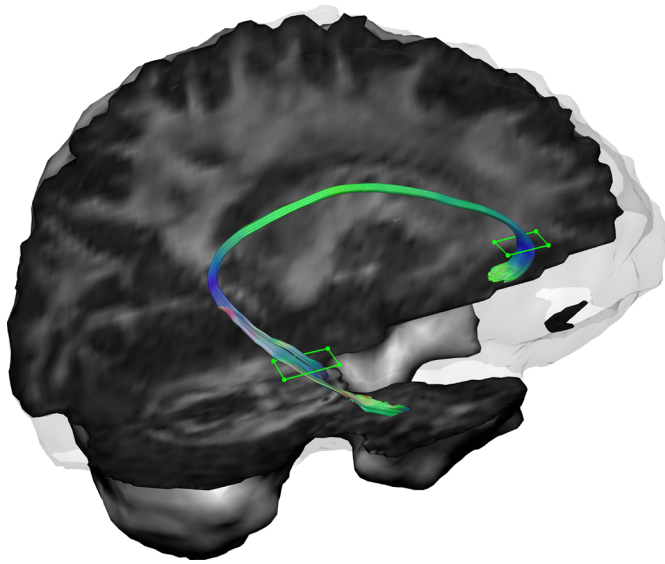

(b) Cingulum

Fig. 3.4: The cingulum bundle (b) is successfully extracted from whole brain tractography (a), using tract-editing with two AND gates (green rectangles).

variability of DTI fiber trajectories as a result of noise. Note that, for large SNR, the variability in the fiber orientation is low, but the fiber orientations can become unreliable at low SNR.

Second, the microscopic anatomy of WM is bound to be more complex than what can be represented by the fiber reconstruction model. As such, streamline tractography is subject to modeling errors. This is especially true for tractography algorithms using the diffusion tensor model, which cannot resolve multiple fiber orientations inside one voxel. As an example, Fig. 3.6 shows the variability of DTI fiber trajectories as a result of modeling errors. Note that the uncertainty suddenly increases as soon as the trajectories enter regions of crossing fibers.

Finally, as seen in Section 3.2.1, streamline tractography is subject to integration errors. It is important to realize that all these errors will accumulate along the streamline (Fig. 3.5,3.6).

3.3 Probabilistic tractography

Deterministic tractography algorithms assume a unique fiber orientation estimate in each voxel and as such provide a single pathway emanating from each seed point (Fig. 3.7a). However, as made clear in the previous section, the local fiber orientation estimates are subject to errors and uncertainty, which will introduce errors in the global fiber trajectory [Tournier et al., 2002, Lori et al., 2002, Jones, 2003, Lazar and Alexander, 2003]. Even a small error at one point in the trajectory can cause the algorithm to enter and follow a different WM tract, leading to erroneous statements about the WM connectivity. To characterize this uncertainty, probabilistic tractography algorithms generate a large collection or *distribution* of possible trajectories from each seed point (Fig. 3.7b). Brain regions that contain higher densities of the resulting trajectories are then deemed to have a higher probability of connection with the seed point [Behrens et al., 2003b, Parker et al., 2003]. Probabilistic streamlines results are, therefore, often quantified by generating visitation count maps of the number of trajectories that traverse each voxel, which can then be analyzed and compared more readily (Fig. 3.7c) [Behrens et al., 2003b, Parker et al., 2003].

By treating the problem in a probabilistic fashion, it also becomes possible to track through regions of high uncertainty, where deterministic techniques would usually stop, acknowledging, however, that the probability of connection beyond this region is lower. Typically, probabilistic tractography algorithms derive heavily from the deterministic streamline approach described in the previous section, and as such they are subject to the same limitations. The fundamental difference is that the orientations for tract propagation are drawn at random from a local uncertainty orientation density function (uODF) [Seunarine and Alexander, 2009]. The main difference between the various probabilistic algorithms lies in how this uODF is constructed.

3.3.1 Heuristic approaches

The earliest methods, based on DTI, relate the probability of a tract to the number of times it is reconstructed in a Monte Carlo random walk, where the characteristics

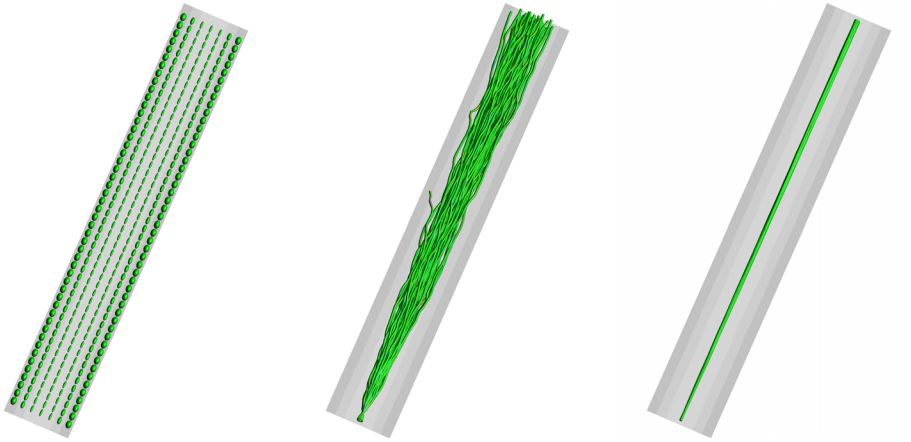

(a) DTI ellipsoids (b) low SNR trajectories (c) high SNR trajectories

Fig. 3.5: DTI tractography errors due to noise. A numerical phantom data set was constructed consisting of a single straight fiber bundle (a). Multiple trajectories where calculated for 100 noisy instances at low (b) and high (c) SNR.

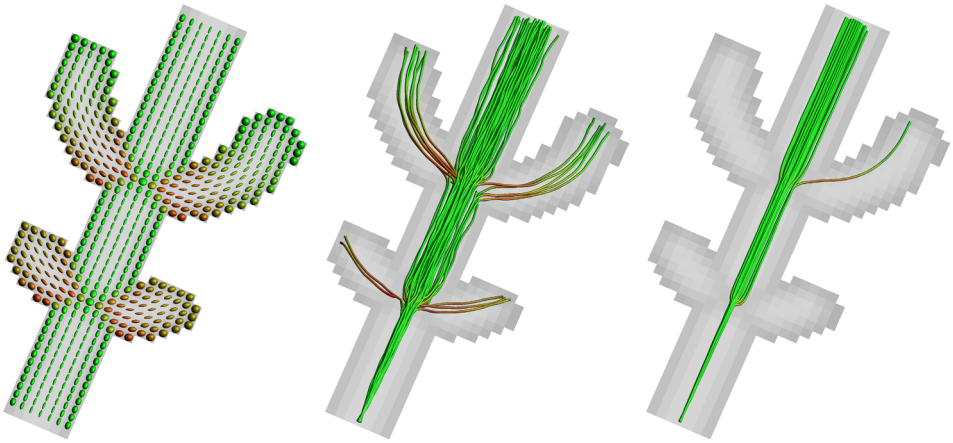

(a) DTI ellipsoids (b) low SNR trajectories (c) high SNR trajectories

Fig. 3.6: DTI tractography errors due to noise and modeling errors. The numerical phantom data set of Fig. 3.5 was extended with two regions of crossing fibers (a). Multiple trajectories where calculated for 100 noisy instances at low (b) and high (c) SNR. Note that, as the trajectories enter the region of crossing fibers, large modeling errors occur.

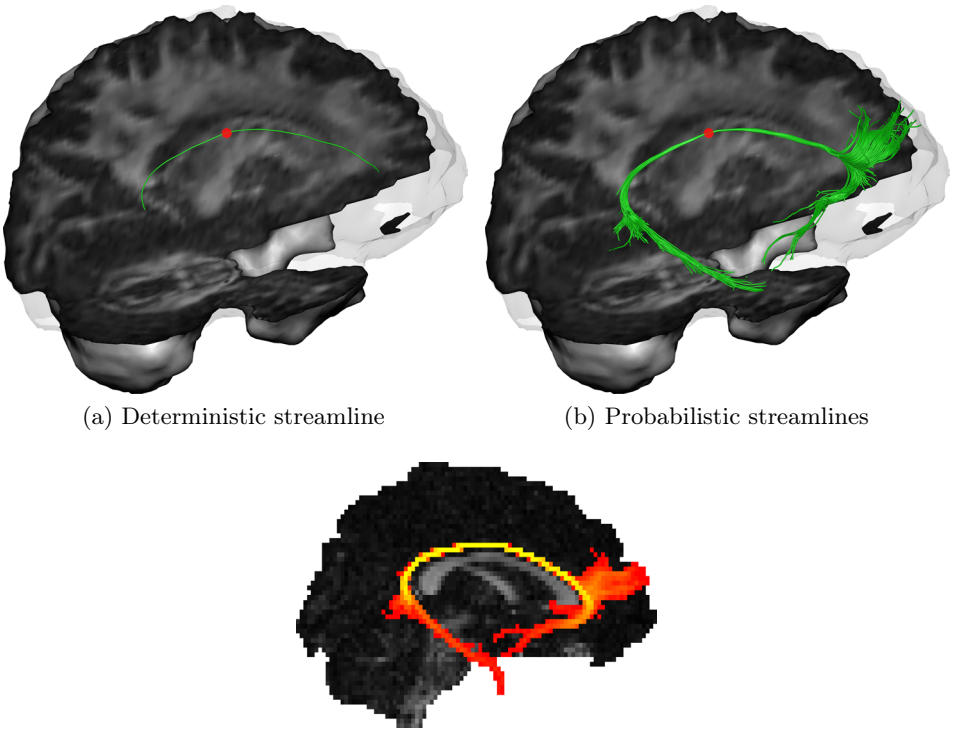

(a) Deterministic streamline

(b) Probabilistic streamlines

(c) Visitation count

Fig. 3.7: Deterministic CSD streamline (a) vs. probabilistic streamlines (b) emanating from the same seed point (red sphere). From the probabilistic streamlines a visitation count map is often created (c), visualized here as a maximum intensity projection along the Y-axis.

of the random walk are determined by the shape of the underlying diffusion tensor [Lazar and Alexander, 2002, Parker et al., 2003, Parker and Alexander, 2003, Tournier et al., 2003]. In voxels where there is no anisotropy, the generated vector is completely random. In anisotropic regions, the uODF is skewed to the axis of longest diffusion.

Similar methods were later developed for HARDI-based reconstruction methods where the characteristics of the random walk are determined by the shape of the derived ODFs. Some of these methods sample directly from the dODF [Campbell et al., 2005, Perrin et al., 2005, Descoteaux et al., 2009]. Remember from the previous chapter that, although diffusion is thought to be least hindered along fiber orientations, there is still a significant component of diffusion along other orientations, even perpendicular to the main fiber axis. As a result, the dODF is blurred and potentially provides biased fiber orientation estimates. For this reason, it is probably better to sample from the fODF, as it directly describes the proportion of fibers that are believed to lie along each orientation. Some methods sample directly from the fODF [Tournier et al., 2005]. Other methods first map the fODF parameters to the parameters of another distribution and take samples from this distribution in an attempt to better model the underlying anatomy [Seunarine et al., 2007].

An important drawback of these methods is that they assume an ad hoc relationship between the measured biophysical properties of the underlying microstructure and the uODF and don't truly take into account the variability due to noise and modeling errors. For example, smaller fODF lobes don't necessarily indicate a higher uncertainty that fibers are running along these orientations, it merely tells us that only a small proportion of fibers is expected along these orientations. At high SNR, a small fODF lobe can have high certainty associated with it. Conversely, large fODF lobes don't always indicate a high certainty in the fiber orientation. A large fODF lobe could still have a large associated uncertainty as a consequence of noise or artifacts.

3.3.2 Rigorous approaches

To address the limitations of the heuristic approaches, more rigorous approaches were proposed that try to construct the true uODF.

3.3.2.1 Calibration approach

Instead of relying on a heuristic approach, some methods perform a calibration experiment to determine an empirical relationship between the features of the data and expected uODF [Parker and Alexander, 2003, 2005].

3.3.2.2 Bayesian approach

Bayesian techniques offer formal methods for calculating and representing the uncertainty associated with inference on any parametric model. Uncertainty and belief are represented in the form of posterior probability density functions. Bayes' rule states that the posterior probability of the model parameters $\boldsymbol{\omega}$ given the data $\boldsymbol{s}$ and the model M, $P(\boldsymbol{\omega} \mid \boldsymbol{s}, M)$, is proportional to the likelihood of seeing this

data set given these parameters, $P(\boldsymbol{s} \mid \boldsymbol{\omega}, M)$, multiplied by the prior belief about the model parameters, $P(\boldsymbol{\omega} \mid M)$:

$$P(\boldsymbol{\omega} \mid \boldsymbol{s}, M) = \frac{P(\boldsymbol{s} \mid \boldsymbol{\omega}, M) P(\boldsymbol{\omega} \mid M)}{P(\boldsymbol{s} \mid M)} \tag{3.6}$$

The likelihood must include the parametric assumptions about the relation between the model parameters and the data. The earliest implementation assumed the tensor or the ball-and-stick model [Behrens et al., 2003b, Friman et al., 2006], modeling only a single fiber orientation. Later implementations accommodated multiple fiber orientations by applying a multi-tensor model [Hosey et al., 2005, Behrens et al., 2007] or the spherical convolution model [Kaden et al., 2007]. In addition, the likelihood must include the parametric assumptions about the noise statistics. Some implementations assume a Gaussian noise model [Behrens et al., 2003b, 2007]. However, as MR data are Rice distributed [Gudbjartsson and Patz, 1995], the Gaussian assumption might only be valid for data with reasonable SNR. As such, other implementations use the more accurate Rician noise model [Hosey et al., 2005, Kaden et al., 2007].

The prior distribution describes the information known about the parameters before any data are collected. As such, the prior distribution allows to impose constraints on the parameters such as positivity of the diffusion coefficients [Behrens et al., 2003b, 2007] or spatial smoothness of the fiber orientations [Hosey et al., 2005].

Once the likelihood and prior distribution have been established, it is possible to generate samples from the posterior distribution. This problem is usually addressed using Markov chain Monte Carlo (MCMC) methdods, a random sampling technique that produces samples in areas of high probability, allowing the posterior distribution to be characterized in a relatively short period of time [Behrens et al., 2003b, Hosey et al., 2005, Behrens et al., 2007, Kaden et al., 2007]. The individual samples of the posterior distribution can now be used as samples from the uODF for probabilistic tractography. Given that the Bayesian methods require explicit modeling of the sources of uncertainty in the data, it is often called a parametric method. This is also the main weakness of the approach: it cannot account for additional sources of uncertainty that are not present in the model.

3.3.2.3 Bootstrap approach

Conceptually the easiest way to build the uODF would be to acquire repeated DW data sets from the same subject, extract the fiber orientations and then treat these repeated fiber orientations as samples from the uODF [Jones, 2003]. Such an approach does not require us to do any modeling of the uncertainty in the data, and as such it is completely non-parametric. However, in order to build a good representation of the uODF, this procedure would require a large number of independent data sets, making the method not feasible in practice.

Fortunately, it is possible to generate a large number of samples from just a few independent data sets by means of bootstrapping. The bootstrap is a non-parametric statistical procedure that enables one to estimate the uncertainty of a given statistic, by randomly selecting individual measurements, with replacement,

from a set of repeated measurements, thus generating many bootstrap realizations of the data. Each realization provides a random estimate of a given statistic. By generating a sufficient number of realizations, one obtains a measure of the uncertainty of a given statistic from the data itself without requiring a priori assumptions about the sources of uncertainty [Efron, 1979, Jones, 2003, Pajevic and Basser, 2003]. Bootstrapping has previously been combined with DTI tractography in order to produce probabilistic fiber trajectories [Jones and Pierpaoli, 2005, Lazar and Alexander, 2005]. However, in a clinical setting, even the small amount of repeated measurements to allow accurate and precise bootstrapping can render acquisition time unacceptably long [O'Gorman and Jones, 2006, **Jeurissen** et al., 2008].

The problem of long acquisition times can be addressed using the residual bootstrap [Chung et al., 2006, Whitcher et al., 2007]. This approach obtains probability distributions for model parameters by resampling residuals from a model fit (e.g., diffusion tensor fit). The huge advantage of this method is that it does not require repeated measurements, bringing acquisition time into the clinical range. This method of uODF construction was first applied to probabilistic DTI tractography [Jones, 2008] and later to probabilistic QBI tractography [Berman et al., 2008, Haroon et al., 2009] and probabilistic CSD tractography [**Jeurissen** et al., 2011].

As this thesis uses bootstrap methods to infer the uncertainty in CSD fiber orientations, it will be discussed more thoroughly in Chapter 5.

3.4 Global approaches

The previously mentioned tractography algorithms propagate the local fiber orientation estimates to obtain long-range fiber pathways. Recently, a number of tractography algorithms have been proposed based on a more global approach [Jbabdi et al., 2007, Kreher et al., 2008, Fillard et al., 2009, Reisert et al., 2011]. Essentially, these algorithms attempt to find the configuration of fibers that best explains the observed data. As such, they do not rely on the preprocessing step to extract the fiber orientations, but rather operate directly on the acquired DW data, making tractography a one stage process. These methods rely on a model that predicts the DW signal intensities for a given arrangement of fiber orientations. These approaches have the potential to provide more robust results than current local streamlines methods. Unfortunately, these approaches are currently extremely computationally expensive limiting their immediate use in clinical environments. In addition, the use of strong priors on the smoothness of fiber trajectories could result in trajectories that, while spatially plausible, no longer correspond to the data.

3.5 Applications

Diffusion MRI based fiber tractography is unique in its ability to delineate the WM pathways of the brain in a non-invasive fashion. This raises possibilities for clinical applications and there has been a rapid increase in publications using fiber

tractography in neuroscience [Johansen-Berg and Behrens, 2006, Ciccarelli et al., 2008]. In this section we provide a brief overview of the most important applications [Lazar, 2010].

3.5.1 Delineation of specific WM pathways

The combination of whole-brain tractography with tract-editing techniques has allowed the delineation of specific WM pathways in the brain that are in agreement with known anatomy [Conturo et al., 1999, Stieltjes et al., 2001, Mori et al., 2002b, Catani et al., 2002, Lazar et al., 2003, Jellison et al., 2004, Wakana et al., 2004, 2007], providing new insights in brain anatomy and development [Parker et al., 2005, Catani et al., 2005, Oishi et al., 2008].

3.5.2 WM parcellation

As fiber tractography has the unique ability to delineate specific WM tracts *in vivo*, it is often used to segment the different WM structures. These segmented volumes can be used in morphometric analysis or serve as ROIs for the quantitative analyses of scalar diffusion indices such as FA. Recently, this approach has been applied to investigate the WM integrity in a variety of brain disorders, such as schizophrenia [Jones et al., 2003], epilepsy [Concha et al., 2005], autism [Conturo et al., 2008] and Tourette syndrome [Makki et al., 2009] .

3.5.3 GM parcellation

Given that the GM is connected by means of the WM bundles, fiber tractography also offers the possibility to segment distinct functional regions of the cortex depending on their WM connections [Johansen-Berg et al., 2004, Rushworth et al., 2006, Anwander et al., 2007, Beckmann et al., 2009]. Conversely, the WM bundles can be subdivided on the basis of their connectivity with functional regions of the cortex as derived with fMRI [Behrens et al., 2003a]. This allows researchers to study the relation between function and structure and can potentially provide new insights into the inner workings of our brain.

3.5.4 Studying the structural network

Recently, fiber tractography has been used to study brain structure at the network level, by generating connectivity matrices that define the properties of the connections between different nodes of the brain network. This approach allows to study the global network organization and identify the interrelations between the nodes [Hagmann et al., 2008]. Recent work has suggested that the global connectivity network is affected in a specific way by different neurodegenerative diseases [Seeley et al., 2009] and neuropsychiatric disorders [Calhoun et al., 2009].

3.5.5 Presurgical planning

The main clinical application of fiber tractography is presurgical planning. In patients with brain tumors and space-occupying lesions, WM tracts are often

displaced by the mass effect of the tumor or lesion. As tractography is able to delineate the WM tracts and their associated cortical regions, it may be used to identify fiber pathways that are related to vital neural functions and that should be preserved by the surgical procedures [Mori et al., 2002a, Clark et al., 2003, Nimsky et al., 2006, Lazar et al., 2006, Berman et al., 2007, Leclercq et al., 2010].

Bibliography

A. Anwander, M. Tittgemeyer, D. Y. Von Cramon, A. D. Friederici, and T. R. Knösche. Connectivity-based parcellation of Broca's area. *Cerebral Cortex*, 17 (4):816, 2007.

V. Arsigny, P. Fillard, X. Pennec, and N. Ayache. Log-Euclidean metrics for fast and simple calculus on diffusion tensors. *Magnetic Resonance in Medicine*, 56 (2):411–421, 2006.

P. J. Basser, S. Pajevic, C. Pierpaoli, J. Duda, and A. Aldroubi. In vivo fiber tractography using DT-MRI data. *Magnetic Resonance in Medicine*, 44(4): 625–632, 2000.

P. G. Batchelor, M. Moakher, D. Atkinson, F. Calamante, and A. Connelly. A rigorous framework for diffusion tensor calculus. *Magnetic Resonance in Medicine*, 53(1):221–225, 2005.

P. G. Batchelor, F. Calamante, J. D. Tournier, D. Atkinson, D. L. G. Hill, and A. Connelly. Quantification of the shape of fiber tracts. *Magnetic Resonance in Medicine*, 55(4):894–903, 2006.

M. Beckmann, H. Johansen-Berg, and M. F. S. Rushworth. Connectivity-based parcellation of human cingulate cortex and its relation to functional specialization. *The Journal of Neuroscience*, 29(4):1175, 2009.

T. E. J. Behrens and S. Jbabdi. MR diffusion tractography. In *Diffusion MRI: from quantitative measurement to in vivo neuroanatomy*, pages 333–351. Academic Press, 2009.

T. E. J. Behrens, H. Johansen-Berg, M. W. Woolrich, S. M. Smith, C. A. M Wheeler-Kingshott, P. A. Boulby, G. J. Barker, E. L. Sillery, K. Sheehan, O. Ciccarelli, A. J. Thompson, J. M. Brady, and P. M. Matthews. Non-invasive mapping of connections between human thalamus and cortex using diffusion imaging. *Nature Neuroscience*, 6(7):750–757, 2003a.

T. E. J. Behrens, M. W. Woolrich, M. Jenkinson, H. Johansen-Berg, R. G. Nunes, S. Clare, P. M. Matthews, J. M. Brady, and S. M. Smith. Characterization and propagation of uncertainty in diffusion-weighted MR imaging. *Magnetic Resonance in Medicine*, 50(5):1077–1088, 2003b.

T. E. J. Behrens, H. Johansen-Berg, S. Jbabdi, M. F. S. Rushworth, and M. W. Woolrich. Probabilistic diffusion tractography with multiple fibre orientations: what can we gain? *NeuroImage*, 34(1):144–155, 2007.

J. I. Berman, M. S. Berger, S. Chung, S. S. Nagarajan, and R. G. Henry. Accuracy of diffusion tensor magnetic resonance imaging tractography assessed using intraoperative subcortical stimulation mapping and magnetic source imaging. *Journal of Neurosurgery: Pediatrics*, 107(3):488–494, 2007.

J. I. Berman, S. W. Chung, P. Mukherjee, C. P. Hess, E. T. Han, and R. G. Henry. Probabilistic streamline q-ball tractography using the residual bootstrap. *NeuroImage*, 39(1):215–222, 2008.

V. D. Calhoun, T. Eichele, and G. Pearlson. Functional brain networks in schizophrenia: a review. *Frontiers in Human Neuroscience*, 3, 2009.

J. S. W. Campbell, K. Siddiqi, V. V. Rymar, A. F. Sadikot, and G. B. Pike. Flow-based fiber tracking with diffusion tensor and q-ball data: validation and comparison to principal diffusion direction techniques. *NeuroImage*, 27(4):725–736, 2005.

M. Catani, R. J. Howard, S. Pajevic, and D. K. Jones. Virtual in vivo interactive dissection of white matter fasciculi in the human brain. *NeuroImage*, 17(1):77–94, 2002.

M. Catani, D. K. Jones, and Ffytche D. H. Perisylvian language networks of the human brain. *Annals of Neurology*, 57(1):8–16, 2005.

S. W. Chung, Y. Lu, and R. G. Henry. Comparison of bootstrap approaches for estimation of uncertaintiesof DTI parameters. *NeuroImage*, 33(2):531–541, 2006.

O. Ciccarelli, M. Catani, H. Johansen-Berg, C. Clark, and A. Thompson. Diffusion-based tractography in neurological disorders: concepts, applications, and future developments. *The Lancet Neurology*, 7(8):715–727, 2008.

C. A. Clark, T. R. Barrick, M. M. Murphy, and B. A. Bell. White matter fiber tracking in patients with space-occupying lesions of the brain: a new technique for neurosurgical planning? *NeuroImage*, 20(3):1601–1608, 2003.

L. Concha, C. Beaulieu, and D. W. Gross. Bilateral limbic diffusion abnormalities in unilateral temporal lobe epilepsy. *Annals of Neurology*, 57(2):188–196, 2005.

T. E. Conturo, N. F. Lori, T. S. Cull, E. Akbudak, A. Z. Snyder, J. S. Shimony, R. C. McKinstry, H. Burton, and M. E. Raichle. Tracking neuronal fiber pathways in the living human brain. *Proceedings of the National Academy of Sciences of the United States of America*, 96(18):10422–10427, 1999.

T. E. Conturo, D. L. Williams, C. D. Smith, E. Gultepe, E. Akbudak, and N. J. Minshew. Neuronal fiber pathway abnormalities in autism: an initial MRI diffusion tensor tracking study of hippocampo-fusiform and amygdalo-fusiform pathways. *Journal of the International Neuropsychological Society*, 14(6):933–946, 2008.

M. Descoteaux, R. Deriche, TR Knösche, and A. Anwander. Deterministic and probabilistic tractography based on complex fibre orientation distributions. *IEEE Transactions on Medical Imaging*, 28(2):269–286, 2009.

B. Efron. Bootstrap methods: another look at the jackknife. *The Annals of Statistics*, 7(1):1–26, 1979.

P. Fillard, C. Poupon, and J. F. Mangin. A novel global tractography algorithm based on an adaptive spin glass model. In *Proceedings of the International Conference on Medical Image Computing and Computer-Assisted Intervention: Part I*, pages 927–934, London, United Kingdom, 2009.

O. Friman, G. Farneback, and C. F. Westin. A Bayesian approach for stochastic white matter tractography. *IEEE Transactions on Medical Imaging*, 25(8): 965–978, 2006.

H. Gudbjartsson and S. Patz. The Rician distribution of noisy MRI data. *Magnetic Resonance in Medicine*, 34(6):910–914, 1995.

P. Hagmann, L. Cammoun, X. Gigandet, R. Meuli, C. J. Honey, V. J. Wedeen, and O. Sporns. Mapping the structural core of human cerebral cortex. *PLoS Biology*, 6(7):e159, 2008.

H. A. Haroon, D. M. Morris, K. V. Embleton, D. C. Alexander, and G. Parker. Using the model-based residual bootstrap to quantify uncertainty in fiber orientations from Q-ball analysis. *IEEE Transactions on Medical Imaging*, 28(4):535–550, 2009.

T. Hosey, G. Williams, and R. Ansorge. Inference of multiple fiber orientations in high angular resolution diffusion imaging. *Magnetic Resonance in Medicine*, 54 (6):1480–1489, 2005.

S. Jbabdi, MW Woolrich, JLR Andersson, and TEJ Behrens. A Bayesian framework for global tractography. *NeuroImage*, 37(1):116–129, 2007.

B. J. Jellison, A. S. Field, J. Medow, M. Lazar, M. S. Salamat, and A. L. Alexander. Diffusion tensor imaging of cerebral white matter: a pictorial review of physics, fiber tract anatomy, and tumor imaging patterns. *American Journal of Neuroradiology*, 25(3):356, 2004.

B. Jeurissen, A. Leemans, J. D. Tournier, and J. Sijbers. Bootstrap methods for estimating uncertainty in Constrained Spherical Deconvolution fiber orientations. In *Proceedings of the International Society for Magnetic Resonance in Medicine*, volume 16, page 3324, Toronto, Canada, 2008.

B. Jeurissen, A. Leemans, J. D. Tournier, and J. Sijbers. Fiber tracking on the 'Fiber Cup phantom' using constrained spherical deconvolution. In *Proceedings of the MICCAI'09 Workshop on Diffusion Modelling and the Fiber Cup*, pages 232–235, London, United Kingdom, 2009.

B. Jeurissen, A. Leemans, D. K. Jones, J. D. Tournier, and J. Sijbers. Probabilistic fiber tracking using the residual bootstrap with constrained spherical deconvolution. *Human Brain Mapping*, 32:461–479, 2011.

H. Johansen-Berg and T. E. J. Behrens. Just pretty pictures? What diffusion tractography can add in clinical neuroscience. *Current Opinion in Neurology*, 19: 379–385, 2006.

H. Johansen-Berg, T. E. J. Behrens, M. D. Robson, I. Drobnjak, M. F. S. Rushworth, J. M. Brady, S. M. Smith, D. J. Higham, and P. M. Matthews. Changes in connectivity profiles define functionally distinct regions in human medial frontal cortex. *Proceedings of the National Academy of Sciences of the United States of America*, 101(36):13335–13340, 2004.

D. K. Jones. Determining and visualizing uncertainty in estimates of fiber orientation from diffusion tensor MRI. *Magnetic Resonance in Medicine*, 49(1):7–12, 2003.

D. K. Jones. Tractography gone wild: probabilistic fibre tracking using the wild bootstrap with diffusion tensor MRI. *IEEE Transactions on Medical Imaging*, 27(9):1268–1274, 2008.

D. K. Jones and C. Pierpaoli. Confidence mapping in diffusion tensor magnetic resonance imaging tractography using a bootstrap approach. *Magnetic Resonance in Medicine*, 53(5):1143–1149, 2005.

D. K. Jones, M. Catani, S. J. Reeves, S. S. Shergill, P. McGuire, M. A. Horsfield, A. Simmons, S. C. R. Williams, and R. J. Howard. A tractography approach to studying fronto-temporal fasciculi in schizophrenia and late onset schizophrenia-like psychosis. In *Proceedings of the International Society for Magnetic Resonance in Medicine*, volume 11, page 244, Toronto, Canada, 2003.

E. Kaden, T. R. Knösche, and A. Anwander. Parametric spherical deconvolution: Inferring anatomical connectivity using diffusion MR imaging. *NeuroImage*, 37 (2):474–488, 2007.

BW Kreher, I. Mader, and VG Kiselev. Gibbs tracking: a novel approach for the reconstruction of neuronal pathways. *Magnetic Resonance in Medicine*, 60(4): 953–963, 2008.

M. Lazar. Mapping brain anatomical connectivity using white matter tractography. *NMR in Biomedicine*, 23:821–835, 2010.

M. Lazar and A. L. Alexander. White matter tractography using random vector (RAVE) perturbation. In *Proceedings of the International Society for Magnetic Resonance in Medicine*, volume 10, page 539, Honolulu, USA, 2002.

M. Lazar and A. L. Alexander. An error analysis of white matter tractography methods: synthetic diffusion tensor field simulations. *NeuroImage*, 20(2):1140–1153, 2003.

M. Lazar and A. L. Alexander. Bootstrap white matter tractography (BOOT-TRAC). *NeuroImage*, 24(2):524–532, 2005.

M. Lazar, D. M. Weinstein, J. S. Tsuruda, K. M. Hasan, K. Arfanakis, M. E. Meyerand, B. Badie, H. A. Rowley, V. Haughton, A. Field, and A. L. Alexander. White matter tractography using diffusion tensor deflection. *Human Brain Mapping*, 18(4):306–321, 2003.

M. Lazar, A. L. Alexander, P. J. Thottakara, B. Badie, and A. S. Field. White matter reorganization after surgical resection of brain tumors and vascular malformations. *American Journal of Neuroradiology*, 27(6):1258, 2006.

D. Leclercq, H. Duffau, C. Delmaire, L. Capelle, P. Gatignol, M. Ducros, J. Chiras, and S. Lehéricy. Comparison of diffusion tensor imaging tractography of language tracts and intraoperative subcortical stimulations. *Journal of Neurosurgery*, 112 (3):503–511, 2010.

N. F. Lori, E. Akbudak, J. S. Shimony, T. S. Cull, A. Z. Snyder, R. K. Guillory, and T. E. Conturo. Diffusion tensor fiber tracking of human brain connectivity: aquisition methods, reliability analysis and biological results. *NMR in Biomedicine*, 15(7-8):494–515, 2002.

M. I. Makki, R. Munian Govindan, B. J. Wilson, M. E. Behen, and H. T. Chugani. Altered fronto-striato-thalamic connectivity in children with Tourette syndrome assessed with diffusion tensor MRI and probabilistic fiber tracking. *Journal of Child Neurology*, 24(6):669, 2009.

A. Mishra, Y. Lu, J. Meng, A. W. Anderson, and Z. Ding. Unified framework for anisotropic interpolation and smoothing of diffusion tensor images. *NeuroImage*, 31(4):1525–1535, 2006.

S. Mori and P. C. M. Van Zijl. Fiber tracking: principles and strategies-a technical review. *NMR in Biomedicine*, 15(7-8):468–480, 2002.

S. Mori, B. J. Crain, V. P Chacko, and P. Van Zijl. Three-dimensional tracking of axonal projections in the brain by magnetic resonance imaging. *Annals of Neurology*, 45(2):265–269, 1999.

S. Mori, K. Frederiksen, P. van Zijl, B. Stieltjes, M. A. Kraut, M. Solaiyappan, and M. G. Pomper. Brain white matter anatomy of tumor patients evaluated with diffusion tensor imaging. *Annals of Neurology*, 51(3):377–380, 2002a.

S. Mori, W. E. Kaufmann, C. Davatzikos, B. Stieltjes, L. Amodei, K. Fredericksen, G. D. Pearlson, E. R. Melhem, M. Solaiyappan, G. V. Raymond, Moser H. W., and P. C. van Zijl. Imaging cortical association tracts in the human brain using diffusion-tensor-based axonal tracking. *Magnetic Resonance in Medicine*, 47(2): 215–223, 2002b.

C. Nimsky, O. Ganslandt, D. Merhof, A. G. Sorensen, and R. Fahlbusch. Intraoperative visualization of the pyramidal tract by diffusion-tensor-imaging-based fiber tracking. *NeuroImage*, 30(4):1219–1229, 2006.

L. J. O'Donnell and C. F. Westin. Automatic tractography segmentation using a high-dimensional white matter atlas. *IEEE Transactions on Medical Imaging*, 26 (11):1562–1575, 2007.

L. J. O'Donnell, M. Kubicki, M. E. Shenton, M. H. Dreusicke, W. E. L. Grimson, and C. F. Westin. A method for clustering white matter fiber tracts. *American Journal of Neuroradiology*, 27(5):1032, 2006.

R. L. O'Gorman and D. K. Jones. Just how much data need to be collected for reliable bootstrap DT-MRI? *Magnetic Resonance in Medicine*, 56(4):884–890, 2006.

K. Oishi, K. Zilles, K. Amunts, A. Faria, H. Jiang, X. Li, K. Akhter, K. Hua, R. Woods, A. W. Toga, G.B. Pike, P. Rosa-Neto, A. Evans, J. Zhang, H. Huang, M. I. Miller, van Zijlb P. C., J. Mazziotta, and S. Mori. Human brain white matter atlas: identification and assignment of common anatomical structures in superficial white matter. *NeuroImage*, 43(3):447–457, 2008.

S. Pajevic and P. J. Basser. Parametric and non-parametric statistical analysis of DT-MRI data. *Journal of Magnetic Resonance*, 161(1):1–14, 2003.

S. Pajevic, A. Aldroubi, and P. J. Basser. A continuous tensor field approximation of discrete DT-MRI data for extracting microstructural and architectural features of tissue. *Journal of Magnetic Resonance*, 154(1):85–100, 2002.

G. J. M. Parker and D. C. Alexander. Probabilistic Monte Carlo based mapping of cerebral connections utilising whole-brain crossing fibre information. In *Proceedings of the International Conference on Information Processing in Medical Imaging*, pages 684–695, Lake District, United Kingdom, 2003.

G. J. M. Parker and D. C. Alexander. Probabilistic anatomical connectivity derived from the microscopic persistent angular structure of cerebral tissue. *Philosophical Transactions of the Royal Society B: Biological Sciences*, 360(1457):893, 2005.

G. J. M. Parker, H. A. Haroon, and C. A. M. Wheeler-Kingshott. A framework for a streamline-based probabilistic index of connectivity (PICo) using a structural interpretation of MRI diffusion measurements. *Journal of Magnetic Resonance Imaging*, 18(2):242–254, 2003.

G. J. M. Parker, S. Luzzi, D.C . Alexander, C. A. M. Wheeler-Kingshott, O. Ciccarelli, and M. A. Lambon Ralph. Lateralization of ventral and dorsal auditory-language pathways in the human brain. *NeuroImage*, 24(3):656–666, 2005.

M. Perrin, C. Poupon, Y. Cointepas, B. Rieul, N. Golestani, C. Pallier, D. Riviere, A. Constantinesco, D. Le Bihan, and J. F. Mangin. Fiber tracking in q-ball fields using regularized particle trajectories. In *Proceedings of the International Conference on Information Processing in Medical Imaging*, pages 52–63, Glenwood Springs, Colorado, USA, 2005. Springer.

M. Reisert, I. Mader, C. Anastasopoulos, M. Weigel, S. Schnell, and V. Kiselev. Global fiber reconstruction becomes practical. *NeuroImage*, 54(2):955–962, 2011.

M. F. S. Rushworth, T. E. J. Behrens, and H. Johansen-Berg. Connection patterns distinguish 3 regions of human parietal cortex. *Cerebral Cortex*, 16(10):1418, 2006.

W. W. Seeley, R. K. Crawford, J. Zhou, B. L. Miller, and M. D. Greicius. Neurodegenerative diseases target large-scale human brain networks. *Neuron*, 62(1): 42–52, 2009.

K. K. Seunarine and D. C. Alexander. Multiple fibers: beyond the diffusion tensor. In *Diffusion MRI: from quantitative measurement to in vivo neuroanatomy*, pages 55–72. Academic Press, 2009.

K. K. Seunarine, P. A. Cook, M. G. Hall, K. V. Embleton, G. J. M. Parker, and D. C. Alexander. Exploiting peak anisotropy for tracking through complex structures. In *Proceedings of the International Conference on Computer Vision*, pages 1–8, Rio De Janeiro, Brazil, 2007.

B. Stieltjes, W. E. Kaufmann, P. van Zijl, K. Fredericksen, G. D. Pearlson, M. Solaiyappan, and S. Mori. Diffusion tensor imaging and axonal tracking in the human brainstem. *NeuroImage*, 14(3):723–735, 2001.

J. D. Tournier, F. Calamante, M. D. King, D. G. Gadian, and A. Connelly. Limitations and requirements of diffusion tensor fiber tracking: an assessment using simulations. *Magnetic Resonance in Medicine*, 47(4):701–708, 2002.

J. D. Tournier, F. Calamante, D. G. Gadian, and A. Connelly. Diffusion-weighted magnetic resonance imaging fibre tracking using a front evolution algorithm. *NeuroImage*, 20(1):276–288, 2003.

J. D. Tournier, F. Calamante, D. G. Gadian, and A. Connelly. Probabilistic fibre tracking through regions containing crossing fibres. In *Proceedings of the International Society for Magnetic Resonance In Medicine*, volume 13, page 1343, Miami, USA, 2005.

S. Wakana, H. Jiang, L. M. Nagae-Poetscher, P. Van Zijl, and S. Mori. Fiber tract-based atlas of human white matter anatomy. *Radiology*, 230(1):77, 2004.

S. Wakana, A. Caprihan, M. M. Panzenboeck, J. H. Fallon, M. Perry, R. L. Gollub, K. Hua, J. Zhang, H. Jiang, P. Dubey, A. Blitz, P. van Zijl, and S. Mori. Reproducibility of quantitative tractography methods applied to cerebral white matter. *NeuroImage*, 36(3):630–644, 2007.

V. J. Wedeen, R. P. Wang, J. D. Schmahmann, T. Benner, W. Y. I. Tseng, G. Dai, D. N. Pandya, P. Hagmann, H. D'Arceuil, and A. J. de Crespigny. Diffusion spectrum magnetic resonance imaging (DSI) tractography of crossing fibers. *NeuroImage*, 41(4):1267–1277, 2008.

B. Whitcher, D. S. Tuch, J. J. Wisco, A. G. Sorensen, and L. Wang. Using the wild bootstrap to quantify uncertainty in diffusion tensor imaging. *Human Brain Mapping*, 29(3):346–362, 2007.

Q. Xu, A. W. Anderson, J. C. Gore, and Z. Ding. Unified bundling and registration of brain white matter fibers. *IEEE Transactions on Medical Imaging*, 28(9): 1399–1411, 2009.

R. Xue, P. van Zijl, B. J. Crain, M. Solaiyappan, and S. Mori. In vivo three-dimensional reconstruction of rat brain axonal projections by diffusion tensor imaging. *Magnetic Resonance in Medicine*, 42(6):1123–1127, 1999.

Part II

Contributions

4

Deterministic tractography using CSD

Contents

The work in this chapter has been published as:

- **B. Jeurissen**, A. Leemans, E. Fieremans, and J. Sijbers. Fiber tractography on a crossing fiber phantom using constrained spherical deconvolution MRI. In *Proceedings of Liège Image Days*, Liège, Belgium, 2008
- **B. Jeurissen**, A. Leemans, J. D. Tournier, and J. Sijbers. Fiber tracking on the 'Fiber Cup phantom' using constrained spherical deconvolution. In *Proceedings of the MICCAI'09 Workshop on Diffusion Modelling and the Fiber Cup*, pages 232–235, London, United Kingdom, 2009
- A. Leemans, **B. Jeurissen**, J. Sijbers, and D. K. Jones. ExploreDTI: a graphical toolbox for processing, analyzing, and visualizing diffusion MR data. In *Proceedings of the International Society for Magnetic Resonance in Medicine*, volume 17, page 3537, Honolulu, USA, 2009
- P. Fillard, M. Descoteaux, A. Goh, S. Gouttard, **B. Jeurissen**, J. G. Malcolm, A. Ramirez-Manzanares, M. Reisert, K. Sakaie, F. Tensaouti, T. Yo, J. F. Mangin, and C. Poupon. Quantitative evaluation of 10 tractography algorithms on a realistic diffusion MR phantom. *NeuroImage*, 56(1):220–234, 2011
- M. Froeling, G. J. Strijkers, **B. Jeurissen**, M. P. van der Paardt, J. Stoker, Nicolay K., A. J. Nederveen, and A. Leemans. Fiber architecture of the female pelvic floor: an exploratory investigation using different diffusion MRI tractography algorithms. In *Proceedings of the International Society for Magnetic Resonance in Medicine*, volume 19, page 3260, Montréal, Canada, 2011
- Y. D. Reijmer, A. Leemans, S. M. Heringa, I. Wielaard, **B. Jeurissen**, H. L. Koek, and G. J. Biessels. Constrained spherical deconvolution based tractography and cognition in Alzheimer's disease. In *Proceedings of the Organization for Human Brain Mapping*, Québec, Canada, 2011a
- Y. D. Reijmer, A. Leemans, S. M. Heringa, I. Wielaard, **B. Jeurissen**, H. L. Koek, and G. J. Biessels. Constrained spherical deconvolution based tractography and cognition in Alzheimer's disease. In *Proceedings of the International Conference on Alzheimer's Disease*, Paris, France, 2011b

4.1 Introduction

Currently, diffusion tensor imaging (DTI) is most commonly used to extract fiber orientations from the DW signal [Basser et al., 1994a,b]. However, in voxels containing multiple fiber orientations, this model has been shown to be inadequate [Alexander et al., 2002, Frank, 2001, 2002, Tuch et al., 2002]. Such voxels occur frequently throughout the WM due to partial volume effects between adjacent tracts. A recent study estimated that a third of the white matter voxels contain complex fiber architecture [Behrens et al., 2007]. This has important implications for fiber tractography, as most white matter tracts will traverse regions with multiple fiber orientations at some point along their path. In such regions, the orientation extracted from the diffusion tensor is unreliable and may cause false negatives, in which tracking terminates [Behrens et al., 2007], or false positives, in which tracking switches to an unrelated adjacent tract [Pierpaoli et al., 2001].

To address the limitations of the DTI model, a number of approaches have recently been proposed based on high-angular resolution diffusion imaging (HARDI) [Anderson, 2005, Behrens et al., 2007, Dell'Acqua et al., 2007, Descoteaux et al., 2007, Hosey et al., 2005, Jansons and Alexander, 2003, Özarslan et al., 2006, Tuch et al., 2002, Tuch, 2004]. One of these methods, constrained spherical deconvolution (CSD), is especially promising as it can offer a reliable reconstruction of fiber orientation distribution functions (fODFs) within clinically feasible acquisition settings [Tournier et al., 2004, 2007]. CSD is capable of estimating the fODF within each voxel directly from the HARDI data, using the concept of spherical deconvolution. Recent studies, using both simulations and phantom data, have shown that CSD is able to robustly resolve narrow interfiber angles [Tournier et al., 2007, 2008].

In this chapter, a deterministic tractography algorithm is presented based on CSD. Using CSD to extract local fiber orientations, our algorithm will overcome partial volume effects associated with DTI and the poor angular resolution that is achieved with other HARDI methods such as QBI [Tournier et al., 2008]. After a detailed explanation of the algorithm, we proceed with both a quantitative and qualitative evaluation using different MR phantoms. Finally, we briefly discuss some applications of CSD based tractography.

4.2 Theory

4.2.1 Local fODF estimation using CSD

As described at length in Chapter 2, spherical deconvolution estimates the fODF directly from the spherical diffusion-weighted (DW) signal by deconvolving with a single fiber spherical response function [Tournier et al., 2004]. In this chapter we will be making use of the constrained spherical deconvolution (CSD) variant, which introduces a constraint to minimize the appearance of negative values in the reconstructed fODFs, which are clearly physically impossible. With this constraint, it is possible to perform the spherical deconvolution operation with drastically reduced noise sensitivity [Tournier et al., 2007]. A detailed explanation of these steps can be found in Chapter 2.

4.2.2 Tractography using CSD fODFs

The proposed tractography algorithm is based on the well-known streamline tractography algorithm used in DTI [Basser et al., 2000]. It can be summarized as follows (Fig. 4.1). Fiber tracking is started at a given seed point $\boldsymbol{r}_0$. First, the DW signal at the current position of the trajectory $\boldsymbol{r}_i$ is obtained using trilinear interpolation. Next, the fODF is estimated from the interpolated DW signal using CSD. Then, the peak direction $\boldsymbol{v}(\boldsymbol{r}_i)$ that is most closely aligned with the previous stepping direction $\boldsymbol{v}(\boldsymbol{r}_{i-1})$ is extracted from the fODF. Finally, the trajectory is advanced by a fixed step size Δ along the obtained direction:

$$\boldsymbol{r}_{i+1} = \boldsymbol{r}_i + \boldsymbol{v}(\boldsymbol{r}_i)\Delta \tag{4.1}$$

Tracking is ended when the amplitude of the most closely aligned fODF peak is beneath a fixed threshold, a maximum angle between two successive steps is exceeded, or the tract leaves a specified brain mask. In the seed points, all fODF peak directions with an amplitude above a fixed threshold are extracted and a separate streamline is started for each direction, in order to accommodate for seed points with multiple underlying fiber orientations.

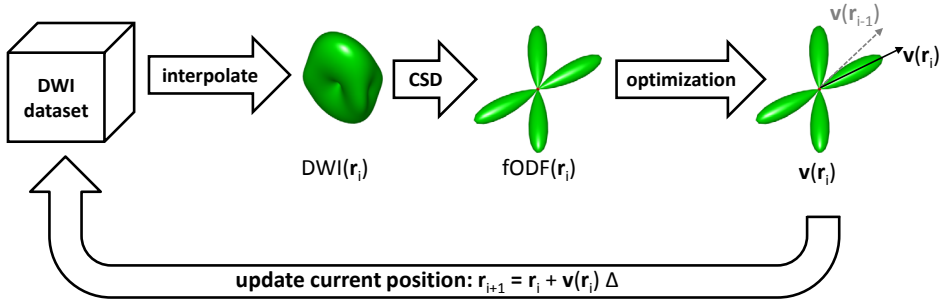

Fig. 4.1: Streamline tractography with CSD: DWI interpolation.

Note that, in the above implementation, we choose to interpolate on the raw DW signal rather than on the SH coefficients of the fODF. Since CSD is a nonlinear operator, in theory, interpolating linearly is only justified in the signal domain (raw DW signal) and not in the frequency domain (SH coefficients). In practice, however, the SH coefficients of the fODF are *almost* linearly related to the signal. In an alternative implementation, we first calculate the full fODF field and perform the interpolation directly on this field, bypassing the need of CSD at every tractography step (Fig. 4.2). This can greatly reduce the computation time.

4.2.3 fODF maxima extraction

Regardless of whether the interpolation is performed on the DW signal or the fODF, a deterministic streamline algorithm requires a way to extract discrete fiber orientations from the continuous fODF. In this section we will introduce a fast numerical method that allows to extract fODF maxima. Remember from Chapter 2

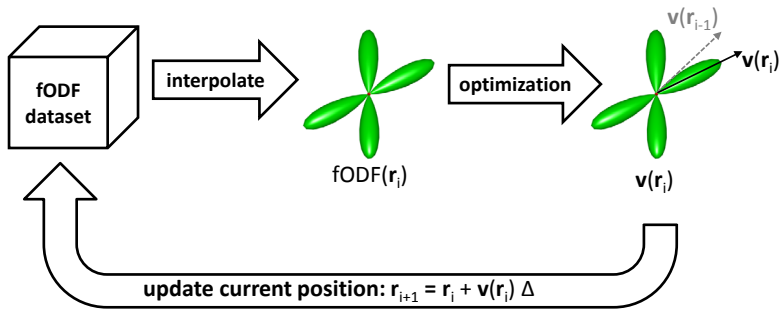

Fig. 4.2: Streamline tractography with CSD: fODF interpolation.

that the fODF is typically represented using a truncated modified SH series:

$$\mathrm{fODF}(\theta,\phi) = \sum_{l=0}^{l_{\max}} \sum_{m=-l}^{l} c_l^m \cdot {Y_l'}^m(\theta,\phi) \tag{4.2}$$

where $\{c_l^m\}$ denote the SH coefficients and $l_{\max}$ is the SH order at which the series is truncated. Remember also that the modified SH basis functions ${Y_l'}^m(\theta,\phi)$ are given as:

$${Y_l'}^m(\theta,\phi) = \begin{cases} N_l^m \cdot P_l^m(\cos(\theta)) \cdot \cos(m\phi) & \text{if } m > 0 \\ N_l^m \cdot P_l^0(\cos(\theta)) & \text{if } m = 0 \\ N_l^m \cdot P_l^{-m}(\cos(\theta)) \cdot \sin(-m\phi) & \text{if } m < 0 \end{cases} \tag{4.3}$$

with $P_l^m(\cdot)$ the associated Legendre polynomials and N_l^m a normalization factor:

$$N_l^m = \begin{cases} \sqrt{\frac{(2l+1)}{4\pi}} \cdot \sqrt{\frac{2(l-m)!}{(l+m)!}} & \text{if } m \neq 0 \\ \sqrt{\frac{(2l+1)}{4\pi}} & \text{if } m = 0 \end{cases} \tag{4.4}$$

From Eq. (4.2), it is clear that in order to calculate the partial derivatives of the fODF with respect to θ and ϕ, we need to calculate the partial derivatives of the basis functions:

$$\frac{\partial {Y_l'}^m(\theta,\phi)}{\partial\theta} = \begin{cases} -N_l^m \cdot \frac{\partial P_l^m(\cos(\theta))}{\partial\cos(\theta)} \cdot \sin(\theta) \cdot \cos(m\phi) & \text{if } m > 0 \\ -N_l^m \cdot \frac{\partial P_l^0(\cos(\theta))}{\partial\cos(\theta)} \cdot \sin(\theta) & \text{if } m = 0 \\ -N_l^m \cdot \frac{\partial P_l^{-m}(\cos(\theta))}{\partial\cos(\theta)} \cdot \sin(\theta) \cdot \sin(-m\phi) & \text{if } m < 0 \end{cases} \tag{4.5}$$

$$\frac{\partial {Y_l'}^m(\theta,\phi)}{\partial\phi} = \begin{cases} -N_l^m \cdot P_l^m(\cos(\theta)) \cdot m \cdot \sin(m\phi) & \text{if } m > 0 \\ 0 & \text{if } m = 0 \\ -N_l^m \cdot P_l^{-m}(\cos(\theta)) \cdot m \cdot \cos(-m\phi) & \text{if } m < 0 \end{cases} \tag{4.6}$$

With similar equations for the second partial derivatives:

$$\frac{\partial^2 Y_l^{'m}(\theta,\phi)}{\partial\theta^2} = \begin{cases} N_l^m \cdot \left(\frac{\partial^2 P_l^m(\cos(\theta))}{\partial\cos^2(\theta)} \cdot \sin^2(\theta) - \frac{\partial P_l^m(\cos(\theta))}{\partial\cos(\theta)} \cdot \cos(\theta)\right) & \text{if } m > 0 \\ \qquad\qquad \cdot \cos(m\phi) & \\ N_l^m \cdot \left(\frac{\partial^2 P_l^m(\cos(\theta))}{\partial\cos^2(\theta)} \cdot \sin^2(\theta) - \frac{\partial P_l^m(\cos(\theta))}{\partial\cos(\theta)} \cdot \cos(\theta)\right) & \text{if } m = 0 \\ N_l^m \cdot \left(\frac{\partial^2 P_l^{-m}(\cos(\theta))}{\partial\cos^2(\theta)} \cdot \sin^2(\theta) - \frac{\partial P_l^{-m}(\cos(\theta))}{\partial\cos(\theta)} \cdot \cos(\theta)\right) & \text{if } m < 0 \\ \qquad\qquad \cdot \sin(-m\phi) & \end{cases} \tag{4.7}$$

$$\frac{\partial^2 Y_l^{'m}(\theta,\phi)}{\partial\phi^2} = \begin{cases} -N_l^m \cdot P_l^m(\cos(\theta)) \cdot m \cdot m \cdot \cos(m\phi) & \text{if } m > 0 \\ 0 & \text{if } m = 0 \\ -N_l^m \cdot P_l^{-m}(\cos(\theta)) \cdot m \cdot m \cdot \sin(-m\phi) & \text{if } m < 0 \end{cases} \tag{4.8}$$

$$\frac{\partial^2 Y_l^{'m}(\theta,\phi)}{\partial\theta\partial\phi} = \begin{cases} N_l^m \cdot \frac{\partial P_l^m(\cos(\theta))}{\partial\cos(\theta)} \cdot \sin(\theta) \cdot m \cdot \sin(m\phi) & \text{if } m > 0 \\ 0 & \text{if } m = 0 \\ N_l^m \cdot \frac{\partial P_l^{-m}(\cos(\theta))}{\partial\cos(\theta)} \cdot \sin(\theta) \cdot m \cdot \cos(-m\phi) & \text{if } m < 0 \end{cases} \tag{4.9}$$

The first and second derivatives of the associated Legendre polynomials in Eqs. (4.5), (4.7) and (4.9) can be calculated directly from different order associated Legendre polynomials using the following recurrence relations:

$$\frac{\partial P_l^m(x)}{\partial x} = \begin{cases} -P_l^1(x) & \text{if } m = 0 \\ \frac{(l+m)(l-m+1)P_l^{m-1}(x) - P_l^{m+1}(x)}{2} & \text{if } m > 0 \end{cases} \tag{4.10}$$

$$\frac{\partial^2 P_l^m(x)}{\partial x^2} = \begin{cases} -\frac{\partial P_l^1(x)}{\partial x} & \text{if } m = 0 \\ \frac{(l+m)(l-m+1)\frac{\partial P_l^{m-1}(x)}{\partial x} - \frac{\partial P_l^{m+1}(x)}{\partial x}}{2} & \text{if } m > 0 \end{cases} \tag{4.11}$$

From Eqs. (4.2)-(4.11), it is clear that a fast evaluation of the fODF(θ,ϕ) and its first and second partial derivatives, hinges entirely on a fast evaluation of the associated Legendre polynomials $P_l^m(\cos(\theta))$. Fortunately, it is possible to precalculate values of $P_l^m(\cos(\theta))$ at equally spaced points in the domain $[0, 2\pi]$[1]. From these tables, $P_l^m(\cos(\theta))$ can then be evaluated for any θ by means of linear interpolation between two neighboring precalculated points (Fig. 4.3).

Now that we have established a fast way of calculating $f(\theta,\phi)$ and its first and second partial derivatives, we can search for the maximum of fODF(θ,ϕ) most closely aligned to an initial orientation (θ_0,ϕ_0), by means of Newton optimization:

$$(\theta_{n+1},\phi_{n+1}) = (\theta_n,\phi_n) - \nabla(f)(\theta_n,\phi_n) \cdot [\mathrm{H}(f)(\theta_n,\phi_n)]^{-1} \tag{4.12}$$

where

$$\nabla(f)(\theta,\phi) = \left(\frac{\partial f(\theta,\phi)}{\partial\theta}, \frac{\partial f(\theta,\phi)}{\partial\phi}\right) \tag{4.13}$$

[1] idea taken from J. D. Tournier. MRtrix - tractography through crossing fibres (`http://www.nitrc.org/projects/mrtrix/`)

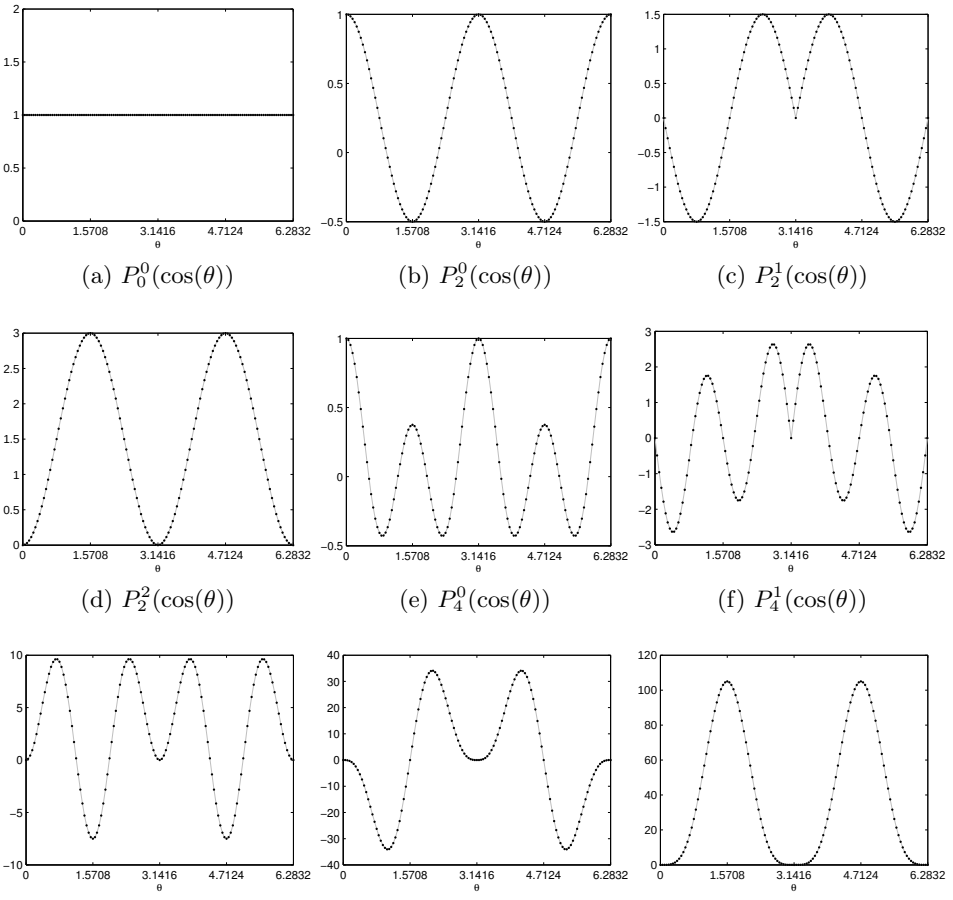

(a) $P_0^0(\cos(\theta))$ (b) $P_2^0(\cos(\theta))$ (c) $P_2^1(\cos(\theta))$

(d) $P_2^2(\cos(\theta))$ (e) $P_4^0(\cos(\theta))$ (f) $P_4^1(\cos(\theta))$

(g) $P_4^2(\cos(\theta))$ (h) $P_4^3(\cos(\theta))$ (i) $P_4^4(\cos(\theta))$

Fig. 4.3: Precalculated values (black dots) of $P_l^m(\cos(\theta))$ up till order 4 in 128 evenly distributed points in the interval $[0, 2\pi]$. Intermediate function values can be obtained fast by means of linear interpolation (grey lines).

and

$$\mathrm{H}(f)(\theta,\phi) = \begin{bmatrix} \frac{\partial^2 f(\theta,\phi)}{\partial\theta^2} & \frac{\partial^2 f(\theta,\phi)}{\partial\theta\partial\phi} \\ \frac{\partial^2 f(\theta,\phi)}{\partial\theta\partial\phi} & \frac{\partial^2 f(\theta,\phi)}{\partial\phi^2} \end{bmatrix} \tag{4.14}$$

are the gradient vector and hessian matrix of f, respectively.

4.3 Evaluation using MR phantoms

4.3.1 Proof-of-concept using a simple phantom

4.3.1.1 Materials and methods

Phantom construction A 90° crossing fiber phantom was constructed using synthetic Dyneema® fibers (Fig. 4.4a), following the methodology of Fieremans et al. [2008a,b]. The individual fibers with a diameter of 20 µm were grouped in parallel bundles of 780 fibers and then crossed (Fig. 4.4b). The bundles were surrounded by a polyolefin low-temperature shrinking tube (Fig. 4.4c) and placed in a Plexiglas cylindrical container filled with water. Consequently, the water was heated up and kept constant at 90 °C during at least 600 s to shrink the shrinking tube in order to produce a homogeneously, densely packed fiber phantom. To avoid susceptibility differences caused by air bubbles, the whole fabrication process was performed under water. Remaining air bubbles were removed by squeezing and placing the phantoms in a vacuum chamber and subsequently in an ultrasonic bath to remove small bubbles attached to the fibers and the shrinking tube.

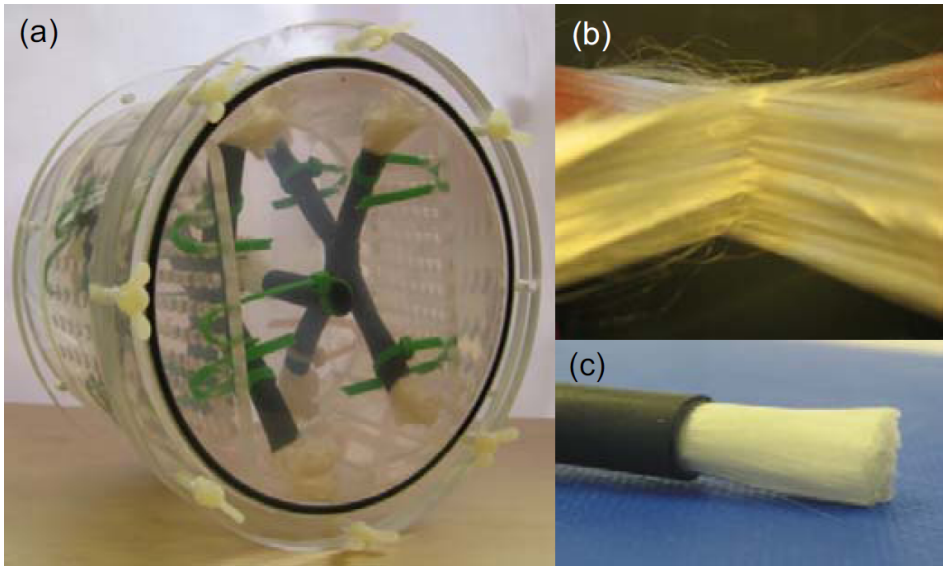

Fig. 4.4: Crossing fiber phantom (a) with details of the interwoven fiber bundles (b) and the shrinking tube (c).

Acquisition DW imaging was performed on a 3 T MRI scanner with 256 gradient directions and a b-value of 0 and 2500 s/mm^2 with an EPI sequence with a receiver band width of 1565 Hz/pixel. A total of 44 slices was acquired in a repetition time of 6.7 s and with an echo time of 109 ms. The resolution was $2 \times 2 \times 2\,\text{mm}^3$.

Local fiber orientation estimation fODFs were obtained using CSD using the following parameters: $l_{\max} = 8$, $\lambda = 0.1$, $\tau = 10\%$. For reference, we also calculated the corresponding DTI ellipsoids.

Tractography Deterministic streamline tractography was performed using both CSD and DTI. Parameters for the streamline algorithm were: step size = 1 mm; maximum angle = 70°; minimal fODF amplitude = 0.1; minimal FA = 0.1.

4.3.1.2 Results

Fig. 4.5 shows the DTI ellipsoids and CSD fODFs in the crossing fiber region. From Fig. 4.5a, it is clear that DTI is unable to resolve the fiber crossing and reports oblate DTI ellipsoids. CSD fODFs on the other hand are very sharp, clearly resolving the fiber orientations in the crossing fiber region (Fig. 4.5c).

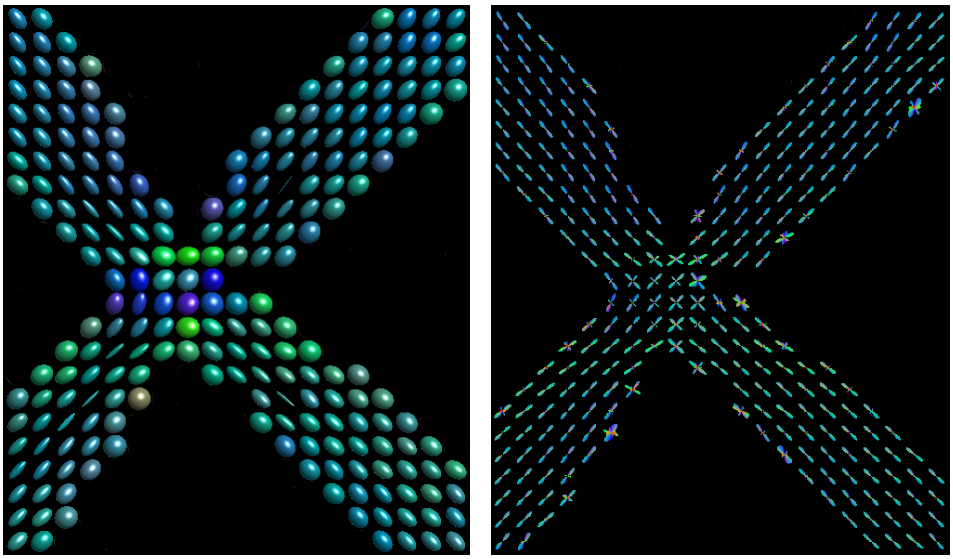

(a) DTI ellipsoids (b) CSD fODFs

Fig. 4.5: Detail of the fiber crossing. At the crossing DTI reports oblate DT ellipsoids, highlighting DTI's inability to resolve crossing fibers (a). CSD on the other hand reports very sharp fODFs at the fiber crossing, with the fODF maxima along the expected fiber orientations (b).

Fig. 4.6 shows tractography results using both DTI and CSD. At the fiber crossing, the first eigenvector of the DT becomes undefined and is mostly determined

by the noise in the data. As a consequence, DTI fiber trajectories will either jump to the crossing fiber bundle (false positive); or make it through the fiber crossing (either by chance or due to one fiber population being slightly dominant over the other). CSD trajectories, on the other hand, all pass through the crossing fiber region, faithfully representing the true fiber configuration.

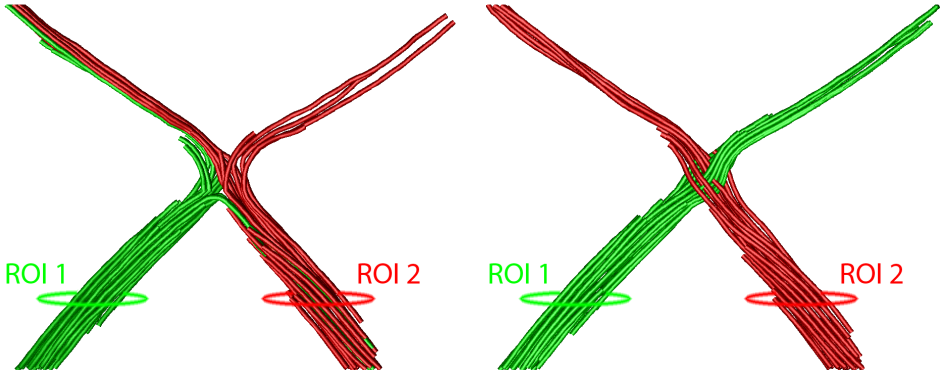

(a) DTI tractography (b) CSD tractography

Fig. 4.6: ROI-based tractography with DTI (a) and CSD (b) starting from ROI 1 (green trajectories) and ROI 2 (red trajectories). In the fiber crossing region, DTI trajectories jump to the other fiber bundle. These trajectories do not correspond to the actual fiber configuration in the phantom. CSD trajectories, on the other hand, accurately pass through the crossing fiber region.

4.3.2 Quantitative evaluation using a complex phantom

Our CSD tractography algorithm was evaluated quantitatively on a HW phantom as part of the MICCAI 2009 Fiber Cup (FC). For this contest, the organizers made DW data available from an MR phantom containing complex fiber configurations, together with 16 seed points from which the participants were to launch tractography. After submission, the reconstructed trajectories were compared to a set of ground truth trajectories, based on the spatial distance, tangent difference, and curvature difference [Fillard et al., 2011].

4.3.2.1 Materials and methods

Phantom construction The FC organizers constructed a physical phantom containing realistic crossing, kissing, splitting and bending fiber configurations (Fig. 4.7). Fiber bundles were created out of hydrophobic acrylic fibers with a diameter of 20 µm. Polyurethane negative and positive prints of the target bundles were manufactured. Bundles were carefully positioned such that they rigorously follow the pathways sketched in Fig. 4.7a. Bundles of about 100 fibers were used to progressively fill it. First, a layer of bundles was placed everywhere in the phantom. Then, a second layer was placed everywhere except at the intersections,

to ensure an even distribution of fibers. Finally, this process was reiterated until the desired number of fibers was positioned. In the next step, the positive and negative prints were squeezed, while keeping the fibers strongly tightened, until the fiber bundles were 1 cm in diameter. The resulting fiber packing was approximately 1900 fibers/mm^2. The phantom was placed in a Plexiglas cylindrical container filled with pure distilled water. To avoid air bubbles, a dedicated platform was designed that enabled preliminary degassing of the solution, and filling under vacuum conditions. An ultrasound beam was finally used to destroy any remaining air bubbles.

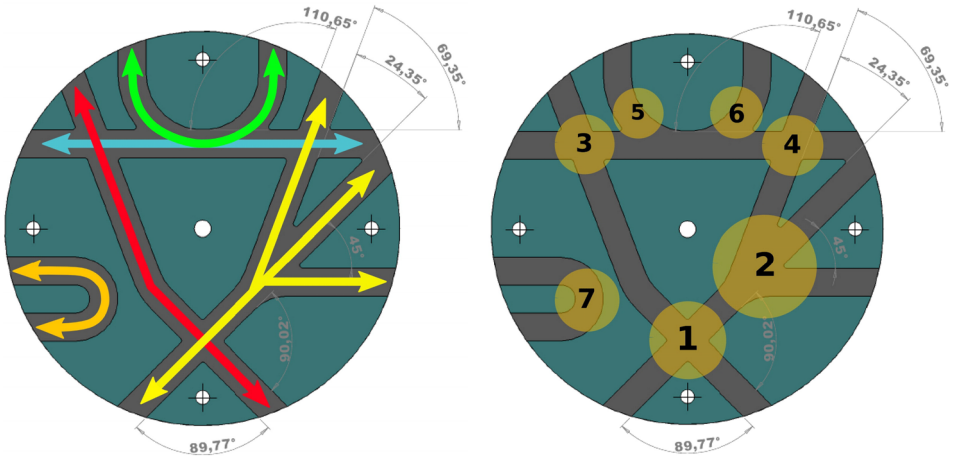

(a) (b)

Fig. 4.7: Schematic representation of the complex fiber phantom with: (a) the trajectories of the underlying fiber bundles; (b) the different regions of complex fiber architecture (1, 3, 4: crossing; 2: branching; 5, 6: kissing; 7: bending).

Acquisition The FC organizers acquired DW data of the phantom on a 3 T MRI scanner equipped with a whole body gradient coil and using a 12-channel receive only head coil, in combination with the whole body transmit coil of the MRI system. A single-shot DW twice refocused spin echo echoplanar pulse sequence was used to perform the acquisitions. Data sets were acquired at two different spatial resolutions: $3 \times 3 \times 3$ mm^3 and $6 \times 6 \times 6$ mm^3.

Parameters for the $3 \times 3 \times 3$ mm^3 acquisition were as follows: field of view FOV = 19.2 cm, matrix 64×64, slice thickness TH = 3 mm, read bandwidth RBW = 1775 Hz/pixel, partial Fourier factor 6/8, parallel reduction factor GRAPPA = 2, repetition time TR = 5 s, NEX = 2. Three diffusion sensitizations at b-values $b = 650/1500/2000$ s/mm^2 corresponding to the echo times TE = 77/94/112 ms respectively were used. 3 slices were acquired. Parameters for the $6 \times 6 \times 6$ mm^3 acquisition were as follows: field of view FOV = 38.4 cm, matrix 64×64, slice thickness TH = 6 mm, read bandwidth RBW = 1775 Hz/pixel, partial Fourier factor 6/8, parallel reduction factor GRAPPA = 2, repetition time TR = 5 s, NEX = 1. Three diffusion sensitizations at b-values $b = 650/1500/2650$ s/mm^2

corresponding to the echo times TE = 77/94/110 ms respectively were used. 1 slice was acquired. For both the $3 \times 3 \times 3\,\mathrm{mm}^3$ and the $6 \times 6 \times 6\,\mathrm{mm}^3$ data sets, diffusion gradients were applied along a set of 64 orientations uniformly distributed over the sphere [Jones et al., 1999]. Average SNRs and FA values for all data sets are summarized in Table 4.1.

voxel size (mm^3)	b-value ($\mathrm{s/mm}^2$)	average SNR	average FA
$3 \times 3 \times 3$	650	9.1	0.11
	1500	2.6	0.11
	2000	1.1	0.08
$6 \times 6 \times 6$	650	18.9	0.11
	1500	17.6	0.13
	2650	4.5	0.19

Table 4.1: Summary of the available data sets and their voxel sizes, b-values, average SNRs and average FA values.

For our submission, the data set with a voxel size of $6 \times 6 \times 6$ mm^3 and a b-value of $2650\,\mathrm{s/mm}^2$ was selected, favoring angular contrast and SNR over spatial resolution.

Preprocessing Exploratory diffusion tensor analysis [Leemans et al., 2009] revealed unusually low fractional anisotropy (FA) values in single fiber voxels (in the range [0.1, 0.2]), meaning there is very little directionality in the DW signal. This low angular contrast, in combination with the low SNR of the DW images (intrinsic to the high b-value DW measurements), makes the estimated fiber orientations very susceptible to noise contamination.

To increase SNR, an adaptive anisotropic Gaussian filter was applied to the DW data (where σ of the Gaussian kernel in a homogeneous region was 8.4 mm). This filter was previously shown to be efficient in reducing noise while retaining edge information [Sijbers et al., 1999].

Local fiber orientation estimation fODFs were obtained using CSD with the following parameters: $l_{\max} = 6$, $\lambda = 0.1$, $\tau = 10\%$. While the maximum modified SH degree one can estimate directly based on 64 DW images is 8, $l_{\max} = 6$ was chosen to further improve robustness to noise.

Tractography Deterministic streamline tractography was performed using CSD derived fODFs. Parameters for the streamline algorithm were: step size = 0.1 mm; maximum angle = 50°; and minimal fODF amplitude = 0.1.

Quantitative evaluation The candidate fiber trajectories were first parameterized by interpolating cubic b-splines. Subsequently, they were compared with the ground truth trajectories by calculating the Root Mean Square Error (RMSE) of

point-based distance metrics:

$$\mathrm{RMSE}(\boldsymbol{f}_1, \boldsymbol{f}_2) = \sqrt{\int_0^1 \mathrm{dist}^2(\boldsymbol{f}_1(s), \boldsymbol{f}_2(c(s)))\,\mathrm{d}s} \tag{4.15}$$

where $\boldsymbol{f}_1$ and $\boldsymbol{f}_2$ are the two fiber trajectories being compared, s is the arc length in the range $[0, 1]$ and c is a function providing for each arc length s of $\boldsymbol{f}_1$, the corresponding arc length of $\boldsymbol{f}_2$. The function c is established such that the distance between corresponding trajectory points is minimal:

$$c = \min_c \int_0^1 \|\boldsymbol{f}_1(s) - \boldsymbol{f}_2(c(s))\|^2\,\mathrm{d}s \tag{4.16}$$

Since, in general, $\mathrm{RMSE}(\boldsymbol{f}_1, \boldsymbol{f}_2) \neq \mathrm{RMSE}(\boldsymbol{f}_2, \boldsymbol{f}_1)$, a symmetrized version of RMSE was used instead:

$$\mathrm{sRMSE}(\boldsymbol{f}_1, \boldsymbol{f}_2) = \frac{1}{2}\left[\mathrm{RMSE}(\boldsymbol{f}_1, \boldsymbol{f}_2) + \mathrm{RMSE}(\boldsymbol{f}_2, \boldsymbol{f}_1)\right] \tag{4.17}$$

The sRMSE was evaluated for three different distance metrics:

1. A *spatial metric*, which is the Euclidian distance between two corresponding fiber positions:

$$\mathrm{dist}_{\mathrm{spatial}}[\boldsymbol{f}_1(s), \boldsymbol{f}_2(c(s))] = \|\boldsymbol{f}_1(s) - \boldsymbol{f}_2(c(s))\| \tag{4.18}$$

2. A *tangent metric*, which measures the absolute angular difference of the tangent at two corresponding fiber positions:

$$\mathrm{dist}_{\mathrm{tangent}}[\boldsymbol{f}_1(s), \boldsymbol{f}_2(c(s))] = \mathrm{acos}\left(\left|\frac{\boldsymbol{f}_1'(s)}{\|\boldsymbol{f}_1'(s)\|} \cdot \frac{\boldsymbol{f}_2'(c(s))}{\|\boldsymbol{f}_2'(c(s))\|}\right|\right)\frac{180}{\pi} \tag{4.19}$$

3. A *curvature metric*, which measures the absolute difference of the curvature at two corresponding fiber positions:

$$\mathrm{dist}_{\mathrm{curvature}}[\boldsymbol{f}_1(s), \boldsymbol{f}_2(c(s))] = \left|\frac{\|\boldsymbol{f}_1'(s) \times \boldsymbol{f}_1''(s)\|}{\|\boldsymbol{f}_1'(s)\|} - \frac{\|\boldsymbol{f}_2'(c(s)) \times \boldsymbol{f}_2''(c(s))\|}{\|\boldsymbol{f}_2'(c(s))\|}\right| \tag{4.20}$$

These metrics allow quantitative comparison of fiber trajectories not only in terms of their spatial position, but also in terms of their direction and curvature.

The three best solutions that participated in the FC (including our submission) will be compared using the above criteria. Our solution will be referred to as 'CSD streamline', and has been described at length in the previous sections. The other two solutions will be referred to as 'global tractography' and 'filtered 2-tensor streamline tractography'. Note that we did not run these algorithms ourselves, but the results were taken from each algorithm's originator for comparison.

The 'global tractography' approach uses the concept of global tractography as introduced in Chapter 3. In brief, this method minimizes the energy of a collection of line segments. The energy term is the sum of two energy terms. The first 'internal

energy' term encourages line segments to connect with neighboring segments and take on similar orientations. This term implicitly embeds the prior belief that fiber trajectories exhibit low curvature. The second 'external energy' term encourages that the DW signal predicted by the line segments is in agreement with the measured DW signal. As such, all fiber trajectories are estimated concurrently without the need for prior fiber orientation estimation. This solution used the data set with a voxel size of $3 \times 3 \times 3$ mm^3 and a b-value of 2000 s/mm^2, which exhibited the lowest average SNR and FA.

The 'filtered 2-tensor streamline' approach uses a 2-tensor streamline algorithm. However, the local fiber orientation estimation step is improved by means of a Kalman filter, which takes into account the currently traversed trajectory during the fiber orientation estimation. A detailed description of both methods is considered beyond the scope of this dissertation and can be found in Reisert et al. [2009, 2011] and Malcolm et al. [2009, 2010] respectively. This solution used the data set with a voxel size of $3 \times 3 \times 3$ mm^3 and a b-value of 1500 s/mm^2.

4.3.2.2 Results

Qualitative results Fig. 4.8 shows the CSD fODFs calculated from the FC data set. In the fiber crossings, the fODF maxima correspond to the expected fiber orientations. The corresponding CSD streamlines are shown in Fig. 4.9a along

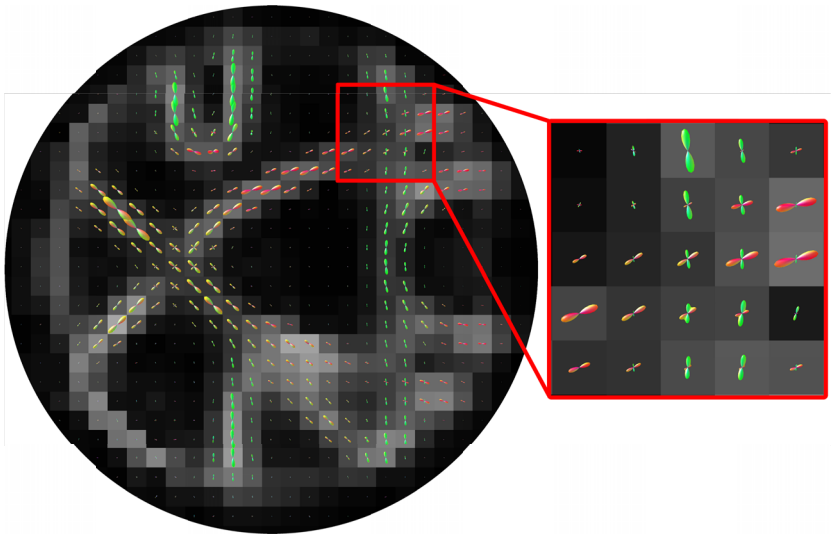

Fig. 4.8: CSD fODFs imposed on the non-DW image. Note that the fODFs maxima agree with the expected underlying fiber orientations.

with the ground truth trajectories (Fig. 4.9b). The colored voxels indicate the seed points provided by the organizers of the FC. While the reconstructed trajectories are slightly displaced compared to the ground truth, our solution was able to resolve all fiber crossings correctly.

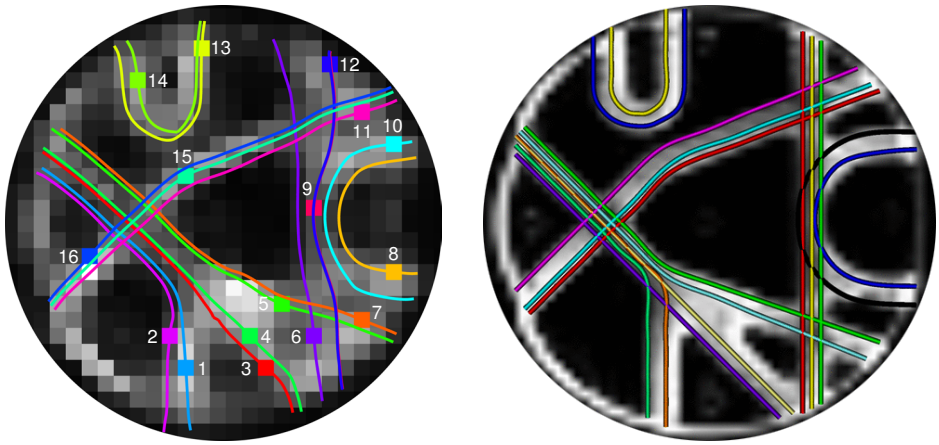

(a) CSD fiber trajectories (b) Ground truth fiber trajectories

Fig. 4.9: CSD fiber trajectories, reconstructed from the given seed points, imposed on the non-DW image.

Quantitative results Figs. 4.10-4.11 shows the results from the quantitative evaluation. In Fig. 4.10, our set of fiber trajectories is compared with the top 3 results. Looking at the spatial metric (Fig. 4.10a), the set of CSD trajectories is the only one successfully following all trajectories from start to end (no large peaks). The global tractography solution performs similar to the CSD solution, but fails to follow fiber bundle 12 from start to end (large peak at bundle 12). The filtered 2-tensor solution fails in fiber bundle 6, 7, 9, and 11. Consequently, our solution has the lowest mean spatial error, followed by the global tractography solution and the filtered 2-tensor solution. It should be noted that, although the global tractography algorithm fails for one fiber bundle, when it works it provides the closest match to the gold standard trajectory. This is not surprising given that it explores many more candidate trajectories than the other algorithms, which are much faster.

Similar conclusions can be drawn by looking at the tangent metric (Fig. 4.10b). The CSD solution shows no large peaks in the tangent error indicating that our solution is able to follow the correct trajectories from start to end. The global tractography solution shows a large peak at bundle 12, indicating that it chose the wrong pathway within a crossing. The filtered 2-tensor solution clearly followed the wrong fiber orientation in bundle 6, 7, 9, 11, and 16. As a consequence, our CSD solution has the lowest mean tangent error, followed by the global tractography solution and the filtered 2-tensor solution.

The curvature metric in Fig. 4.10c penalizes fibers with high curvature, since the ground truth only contains straight or low-curved fibers. For this metric, the CSD streamline solution exhibits large peaks for fiber bundles 3 and 14, due to a discontinuity at one point along those fiber bundles. The global tractography solution shows no peaks in the curvature error, indicating that the curvature of the fibers in this solution is low. The filtered 2-tensor solution exhibits no large peaks

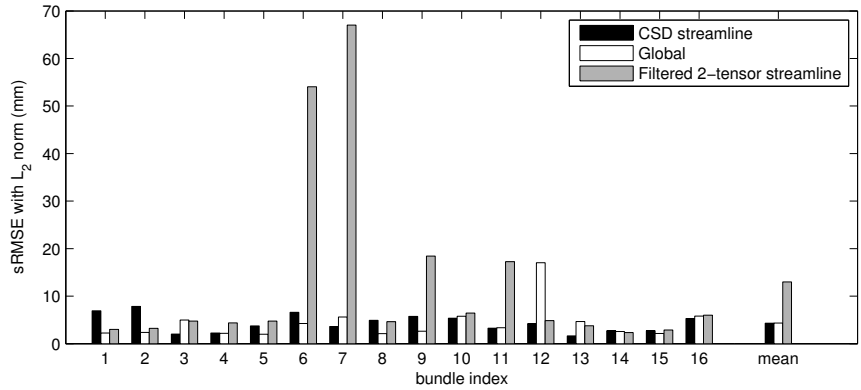

(a) Spatial metric

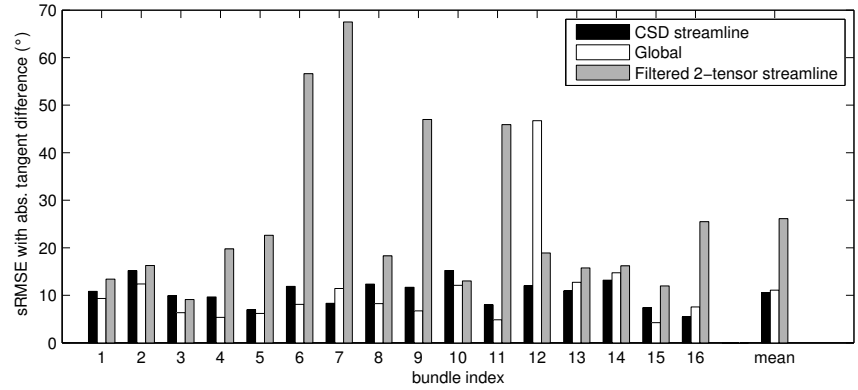

(b) Tangent metric

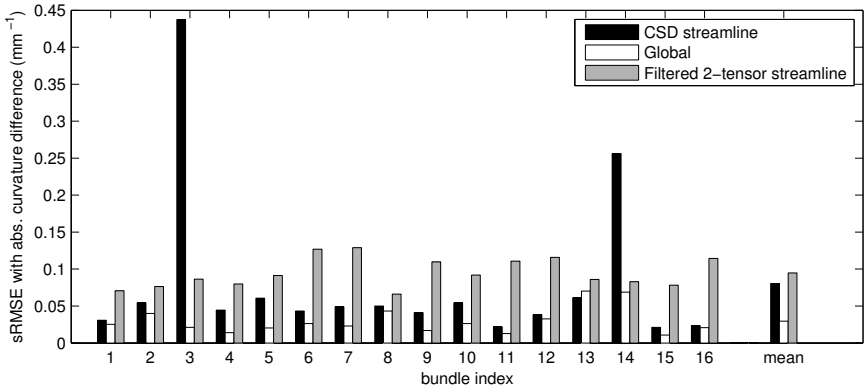

(c) Curvature metric

Fig. 4.10: Quantitative comparison of the 3 best solutions: CSD streamline tractography, global tractography and filtered 2-tensor streamline tractography. Bundle indices correspond to the numbers in Fig. 4.9.

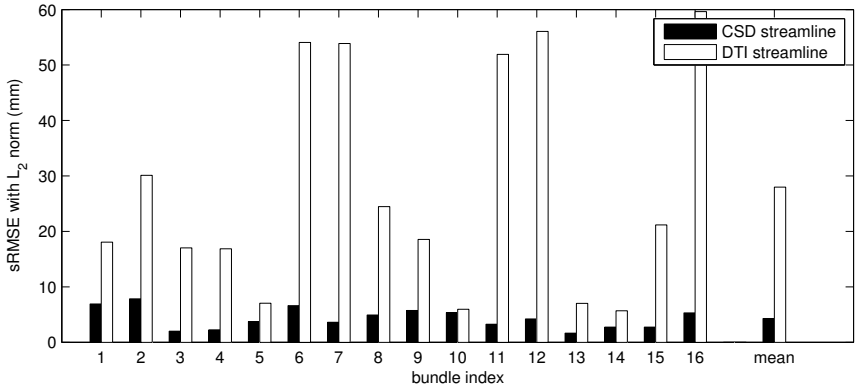

(a) Spatial metric

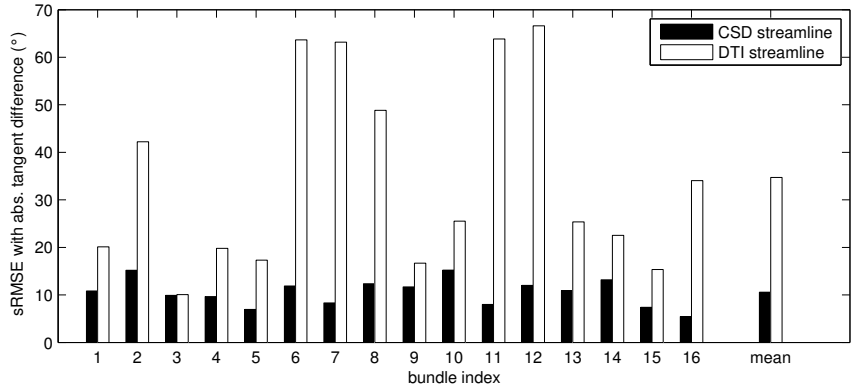

(b) Tangent metric

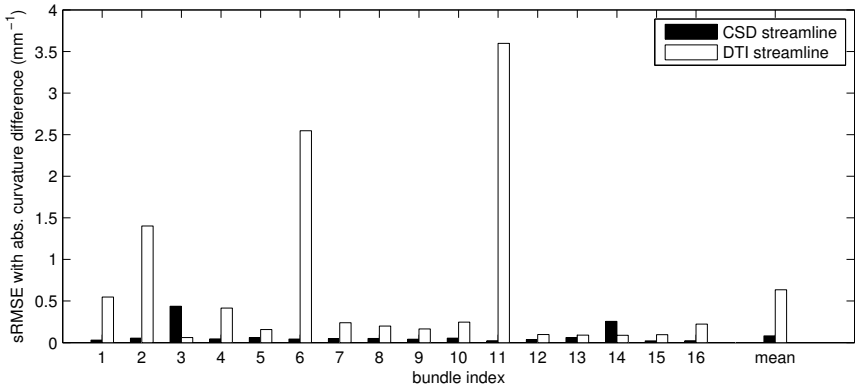

(c) Curvature metric

Fig. 4.11: Quantitative comparison between the CSD streamline solution and the best DTI streamline solution. Bundle indices correspond to the numbers in Fig. 4.9.

in the curvature metric, but the errors are on average larger than for the two other methods. As a consequence, the global tractography solution has the lowest mean curvature error, followed by the CSD solution and the filtered 2-tensor solution.

In Fig. 4.11, our set of fiber trajectories is compared with the best DTI based tractography result [Gouttard et al., 2009]. As expected, the spatial and tangent errors are much higher for the DTI solution, since DTI cannot resolve crossing fibers and is bound to make wrong decisions in crossing fiber regions (Fig. 4.11a-b). Also, the curvature error is typically higher for the DTI result due to high curvature bends in crossing fiber regions (Fig. 4.11c). These results highlight once more the limits of DTI based tractography: in regions of fiber crossings it is extremely sensitive to false positives and false negatives.

4.4 Evaluation on a real data set

4.4.1 Materials and methods

4.4.1.1 Acquisition

Whole-brain HARDI data were acquired from a healthy adult volunteer on a General Electric 3 T HDx Signa system. An eight-channel head coil with parallel imaging factor of 2 was used to acquire twice-refocused spin echo echoplanar images with TE = 109 ms and $2.4 \times 2.4 \times 2.4\,\mathrm{mm}^3$ voxel size (FOV $23 \times 23\,\mathrm{cm}^2$, 96×96 acquisition matrix, NEX = 1, partial Fourier encoding with 16 overscans before the center of k, 60 slices with 2.4 mm thickness with no gap). Diffusion gradients were applied in 60 directions uniformly distributed on a sphere through electrostatic repulsion [Jones et al., 1999] with $b = 3000\,\mathrm{s/mm}^2$. Six images with $b = 0\,\mathrm{s/mm}^2$ were also acquired. Cardiac gating was applied using a peripheral pulse oximeter with an effective TR = 20 R-R intervals. Total scan time was approximately 20 minutes. Motion and eddy-current distortion correction was applied taking into account the B-matrix rotation [Leemans and Jones, 2009] and the tensor model was fitted to the data using a weighted (anisotropic covariance matrix) linear regression method [Basser et al., 1994a]. These processing steps were performed with the diffusion MR toolbox ExploreDTI [Leemans et al., 2009]. SNR within the $b = 0\,\mathrm{s/mm}^2$ images was approximately 30, calculated using the difference method to compensate for spatial noise variations in parallel imaging [Dietrich et al., 2007]. The subject gave written informed consent to participate in this study under a protocol approved by the Cardiff University Ethics Committee.

4.4.1.2 Local fiber orientation estimation

fODFs were obtained using CSD using the following parameters: $l_{\max} = 8$, $\lambda = 0.1$, $\tau = 10\%$. For reference, we also calculated the corresponding DTI ellipsoids, and QBI dODFs (with $l_{\max} = 8$).

4.4.1.3 Tractography

Deterministic streamline tractography was performed using both CSD and DTI. Parameters for the streamline algorithm were: step size = 1 mm; maximum angle

= 70°; minimal fODF amplitude = 0.1; minimal FA = 0.1.

4.4.2 Results

Fig. 4.12 displays deterministic CSD and DTI trajectories at the crossing of commissural (the corpus callosum, CC), association (the superior longitudinal fasciculus, SLF) and projection fibers (the corticospinal tract, CST) along with the associated CSD fODFs and DTI ellipsoids. Note that for the CST, which is the dominant fiber bundle in this region, both CSD and DTI tractography produce similar results. However, for the non-dominant fiber bundles, large differences can be observed between CSD and DTI tractography. While both DTI and CSD tractography are able to reconstruct the superior projections of the CC, only CSD is able to reconstruct the lateral projections of the CC. DTI tractography is not able to find these lateral projections (false negatives) and instead switches to the superior projections and to the tail of caudate nucleus (false positives). CSD tractography is able to reconstruct the SLF from front to back. DTI tractography on the other hand suffers from partial volume effect between the true SLF and the CST, causing the trajectories to bend downwards.

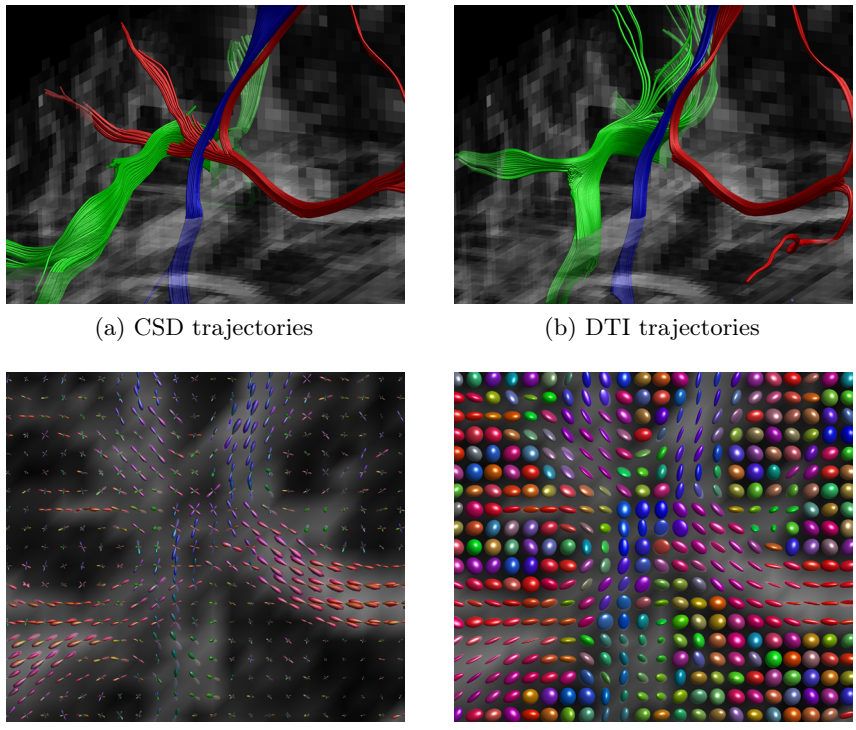

(a) CSD trajectories

(b) DTI trajectories

(c) CSD fODFs

(d) DTI ellipsoids

Fig. 4.12: Deterministic tractography in the corpus callosum (red), superior longitudinal fasciculus (green) and corticospinal tract (blue) using both CSD (a) and DTI (b). Corresponding CSD fODFs and DTI ellipoids are shown in (c) and (d), respectively.

4.5 Discussion and conclusion

In this chapter, we have introduced a deterministic tractography algorithm based on CSD-derived fODFs and streamlines. By means of a simple crossing fiber phantom and a real data example, we showed that the algorithm is able to track through regions containing crossing fibers where DTI tractography fails.

In addition, our method was evaluated quantitatively on a more complex fiber phantom, as part of the MICCAI 2009 FC contest. FA values in the FC phantom data sets were found to be extremely low compared to the values found in human WM, ranging from 0.08 to 0.19 depending on the b-values and voxel dimensions. The combination of such low angular contrast with the intrinsic low SNR of DW images, made fiber orientation estimation a challenging task. This motivated us to select the data set with a voxel size of $6 \times 6 \times 6\,\mathrm{mm}^3$ and $b = 2650\,\mathrm{s/mm}^2$, favoring SNR and angular contrast over spatial resolution. In order to reconstruct spatially consistent fiber orientations, SNR was further improved by filtering the data with an adaptive anisotropic smoothing kernel. Using such a filter, it was possible to reduce spatial blurring to a minimum, avoiding the artificial widening of fiber bundles and the introduction of artificial multi-fiber voxels. After this preprocessing step, our tractography algorithm was able to reconstruct convincing fiber trajectories.

While the tractography results look plausible, the low spatial resolution, however, could introduce artificial fiber trajectories, since, at the voxel level, we are unable to differentiate crossing from kissing or bending fiber configurations. Also, streamline tractography is basically an 'all-or-nothing approach', where a single error along the fiber trajectory can steer the tracking of course with no hope for recovery and no indication of confidence.

Notwithstanding these limitations, a quantitative analysis of the FC results revealed our solution was among the top contenders for the FC. Indeed, our trajectories were characterized by the lowest average error for both the spatial and directional metric and our method was the only one tracing the correct fiber bundles from start to end. Our solution was only bested in terms of curvature error by the global tractography solution which produces smooth fiber trajectories by design. This proves that performing good fiber tractography is not all about choosing the most advanced tractography method, but that much is to be gained by choosing the right data. We may argue that SNR and angular contrast play a key role in diffusion model estimation and should not always be sacrificed for the benefit of spatial resolution.

4.6 Applications

4.6.1 Tractography of the SLF in Alzheimer's patients

The association fibers of the superior longitudinal fasciculus (SLF) exhibit partial voluming with the projection fibers of the corticospinal tract (CST) and the commissural tracts of the corpus callosum (CC), making accurate delineation of the SLF a challenging task. CSD tractography has recently been shown to markedly improve the delineation of the SLF as opposed to DTI tractography

[**Jeurissen** et al., 2011]. These improved delineations can be used as ROIs for the quantitative analysis of popular scalar diffusion indices such as FA. In a recent study on Alzheimer's disease, CSD tractography was used for improved SLF delineation (Fig. 4.13). It was shown that this significantly increased the sensitivity to detect WM abnormalities as opposed to results obtained with conventional DTI based tractography [Reijmer et al., 2011a,b].

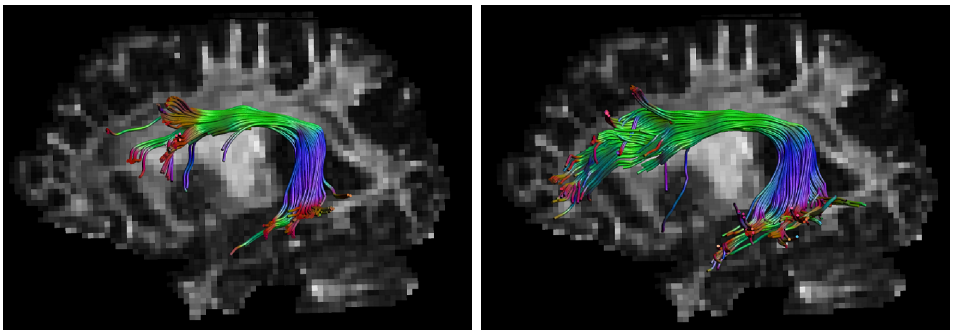

(a) DTI tractography (b) CSD tractography

Fig. 4.13: Reconstruction of the SLF with DTI (a) and CSD (b) based tractography in a representative Alzheimer's disease patient. The corresponding SLF volumes were subsequently used as ROIs and the scalar diffusion indices such as FA, MD and axial and radial diffusivity were correlated with memory performance.

4.6.2 Tractography of the female pelvic floor

Our approach was recently used to perform fiber tracking in the muscles of the female pelvic floor [Froeling et al., 2011].

4.6.3 Tractography of the optic chiasm in the starling brain

The optic chiasm is composed of two optic nerve bundles that connect the visual system of the brain with the retina of each eye (Fig. 4.14a). As opposed to the human optic chiasm, the optic chiasm of birds, such as the starling, consists entirely of crossing fibers [Cowan et al., 1961]. This makes it an interesting structure for the validation of fiber tracking techniques. Fig. 4.14b shows that DTI based fiber tracking is unable to resolve the crossing due to the oblate ellipsoids found at the avian optic chiasm (Fig. 4.14c). CSD-derived fODFs on the other hand, can resolve the crossing fibers (Fig. 4.14e), resulting in improved fiber tracking in the optic chiasm in the starling (Fig. 4.14d) [De Groof and Van der Linden, 2010].

Bibliography

D. C. Alexander, G. J. Barker, and S. R. Arridge. Detection and modeling of non-Gaussian apparent diffusion coefficient profiles in human brain data. *Magnetic*

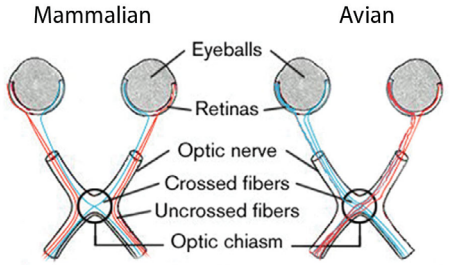

(a) Schematic representation of the optic chiasm in humans (left) and birds (right)

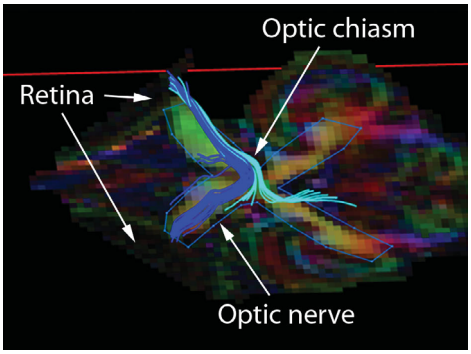

(b) DTI tractography

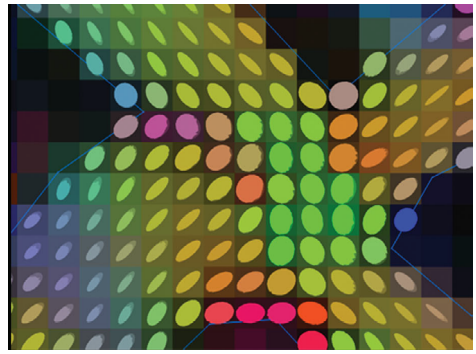

(c) DTI ellipsoids

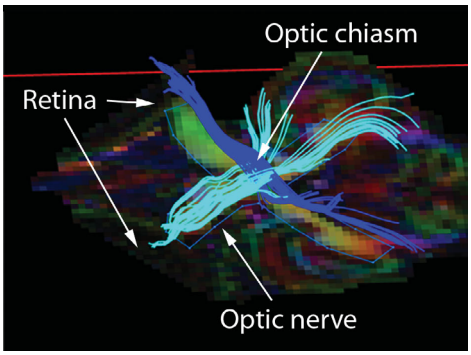

(d) CSD tractography

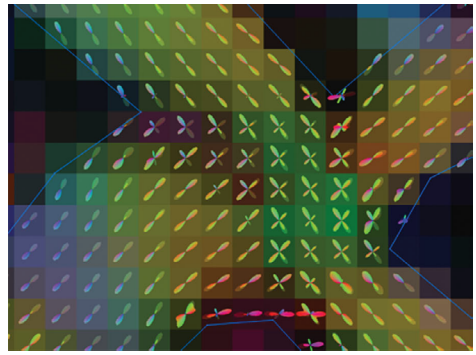

(e) CSD fODFs

Fig. 4.14: Tractography of the optic chiasm in the starling brain. As opposed to the human optic chiasm, the avian chiasm consists of 100% crossing fibers (a). DTI fiber tracking is unable to resolve the crossing fibers (b). The shape of the tensor ellipsoids is oblate at the optic chiasm, resulting in low FA values and incorrect fiber tracking results (c). The fODFs obtained with CSD describe the crossing fibers quite well (e), resulting in improved fiber tracking in the optic chiasm (e).

Resonance in Medicine, 48(2):331–340, 2002.

A. W. Anderson. Measurement of fiber orientation distributions using high angular resolution diffusion imaging. *Magnetic Resonance in Medicine*, 54(5):1194–1206, 2005.

P. J. Basser, J. Mattiello, and D. LeBihan. Estimation of the effective self-diffusion tensor from the NMR spin echo. *Journal of Magnetic Resonance Series B*, 103: 247–247, 1994a.

P. J. Basser, J. Mattiello, and D. LeBihan. MR diffusion tensor spectroscopy and imaging. *Biophysical Journal*, 66(1):259–267, 1994b.

P. J. Basser, S. Pajevic, C. Pierpaoli, J. Duda, and A. Aldroubi. In vivo fiber tractography using DT-MRI data. *Magnetic Resonance in Medicine*, 44(4): 625–632, 2000.

T. E. J. Behrens, H. Johansen-Berg, S. Jbabdi, M. F. S. Rushworth, and M. W. Woolrich. Probabilistic diffusion tractography with multiple fibre orientations: what can we gain? *NeuroImage*, 34(1):144–155, 2007.

W. M. Cowan, L. Adamson, and T. P. S. Powell. An experimental study of the avian visual system. *Journal of Anatomy*, 95(4):545–563, 1961.

G. De Groof and A. Van der Linden. Love songs, bird brains and diffusion tensor imaging. *NMR in Biomedicine*, 23(7):873–883, 2010.

F. Dell'Acqua, G. Rizzo, P. Scifo, R. A. Clarke, G. Scotti, and F. Fazio. A model-based deconvolution approach to solve fiber crossing in diffusion-weighted MR imaging. *IEEE Transactions on Biomedical Engineering*, 54(3):462–472, 2007.

M. Descoteaux, E. Angelino, S. Fitzgibbons, and R. Deriche. Regularized, fast, and robust analytical Q-ball imaging. *Magnetic Resonance in Medicine*, 58(3): 497–510, 2007.

O. Dietrich, J. G. Raya, S. B. Reeder, M. F. Reiser, and S. O. Schoenberg. Measurement of signal-to-noise ratios in MR images: influence of multichannel coils, parallel imaging, and reconstruction filters. *Journal of Magnetic Resonance Imaging*, 26(2):375–385, 2007.

E. Fieremans, Y. De Deene, S. Delputte, M. S. Özdemir, E. Achten, and I. Lemahieu. The design of anisotropic diffusion phantoms for the validation of diffusion weighted magnetic resonance imaging. *Physics in Medicine and Biology*, 53:5405, 2008a.

E. Fieremans, Y. De Deene, S. Delputte, M. S. Özdemir, Y. D'Asseler, J. Vlassenbroeck, K. Deblaere, E. Achten, and I. Lemahieu. Simulation and experimental verification of the diffusion in an anisotropic fiber phantom. *Journal of Magnetic Resonance*, 190(2):189–199, 2008b.

P. Fillard, M. Descoteaux, A. Goh, S. Gouttard, **B. Jeurissen**, J. G. Malcolm, A. Ramirez-Manzanares, M. Reisert, K. Sakaie, F. Tensaouti, T. Yo, J. F. Mangin, and C. Poupon. Quantitative evaluation of 10 tractography algorithms on a realistic diffusion MR phantom. *NeuroImage*, 56(1):220–234, 2011.

L. R. Frank. Anisotropy in high angular resolution diffusion-weighted MRI. *Magnetic Resonance in Medicine*, 45(6):935–939, 2001.

L. R. Frank. Characterization of anisotropy in high angular resolution diffusion-weighted MRI. *Magnetic Resonance in Medicine*, 47:1083–1099, 2002.

M. Froeling, G. J. Strijkers, **B. Jeurissen**, M. P. van der Paardt, J. Stoker, Nicolay K., A. J. Nederveen, and A. Leemans. Fiber architecture of the female pelvic floor: an exploratory investigation using different diffusion MRI tractography algorithms. In *Proceedings of the International Society for Magnetic Resonance in Medicine*, volume 19, page 3260, Montréal, Canada, 2011.

S. Gouttard, A. Sharma, and G. Gerig. Fiber Challenge - SCI Utah Solution. In *Proceedings of the MICCAI'09 Workshop on Diffusion Modelling and the Fibre Cup*, pages 201–206, London, United Kingdom, 2009.

T. Hosey, G. Williams, and R. Ansorge. Inference of multiple fiber orientations in high angular resolution diffusion imaging. *Magnetic Resonance in Medicine*, 54 (6):1480–1489, 2005.

K. M. Jansons and D. C. Alexander. Persistent angular structure: new insights from diffusion magnetic resonance imaging data. *Inverse problems*, 19(5):1031–1046, 2003.

B. Jeurissen, A. Leemans, E. Fieremans, and J. Sijbers. Fiber tractography on a crossing fiber phantom using constrained spherical deconvolution MRI. In *Proceedings of Liège Image Days*, Liège, Belgium, 2008.

B. Jeurissen, A. Leemans, J. D. Tournier, and J. Sijbers. Fiber tracking on the 'Fiber Cup phantom' using constrained spherical deconvolution. In *Proceedings of the MICCAI'09 Workshop on Diffusion Modelling and the Fiber Cup*, pages 232–235, London, United Kingdom, 2009.

B. Jeurissen, A. Leemans, D. K. Jones, J. D. Tournier, and J. Sijbers. Probabilistic fiber tracking using the residual bootstrap with constrained spherical deconvolution. *Human Brain Mapping*, 32:461–479, 2011.

D. K. Jones, M. A. Horsfield, and A. Simmons. Optimal strategies for measuring diffusion in anisotropic systems by magnetic resonance imaging. *Magnetic Resonance in Medicine*, 42(3):515–525, 1999.

A. Leemans and D. K. Jones. The B-matrix must be rotated when correcting for subject motion in DTI data. *Magnetic Resonance in Medicine*, 61(6):1336–1349, 2009.

A. Leemans, **B. Jeurissen**, J. Sijbers, and D. K. Jones. ExploreDTI: a graphical toolbox for processing, analyzing, and visualizing diffusion MR data. In *Proceedings of the International Society for Magnetic Resonance in Medicine*, volume 17, page 3537, Honolulu, USA, 2009.

J. G. Malcolm, M. E. Shenton, and Y. Rathi. Filtered Tractography: validation on a physical phantom. In *Proceedings of the MICCAI'09 Workshop on Diffusion Modelling and the Fiber Cup*, pages 220–223, London, United Kingdom, 2009.

J. G. Malcolm, M. E. Shenton, and Y. Rathi. Filtered Multitensor Tractography. *IEEE Transactions on Medical Imaging*, 29(9):1664–1675, 2010.

E. Özarslan, T. M. Shepherd, B. C. Vemuri, S. J. Blackband, and T. H. Mareci. Resolution of complex tissue microarchitecture using the diffusionorientation transform (DOT). *NeuroImage*, 31(3):1086–1103, 2006.

C. Pierpaoli, A. Barnett, S. Pajevic, R. Chen, L. R. Penix, A. Virta, and P. J. Basser. Water diffusion changes in Wallerian degeneration and their dependence on white matter architecture. *NeuroImage*, 13(6):1174–1185, 2001.

Y. D. Reijmer, A. Leemans, S. M. Heringa, I. Wielaard, **B. Jeurissen**, H. L. Koek, and G. J. Biessels. Constrained spherical deconvolution based tractography and cognition in Alzheimer's disease. In *Proceedings of the Organization for Human Brain Mapping*, Québec, Canada, 2011a.

Y. D. Reijmer, A. Leemans, S. M. Heringa, I. Wielaard, **B. Jeurissen**, H. L. Koek, and G. J. Biessels. Constrained spherical deconvolution based tractography and cognition in Alzheimer's disease. In *Proceedings of the International Conference on Alzheimer's Disease*, Paris, France, 2011b.

M. Reisert, I. Mader, and V. Kiselev. Tracking a physical phantom by global fibre reconstruction. In *Proceedings of the MICCAI'09 Workshop on Diffusion Modelling and the Fiber Cup*, pages 224–227, London, United Kingdom, 2009.

M. Reisert, I. Mader, C. Anastasopoulos, M. Weigel, S. Schnell, and V. Kiselev. Global fiber reconstruction becomes practical. *NeuroImage*, 54(2):955–962, 2011.

J. Sijbers, A. J. den Dekker, A. Van der Linden, T. M. Verhoye, and D. Van Dyck. Adaptive anisotropic noise filtering for magnitude MR data. *Magnetic Resonance Imaging*, 17:1533–1539, 1999.

J. D. Tournier, F. Calamante, D. G. Gadian, and A. Connelly. Direct estimation of the fiber orientation density function from diffusion-weighted MRI data using spherical deconvolution. *NeuroImage*, 23(3):1176–1185, 2004.

J. D. Tournier, F. Calamante, and A. Connelly. Robust determination of the fibre orientation distribution in diffusion MRI: non-negativity constrained super-resolved spherical deconvolution. *NeuroImage*, 35(4):1459–1472, 2007.

J. D. Tournier, C. H. Yeh, F. Calamante, K. H. Cho, A. Connelly, and C. P. Lin. Resolving crossing fibres using constrained spherical deconvolution: validation using diffusion-weighted imaging phantom data. *NeuroImage*, 42(2):617–625, 2008.

D. S. Tuch. Q-ball imaging. *Magnetic Resonance in Medicine*, 52(6):1358–1372, 2004.

D. S. Tuch, T. G. Reese, M. R. Wiegell, N. Makris, J. W. Belliveau, and V. J. Wedeen. High angular resolution diffusion imaging reveals intravoxel white matter fiber heterogeneity. *Magnetic Resonance in Medicine*, 48(4):577–582, 2002.

5

Bootstrap methods for estimating CSD fiber orientation uncertainty

Contents

The work in this chapter has been published as:

- **B. Jeurissen**, A. Leemans, J. D. Tournier, and J. Sijbers. Bootstrap methods for estimating uncertainty in Constrained Spherical Deconvolution fiber orientations. In *Proceedings of the International Society for Magnetic Resonance in Medicine*, volume 16, page 3324, Toronto, Canada, 2008a
- **B. Jeurissen**, A. Leemans, J. D. Tournier, and J. Sijbers. Can residual bootstrap reliably estimate uncertainty in fiber orientation obtained by spherical deconvolution from diffusion-weighted MRI? In *Proceedings of the Organization for Human Brain Mapping*, volume 14, Melbourne, Australia, 2008b
- **B. Jeurissen**, A. Leemans, J. D. Tournier, and J. Sijbers. Estimation of uncertainty in constrained spherical deconvolution fiber orientations. In *Proceedings of the IEEE International Symposium on Biomedical Imaging: From nano to macro*, pages 907–910, Paris, France, 2008c

5.1 Introduction

Diffusion MRI is currently the only non-invasive imaging technique that allows to estimate the WM fiber orientations in the *in vivo* brain [Tournier et al., 2011], opening up the possibility of investigating brain connectivity *in vivo* using so called fiber tracking algorithms [Mori and Van Zijl, 2002]. However, as diffusion MRI is based on the measurement of 'signal loss', it is inherently a noisy technique [Stejskal and Tanner, 1965]. As a consequence, fiber orientations – and other parameters of interest – estimated from diffusion MRI are subject to uncertainty [Jones, 2003, Pajevic and Basser, 2003]. This uncertainty is especially important in the context of fiber tractography as previous studies using DTI have shown that measurement uncertainty can propagate errors in streamlines [Lazar and Alexander, 2003].

Recent methods based on high angular resolution diffusion imaging (HARDI) acquisitions, acquire a large number of DW images with high b-values in order to resolve complex intra-voxel fiber configurations [Tuch et al., 2002]. However, as the signal falls off monotonically with the strength of diffusion weighting, SNR in HARDI is typically much lower than in more conventional diffusion MRI. Recently, a new HARDI technique was proposed, called constrained spherical deconvolution (CSD), which estimates the fiber orientation distribution function (fODF) directly from the DW signal by means of spherical deconvolution [Tournier et al., 2007]. While CSD offers a more accurate estimate of fiber orientations in the presence of partial volume effects, it is nevertheless important to also consider the precision of these estimates.

Bootstrapping is a statistical method that allows to estimate the precision of an estimate by means of resampling the data [Efron, 1979]. As opposed to parametric methods which require explicit assumptions about the sources of uncertainty, the bootstrap is a non-parametric method. This property makes the bootstrap a very powerful device when such assumptions are in doubt or the full modeling of all sources of uncertainty would lead to overly complicated models. E.g. in diffusion MRI, parametric models will typically model the noise characteristics of the MR data. However, many other sources of uncertainty exist, such as pulsation, head motion, etc. which are hard to model explicitly, making bootstrapping techniques a valuable tool for uncertainty estimation in diffusion MRI. An important drawback of the classic repetition bootstrap is that it requires repeated data samples, which limits the applicability in a clinical setting, due to increased acquisition times. However, this limitation can be overcome by the use of model-based bootstrapping. Here only a single data set is acquired and the resampling is performed on the residuals of a model fit [Davison and Hinkley, 1997].

It has already been shown that bootstrap methods are a powerful tool for characterizing uncertainty in estimates of DTI fiber orientations [Pajevic and Basser, 2003, Jones, 2003, Chung et al., 2006] and it has been successfully used to perform probabilistic DTI tractography [Jones and Pierpaoli, 2005]. However, these techniques have not yet been assessed for CSD. In this work, Monte Carlo simulations will be used to investigate the performance of several bootstrap methods in terms of accuracy and precision, when estimating confidence intervals for CSD fiber orientations.

5.2 Theory

Conceptually the easiest way to assess the uncertainty of CSD fiber orientations would be to acquire repeated DW data sets from the same subject, extract the fiber orientations and then treat these repeated fiber orientations as samples from the uncertainty orientation distribution function (uODF) [Jones, 2003]. Such an approach does not require us to do any modeling of the uncertainty in the data, and as such it is completely non-parametric. This would allow us to calculate 95% confidence intervals (CI) around the extracted fiber orientations, which give an indication of the precision of the fiber orientation estimates (Fig. 5.1). However, in order to build a good representation of the uODF, this procedure would require a large number of independent data sets, making the method not feasible in practice.

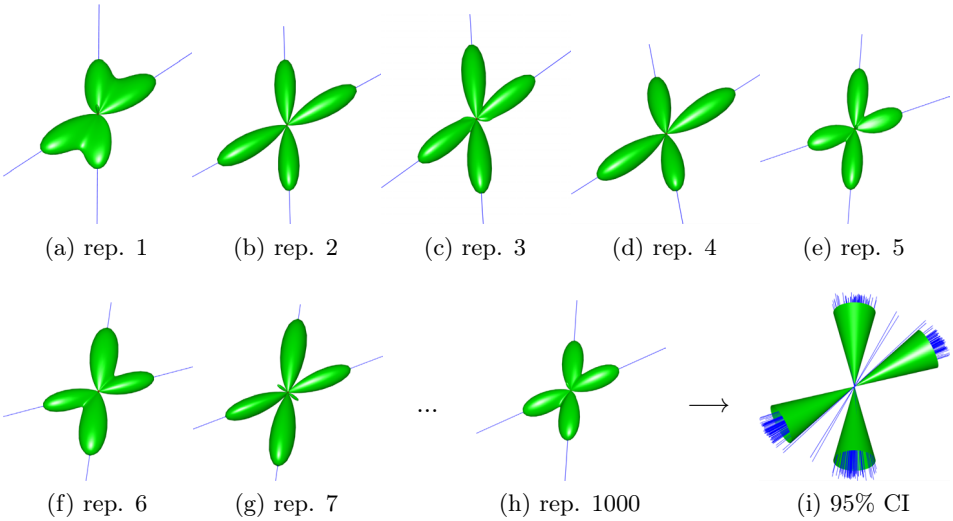

Fig. 5.1: Estimating fODF uncertainty using a large number of repeated DWI measurements. For 1000 repeated measurements, the fODF is estimated (a)-(h). For each fODF the main fiber orientations are extracted (blue lines). The precision of these fiber orientations can be measured by calculating a 95% CI, which can be visualized as a cone of uncertainty (i).

5.2.1 Repetition bootstrap

5.2.1.1 Classic repetition bootstrap

Fortunately, it is possible to generate a large number of samples from just a few repeated acquisitions sets by means of bootstrapping. The repetition bootstrap is a non-parametric statistical procedure that enables one to estimate the uncertainty of a given statistic, by randomly selecting individual measurements, with replacement, from a set of repeated measurements, thus generating many bootstrap realizations of the data. Each realization provides a random estimate of a given statistic.

By generating a sufficient number of realizations, one obtains a measure of the uncertainty of a given statistic from the data itself without requiring a priori assumptions about the sources of uncertainty [Efron, 1979].

In the case of diffusion MRI, this method requires the acquisition of N repeats of a complete DW data set, so that N samples are available for each gradient orientation [Jones, 2003, Pajevic and Basser, 2003, Chung et al., 2006]. A resampled DW data set can then be produced by randomly selecting N samples with replacement for each orientation. Consider N repeated data sets of U DW measurements (Fig. 5.2). The total data available to us is a matrix $\boldsymbol{S}$, of dimensions $U \times N$, where each column in S is one complete acquisition. To generate a single bootstrap realization, we create a new matrix $\boldsymbol{S}_b$, of dimension $U \times N$, where each row contains N values randomly sampled with replacement from the corresponding row in $\boldsymbol{S}$.

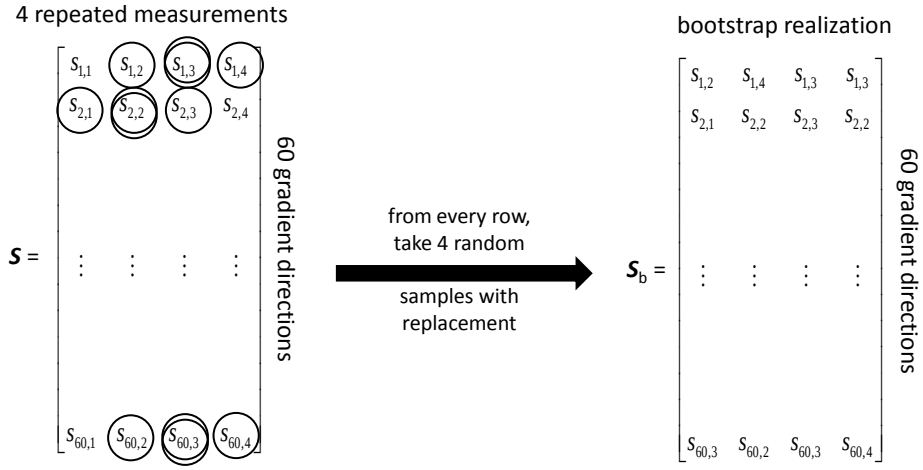

Fig. 5.2: Classic repetition bootstrap sampling. Example with 4 repeated measurements acquired along 60 gradient orientations. For each row (gradient orientation), we take 4 random samples with replacement to form a new bootstrap realization of the data.

In this way, a full $U \times N$ DW data set is produced from a random combination of the images in the N repeats of the original data set. This bootstrap realization can then be processed using the method under investigation. In our case the bootstrap realization will be processed using CSD. By repeating this procedure N_b times, we obtain N_b estimates of the fODF and the associated peak orientations, which can be used to estimate the reproducibility of the reconstructed fiber orientations (Fig. 5.3).

5.2.1.2 Bootknife

When the number of repeats N is small, bootstrap-estimated uncertainties are noticeably downwardly biased, in the same way that the uncorrected variance is not an unbiased estimator of the true population variance. To remedy this bias, the bootknife method was proposed [Hesterberg, 2004]. Basically, the bootknife is

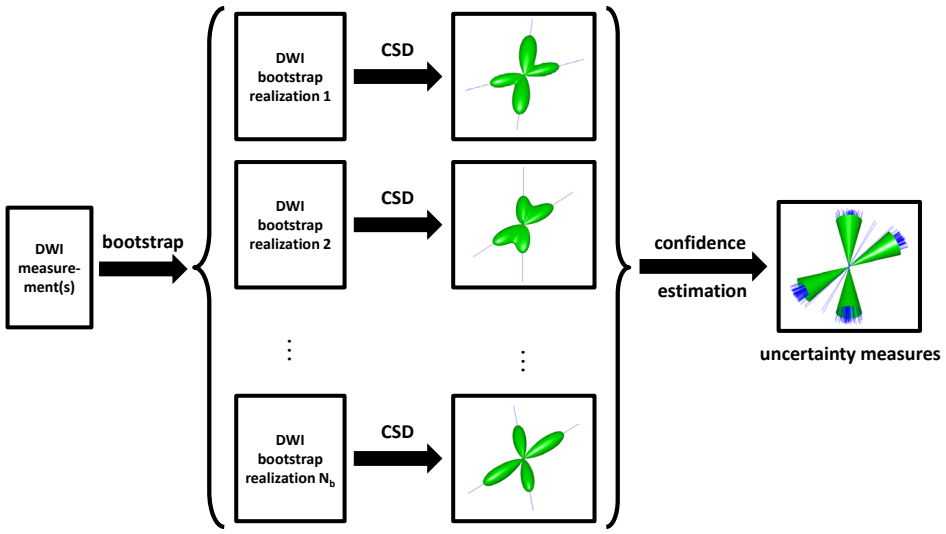

Fig. 5.3: Estimating fODF uncertainty using the bootstrap. N_b bootstrap realizations are generated from the same data. Each bootstrap realization can then be processed using CSD, resulting in N_b bootstrap realizations of the fODF. From this large collection of fODF estimates, one can estimate the precision of the fiber orientation estimates, e.g. as a 95% confidence interval.

a combination of the jackknife and the bootstrap. Prior to selecting one of the N available samples for each orientation, we eliminate one measurement at random from each row in $\boldsymbol{S}$, giving us a matrix $\boldsymbol{S}_j$ of dimension $U \times (N-1)$ (jackknife). We then create a bootstrap matrix $\boldsymbol{S}_b$ of dimension $U \times N$, but because we are choosing N samples from a row of length $N-1$, we guarantee that at least one of the measurements will be repeated [Chung et al., 2006]. The way the bootknife is advantageous over the classic repetition bootstrap is analogous to the way the corrected sample variance:

$$s^2 = \frac{1}{n-1}\sum_{i=1}^{n}(y_i - \bar{y})^2 \qquad \text{with} \qquad \mathrm{E}[s^2] = \sigma^2 \tag{5.1}$$

is advantageous over the uncorrected sample variance:

$$s_n^2 = \frac{1}{n}\sum_{i=1}^{n}(y_i - \bar{y})^2 \qquad \text{with} \qquad \mathrm{E}[s_n^2] = \frac{n-1}{n}\sigma^2 \tag{5.2}$$

with n the number of samples, $\bar{y}$ the sample mean, σ^2 the true population variance and $\mathrm{E}[\cdot]$ the expected value operator. For small sample sizes, the uncorrected estimator produces highly biased variance estimates, whereas the corrected estimator is unbiased even for small n.

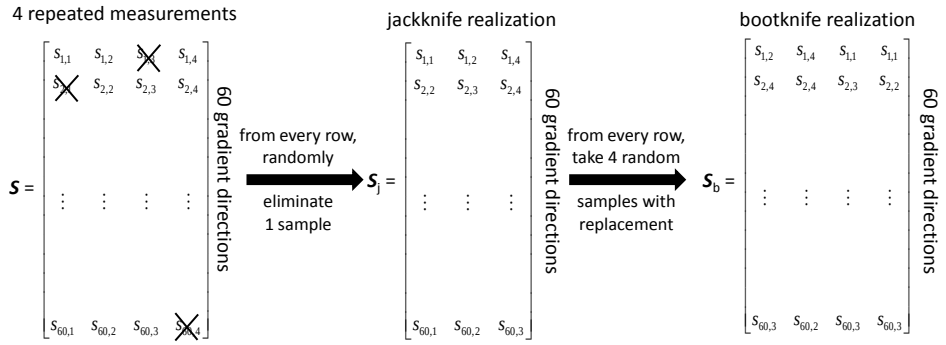

Fig. 5.4: Bootknife sampling. Example with 4 repeated measurements acquired along 60 gradient orientations. For each row (gradient orientation), we first randomly eliminate 1 sample to resulting in a jackknife realization consisting of 3 repeated measurements. From the jackknife realization, we then take 4 random samples with replacement to form a new bootknife realization of the data.

5.2.2 Residual bootstrap

An important drawback of the repetition bootstrap approach, is that it requires multiple acquisitions for each diffusion gradient, imposing a large load on the data acquisition. For just a small number of diffusion gradients, acquiring repeated measurements might be feasible. However, for HARDI acquisitions, which acquire DW images along a large collection of gradient orientations acquiring multiple acquisitions would increase scanning time to such extent that it would be no longer feasible in clinical practice. An alternative is to use model-based resampling. Such methods first fit the data to a model, after which the residuals are resampled, rather than the raw data values. Since model-based resampling doesn't require repeated acquisitions, it is a powerful alternative to the repetition bootstrap to estimate the precision of parameters derived from HARDI data. In what follows, we will describe the model-based resampling technique called the residual bootstrap [Wu, 1986].

The entire procedure is summarized in Fig. 5.5. First, the DW signal S, which is acquired along a set of n_g gradient orientations $\{(\theta, \phi)\}$ needs to be fitted to a model. Remember from Chapter 2, the DW signal can be expressed as a linear combination of the modified spherical harmonics (SH) $Y_l^{'m}(\theta, \phi)$ of degree l and order m:

$$S(\theta, \phi) = \sum_{l=0}^{L} \sum_{m=-l}^{l} c_l^m Y_l^{'m}(\theta, \phi) \tag{5.3}$$

where $\{c_l^m\}$ denote the harmonic series coefficients, and L is the maximum harmonic degree [Frank, 2002]. Eq. (5.3) can be expressed as a linear system:

$$\boldsymbol{s} = \boldsymbol{B}\boldsymbol{c} + \boldsymbol{\epsilon} \tag{5.4}$$

where $\boldsymbol{B}$ is the $n_g \times n_c$ matrix constructed with the modified SH basis, $\boldsymbol{c}$ is the $n_c \times 1$ of modified SH coefficients, $\boldsymbol{s}$ is the $n_g \times 1$ DW signal vector and $\boldsymbol{\epsilon}$ is the noise

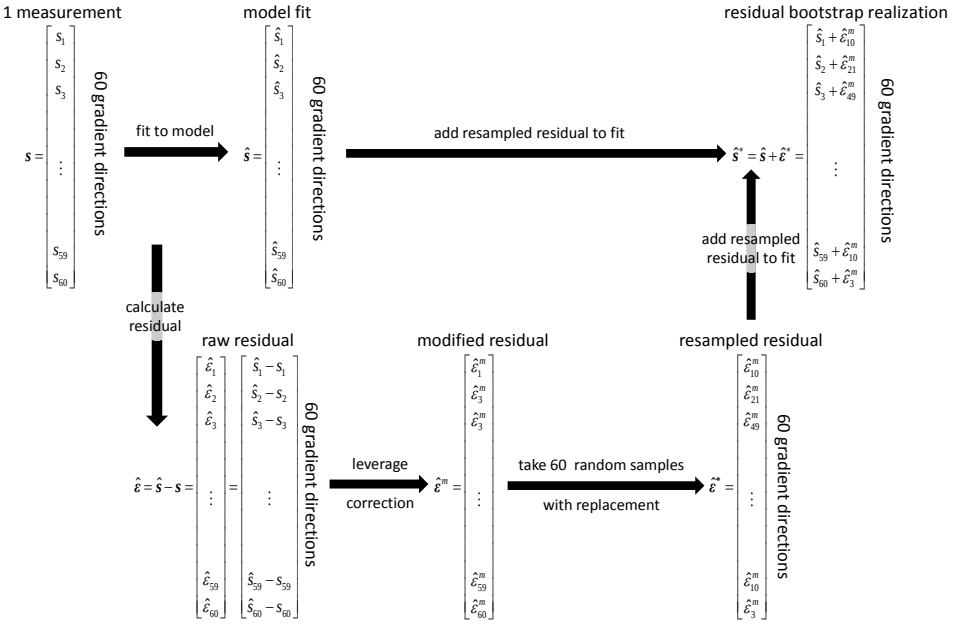

Fig. 5.5: Residual bootstrap sampling. Example with data acquired along 60 gradient orientations. First, the sample is fitted to a model and the corresponding residuals are calculated. The residuals are corrected such that they have the same variance as the true underlying errors. Then from the set of residuals we take 60 random samples with replacement, resulting in a resampled residual. The resampled residual is then added back to the model fit, resulting in a new residual bootstrap realization of the data.

vector. The coefficients $\boldsymbol{c}$ can then be estimated using least-squares minimization:

$$\hat{\boldsymbol{c}} = (\boldsymbol{B}^{\mathrm{T}}\boldsymbol{B})^{-1}\boldsymbol{B}^{\mathrm{T}}\boldsymbol{s} \tag{5.5}$$

Given Eq. (5.4) and Eq. (5.5), the signal $\hat{\boldsymbol{s}}$ predicted by the least squares SH fit to the measured signal $\boldsymbol{s}$ is given as:

$$\hat{\boldsymbol{s}} = \boldsymbol{B}\hat{\boldsymbol{c}} = \boldsymbol{B}(\boldsymbol{B}^{\mathrm{T}}\boldsymbol{B})^{-1}\boldsymbol{B}^{\mathrm{T}}\boldsymbol{s} = \boldsymbol{H}\boldsymbol{s} \tag{5.6}$$

with

$$\boldsymbol{H} = \boldsymbol{B}(\boldsymbol{B}^{\mathrm{T}}\boldsymbol{B})^{-1}\boldsymbol{B}^{\mathrm{T}} \tag{5.7}$$

the so-called hat-matrix.

Remember also that the higher order basis functions in the modified SH series correspond to the higher angular frequency modes of the unit sphere, and thus relatively smooth functions, such as the DW signal, can be represented concisely using a SH series truncated at a relatively low order. In fact, a recent study has shown that the highest order for which significant terms can be found in *in vivo* HARDI signal profiles at $b = 3000$ s/mm^2 is 8 [Tournier et al., 2009].

Once the signal $\hat{\boldsymbol{s}}$ has been estimated by the least squares SH fit to the measured signal $\boldsymbol{s}$, the raw residual vector can be calculated as:

$$\hat{\boldsymbol{\epsilon}} = \boldsymbol{s} - \hat{\boldsymbol{s}} \tag{5.8}$$

From regression analysis it is known that:

$$\mathrm{Var}[\hat{\boldsymbol{\epsilon}}_i] = \sigma^2(1 - h_{ii}) \tag{5.9}$$

with σ^2 the variance of true underlying error and h_{ii} the i-th diagonal entry in the hat matrix $\boldsymbol{H}$ from Eq. (5.7) [Weisberg, 2005]. To ensure that the residuals have the same variance as the underlying errors $\boldsymbol{\epsilon}$, the raw residual vector $\hat{\boldsymbol{\epsilon}}$ is corrected to yield the modified residual vector $\hat{\boldsymbol{\epsilon}}^m$ [Davison and Hinkley, 1997]:

$$\hat{\boldsymbol{\epsilon}}_i^m = \frac{\hat{\boldsymbol{\epsilon}}_i}{\sqrt{1 - h_{ii}}} \tag{5.10}$$

with

$$\mathrm{Var}[\hat{\boldsymbol{\epsilon}}_i^m] = \sigma^2 \tag{5.11}$$

Values from $\hat{\boldsymbol{\epsilon}}^m$ are then randomly chosen with replacement to form a new bootstrapped residual $\hat{\boldsymbol{\epsilon}}^*$. Finally, the bootstrapped residual is added back to the signal fit, to create a synthetic bootstrap realization $\hat{\boldsymbol{s}}^*$ of the DW signal:

$$\hat{\boldsymbol{s}}^* = \hat{\boldsymbol{s}} + \hat{\boldsymbol{\epsilon}}^* \tag{5.12}$$

By repeating this procedure N_b times, we obtain N_b realizations of $\boldsymbol{s}$. Each of these realizations can then be processed individually (e.g. by CSD), to derive the statistic of interest (e. g. the fiber orientation).

5.3 Experiments

Simulation experiments were performed to compare the bootstrap estimates of CSD fiber orientation uncertainty to the gold standard uncertainty.

5.3.1 Gold standard

Two diffusion tensor profiles at angles ranging from 60° to 90° were combined to simulate the noiseless DW signal for two fiber populations:

$$S(\boldsymbol{q}) = \frac{S(\mathbf{0})e^{-b\hat{\boldsymbol{g}}^{\mathrm{T}}\boldsymbol{D}_1\hat{\boldsymbol{g}}} + S(\mathbf{0})e^{-b\hat{\boldsymbol{g}}^{\mathrm{T}}\boldsymbol{D}_2\hat{\boldsymbol{g}}}}{2} \tag{5.13}$$

where $S(\mathbf{0})$, the non-DW signal, was set to 1 without loss of generality. The diffusion weighting b was set to $3000\,\mathrm{s/mm^2}$. Sixty diffusion-encoding gradient directions $\hat{\boldsymbol{g}}$ were used, distributed evenly on the half sphere [Jones et al., 1999]. This setup corresponds to a realistic high angular resolution DW acquisition. Both diffusion tensors $\boldsymbol{D}_i$ ($i = 1, 2$) had a FA of 0.8. The mean ADC was set to $600 \times 10^{-6}\,\mathrm{mm^2/s}$. Rician noise was added to give a SNR (for $b = 0\,\mathrm{s/mm^2}$) of 15 to 40, which is the clinical range. This experiment was repeated 10,000 times. The fODF was calculated for every DW signal, using CSD with harmonic degree $l_{\max} = 8$. From these fODFs, the unique peak orientations were extracted using the optimization method explained in the previous chapter. The average peak directions were calculated as the first eigenvector of the mean dyadic tensor of all 10,000 peak directions [Pajevic and Basser, 2003]. Finally, the 95% CI of the angular deviation between the individual and average peak orientations was calculated, representing the 'cone of uncertainty' [Jones, 2003] around the average peak orientation. Fig. 5.6 shows a visualization of such cones for different SNR values. Note that the cones are wider at low SNR, indicating a higher uncertainty of the fiber orientations.

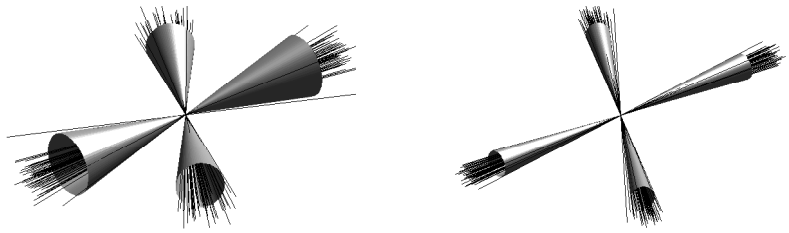

(a) SNR=15 (b) SNR=30

Fig. 5.6: Example of a 95% CI of two fiber orientations with inter-fiber angle of 60° at different SNR levels. For clarity, the number of repeats was only 60. The cones represent the 95% CI, the black lines the fiber orientation estimates from the individual repeats. This means 95% of the black lines lie within the cone.

5.3.2 Repetition bootstrap

Nine bootstrap experiments were considered, with the number of repeated acquisitions, N, ranging from 2 to 10. For each bootstrap design, we derived N_b bootstrap/bootknife realizations of the fODF. Fiber orientations were extracted as described above. To determine the effect of the number of bootstrap realizations on the estimated fiber orientations, N_b was incremented from 100 to 1000 in steps

of 100. The entire procedure was repeated 100 times to determine the precision of a particular bootstrap experiment. Mean and standard deviation of the 95% CI (across the 100 repeats) were computed.

5.3.3 Residual bootstrap

The 95% CI was calculated as before, but now over $N_b = 1000$ residual bootstrap realizations. The CI calculation was repeated 100 times with different noise instances to obtain mean and standard deviation of the CI.

5.4 Results

5.4.1 Repetition bootstrap

Fig. 5.7 shows the bias of the 95% CI relative to the gold standard 95% CI as a function of the number of repeated measurements N. The number of bootstrap realizations N_b was fixed to 1000 and SNR was set to 25. The dotted lines represent the bias of the bootstrap estimates. The dashed lines show the bias of the bootknife estimates. Only inter-fiber angles of 60° (Fig. 5.7a) and 90° (Fig. 5.7b) are shown. Note that other inter-fiber angles and SNR levels yielded similar results, but were left out for clarity. As expected, the CIs are significantly underestimated by the bootstrap when the number of repeated acquisitions N is small. Accuracy can be improved by increasing N, but there still remains a negative bias even at $N = 10$ repeated measurements. The bootknife estimates on the other hand tend to be very close to the gold standard over the entire range of N and at different inter-fiber angles.

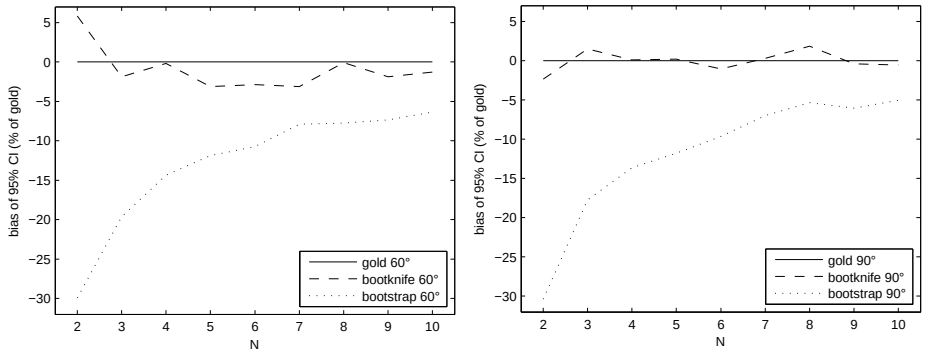

(a) Two fiber bundles at 60° (b) Two fiber bundles at 90°

Fig. 5.7: Bias of mean repetition bootstrap 95% CI as a function of N with SNR = 25 in a single repetition.

Fig. 5.8 shows the relative standard deviation over 100 bootstrap experiments of the 95% CIs as a function of the number of bootstrap realizations N_b. The number of repeated experiments N was fixed to 6 and SNR was set to 25. The dotted lines

represent the bootstrap estimates. The dashed lines show the bootknife estimates. Smaller standard deviations are better. Only inter-fiber angles of 60° (indicated by ×) and 90° are shown. Note that other inter-fiber angles and SNR levels yielded similar results, but were left out for clarity. The plot shows improvement in precision of the CIs by increasing the number of bootstrap realizations N_b, but increasing the number of bootstrap iterations only seems sensible up to approximately 800.

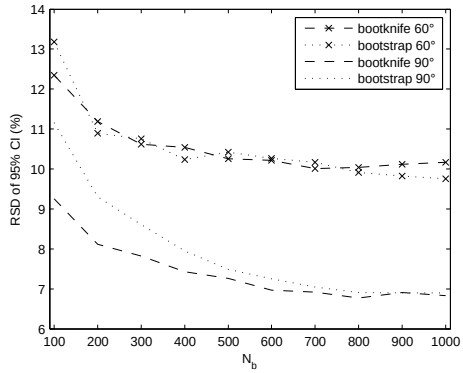

Fig. 5.8: Relative standard deviation (RSD) of repetition bootstrap 95% CI as a function of N_b with SNR = 25 in a single repetition.

5.4.2 Residual bootstrap

Fig. 5.9 shows the 95% CI as a function of SNR for different inter-fiber angles. The plots show that the residual bootstrap CIs agree with the gold standard CIs over the entire range of SNRs and at all inter-fiber angles.

5.5 Discussion and conclusion

In this chapter, we investigated the performance of the bootstrap method in terms of accuracy and precision when estimating confidence intervals of CSD fiber orientations and compared it to an alternative bootstrap method, called bootknife. The precision of the bootstrap and bootknife method depends on the number of bootstrap realizations and our results show that the number of bootstrap iterations should be 800, which is not a problem since it doesn't impact acquisition time. On the other hand, the accuracy of the bootstrap and bootknife method depends on the number of repeated acquisitions. Our results show that the 'classic' repetition bootstrap significantly underestimates the uncertainty when few repeated acquisitions are available. This is in accordance with earlier studies that were performed using DTI [O'Gorman and Jones, 2006, Chung et al., 2006]. However, high angular resolution diffusion imaging data, like CSD data, typically have very few repeated acquisitions available. While it may be tempting to use this bootstrap procedure with just a few repeats, our results show that this yields poor accuracy. Using the bootstrap for probabilistic tractography can thus have

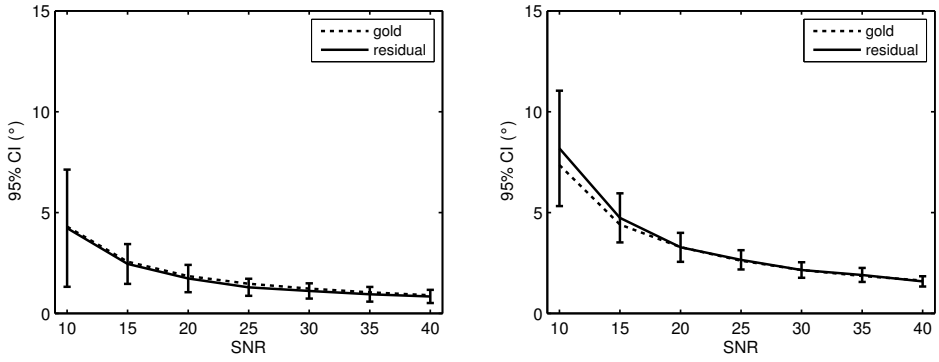

(a) One fiber bundle

(b) Two fiber bundles at 90°

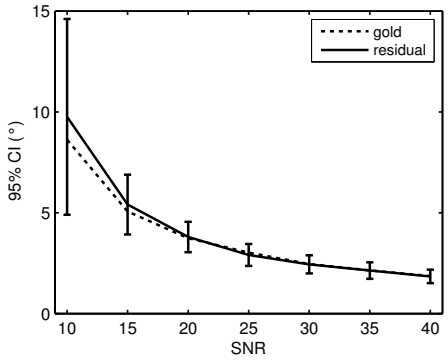

(c) Two fiber bundles at 75°

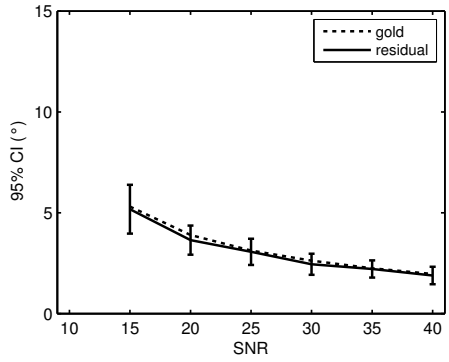

(d) Two fiber bundles at 60°

Fig. 5.9: Average 95% CI derived with residual bootstrap for different inter-fiber angles.

considerable consequences, since the error introduced by this bias will produce tracts that do not represent the true variability inherent in the data. We also showed that the downward bias of the 'classic' repetition bootstrap for CSD can be removed using the bootknife approach. This allows good CI estimates and probabilistic tractography, using only a few repeated acquisitions, without making assumptions about the sources of uncertainty in the data. However, in a clinical setting, even a few repeated measurements can already render acquisition time unacceptably long.

For this reason we also investigated the performance of the residual bootstrap method. The huge advantage over the classic repetition bootstrap is that the residual bootstrap does not require the collection of extra data, bringing acquisition time into the clinical realm. Our simulation results indicate that the combination of the residual bootstrap with the modified SH model allows accurate estimates of the uncertainty in the fiber orientations reconstructed with CSD. This enables probabilistic tractography of CSD fiber orientations from data measured in a clinically feasible time frame. Note that, while we focused on estimating the uncertainty of the main fiber orientations of the fODF, the same technique can be applied to estimate the uncertainty of full fODF. In addition, since our procedure uses the very general SH model, directly fitted to the DW signal itself, the same procedure can be applied to estimate the uncertainty in other HARDI methods than CSD [Tournier et al., 2009].

A potential problem of the residual bootstrap is that if the model overfits the data, so the residuals tend to zero, it will dramatically underestimate the uncertainty of the fODF. In the current study we have used the SH model with $l_{\max} = 8$, as this was shown to be the highest SH order for which significant terms can be found in *in vivo* HARDI signal profiles at $b = 3000$ s/mm^2 [Tournier et al., 2009]. Our simulation results also indicated that using $l_{\max} = 8$, produced accurate 95% CIs for the clinical SNR range. In theory, the accuracy of the procedure could be improved by performing model order selection to determine the appropriate SH order in each voxel separately [Alexander et al., 2002], prior to the residual bootstrap procedure.

Bibliography

D. C. Alexander, G. J. Barker, and S. R. Arridge. Detection and modeling of non-Gaussian apparent diffusion coefficient profiles in human brain data. *Magnetic Resonance in Medicine*, 48(2):331–340, 2002.

S. W. Chung, Y. Lu, and R. G. Henry. Comparison of bootstrap approaches for estimation of uncertaintiesof DTI parameters. *NeuroImage*, 33(2):531–541, 2006.

A. C. Davison and D. V. Hinkley. *Bootstrap methods and their application*. Cambridge Univ Pr, 1997.

B. Efron. Bootstrap methods: another look at the jackknife. *The Annals of Statistics*, 7(1):1–26, 1979.

L. R. Frank. Characterization of anisotropy in high angular resolution diffusion-weighted MRI. *Magnetic Resonance in Medicine*, 47:1083–1099, 2002.

T. C. Hesterberg. Unbiasing the bootstrap-bootknife sampling vs. smoothing. In *Proceedings of the American Statistical Association*, pages 2924–2930, 2004.

B. Jeurissen, A. Leemans, J. D. Tournier, and J. Sijbers. Bootstrap methods for estimating uncertainty in Constrained Spherical Deconvolution fiber orientations. In *Proceedings of the International Society for Magnetic Resonance in Medicine*, volume 16, page 3324, Toronto, Canada, 2008a.

B. Jeurissen, A. Leemans, J. D. Tournier, and J. Sijbers. Can residual bootstrap reliably estimate uncertainty in fiber orientation obtained by spherical deconvolution from diffusion-weighted MRI? In *Proceedings of the Organization for Human Brain Mapping*, volume 14, Melbourne, Australia, 2008b.

B. Jeurissen, A. Leemans, J. D. Tournier, and J. Sijbers. Estimation of uncertainty in constrained spherical deconvolution fiber orientations. In *Proceedings of the IEEE International Symposium on Biomedical Imaging: From nano to macro*, pages 907–910, Paris, France, 2008c.

D. K. Jones. Determining and visualizing uncertainty in estimates of fiber orientation from diffusion tensor MRI. *Magnetic Resonance in Medicine*, 49(1):7–12, 2003.

D. K. Jones and C. Pierpaoli. Confidence mapping in diffusion tensor magnetic resonance imaging tractography using a bootstrap approach. *Magnetic Resonance in Medicine*, 53(5):1143–1149, 2005.

D. K. Jones, M. A. Horsfield, and A. Simmons. Optimal strategies for measuring diffusion in anisotropic systems by magnetic resonance imaging. *Magnetic Resonance in Medicine*, 42(3):515–525, 1999.

M. Lazar and A. L. Alexander. An error analysis of white matter tractography methods: synthetic diffusion tensor field simulations. *NeuroImage*, 20(2):1140–1153, 2003.

S. Mori and P. C. M. Van Zijl. Fiber tracking: principles and strategies-a technical review. *NMR in Biomedicine*, 15(7-8):468–480, 2002.

R. L. O'Gorman and D. K. Jones. Just how much data need to be collected for reliable bootstrap DT-MRI? *Magnetic Resonance in Medicine*, 56(4):884–890, 2006.

S. Pajevic and P. J. Basser. Parametric and non-parametric statistical analysis of DT-MRI data. *Journal of Magnetic Resonance*, 161(1):1–14, 2003.

E. O. Stejskal and J. E. Tanner. Spin diffusion measurements: spin echoes in the presence of a time-dependent field gradient. *The Journal of Chemical Physics*, 42(1):288, 1965.

J. D. Tournier, F. Calamante, and A. Connelly. Robust determination of the fibre orientation distribution in diffusion MRI: non-negativity constrained super-resolved spherical deconvolution. *NeuroImage*, 35(4):1459–1472, 2007.

J. D. Tournier, F. Calamante, and A. Connelly. How many diffusion gradient directions are required for HARDI? In *Proceedings of the International Society for Magnetic Resonance In Medicine*, volume 17, page 358, Honolulu, USA, 2009.

J. D. Tournier, S. Mori, and A. Leemans. Diffusion tensor imaging and beyond. *Magnetic Resonance in Medicine*, 65(6):1532–1556, 2011.

D. S. Tuch, T. G. Reese, M. R. Wiegell, N. Makris, J. W. Belliveau, and V. J. Wedeen. High angular resolution diffusion imaging reveals intravoxel white matter fiber heterogeneity. *Magnetic Resonance in Medicine*, 48(4):577–582, 2002.

S. Weisberg. *Applied linear regression*. Wiley, 2005.

C. F. J. Wu. Jackknife, bootstrap and other resampling methods in regression analysis. *The Annals of Statistics*, 14(4):1261–1295, 1986.

6

Probabilistic tractography using CSD

Contents

The work in this chapter has been published as:

- **B. Jeurissen**, A. Leemans, J. D. Tournier, and J. Sijbers. Probabilistic Fiber Tracking using the Residual Bootstrap with Constrained Spherical Deconvolution MRI. In *Proceedings of the International Society for Magnetic Resonance in Medicine*, volume 17, page 1438, Honolulu, USA, 2009
- A. Leemans, **B. Jeurissen**, J. Sijbers, and D. K. Jones. ExploreDTI: a graphical toolbox for processing, analyzing, and visualizing diffusion MR data. In *Proceedings of the International Society for Magnetic Resonance in Medicine*, volume 17, page 3537, Honolulu, USA, 2009
- **B. Jeurissen**, A. Leemans, D. K. Jones, J. D. Tournier, and J. Sijbers. Probabilistic fiber tracking using the residual bootstrap with constrained spherical deconvolution. *Human Brain Mapping*, 32:461–479, 2011

6.1 Introduction

While HARDI techniques offer an improved estimate of fiber orientations in the presence of partial volume effects, DW-MRI is inherently a noisy technique, resulting in uncertainty associated with each fiber orientation estimate. This uncertainty is especially important in the context of fiber tractography. Previous DTI studies have shown that measurement uncertainty can propagate errors in streamlines [Lazar and Alexander, 2003]. To take this uncertainty into account, probabilistic tractography algorithms were proposed, which assign a probability to the reconstructed pathways by considering multiple pathways emanating from the same seed point. Random vector generation, for example [Lazar and Alexander, 2002, Parker et al., 2003], relates the probability of a tract to the number of times it is reconstructed in a Monte Carlo random walk, where the characteristics of the random walk are determined by the properties of the underlying diffusion tensor. In voxels where there is no anisotropy, the generated vector is completely random. In anisotropic regions, the orientation probability is skewed to the axis of longest diffusion. Similar methods were developed for HARDI-based reconstruction methods where the characteristics of the random walk are determined by the shape of the underlying orientation distribution functions (ODFs). Some of these methods sample directly from the ODF [Campbell et al., 2005, Descoteaux et al., 2009, Perrin et al., 2005, Tournier et al., 2005]. Other methods first map the ODF parameters to the parameters of another distribution and take samples from this distribution during probabilistic tractography in an attempt to better model the underlying anatomy [Seunarine et al., 2007]. These approaches, however, have an important drawback: they assume an ad-hoc relationship between the shape of the diffusion profile and the uncertainty in local fiber orientation. A more rigorous approach computes the local fiber orientation uncertainty given the MR data using a Bayesian model [Behrens et al., 2003, 2007]. While this method is theoretically sound, it still requires the uncertainty to be modeled and it does not account for artifacts such as physiological noise and system instabilities.

An alternative to the ad-hoc methods is to use the bootstrap method. This is a nonparametric statistical procedure that enables one to estimate the uncertainty of a given statistic, by randomly selecting individual measurements, with replacement, from a set of repeated measurements, thus generating many bootstrap realizations of the data. Each realization provides a random estimate of a given statistic. By generating a sufficient number of realizations, one obtains a measure of the uncertainty of a given statistic from the data itself without requiring a priori assumptions about the sources of uncertainty [Efron, 1979, Pajevic and Basser, 2003]. Bootstrapping has previously been combined with DTI tractography to produce probabilistic fiber trajectories [Jones and Pierpaoli, 2005, Lazar and Alexander, 2005]. However, in a clinical setting, the amount of repeated measurements to allow accurate and precise bootstrapping can render acquisition time unacceptably long [**Jeurissen** et al., 2008b, O'Gorman and Jones, 2006].

The problem of long acquisition times can be addressed using model-based bootstrapping methods [Chung et al., 2006, Jones, 2008, Whitcher et al., 2007]. This approach obtains probability distributions for model parameters by resampling residuals from a model fit (e.g., diffusion tensor fit). The huge advantage of this

method is that it does not require repeated measurements, bringing acquisition time into the clinical range. Recent work has shown that the residual bootstrap can accurately estimate the uncertainty in DTI [Chung et al., 2006] and Q-ball Imaging (QBI) [Berman et al., 2008, Haroon et al., 2009].

In this chapter, a probabilistic tractography algorithm is presented based on CSD and the residual bootstrap. Using CSD to extract local fiber orientations, our algorithm will overcome partial volume effects associated with DTI and the poor angular resolution that is achieved with other HARDI methods such as QBI [Tournier et al., 2008]. Using the residual bootstrap, we allow fiber tract probability estimation within the clinical time frame, without prior assumptions about the form of the uncertainty in the data. Using Monte Carlo simulations, the accuracy and precision of the residual bootstrap method when estimating DTI and CSD fiber pathway uncertainty, is measured. We also apply our algorithm to clinical DW data and compare our method to state-of-the-art DTI residual bootstrap tractography [Chung et al., 2006, Jones, 2008] and to an established probabilistic multi-fiber CSD tractography algorithm [Tournier et al., 2005].

6.2 Materials and methods

6.2.1 Fiber tractography

In Chapter 4, we introduced a deterministic tractography algorithm based on CSD. This algorithm is an extension from the standard DTI streamline tractography algorithm [Basser et al., 2000] and can be summarized as follows. Fiber tracking is started at a given seed point. First, the DW signal at the current position of the trajectory is obtained using trilinear interpolation. Next, the fODF is estimated using CSD. Then, the fODF peak direction that is closest to the previous stepping direction is extracted (Newton optimization on the sphere). Finally, the trajectory is advanced by a fixed step size along the obtained direction. Tracking is ended when the fODF peak intensities are beneath a fixed threshold, a maximum angle is exceeded, or the tract leaves a specified brain mask.

Using the residual bootstrap approach outlined in Chapter 5, this deterministic tractography algorithm can be extended into a probabilistic one. First, N_b bootstrap realizations are generated from the measured DW data set. Then, the above deterministic algorithm is run separately on each generated data set, producing N_b tracts emanating from the same seed point. Finally, visitation maps can be generated by assigning to each voxel the number of bootstrapped trajectories that pass through it [Jones and Pierpaoli, 2005].

Note that by extracting the peaks with a bootstrap procedure, we are implicitly estimating a new, sharper fODF, with the underlying assumption that the fiber orientations are discrete (i.e., delta functions), as in [Behrens et al., 2007, Hosey et al., 2005]. In fact, we are estimating a new fODF that accounts for uncertainty in the data and has the underlying assumption of 'sparsity' of the fiber orientations.

Unless specified, the following tractography parameters were used in this work: a step size of 1 mm, a minimum fODF peak intensity of 0.1 and a maximum angle between two consecutive steps of 30°. The 0.1 fODF threshold was a trade-off between sensitivity and specificity. Increasing the threshold reduced the likelihood

of false positives, but at the cost of missing small fiber populations. Decreasing the threshold facilitated tracking through regions with small fiber populations, but at the cost of many spurious fibers. In the remainder of this chapter, this algorithm will be referred to as 'CSD residual bootstrap tractography'.

We compared the proposed method with two other tractography algorithms. The first one, which will be referred to as 'DTI residual bootstrap tractography', is very similar to our method, but uses the diffusion tensor model to estimate the local fiber orientations and to perform the residual bootstrap [Chung et al., 2006, Jones, 2008]. The FA threshold used in this method was 0.1. The second one, which will be referred to as 'CSD fODF sampling tractography', generates probabilistic fiber orientations by taking samples directly from the fODFs using a rejection sampling scheme [Tournier et al., 2005]. The same parameters as for the CSD residual bootstrap tractography were used. Note that in contrast to the CSD residual bootstrap algorithm, this method does not assume that the fiber orientations are discrete, but instead tries to account for uncertainty due to the fODF shape itself, which is assumed to represent the underlying anatomical dispersion.

6.2.2 Simulations

In Chapter 5 we have shown, using numerical simulations, that the residual bootstrap realizations of local CSD fiber orientation (at the voxel level) accurately represent the true uncertainty in fiber orientation [**Jeurissen** et al., 2008a]. In this chapter, the uncertainty of global fiber trajectories (at the data set level) was estimated by means of probabilistic tractography based on the residual bootstrap. Using a numerical phantom [Leemans et al., 2005], the accuracy and precision of the residual bootstrap for both DTI and CSD probabilistic tractography was measured.

Two properties of the probabilistic tracts were studied: fiber dispersion and success rate. Fiber dispersion of a set of probabilistic trajectories was defined as described in [Lazar and Alexander, 2005]. This method takes regular steps along the true noiseless trajectory and computes planes that are perpendicular to the tangent vector. The spatial locations of the intersection of each trajectory with the plane are determined and the distribution of these locations is characterized using principal component analysis. This yields two dispersion measures, λ_1 and λ_2, indicating the amount of fiber spread along the principal axes of dispersion in this transverse plane. Success rate was defined as the number of trajectories that successfully reached each plane. Using Monte Carlo simulations, dispersion and success rate of gold standard CSD, gold standard DTI, CSD residual bootstrap and DTI residual bootstrap trajectories were compared. For comparison, we also studied the dispersion and success rate of the CSD fODF sampling method.

6.2.2.1 Gold standard

A noiseless DW data set was simulated as in Leemans et al. [2005]. In this framework, diffusion tensor profiles with different orientations are combined to

simulate the noiseless DW signal for a multi-fiber voxel:

$$S(\boldsymbol{u}) = \sum_{i=1}^{N} f_i S_0 e^{-b\boldsymbol{u}\boldsymbol{D}_i\boldsymbol{u}^T} \qquad \text{with} \qquad \sum_{i=1}^{N} f_i = 1 \quad . \tag{6.1}$$

The fractions f_i $(i = 1, ..., N)$ represent the relative contribution of the i-th fiber orientation along unit direction $\boldsymbol{u}$. The non-DW signal, S_0, was set to 1 without loss of generality. Individual diffusion tensors $\boldsymbol{D}_i$ $(i = 1, ..., N)$ had a fractional anisotropy (FA) of 0.8 and a mean apparent diffusion coefficient (ADC) of $4 \times 10^{-4}\,\mathrm{mm}^2/\mathrm{s}$ (average value measured at the corpus callosum in the real HARDI data set below). The diffusion weighting b was set to $3000\,\mathrm{s/mm}^2$. Sixty diffusion encoding gradient directions were used, distributed evenly on the half sphere [Jones et al., 1999]. Voxel size was $2.4 \times 2.4 \times 2.4\,\mathrm{mm}^3$. This setup corresponds to a realistic and clinically feasible HARDI acquisition. The simulated data set contained three fiber bundles with a crossing arrangement as shown in Fig. 6.1a. Fig. 6.1b-e shows the corresponding DTI ellipsoids and CSD fODFs that can be found in the phantom. Rician noise was added to the noiseless data set to generate 10000 noisy data sets. The SNR in the individual data sets was 30 within the $b = 0\,\mathrm{s/mm}^2$ images, which is clinically feasible. Note that all subsequent SNR values are defined on the images without diffusion weighting, since SNR in the DW images depends on the amount of diffusion and its orientation. In the DW images, the average SNR is approximately 5. To show how the tracts behave at different noise levels, we repeated our simulation experiment for lower SNR values: 25, 20, and 15. For each data set, CSD tractography was started from a fixed seed point (red dot), resulting in 10000 gold standard probabilistic tracts (Fig. 6.2b). For reference, 10000 DTI tractography runs were also performed (Fig. 6.2a).

6.2.2.2 Residual bootstrap

Starting from a single noisy simulated data set, $N_b = 1000$ trajectories were calculated using the probabilistic tractography method as detailed in Section 6.2.1 (Fig. 6.2d). For reference, $N_b = 1000$ DTI residual bootstrap tractography runs were also generated (Fig. 6.2c). The above procedure was repeated 50 times to calculate the mean and the standard deviation of the dispersion values.

6.2.2.3 fODF sampling

Starting from a single noisy simulated data set, $N_s = 1000$ trajectories were sampled from the CSD fODFs as detailed in Section 6.2.1 (Fig. 6.2e). The above procedure was repeated 50 times to calculate the mean and the standard deviation of the dispersion values.

6.2.3 Real data

Whole-brain HARDI data were acquired from a healthy adult volunteer on a General Electric 3 T HDx Signa system. An eight-channel head coil with parallel imaging factor of 2 was used to acquire twice-refocused spin echo echoplanar images with TE = 109 ms and $2.4 \times 2.4 \times 2.4\,\mathrm{mm}^3$ voxel size (FOV $23 \times 23\,\mathrm{cm}^2$, 96×96

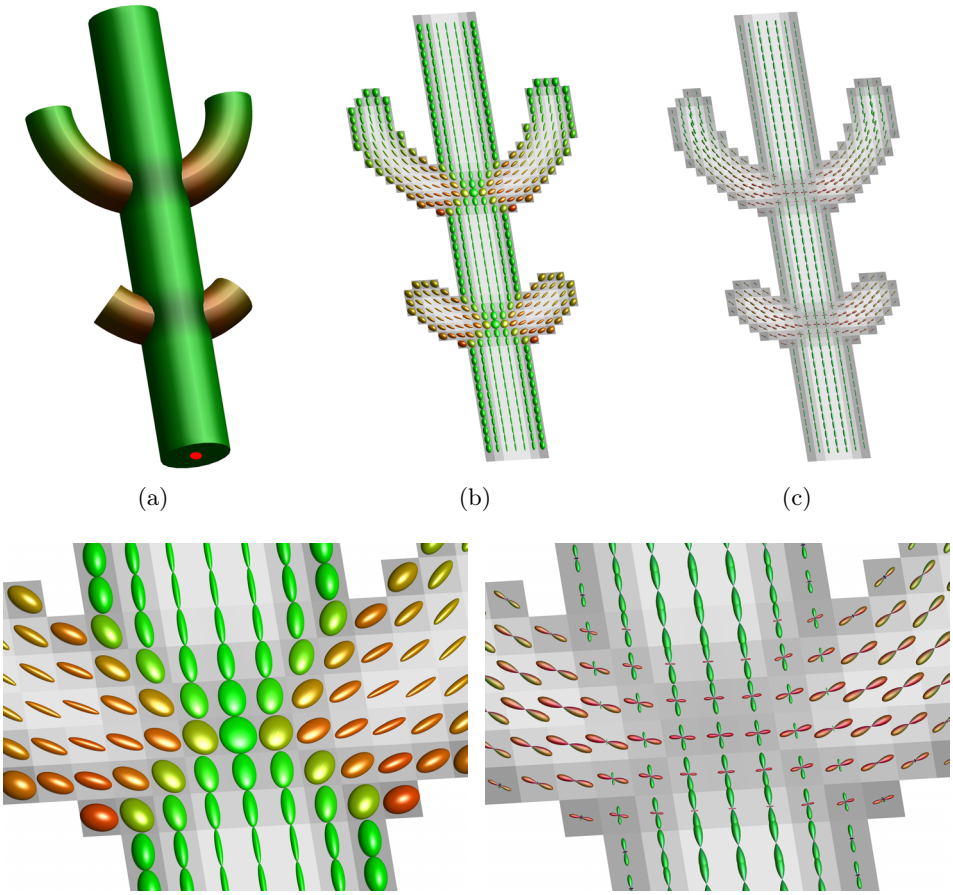

Fig. 6.1: Simulation of DW data. (a) simulated fiber arrangement; (b) noiseless DTI ellipsoids; (c) noiseless CSD fODFs; (d) noiseless DTI ellipsoids at crossing; (e) noiseless CSD fODFs at crossing.

acquisition matrix, NEX = 1, partial Fourier encoding with 16 overscans before the center of k, 60 slices with 2.4 mm thickness with no gap). Diffusion gradients were applied in 60 directions uniformly distributed on a sphere through electrostatic repulsion [Jones et al., 1999] with $b = 3000\,\mathrm{s/mm^2}$. Six images with $b = 0\,\mathrm{s/mm^2}$ were also acquired. Cardiac gating was applied using a peripheral pulse oximeter with an effective TR = 20 R-R intervals. Total scan time was approximately 20 minutes. Motion and eddy-current distortion correction was applied taking into account the B-matrix rotation [Leemans and Jones, 2009] and the tensor model was fitted to the data using a weighted (anisotropic covariance matrix) linear regression method [Basser et al., 1994]. These processing steps were performed with the diffusion MR toolbox ExploreDTI [Leemans et al., 2009]. SNR within the $b = 0\,\mathrm{s/mm^2}$ images was approximately 30, calculated using the difference method to compensate for spatial noise variations in parallel imaging [Dietrich et al., 2007]. The subject gave written informed consent to participate in this study under a protocol approved by the Cardiff University Ethics Committee.

Using the guidelines in Catani and de Schotten [2008], seed points (shown as red dots) were selected at the core of three well known fiber tracts for which DTI is assumed to perform well (i.e., no fiber crossings): the corpus callosum, the cingulum and the fornix (Fig. 6.5a-6.5i). Next, all three tractography methods were started in the predefined seed points. Fiber dispersion was calculated as explained in Section 6.2.2, using the deterministic DTI trajectory as reference trajectory. Fiber dispersion was only calculated in the segment of the reference trajectory where both DTI and CSD reported 75% success rate to avoid too much artificial drop in fiber dispersion due to spurious fibers terminating early.

Next, seed points were placed close to the crossing of the CC, the SLF and the CST[1] and all three tractography methods were started from those seed points. In these regions, dispersion values could no longer be measured objectively, since both algorithms are now expected to follow different paths. Instead, visitation maps were generated by assigning to each voxel the number of trajectories that pass through it [Jones and Pierpaoli, 2005] and the maps were qualitatively compared (Fig. 6.6-6.8).

6.3 Results

6.3.1 Simulated data

Fig. 6.2a shows 1000 gold standard DTI fiber tracts emanating from the same seed point (red dot), superimposed on an FA map. When the tracts enter regions of crossing fibers (low FA), there is considerable increase in tract dispersion due to partial volume effects. At the second fiber crossing, these tracts even disperse into the crossing tract. Fig. 6.2b shows the corresponding CSD tracts, having no bifurcations and much smaller tract dispersion. Fig. 6.2c displays $N_b = 1000$ tracts generated by DTI residual bootstrap tractography (starting from a single noisy measurement), showing an additional tract dispersion in the event of partial volume

[1]Here, we refer to CST as the collection of fiber pathways that travel between the cerebral cortex and the spinal cord. Note that only a part of the CST was reconstructed, as we used only one seed voxel.

effects. Fig. 6.2d shows the corresponding CSD residual bootstrap tracts, which are in close agreement with the gold standard ones from Fig. 6.2b. Fig. 6.2e displays $N_s = 1000$ tracts generated by CSD fODF sampling tractography (starting from a single noisy measurement), showing a very large overall dispersion, even in regions without partial volume effects. At the fiber crossings, some tracts disperse into the crossing tracts.

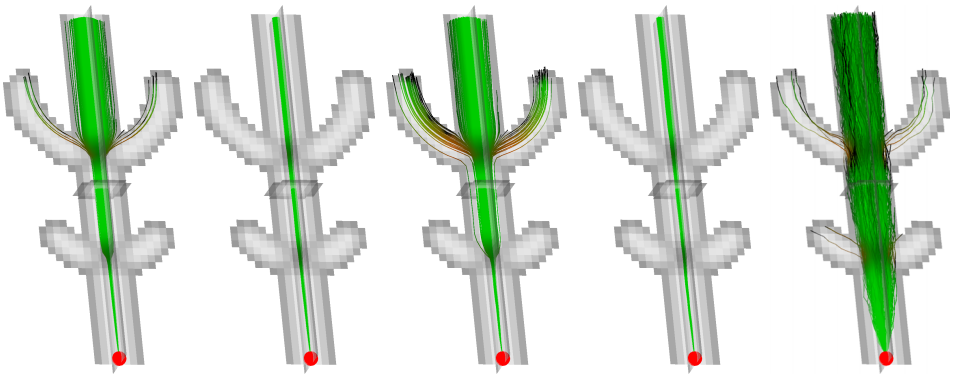

(a) (b) (c) (d) (e)

Fig. 6.2: Simulations of probabilistic tractography at SNR 30: trajectories from a single seed point (red dot). (a) Gold standard DTI; (b) Gold standard CSD; (c) DTI residual bootstrap; (d) CSD residual bootstrap; (e) CSD fODF sampling.

To explore this in more detail, Fig. 6.3, plots fiber dispersion values λ_1 and λ_2 and the success rate as a function of arc length along the trajectory, for gold standard DTI (blue line), gold standard CSD (green line), the mean residual bootstrap approximation (red line), and the CSD fODF sampling tractography (magenta line). The shaded red area is a 95% confidence interval for the mean.

From Fig. 6.3a, it is clear that gold standard DTI trajectories undergo heavy λ_1 dispersion in case of partial voluming (around 30 and 60 mm from the seed point). This is due to the disc shaped diffusion tensors which have no well defined largest eigenvector. Gold standard CSD trajectories on the other hand are much less sensitive to λ_1 dispersion in the event of partial voluming. For λ_2, both gold standard DTI and CSD trajectories, show similar dispersion, though dispersion for gold standard CSD is slightly lower (Fig. 6.3b). This can be explained by the fact that while the disc shaped diffusion tensors have high uncertainty associated with the largest eigenvector, the disc shape does not allow them to disperse out of the plane. Finally, gold standard CSD achieves 100% success rate along the entire phantom, whereas gold standard DTI success rate drops significantly at each fiber crossing (Fig. 6.3c).

Fig. 6.3d-e shows that the DTI residual bootstrap tractography algorithm accurately estimates gold standard DTI fiber dispersion, as long as the tensor model holds (before 30 mm). In the event of partial volume effects, however, there is a large positive bias in the fiber dispersion estimated by DTI residual bootstrap. Fig. 6.3g-h, on the other hand, shows that the bootstrap estimates of CSD fiber

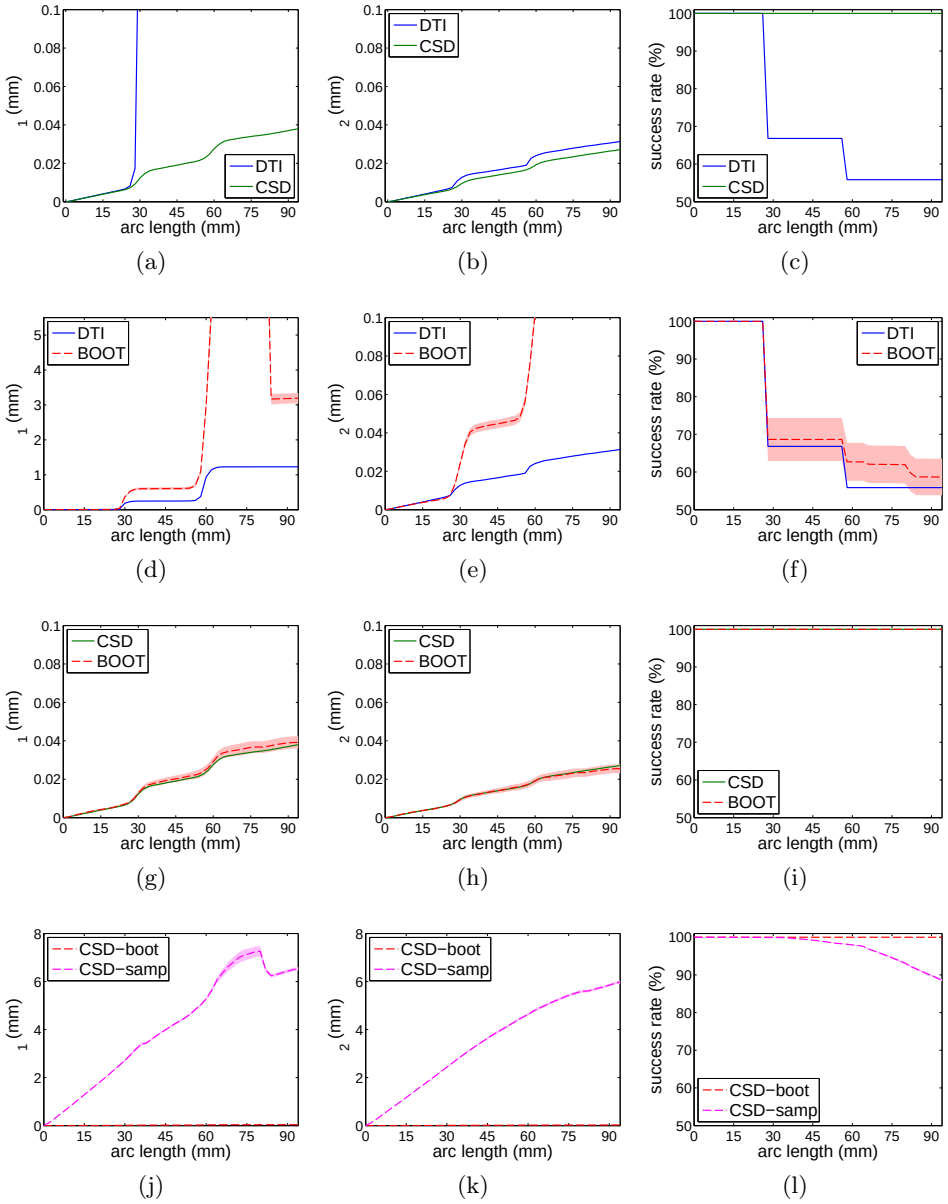

Fig. 6.3: Simulations of probabilistic tractography at SNR 30: fiber dispersion and success rate versus arc length from seed point. λ_1 is the dispersion along the major axis of dispersion; λ_2 is the dispersion along the minor axis of dispersion. (a)-(c) Gold standard DTI vs. CSD; (d)-(f) Gold standard DTI vs. residual bootstrap; (g)-(i) Gold standard CSD vs. residual bootstrap; (j)-(l) CSD residual bootstrap vs. CSD fODF sampling. The shaded area represents the 95% confidence interval of the mean.

dispersion (both λ_1 and λ_2) are very close to the gold standard, even in the event of partial voluming. Fig. 6.3i reports 100% success rate for the CSD residual bootstrap, whereas DTI residual bootstrap tractography results in additional fiber termination, due to dispersing tracts (Fig. 6.3f).

Fig. 6.3j-k shows that the CSD fODF sampling fiber dispersion measures (both λ_1 and λ_2) are rapidly increasing even in perfectly aligned fiber structures. Because of this large degree of dispersion, more trajectories are stopping as the tracts move further away from the seed point (Fig. 6.3l).

Additional simulations at other SNR levels (Fig. 6.4), show that the uncertainty estimates of the CSD residual bootstrap are very close to the gold standard uncertainty for a wide range of SNR levels (Fig. 6.4g-i). The plots also show that the residual bootstrap dispersion increases with decreasing SNR, indicating less confidence in the trajectories (Fig. 6.4g-i). Dispersion of the CSD fODF sampling tractography, however, remains almost constant for different SNR levels and is much higher than for the residual bootstrap (Fig. 6.4j-l).

6.3.2 Real Data

Fig. 6.5 shows probabilistic fiber trajectories and their associated dispersion for DTI residual bootstrap (blue), CSD residual bootstrap (green), and CSD fODF sampling tractography (magenta), for three well-defined fiber bundles. While both DTI and CSD residual bootstrap produced very similar reconstructions of all three tracts (Fig. 6.5a-f), higher fiber dispersion values were observed for DTI residual bootstrap tractography in all three tracts (Fig. 6.5j-o). Looking at the CSD fODF sampling tractography results, there is generally a much higher degree of dispersion, resulting in spurious fibers as we move further away from the seed point (Fig. 6.5g-i). Even close to the seed point, where the fODFs are very sharp and aligned, relatively high dispersion is measured (Fig. 6.5j-o). Also notice that a relatively high dispersion rate was recorded at the base of the corpus callosum (Fig. 6.5j,m), which is the region with the most sharp and well-aligned fODFs in the brain.

Fig. 6.6-6.8 show individual probabilistic fiber trajectories and maximum intensity projections of the visitation maps in the region with complex fiber architecture.

Fig. 6.6a-h shows both DTI and CSD residual bootstrap tractography are able to reconstruct the superior projections of the CC, when placing the seed point high in the CC at the midsagittal plane. DTI trajectories, however, show much more dispersion in the cortical region. Fig. 6.6m-t shows that CSD residual bootstrap tractography is able to reconstruct the lateral projections of the CC, when placing the seed point low in the CC at the midsagittal plane. DTI residual bootstrap tractography on the other hand is not able to find these lateral projections (false negatives) and instead switches to the superior projections and to the tail of caudate nucleus (false positives). Looking at the fODF sampling tractography results (Fig. 6.6i-l,u-x), there is generally a much higher degree of dispersion, especially as the tracts move further away from the seed point. Placing the seed point high in the CC, most of the trajectories follow the superior projections, and some trajectories also follow the lateral projections (Fig. 6.6i-l). Placing the seed point low in the CC, the trajectories follow both the superior and lateral projections (Fig. 6.6u-x) but some trajectories switch to the CST and the SLF (false positives).

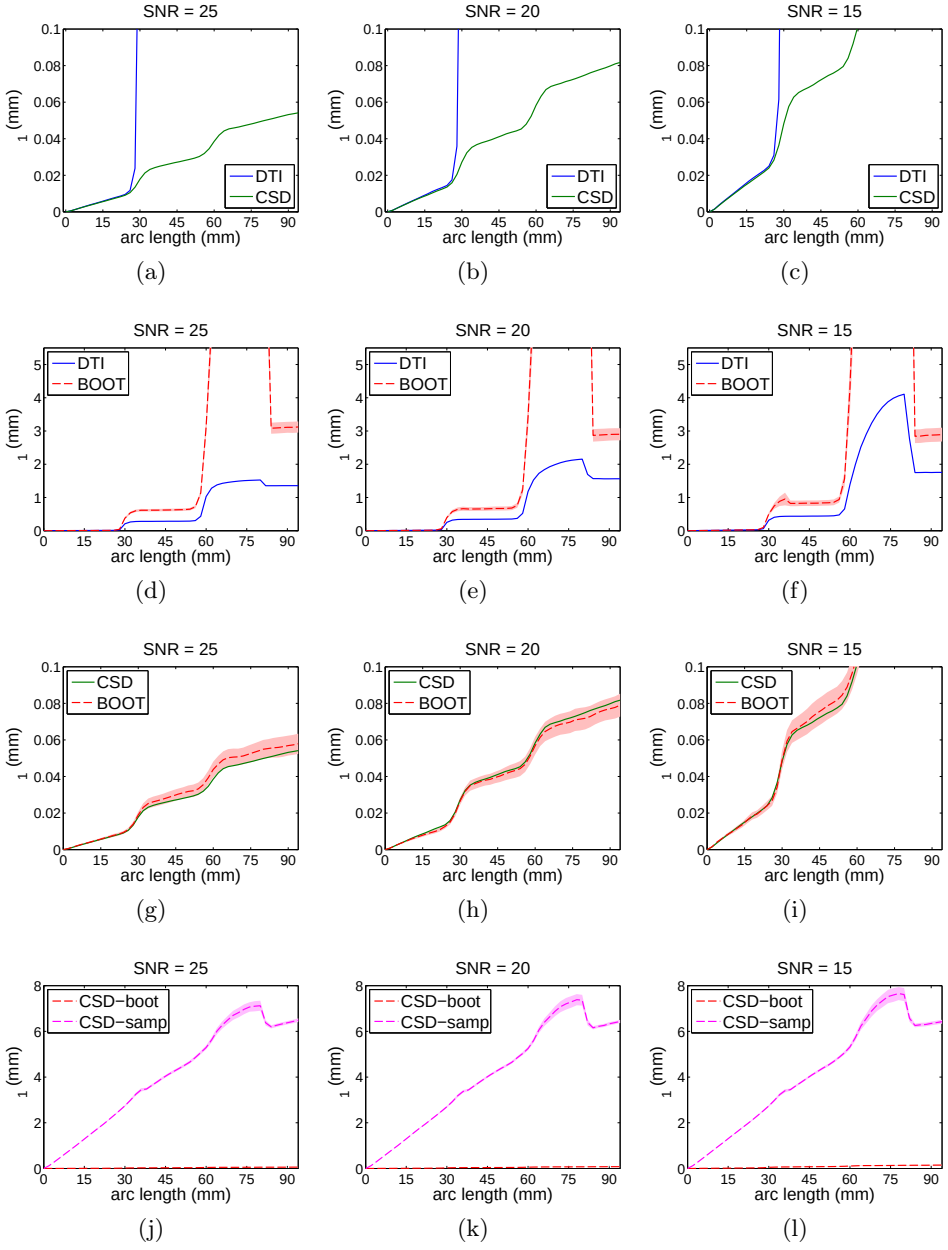

Fig. 6.4: Simulations of probabilistic tractography at SNR 25 (first column), 20 (second column) and 15 (third column): fiber dispersion λ_1 along major axis of dispersion versus arc length from seed point (λ_2 and success rate similar but not shown). (a)-(c) Gold standard DTI vs. CSD; (d)-(f) Gold standard DTI vs. residual bootstrap; (g)-(i) Gold standard CSD vs. residual bootstrap; (j)-(l) CSD residual bootstrap vs. CSD fODF sampling.

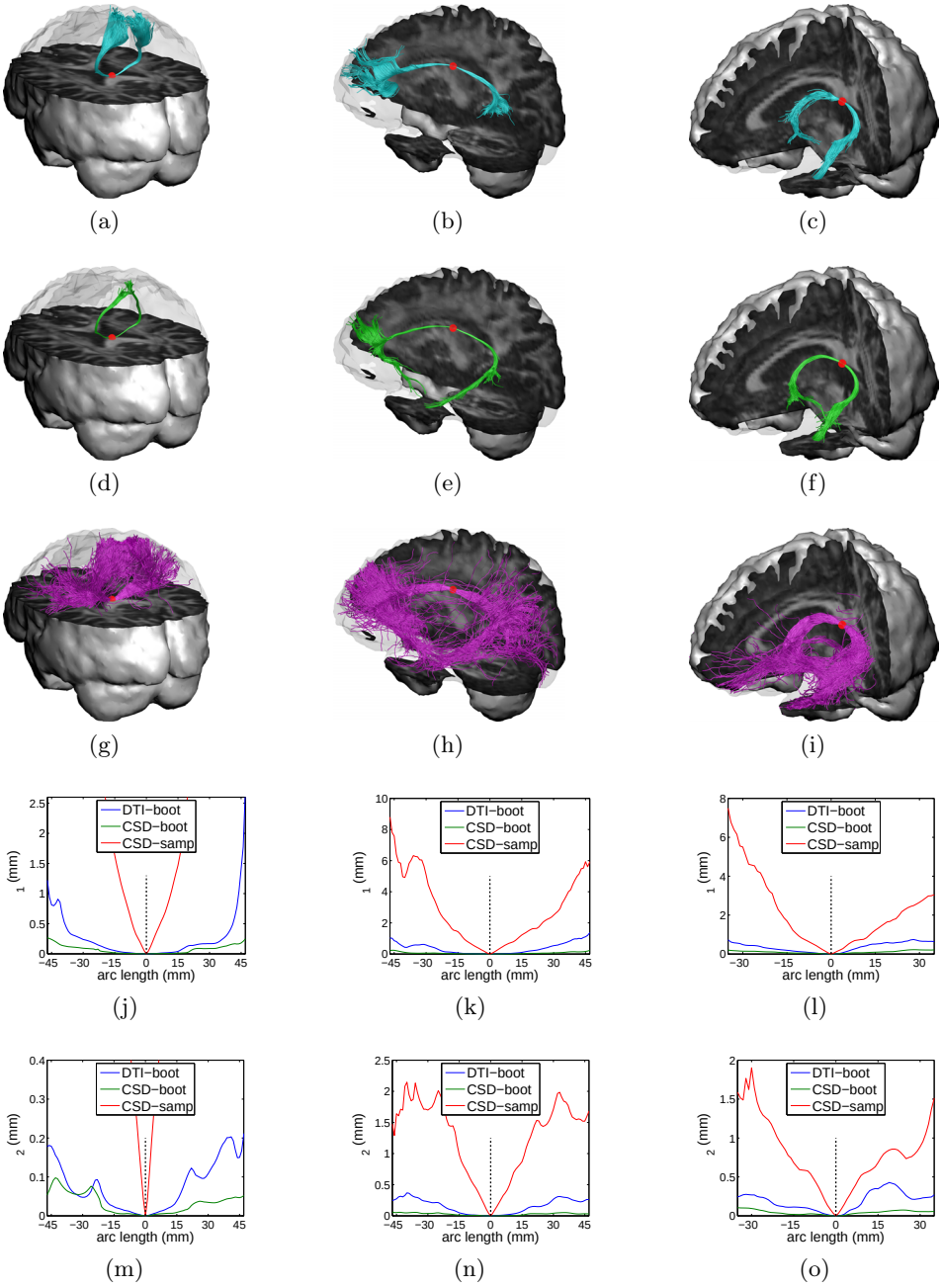

Fig. 6.5: Probabilistic tractography in corpus callosum (first column), cingulum (second column) and fornix (third column). (a)-(c) DTI residual bootstrap trajectories; (d)-(f) CSD residual bootstrap trajectories; (g)-(i) CSD fODF sampling trajectories; emanating from a single seed point (red dot); (j)-(l) fiber dispersion along major axis of dispersion; (m)-(o) fiber dispersion along minor axis of dispersion.

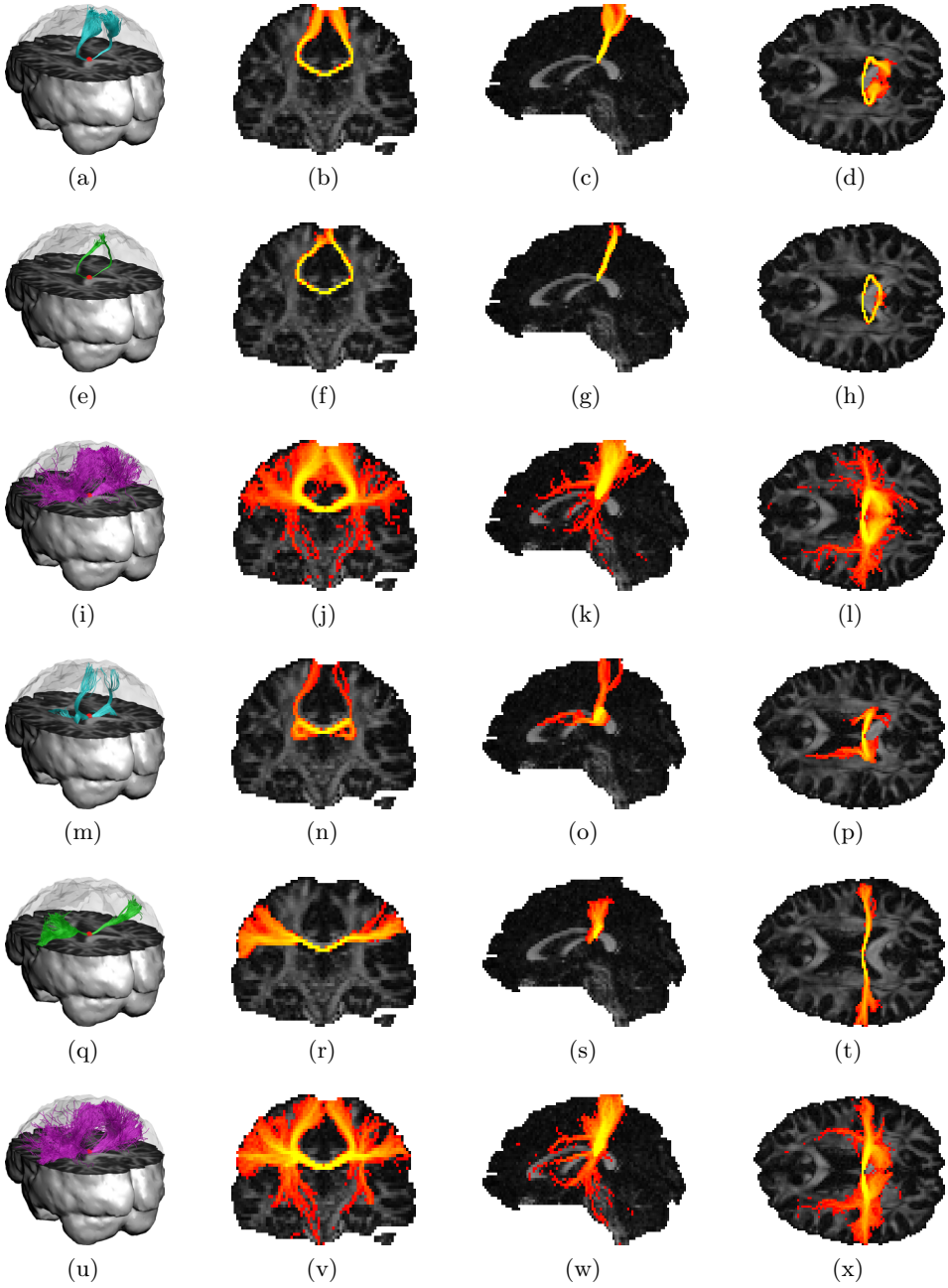

Fig. 6.6: Probabilistic tractography of the superior (first three rows) and lateral projections (last three rows) of the corpus callosum: trajectories emanating from a single seed point (red dot) (first column) and maximum intensity projections of their associated visitation maps (last three columns). (a)-(d), (m)-(p) DTI residual bootstrap; (e)-(h), (m)-(p) CSD residual bootstrap; (i)-(l), (m)-(p) CSD fODF sampling.

Fig. 6.7 shows CSD residual bootstrap tractography is able to reconstruct a well defined path through the SLF (Fig. 6.7e-h). DTI residual bootstrap tractography on the other hand shows a mixture between the true SLF, the CST and the external capsule (Fig. 6.7a-d). CSD fODF sampling tractography shows a mixture between the true SLF, the CST, and the external capsule (false positives) and there is generally a much higher degree of dispersion (Fig. 6.7i-l).

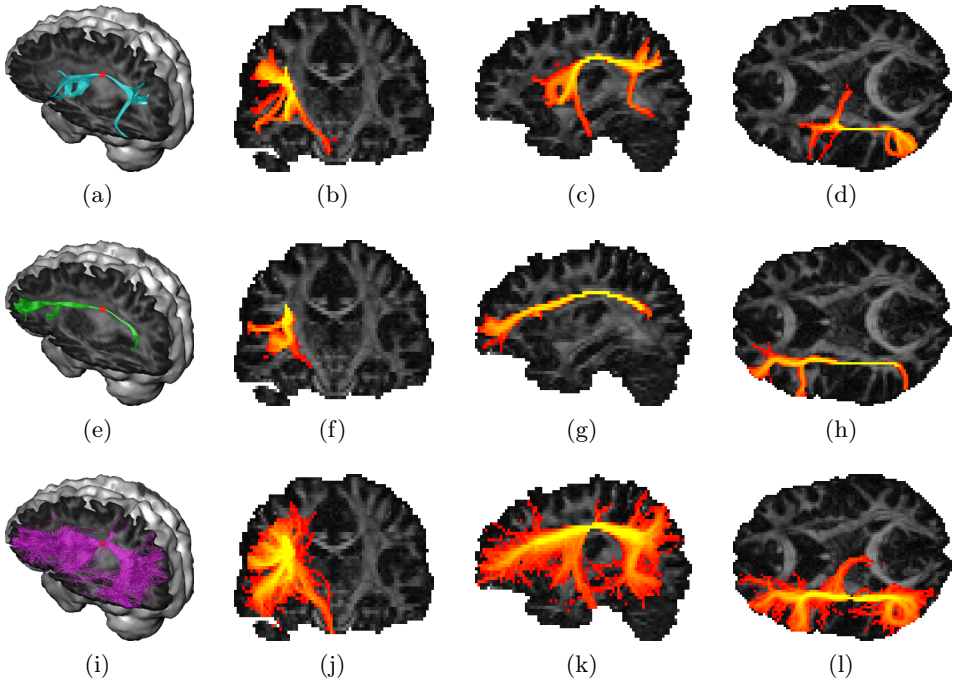

Fig. 6.7: Probabilistic tractography of the superior longitudinal fasciculus: trajectories emanating from a single seed point (red dot) (first column) and maximum intensity projections of their associated visitation maps (last three columns). (a)-(d) DTI residual bootstrap; (e)-(h) CSD residual bootstrap; (i)-(l) CSD fODF sampling.

Fig. 6.8a-h shows that CSD residual bootstrap tractography is able to reconstruct the CST running all the way from the cortex to the spine. DTI residual bootstrap tractography results are very similar, even in the region of crossing fibers. However, placing the seed point on a different location in the CST caused DTI residual bootstrap to switch to the CC and track into the opposite hemisphere, whereas CSD residual bootstrap was still able to reconstruct the CST without false positives (Fig. 6.8m-t). Looking at the CSD fODF sampling tractography results (Fig. 6.8i-l,6.8u-x), there is generally a much higher degree of dispersion, especially as the tracts move further away from the seed point. In both cases, CSD fODF sampling tractography is able to reconstruct the CST running all the way from the cortex to the spine. However, the trajectories also switch to other structures: fibers projecting from the region of the thalamus to the frontal cortex (Fig. 6.8k), CC (Fig. 6.8v) and fibers projecting to the cerebellum (Fig. 6.8k,(w)) (false positives).

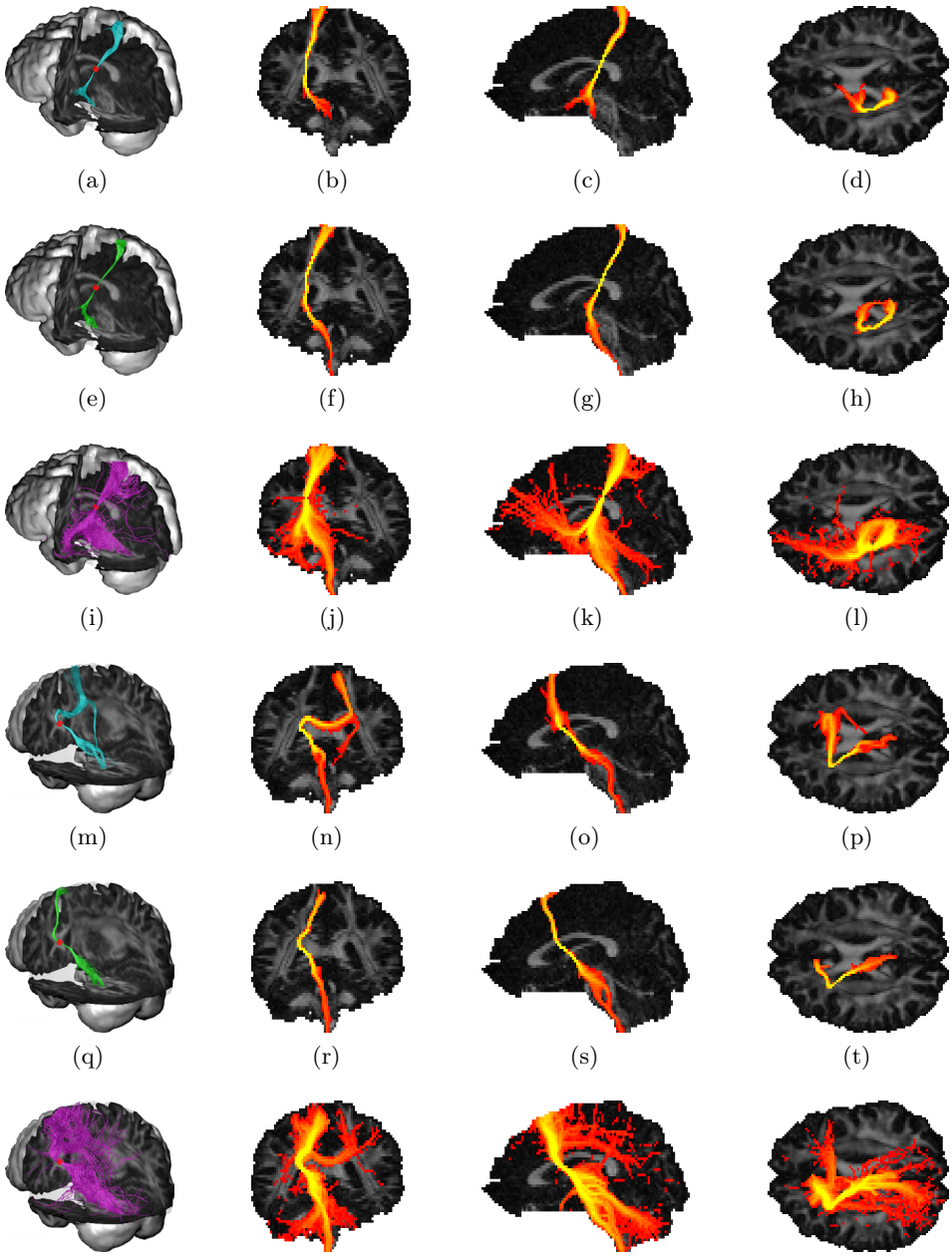

Fig. 6.8: Probabilistic tractography of the corticospinal tract: trajectories emanating from a single seed point (red dot) (first column) and maximum intensity projections of their associated visitation maps (last three columns). (a)-(d), (m)-(p) DTI residual bootstrap; (e)-(h), (q)-(t) CSD residual bootstrap; (i)-(l), (u)-(x) CSD fODF sampling.

Fig. 6.9 shows plots of the DTI ellipsoids (transparent) and the corresponding principal orientations (white lines) along with the CSD fODFs in the regions where probabilistic DTI tractography suffers from partial volume effects. The transparent blue arrow represents the most likely DTI trajectory, while the green arrow represents the most likely CSD trajectory.

Notice that when the seed point is placed high enough in the CC, CSD, and DTI will produce similar trajectories, i.e., the superior projections of the CC (Fig. 6.9a). If the seed point is placed lower in the CC, CSD will produce the lateral projections of the CC, but DTI will produce false positives (Fig. 6.9b).

For the SLF, the dominant fiber orientations of the CST force the DTI trajectories to curve downwards, while the CSD trajectories are allowed to follow a much straighter pathway (Fig. 6.9c).

In regions where the CST is the dominant fiber orientation, the fiber trajectories are the same for both DTI and CSD (Fig. 6.9d). However, in some regions, dominant crossing fibers skew the principal diffusion orientations towards adjacent tracts such as the CC (Fig. 6.9e).

6.4 Discussion

In this chapter, a new probabilistic tractography algorithm was proposed, based on CSD and the residual bootstrap. By using CSD, multiple intravoxel fiber populations could be resolved, allowing our method to confidently track through regions of complex fiber architecture. The residual bootstrap allowed us to estimate local fiber uncertainty to derive global probabilistic tracts.

The use of CSD over other popular HARDI methods such as Q-ball imaging (QBI) was motivated by a recent study showing that CSD is able to estimate multiple intravoxel fiber orientations more accurately than QBI [Tournier et al., 2008]. The study showed a bias in the fiber orientations obtained with QBI, for crossing angles smaller than 90°, which may have adverse effects on fiber-tracking results derived using this method [Berman et al., 2008, Haroon et al., 2009]. Also angular resolution was shown to be higher for CSD, which allows resolving smaller interfiber angles.

The residual bootstrap allowed us to estimate fiber orientation uncertainty without prior assumptions about the form of uncertainty in the data, overcoming the limitations of ad-hoc methods, which assume an ad-hoc relationship between the shape of fODF and the uncertainty in fiber orientation [Campbell et al., 2005, Descoteaux et al., 2009, Perrin et al., 2005, Tournier et al., 2005]. The huge advantage over methods employing the classic bootstrap is that it does not require the collection of extra data, bringing acquisition time into the clinical realm. Since our bootstrap approach uses a SH fit of the DW signal itself, the results are completely general and applicable to other HARDI methods than spherical deconvolution [Tournier et al., 2009].

Numerical simulations of complex fiber architecture showed that our probabilistic algorithm accurately estimates CSD fiber trajectory uncertainty (Fig. 6.3g-i) and that it is superior to DTI residual bootstrap tractography in terms of false positives (fiber dispersion) and false negatives (fibers stopping) (Fig. 6.3d-f). The improve-

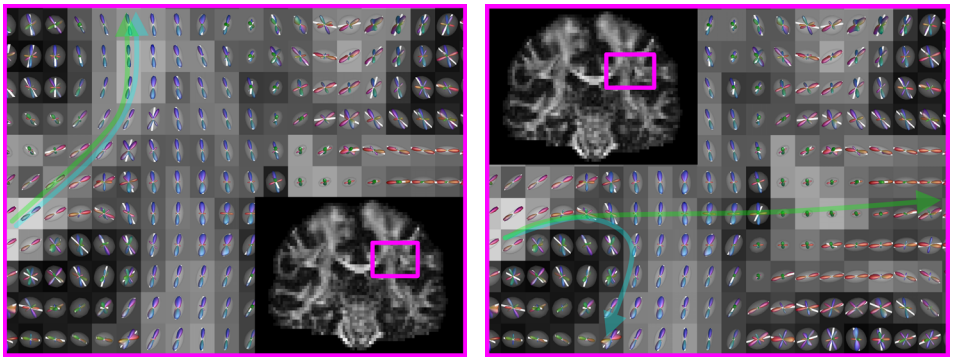

(a) (b)

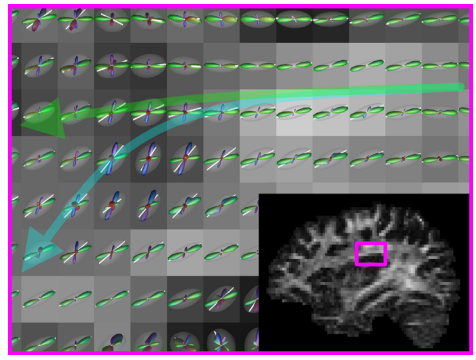

(c)

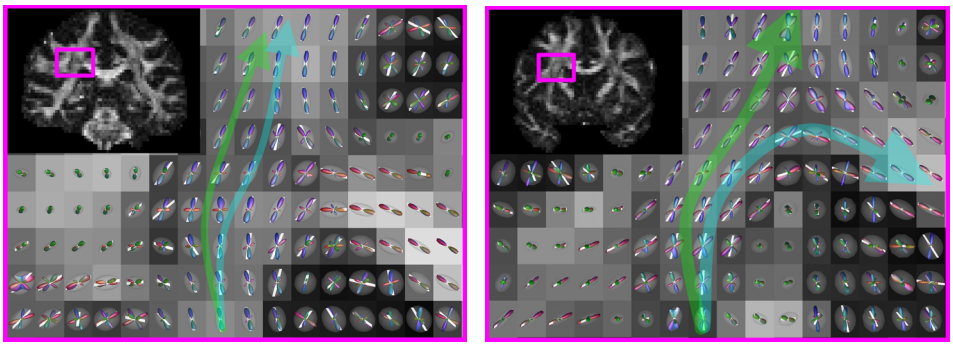

(d) (e)

Fig. 6.9: Partial volume effects of DTI in more detail: FA maps with DTI ellipsoids (transparent), first eigenvectors (white lines) and CSD fODFs for the trajectories in Fig. 6.6-6.8. The arrows are a schematic representation of the probabilistic DTI (blue) and probabilistic CSD (green) trajectories.

ment by moving from DTI to CSD is two-fold. First, CSD allows a more accurate estimation of the local fiber orientations in regions of complex fiber architecture. Second, our method allows more accurate estimation of the uncertainty associated with these orientations. Indeed, in regions where the DTI model does not hold, DTI does not only suffer from errors in the estimation of fiber orientations (Fig. 6.3a-c), it also results in erroneous residual bootstrapping (Fig. 6.3d-f), since the residuals from the diffusion tensor fit no longer match the true noise characteristics of the data.

An important remark is that the residual bootstrap dispersion measures reported in this study are not to be confused with anatomical dispersion values. Instead, the residual bootstrap is measuring dispersion due to noise. Bootstrap dispersion should be viewed as a measure of robustness for the tractography algorithm (e.g. CSD streamline tractography) and a measure for data quality. While data with higher SNR or a more robust tractography algorithm will reduce streamline dispersion, it will certainly not change the actual anatomical dispersion present in the brain. This is in contrast with the CSD fODF sampling dispersion. Here, the sampling procedure tries to account for uncertainty in the fODF itself. While this approach allows tracts to fan out more, possibly allowing a better result in structures with extensive fanning (such as the CST), this approach has some limitations. To begin with, it is very difficult to relate the shape of the fODF to the underlying anatomical dispersion. For example: a noiseless delta peak fODF will already have an intrinsic width related to its SH order (see Fig. 6.10). Sampling from this fODF will result in dispersion that is not anatomically meaningful. So while this method will allow tracts to fan out more, it does so in great part regardless of their actual anatomical dispersion. This can be appreciated from our simulation experiments (Fig. 6.3j-k), where perfectly aligned high amplitude fODF's produce very dispersed trajectories. A practical example of this deficiency is that even in the corpus callosum, which is the region with the most sharp and well-aligned fODFs in the brain, dispersion rate is relatively high (Fig. 6.5j,m). Second, because this method allows the trajectories to disperse more, it is more susceptible to false positives and thus less specific.

Judging from the tractography results on the experimental data, the problem of DTI in regions of fiber crossings is obvious. DTI residual bootstrap was unable to identify the lateral projections of the corpus callosum (false negatives) and instead reported the superior projections and portions of the nearby caudate nucleus (false positives) (see Fig. 6.6). It was also unable to reconstruct the correct path for the superior longitudinal fasciculus and switched to the corticospinal tract and external capsule instead (see Fig. 6.7). These errors are all caused by partial volume effects, as can be appreciated from the DTI ellipsoids and CSD fODFs in Fig. 6.9. These results show that residual bootstrap tractography in itself does not solve the crossing fibers issue and that a HARDI approach is required. DTI residual bootstrap tractography of the corticospinal tract, however, produced an anatomically plausible trajectory from the first seed point, even in the region of crossing fibers (Fig. 6.8a-h). The reason DTI did not fail here, is that the corticospinal tract is the dominant fiber population in this region, causing the principal axes of the diffusion tensors to be skewed towards its orientation. Since the orientation of the CST is nearly perpendicular to the orientation of the crossing structures, the orientation of the first eigenvector is almost perfectly aligned with

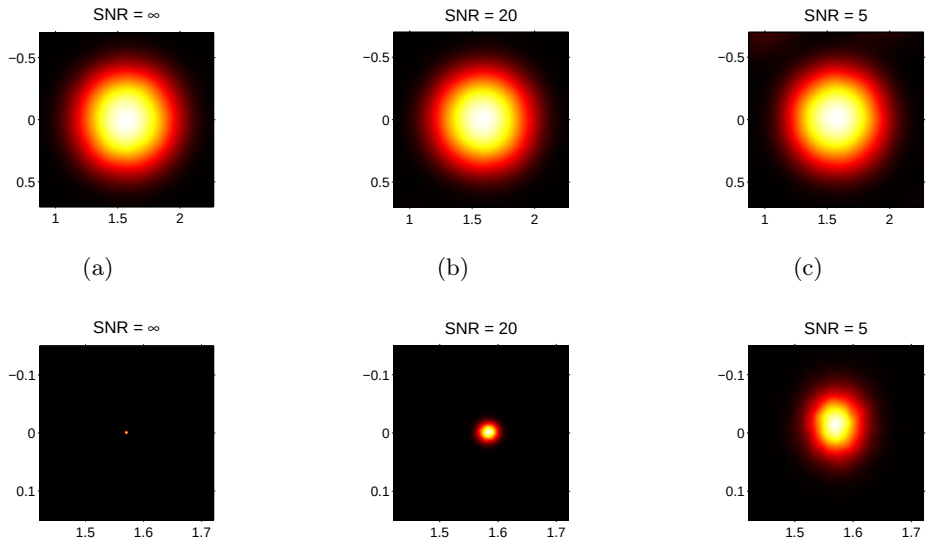

Fig. 6.10: Simulation of a delta function fODF without noise (first column), with low noise level (second column) and with high noise level (third column): 2D polar histogram of the fODF samples (top row) and the bootstrap samples (bottom row) for the different noise levels. Note that the bootstrap histogram uses a different scaling of the axes than the fODF sampling histogram.

the true fiber orientation (Fig. 6.9d). Starting from another seed point, however, does result in false negatives and false positives (Fig. 6.8m-t), again due to partial volume effects (Fig. 6.9e).

The CSD residual bootstrap tractography results are promising: the method was able to consistently reconstruct the lateral projections of the corpus callosum (see Fig. 6.6), the superior longitudinal fasciculus (see Fig. 6.7), and the corticospinal tracts (see Fig. 6.8a-h) and was less prone to dispersion in low FA regions than its DTI counterpart.

In regions where DTI and CSD produced similar trajectories (i.e., regions without too much partial volume effects), dispersion measures were consistently lower for CSD residual bootstrap than for its DTI counterpart (see Fig. 6.5). This may be counterintuitive, since CSD estimates far more parameters than DTI (45 instead of 6) and one might expect higher dispersion when using CSD. However, CSD is using a nonnegativity constraint, effectively reducing the noise in the fODFs, making it more reproducible than the unconstrained diffusion tensor fit. Additionally, even in relatively homogenous fiber structures, small partial volume effects will introduce small errors in the DTI fit, causing the residual bootstrap to overestimate trajectory dispersion. Although these effects are small, they will be important during tractography due to propagation of errors. Not only does the diffusion tensor model result in false positives and false negatives in regions of crossing fibers, it is also generally more prone to dispersion than CSD.

One limitation of our method is that it does not explicitly handle fanning fiber configurations. The fanning problem is a deficiency of tracking algorithms in general, since the fODF itself cannot differentiate between fanning, bending, or acute fiber crossing angles, even in the ideal case without noise. Usually, this is handled with additional explicit (somewhat ad-hoc) processing methods, typically by using shape characteristics of the fODF [Seunarine et al., 2007] or by including local neighborhood information [Savadjiev et al., 2008]. We do not address this deficiency in our CSD residual bootstrap algorithm, although we acknowledge that it is an outstanding problem.

6.5 Conclusion

We have presented a new probabilistic tracking algorithm based on CSD and the residual bootstrap that accurately estimates fiber trajectory uncertainty in regions of complex fiber architecture, without prior assumptions about the form of uncertainty in the data and using only a single acquisition, making the technique clinically feasible. By performing simulations and presenting real data examples, we have clearly demonstrated the advantages of CSD residual bootstrap over DTI residual bootstrap probabilistic tractography: in regions of multiple fiber orientations, CSD is much less prone to fiber dispersion, false positives, and false negatives. We have also shown the advantages of our method over CSD fODF sampling tractography: in regions of well ordered and sharp peak orientations, our method does not suffer from unrealistically high dispersion and our method has a higher specificity in general. On the other hand, because CSD fODF sampling uses the full fODF it can potentially deal better with anatomically disperse structures

(e. g. fanning and bending fiber bundles) and is more sensitive in general.

Bibliography

P. J. Basser, J. Mattiello, and D. LeBihan. Estimation of the effective self-diffusion tensor from the NMR spin echo. *Journal of Magnetic Resonance Series B*, 103: 247–247, 1994.

P. J. Basser, S. Pajevic, C. Pierpaoli, J. Duda, and A. Aldroubi. In vivo fiber tractography using DT-MRI data. *Magnetic Resonance in Medicine*, 44(4): 625–632, 2000.

T. E. J. Behrens, M. W. Woolrich, M. Jenkinson, H. Johansen-Berg, R. G. Nunes, S. Clare, P. M. Matthews, J. M. Brady, and S. M. Smith. Characterization and propagation of uncertainty in diffusion-weighted MR imaging. *Magnetic Resonance in Medicine*, 50(5):1077–1088, 2003.

T. E. J. Behrens, H. Johansen-Berg, S. Jbabdi, M. F. S. Rushworth, and M. W. Woolrich. Probabilistic diffusion tractography with multiple fibre orientations: what can we gain? *NeuroImage*, 34(1):144–155, 2007.

J. I. Berman, S. W. Chung, P. Mukherjee, C. P. Hess, E. T. Han, and R. G. Henry. Probabilistic streamline q-ball tractography using the residual bootstrap. *NeuroImage*, 39(1):215–222, 2008.

J. S. W. Campbell, K. Siddiqi, V. V. Rymar, A. F. Sadikot, and G. B. Pike. Flow-based fiber tracking with diffusion tensor and q-ball data: validation and comparison to principal diffusion direction techniques. *NeuroImage*, 27(4):725–736, 2005.

M. Catani and T. de Schotten. A diffusion tensor imaging tractography atlas for virtual in vivo dissections. *Cortex*, 44(8):1105–1132, 2008.

S. W. Chung, Y. Lu, and R. G. Henry. Comparison of bootstrap approaches for estimation of uncertaintiesof DTI parameters. *NeuroImage*, 33(2):531–541, 2006.

M. Descoteaux, R. Deriche, TR Knösche, and A. Anwander. Deterministic and probabilistic tractography based on complex fibre orientation distributions. *IEEE Transactions on Medical Imaging*, 28(2):269–286, 2009.

O. Dietrich, J. G. Raya, S. B. Reeder, M. F. Reiser, and S. O. Schoenberg. Measurement of signal-to-noise ratios in MR images: influence of multichannel coils, parallel imaging, and reconstruction filters. *Journal of Magnetic Resonance Imaging*, 26(2):375–385, 2007.

B. Efron. Bootstrap methods: another look at the jackknife. *The Annals of Statistics*, 7(1):1–26, 1979.

H. A. Haroon, D. M. Morris, K. V. Embleton, D. C. Alexander, and G. Parker. Using the model-based residual bootstrap to quantify uncertainty in fiber orientations from Q-ball analysis. *IEEE Transactions on Medical Imaging*, 28(4):535–550, 2009.

T. Hosey, G. Williams, and R. Ansorge. Inference of multiple fiber orientations in high angular resolution diffusion imaging. *Magnetic Resonance in Medicine*, 54 (6):1480–1489, 2005.

B. Jeurissen, A. Leemans, J. D. Tournier, and J. Sijbers. Can residual bootstrap reliably estimate uncertainty in fiber orientation obtained by spherical deconvolution from diffusion-weighted MRI? In *Proceedings of the Organization for Human Brain Mapping*, volume 14, Melbourne, Australia, 2008a.

B. Jeurissen, A. Leemans, J. D. Tournier, and J. Sijbers. Estimation of uncertainty in constrained spherical deconvolution fiber orientations. In *Proceedings of the IEEE International Symposium on Biomedical Imaging: From nano to macro*, pages 907–910, Paris, France, 2008b.

B. Jeurissen, A. Leemans, J. D. Tournier, and J. Sijbers. Probabilistic Fiber Tracking using the Residual Bootstrap with Constrained Spherical Deconvolution MRI. In *Proceedings of the International Society for Magnetic Resonance in Medicine*, volume 17, page 1438, Honolulu, USA, 2009.

B. Jeurissen, A. Leemans, D. K. Jones, J. D. Tournier, and J. Sijbers. Probabilistic fiber tracking using the residual bootstrap with constrained spherical deconvolution. *Human Brain Mapping*, 32:461–479, 2011.

D. K. Jones. Tractography gone wild: probabilistic fibre tracking using the wild bootstrap with diffusion tensor MRI. *IEEE Transactions on Medical Imaging*, 27(9):1268–1274, 2008.

D. K. Jones and C. Pierpaoli. Confidence mapping in diffusion tensor magnetic resonance imaging tractography using a bootstrap approach. *Magnetic Resonance in Medicine*, 53(5):1143–1149, 2005.

D. K. Jones, M. A. Horsfield, and A. Simmons. Optimal strategies for measuring diffusion in anisotropic systems by magnetic resonance imaging. *Magnetic Resonance in Medicine*, 42(3):515–525, 1999.

M. Lazar and A. L. Alexander. White matter tractography using random vector (RAVE) perturbation. In *Proceedings of the International Society for Magnetic Resonance in Medicine*, volume 10, page 539, Honolulu, USA, 2002.

M. Lazar and A. L. Alexander. An error analysis of white matter tractography methods: synthetic diffusion tensor field simulations. *NeuroImage*, 20(2):1140–1153, 2003.

M. Lazar and A. L. Alexander. Bootstrap white matter tractography (BOOT-TRAC). *NeuroImage*, 24(2):524–532, 2005.

A. Leemans and D. K. Jones. The B-matrix must be rotated when correcting for subject motion in DTI data. *Magnetic Resonance in Medicine*, 61(6):1336–1349, 2009.

A. Leemans, J. Sijbers, M. Verhoye, A. Van der Linden, and D. Van Dyck. Mathematical framework for simulating diffusion tensor MR neural fiber bundles. *Magnetic Resonance in Medicine*, 53(4):944–953, 2005.

A. Leemans, **B. Jeurissen**, J. Sijbers, and D. K. Jones. ExploreDTI: a graphical toolbox for processing, analyzing, and visualizing diffusion MR data. In *Proceedings of the International Society for Magnetic Resonance in Medicine*, volume 17, page 3537, Honolulu, USA, 2009.

R. L. O'Gorman and D. K. Jones. Just how much data need to be collected for reliable bootstrap DT-MRI? *Magnetic Resonance in Medicine*, 56(4):884–890, 2006.

S. Pajevic and P. J. Basser. Parametric and non-parametric statistical analysis of DT-MRI data. *Journal of Magnetic Resonance*, 161(1):1–14, 2003.

G. J. M. Parker, H. A. Haroon, and C. A. M. Wheeler-Kingshott. A framework for a streamline-based probabilistic index of connectivity (PICo) using a structural interpretation of MRI diffusion measurements. *Journal of Magnetic Resonance Imaging*, 18(2):242–254, 2003.

M. Perrin, C. Poupon, Y. Cointepas, B. Rieul, N. Golestani, C. Pallier, D. Riviere, A. Constantinesco, D. Le Bihan, and J. F. Mangin. Fiber tracking in q-ball fields using regularized particle trajectories. In *Proceedings of the International Conference on Information Processing in Medical Imaging*, pages 52–63, Glenwood Springs, Colorado, USA, 2005. Springer.

P. Savadjiev, J. S. W. Campbell, M. Descoteaux, R. Deriche, G. B. Pike, and K. Siddiqi. Labeling of ambiguous subvoxel fibre bundle configurations in high angular resolution diffusion MRI. *NeuroImage*, 41(1):58–68, 2008.

K. K. Seunarine, P. A. Cook, M. G. Hall, K. V. Embleton, G. J. M. Parker, and D. C. Alexander. Exploiting peak anisotropy for tracking through complex structures. In *Proceedings of the International Conference on Computer Vision*, pages 1–8, Rio De Janeiro, Brazil, 2007.

J. D. Tournier, F. Calamante, D. G. Gadian, and A. Connelly. Probabilistic fibre tracking through regions containing crossing fibres. In *Proceedings of the International Society for Magnetic Resonance In Medicine*, volume 13, page 1343, Miami, USA, 2005.

J. D. Tournier, C. H. Yeh, F. Calamante, K. H. Cho, A. Connelly, and C. P. Lin. Resolving crossing fibres using constrained spherical deconvolution: validation using diffusion-weighted imaging phantom data. *NeuroImage*, 42(2):617–625, 2008.

J. D. Tournier, F. Calamante, and A. Connelly. How many diffusion gradient directions are required for HARDI? In *Proceedings of the International Society for Magnetic Resonance In Medicine*, volume 17, page 358, Honolulu, USA, 2009.

B. Whitcher, D. S. Tuch, J. J. Wisco, A. G. Sorensen, and L. Wang. Using the wild bootstrap to quantify uncertainty in diffusion tensor imaging. *Human Brain Mapping*, 29(3):346–362, 2007.

7

Investigating the prevalence of complex fiber configurations

Contents

The work in this chapter has been published as:

- **B. Jeurissen**, A. Leemans, D. K. Jones, J. D. Tournier, and J. Sijbers. Counting the number of fiber orientations in diffusion MRI voxels using constrained spherical deconvolution. In *Proceedings of the ISMRM Benelux Chapter*, volume 2, page 18, Utrecht, The Netherlands, 2010a

- **B. Jeurissen**, A. Leemans, D. K. Jones, J. D. Tournier, and J. Sijbers. Estimating the number of fiber orientations in diffusion MRI voxels: a constrained spherical deconvolution study. In *Proceedings of the International Society for Magnetic Resonance in Medicine*, volume 18, page 573, Stockholm, Sweden, 2010b

- **B. Jeurissen**, A. Leemans, J. D. Tournier, D. K. Jones, and J. Sijbers. Assessing the implications of complex fiber configurations for DTI metrics in real data sets. In *Proceedings of the International Society for Magnetic Resonance in Medicine*, volume 20, Melbourne, Australia, 2012

- **B. Jeurissen**, A. Leemans, J. D. Tournier, D. K. Jones, and J. Sijbers. Investigating the prevalence of complex fiber configurations. *Human Brain Mapping*, in press

7.1 Introduction

Diffusion-weighted (DW) MRI is a unique non-invasive method for probing tissue microstructure *in vivo*, based on the random thermal motion of water molecules [Stejskal and Tanner, 1965]. Currently, it is amongst the most popular imaging techniques for assessing brain tissue microstructure, particularly in white matter (WM) [Assaf and Pasternak, 2008]. Within the WM, fiber orientations can be extracted from the DW signal, opening up new avenues for investigating brain connectivity *in vivo* using so called fiber tracking algorithms [Jones, 2008]. The ability to assess WM microstructure and pathways of the whole brain from *in vivo* scans raises possibilities for clinical applications and there has been a rapid increase in clinical studies using DW MRI derived indices [Mori and Zhang, 2006] and fiber tractography [Ciccarelli et al., 2008, Johansen-Berg and Behrens, 2006].

Currently, diffusion tensor imaging (DTI) is the established method for assessing WM microstructure and connectivity [Basser et al., 1994a,b, Mori and Van Zijl, 2002]. However, in voxels containing multiple fiber orientations, this model has been shown to be inadequate [Alexander et al., 2001, 2002, Frank, 2001, 2002, Tuch et al., 2002]. Such voxels occur frequently throughout the WM due to partial volume effects between adjacent tracts. This has important implications for DTI-based fiber tractography, as most WM tracts will traverse regions with multiple fiber orientations at some point along their path. In such regions, the orientation extracted from the diffusion tensor is unreliable and may cause false negatives, in which tracking terminates [Behrens et al., 2007, **Jeurissen** et al., 2011], or false positives, in which tracking switches to an unrelated adjacent tract [**Jeurissen** et al., 2011, Pierpaoli et al., 2001]. It also complicates the interpretation of DTI derived diffusion indices such as fractional anisotropy (FA), which are often suggested for use as surrogate markers of WM 'integrity' [Jones, 2010, Vos et al., 2011, 2012, Wheeler-Kingshott and Cercignani, 2009].

Remarkably, the question of what proportion of WM voxels is affected by crossing fibers remains to be addressed in a robust and satisfactory manner. With recent advances in high angular resolution diffusion imaging (HARDI) [Tuch et al., 2002], it is now possible to reliably extract fiber orientations in regions of increased complexity [Alexander, 2006, Tournier et al., 2011]. While a number of studies have attempted to classify voxels according to the complexity of the fiber arrangement, many do not report the proportion of affected voxels, and all of them are likely to seriously underestimate the extent of the problem, for a number of reasons outlined below. Early studies distinguished between voxels with isotropic, single-fiber, and multi-fiber characteristics based on the shape of the ADC profile, and have reported clustered and symmetric regions of increased complexity, supporting genuine effects consistent with anatomical knowledge [Frank, 2002, Alexander et al., 2002]. More recently, a Bayesian automatic relevance determination (ARD) method was proposed to infer the number of fiber orientations in a multi-compartment model [Behrens et al., 2007]; using 60 diffusion gradient orientations and a b-value of $b = 1000\,\mathrm{s/mm^2}$, the model evidence was sufficiently strong to support the presence of more than one fiber orientation in one third of the voxels with FA > 0.1. However, nowhere in the brain was the model evidence sufficiently strong to support the presence of more than two fiber orientations. In another study, Q-Ball imaging

(QBI) was used in conjunction with bootstrapping to estimate the probability of different numbers of fiber populations existing in different brain tissues [Haroon et al., 2009]. This study used 61 diffusion gradient orientations with a slightly higher b-value of $b = 1200\,\mathrm{s/mm^2}$. While the authors did not explicitly assess the number of voxels containing multiple fiber orientations, their results seem to indicate that only a small proportion of WM voxels are affected by partial volume effects and that clustered regions with a high probability of more than two fiber orientations cannot be found. These recent studies are likely to be grossly underpowered for estimating the proportion of crossing fiber voxels (a task that they were not specifically designed to do). On the other hand, there are suggestions in other recent publications that voxels with multiple fiber orientations are actually commonly encountered [Descoteaux et al., 2009, **Jeurissen** et al., 2011, Tournier et al., 2012]. It is clear therefore that a reliable estimate of the proportion of affected voxels remains to be provided.

Given the implications this might have for DTI-based tractography and the interpretation of DTI-derived diffusion indices, in this study we set out *specifically* to estimate the extent of the crossing fiber problem, as well as its likely impact on tensor-based analyses. For this purpose, we acquired large, high quality DW data sets (using a twice-refocused and cardiac-gated sequence) consisting of 720 DW images, roughly 12 times the amount of data that was used in previous studies, with a correspondingly much higher power to detect the effects of interest [Jones, 2004]. For each voxel, the fiber orientations and their respective volume fractions were extracted using two different, readily available approaches: constrained spherical deconvolution (CSD) [Tournier et al., 2007], and the bedpostx algorithm, which implements the ARD method mentioned previously [Behrens et al., 2007] and is distributed as part of the FSL [Woolrich et al., 2009]. In both cases, parameters of the reconstruction were tuned specifically to ensure reliable estimates given our particular acquisition parameters. Based on these data, we report the proportion of multi-fiber voxels detected within the WM, and their orientations. To assess the impact of these voxels on tensor-derived tractography analyses, we also report the angular error between the fiber orientations estimated using CSD and DTI. Finally, to assess the impact on the interpretation of tensor-derived scalar measures, we report the volume fraction of each voxel taken up by secondary or tertiary fiber orientations, whose presence would confound such measures.

7.2 Materials and methods

7.2.1 Overview

To estimate the impact of multi-fiber voxels on DTI, it is first necessary to obtain robust estimates of the fiber orientations and their respective volume fractions within each WM voxel. To achieve this requires both high quality DW data, and robust fiber orientation estimation strategies. To this end, our approach involved: the acquisition of very high quality *in vivo* data sets; extensive simulations to select optimal reconstruction parameters tuned *specifically* for these data sets; and the application of the resulting optimized reconstruction algorithms to the *in vivo* data sets. These steps are described in detail in the following sections. We first provide a

brief overview of both fiber estimation methods, to emphasize which reconstruction parameters needed to be tuned for this study.

7.2.2 Fiber orientation estimation using CSD

The procedure used to estimate fiber orientations using CSD [Tournier et al., 2007] involved first deconvolving the single-fiber 'response function' (described below) from the DW signal to obtain the fiber orientation distribution function (fODF), with maximum harmonic degree $l_{\max} = 8$ [Tournier et al., 2007], followed by a peak-finding procedure to identify distinct orientations. Finally, fiber orientations were only considered if the amplitude of the corresponding peak in the fODF exceeded a threshold specifically tuned for this study (see below for details). An example of this procedure for a voxel with three fiber orientations is shown in Fig. 7.1.

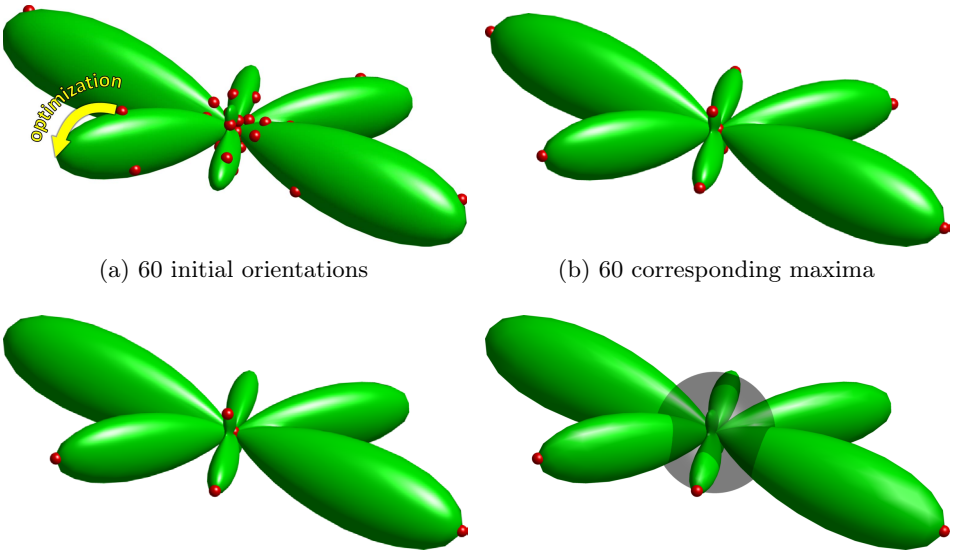

(a) 60 initial orientations

(b) 60 corresponding maxima

(c) 7 *unique* maxima

(d) 3 unique maxima > threshold

Fig. 7.1: Extraction of the CSD fODF fiber orientations: 3 orientation example. (a): points uniformly distributed on the half-sphere (red dots) used as starting points for the maximization of the fODF amplitude (green); (b): the corresponding fODF maxima (note that many overlap); (c): the unique fODF maxima (note that 3 of the spurious maxima have very low amplitude and are clustered near the origin); (d): fODF maxima with amplitude higher than fODF threshold (gray sphere).

The single-fiber response function corresponds to the DW signal that would be expected for an ideal fiber population aligned along the z-axis, and was estimated from the data themselves using a previously published approach [Tournier et al., 2004, 2007]. In brief, WM voxels with FA > 0.7 were identified, and in each of these voxels, the DW signal was reoriented such that the orientation of the major eigenvector of the diffusion tensor was aligned with the z-axis. The spherical

harmonic (SH) decompositions of all the resulting profiles were then averaged to provide a robust estimate of the true response function. To constrain the response function to an axially symmetric function, only SH coefficients with order $m = 0$ were estimated [Tournier et al., 2004].

The peak-finding procedure consisted of a Newton optimization algorithm, started from a dense set of equally distributed spherical sample points to find the local maxima of the fODF (duplicate local maxima were excluded). The number of unique peak fODF orientations with amplitude above threshold was counted and assumed to be equal to the number of fiber orientations. In this study, voxels containing more than 3 orientations will be reported as containing $\geq$3 orientations.

7.2.3 Fiber orientation estimation using bedpostx

The procedure used to estimate fiber orientations using ARD was performed using the FSL tool *bedpostx* [Behrens et al., 2007], which we describe briefly here. Bedpostx uses a Bayesian framework to estimate local probability density functions on the parameters of a multi-compartment model. Using ARD, the method performs online selection of the number of fiber orientations supported by the data at each voxel by forcing the fiber volume fractions to take the value zero if, and only if, there is no evidence in the data for their existence [Behrens et al., 2007]. The maximum number of fiber orientations allowed in the multi-compartment model was set to 3. To extract the number of fiber orientations in each voxel, we thresholded the volume fractions at 0.05, as in Behrens et al. [2007].

Bedpostx uses a Monte Carlo Markov Chain algorithm to infer on the parameters of the model. In this study, we used a modified burn-in period of 10000 iterations, as the default value of 1000 was found to be insufficient to ensure convergence of the Markov chains in a significant proportion of runs [Miller et al., 2011, O'Muircheartaigh et al., 2011].

7.2.4 Data acquisition and preprocessing

Both DW and T_1-weighted images were acquired on a General Electric (Milwaukee, Wisconsin, USA) 3T HDx Signa system with an eight-channel receive-only head coil. The experiment was repeated on two different healthy adult volunteers. Both subjects gave written informed consent to participate in this study under a protocol approved by the Cardiff University School of Psychology Ethics Committee.

Each subject was scanned 12 times using a twice-refocused spin echo EPI sequence with TE = 86 ms and $2.4 \times 2.4 \times 2.4\,\mathrm{mm}^3$ voxel size (FOV = $23 \times 23\,\mathrm{cm}^2$, 96×96 acquisition matrix, NEX = 1, partial Fourier encoding with 16 overscans, 60 axially acquired slices with 2.4 mm thickness with no gap, ASSET factor = 2). Diffusion gradients were applied in 60 directions uniformly distributed on a sphere through electrostatic repulsion with $b = 1200\,\mathrm{s/mm}^2$ [Jones et al., 1999]. For each scan, 6 images with $b = 0\,\mathrm{s/mm}^2$ were also acquired. To avoid pulsation artifacts, cardiac gating was applied using a peripheral pulse oximeter with an effective TR = 20 R-R intervals. Signal-to-Noise Ratio (SNR) within all WM voxels of the $b = 0\,\mathrm{s/mm}^2$ images was on average 24.9 with a standard deviation of 6.1 [Dietrich et al., 2007]. In addition, each subject was scanned with a 3D fast spoiled

gradient echo sequence with TR/TE = 7.9/3.0 ms and $1 \times 1 \times 1\,\mathrm{mm}^3$ voxel size (FOV = $256 \times 256 \times 176\,\mathrm{mm}^3$, $256 \times 256 \times 176$ acquisition matrix, TI = 450 ms, flip angle = 20°, NEX = 1) to produce an anatomical T_1-weighted image.

For each subject, all DW scans were concatenated (not averaged) into a single data set and corrected for subject motion and residual eddy-current induced geometric distortions with the required B-matrix adjustments [Leemans and Jones, 2009], resulting in a total of 720 diffusion weighted (DW) and 72 $b = 0\,\mathrm{s/mm}^2$ images per subject. The tensor model was fitted to the motion-corrected data using a constrained nonlinear regression method [Koay et al., 2006] and, subsequently, mean diffusivity (MD) and fractional anisotropy (FA) were calculated from the tensor's eigenvalues. Glyph visualization was done with *ExploreDTI* [Leemans et al., 2009].

7.2.5 Optimization of reconstruction parameters

While the SNR dependencies of both CSD and bedpostx have previously been studied in great detail [Tournier et al., 2007, 2008, Behrens et al., 2007], in this study, additional experiments were performed to select optimal reconstruction parameters tuned specifically for the data sets used in this study. For this purpose, extensive simulations were performed using parameters measured from the real data themselves, to determine the most suitable reconstruction parameters to use for each method, and hence ensure optimal detection of fiber orientations given our particular acquisition parameters.

These simulations were performed as follows. First, noise-free DW data were generated for voxels assumed to contain a number (1, 2 or 3) of fiber orientations, by combining DW signals generated assuming axially symmetric diffusion tensor profiles for each fiber population [Leemans et al., 2005], with inter-fiber angles ranging from 90° to 10°. The eigenvalues of the constituent tensors were set to $[1.7\ 0.3\ 0.3] \times 10^{-3}\mathrm{mm}^2/\mathrm{s}$, corresponding to the average values found in the midsagittal area of the splenium of the corpus callosum in the real data sets. The same gradient directions and b-value were used as in the real data acquisition. Next, Rician noise was added using SNR = 15, corresponding to the lower end of the range of SNR values measured in the real data sets, and the number of fiber orientations was estimated from the resulting noisy simulated data using both CSD and bedpostx. This procedure was repeated for 1000 Rician noise instances.

For both CSD and bedpostx, outcome was measured as the proportion of false positives, defined as any simulated run where the number of estimated fiber orientations was greater than the actual number simulated. For CSD, the reconstruction parameter of interest was the threshold on the fODF peak amplitude, used to identify distinct orientations (see earlier). For bedpostx, the reconstruction parameter of interest was the ARD weight, with higher weights resulting in fewer secondary fibers per voxel. For both methods, the smallest reconstruction parameter that resulted in *zero* false positives was used for the analysis of the *in vivo* data. The minimum resolvable angle of both methods (i.e., the inter-fiber angle at which the correct number of fiber orientations can still be reliably estimated) was also assessed using these simulations for a range of volume fractions.

7.2.6 In vivo estimation of fiber orientations

To estimate the fiber orientations and their respective volume fractions over all WM voxels, both CSD and bedpostx methods were applied to the real data sets of both subjects, using the procedures described in the previous corresponding sections, and the conservative reconstruction parameters specifically tuned in the simulations above. To avoid partial volume effects with isotropic compartments, such as gray matter (GM) and cerebrospinal fluid (CSF), the analysis was restricted to voxels within a pure WM mask, derived from the T_1-weighted images. The T_1-derived WM mask was generated as follows. First, a tissue probability map was estimated from the T_1-weighted image (Fig. 7.2a) using the unified segmentation tool from SPM [Ashburner and Friston, 2005] (Fig. 7.2b). Next, the T_1-weighted image was registered to the FA image using 3D non-rigid b-spline based registration with Mattes mutual information as the similarity measure [Mattes et al., 2001, Klein et al., 2010] (Fig. 7.2d). The derived transform was then used to warp the WM probability map from the T_1-weighted image to the diffusion images, allowing easy identification of WM voxels inside the DW volume. To restrict the study to pure WM voxels only, a binary WM mask was created by selecting all voxels with WM probability higher than 95% (Fig. 7.2c). Finally, a small number of voxels at the edges of the WM mask were removed, since they were found to contain high MD values resulting from partial voluming with CSF (as indicated by the red voxels in Fig. 7.2c). These outliers were identified using the criterion $\mathrm{MD} > \mathrm{median}(\mathrm{MD}) + 1.5 \times \mathrm{IQR}(\mathrm{MD})$ (where IQR is the inter-quartile range over the whole mask).

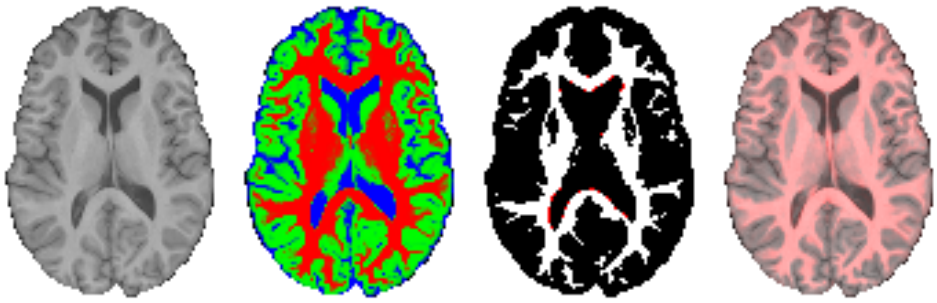

(a) (b) (c) (d)

Fig. 7.2: Computation of the WM mask: T_1-weighted image (a) and the corresponding WM/GM/CSF segmentation (b). WM probability is colored red, GM probability green and CSF probability blue. The WM probability map is thresholded at 95% to create a binary WM map (c). MD outliers resulting from partial volume effect at the interface between WM and CSF are colored red. Co-registered T_1-weighted image (gray) overlayed with FA image (pink) (d).

In addition, the reproducibility of the CSD reconstruction was assessed using a residual bootstrap approach, described previously [**Jeurissen** et al., 2011]. 1000 residual bootstrap realizations of the entire data set were generated, using a spherical

harmonics model with maximum harmonic degree $l_{\max} = 8$ [**Jeurissen** et al., 2011]. Unfortunately, it was not possible to perform the equivalent experiments for bedpostx due to its prohibitively long processing times.

To further illustrate the 'global' consistency of the multi-fiber voxels, a fiber tractography technique was used, based on the CSD fODF maxima [**Jeurissen** et al., 2009, 2011, Fillard et al., 2011]. The step size was set to 0.2 mm. Tracking was terminated when the extracted fODF orientation amplitude dropped below the same threshold that was used for the fiber orientation extraction, or when the angle between two successive steps exceeded 10°. A seed ROI was placed in a region with more than 2 fiber orientations. Tract visualization was performed with the *ExploreDTI* diffusion MRI toolbox [Leemans et al., 2009].

The effect of using different values for the threshold on the fODF amplitude (for CSD) and the partial volume fractions (for bedpostx) was also investigated. This was done by plotting the proportion of WM voxels estimated as containing 1, 2 or $\geq$3 fiber orientations as a function of these thresholds. Finally, both fiber orientation estimation methods are limited by their minimum detectable crossing angle; the angle at which fibers cross will therefore have an impact on the results. This issue was examined by plotting a histogram of the inter-fiber angle over all voxels.

7.2.7 Assessment of impact on DTI

To assess the practical impact of these findings for tractography or anisotropy analyses, two further analyses were performed. Tractography analyses will obviously be affected by errors in the estimated fiber orientations. Therefore, the angle between the fiber orientations estimated by the primary eigenvector of the diffusion tensor, and the nearest peak to this direction in the CSD fODF was measured in each voxel, and displayed both as a map and as a histogram over all WM voxels. For anisotropy analyses, issues will arise if fibers with secondary or tertiary orientations take up a substantial volume fraction of the voxel. Therefore, the ratio of the volume fractions of the non-dominant versus all fiber orientations were estimated in each WM voxel, and displayed both as a map, and using histograms.

7.3 Results

7.3.1 Optimization of reconstruction parameters

Fig. 7.3 demonstrates the need for an appropriate fODF threshold (for CSD) or ARD weight (for bedpostx) to remove spurious fiber orientations from the results. For CSD, the number of false positives dropped rapidly with increasing fODF threshold, and was already below 1 in 1000 with a threshold of 0.02. However, for false positives to be completely removed, a threshold of 0.1 was required. For bedpostx, the number of false positives dropped with increasing ARD weight, and reached zero at a weight value of 10. These values (0.1 for the CSD fODF threshold, 10 for the ARD weight) were therefore used for all subsequent analyses, including the *in vivo* data analyses, unless otherwise stated.

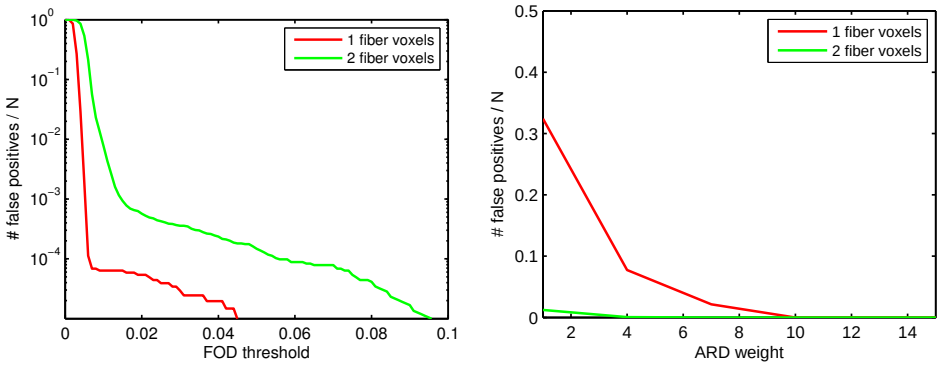

(a) CSD (b) bedpostx

Fig. 7.3: Multi-fiber simulations (specificity): The relative number of false positives as a function of the CSD fODF threshold (a) and the bedpostx ARD weight (b) for 1-fiber (red curve) and 2-fiber (green curve) voxels.

The sensitivity of both methods with respect to volume fraction and inter-fiber angle is shown in Fig. 7.4. As the inter-fiber angle dropped below approximately 60°, CSD fODF peaks started to merge to form a single peak, with merging occurring in almost all cases at an inter-fiber angle of approximately 45°; these would hence no longer be counted as separate fiber orientations (Fig. 7.4a,c). On the other hand, bedpostx was unable to consistently report three fiber orientations when three fiber orientations were simulated, reporting 1 or 2 fiber orientations instead (Fig. 7.4d), in agreement with earlier simulations performed in Behrens et al. [2007]. For the 2 fiber simulations (Fig. 7.4b), bedpostx performed similarly to CSD, although it failed to recover fibers with small volume fractions that could still be reliably detected using CSD. Note that while it is in theory possible to boost the minimum resolvable angle of bedpost using a smaller ARD weight, this would result in an increased number of false positives (Fig. 7.3b).

7.3.2 In vivo estimation of fiber orientations

When applied to the *in vivo* data, both methods performed as predicted by the simulations. In voxels where CSD reports 1 or 2 fiber orientations, bedpostx usually reports the same number of fiber orientations, and the orientations are almost identical (Fig. 7.5), consistent with our simulation results (Fig. 7.4). In voxels where CSD reports $\geq$3 fiber orientations, bedpostx reports only 1 or 2 fiber orientations, again in agreement with the simulation results. Note that while these orientations constitute a subset of the orientations estimated using CSD in most voxels, in some cases they are not consistent with those estimated using CSD. Note also that in voxels with 3 fiber orientations, the CSD orientations are very coherent, showing continuous transitions with the surrounding orientations, even those corresponding to small fODF amplitudes (Fig. 7.5b).

The maps of the number of fiber populations detected (Fig. 7.6), and of their

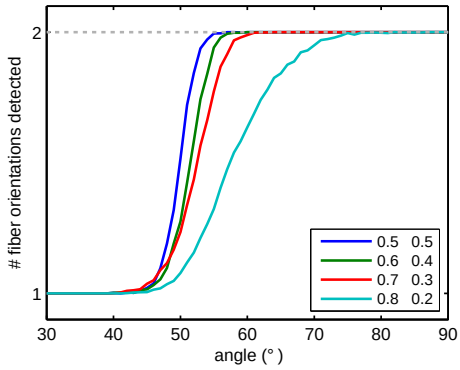

(a) 2-fiber voxels: CSD

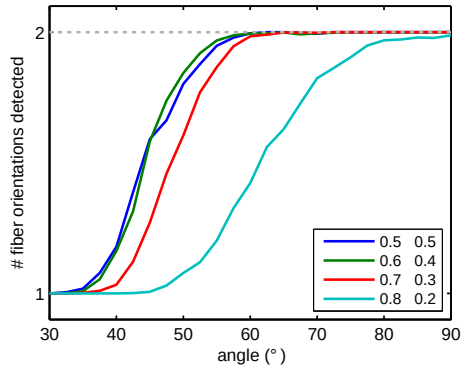

(b) 2-fiber voxels: bedpostx

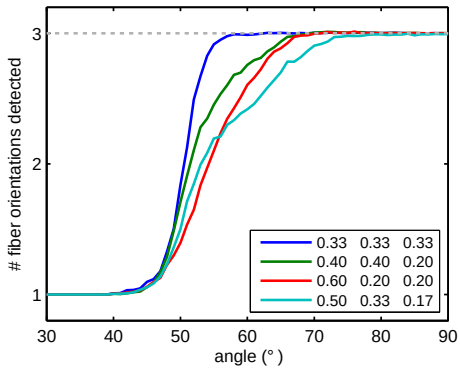

(c) 3-fiber voxels: CSD

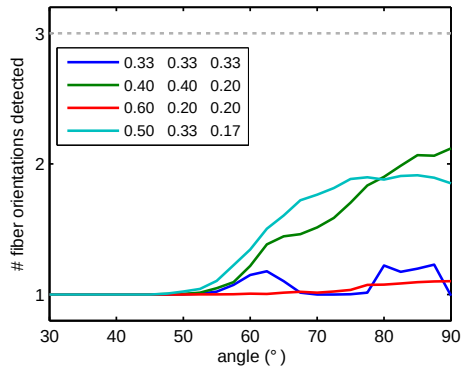

(d) 3-fiber voxels: bedpostx

Fig. 7.4: Multi-fiber simulations (minimum resolvable angle): The average number of detected fiber orientations in 2-fiber and 3-fiber voxels as a function of angle. The different colors represent the different weights of the constituent DWI signals.

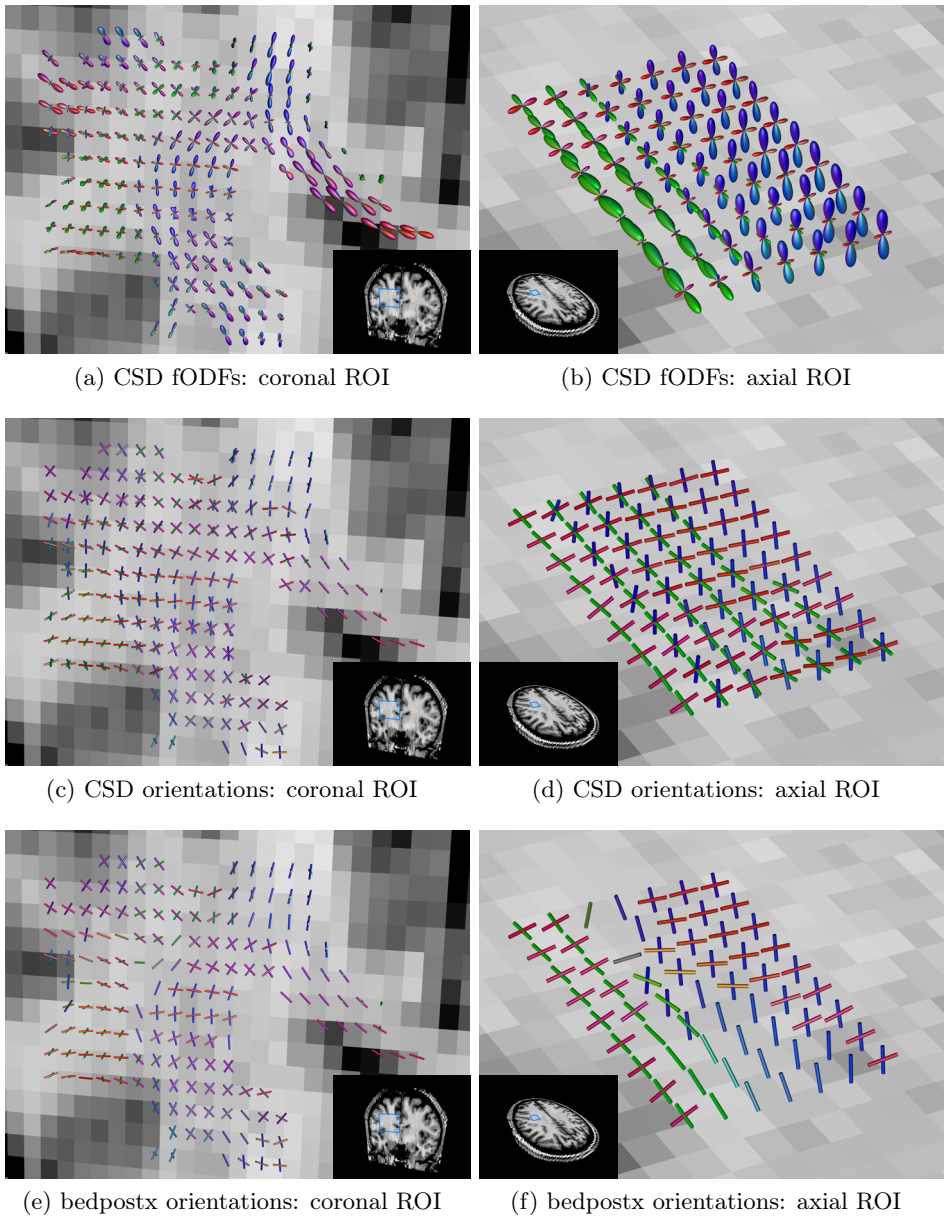

(a) CSD fODFs: coronal ROI

(b) CSD fODFs: axial ROI

(c) CSD orientations: coronal ROI

(d) CSD orientations: axial ROI

(e) bedpostx orientations: coronal ROI

(f) bedpostx orientations: axial ROI

Fig. 7.5: Examples of the extracted fiber orientations in two regions containing crossing fibers. The CSD fODFs and the extracted fiber orientations are shown in (a)-(b) and (c)-(d), respectively. The bedpostx fiber orientations are shown in (e)-(f).

respective orientations (Figs. 7.7 and 7.8) both show a high degree of structural coherence and symmetry, supporting genuine anatomical features. Note that these figures correspond to the results for subject 1 only; the results for subject 2 are broadly equivalent. Large, bilaterally symmetrical clusters of single fiber voxels (colored in red) are found mainly in the largest bundles such as parts of the corpus callosum (CC, arrow 1), middle cerebellar peduncle (arrow 2), and the posterior limb of the internal capsule (arrow 3). Large clusters of voxels containing 2 orientations are also present, again symmetrically distributed throughout the brain. Examples of regions containing 2 fiber orientations (colored in green) include: the mixture of transverse pontine (oriented left-right) and motor (oriented inferior-superior) fibers (arrow 4); and the mixture of fibers from the superior longitudinal fasciculus (SLF) (oriented anterior-posterior) and corona radiata (oriented inferior-superior) (arrow 5). Large clusters of voxels with $\geq$3 fiber populations (colored in blue) can also be found in the CSD results, for example in the regions where fibers from the corona radiata (inferior-superior), SLF (anterior-posterior) and CC (left-right) interdigitate (arrow 6). In contrast, no consistent areas containing $\geq$3 orientations were observed in the bedpostx results: in those regions where CSD identified $\geq$3 orientations, bedpostx reported only 1 or 2 orientations, consistent with the simulation results (Fig. 7.4).

Table 7.1 summarizes the incidence of 1, 2 and $\geq$3 fiber orientations in all WM voxels. Using CSD, these were estimated to be approximately 9%, 46% and 45% respectively; two or more fiber orientations were found in approximately 90% of all WM voxels. Using bedpostx, these were estimated to be approximately 37%, 62% and 1% respectively; in this case, complex fiber configurations were observed in approximately 63% of all WM voxels.

# orientations		1	2	≥ 3	≥ 2
CSD	subject 1	9.5%	47.1%	43.3%	90.5%
	subject 2	8.4%	45.0%	46.6%	91.6%
bedpostx	subject 1	36.1%	62.9%	0.9%	64.0%
	subject 2	37.5%	61.9%	0.4%	62.3%
Behrens et al. [2007]		$\sim$ 67.7%	$\sim$ 33.3%	0%	$\sim$ 33.3%

Table 7.1: Percentages of single- and multi-fiber voxels throughout the WM for CSD and bedpostx and for different subjects. For reference, we also included the estimates previously reported in Behrens et al. [2007].

Fig. 7.9 shows the fiber orientations extracted using CSD from the individual bootstrap realizations in the crossing fiber region depicted in Fig. 7.5b. To aid visibility, only 30 residual bootstrap realizations were plotted. Notice that the orientations are very clustered, indicating that the same fiber orientations are recovered consistently over bootstrap realizations, even in three-fiber voxels.

Fig. 7.10 shows the CSD fiber tracking results when seeding in a three fiber region. Notice how the locally-extracted fiber orientations are globally consistent

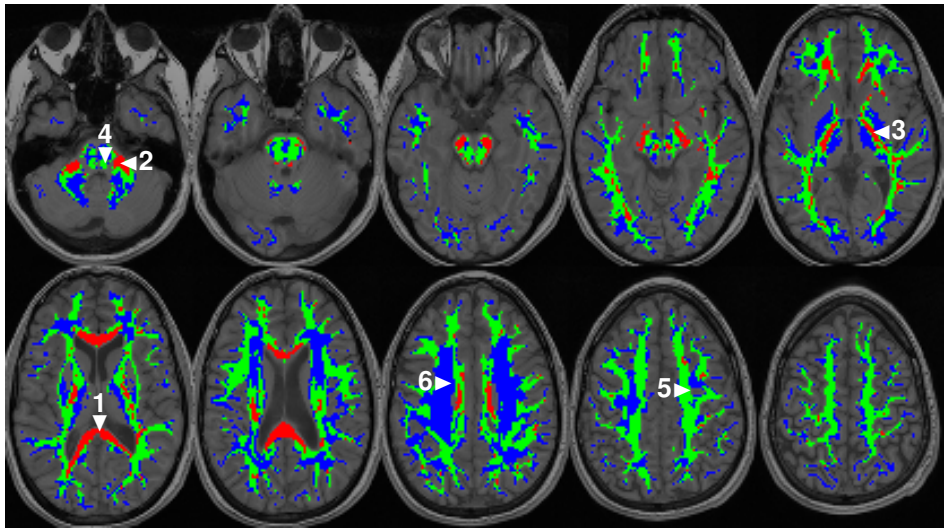

(a) CSD

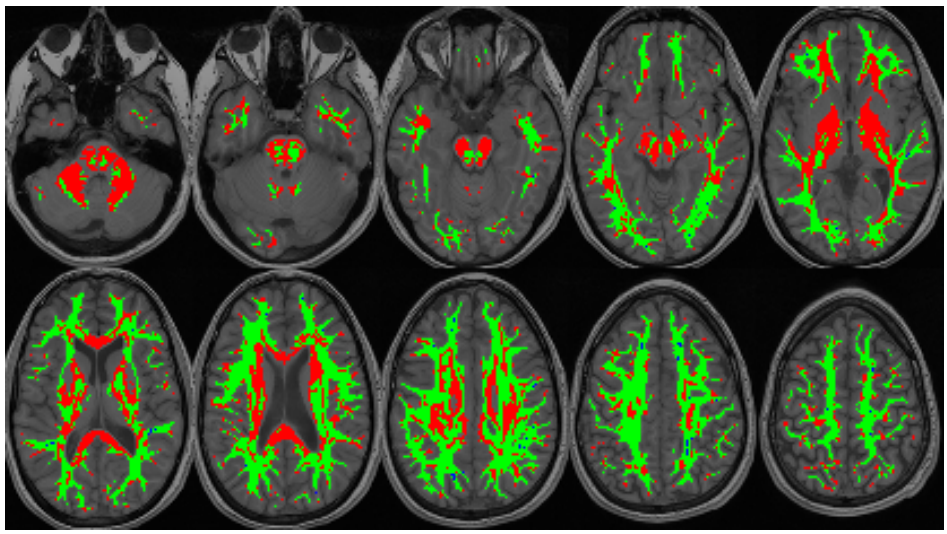

(b) bedpostx

Fig. 7.6: Number of fiber orientations per voxel (red: 1; green: 2; blue: $\geq$3) for subject 1 estimated with CSD (a) and bedpostx (b). The numbered arrows in (a) correspond to the following structures: 1: corpus callosum (CC); 2: middle cerebellar peduncle; 3: posterior limb of the internal capsule; 4: pons/motor pathways; 5: superior longitudinal fasciculus (SLF)/corona radiata; 6: corona radiata/SLF/CC.

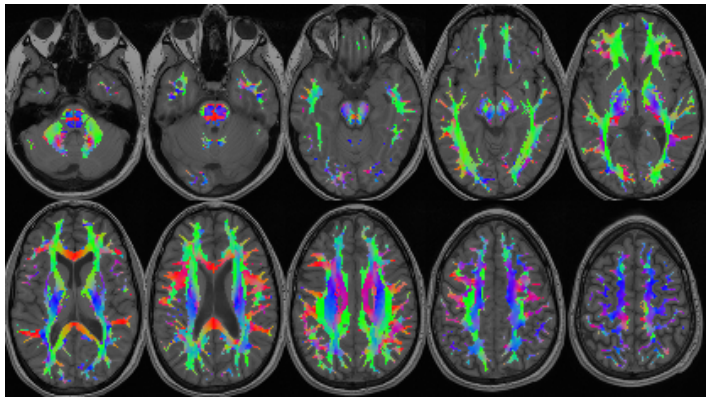

(a) primary fiber orientation

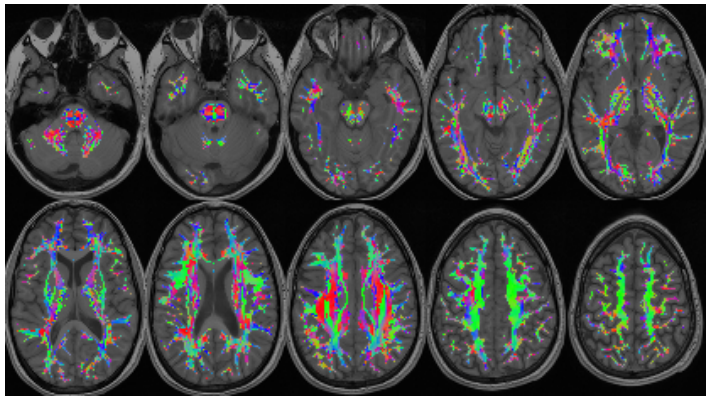

(b) secondary fiber orientation

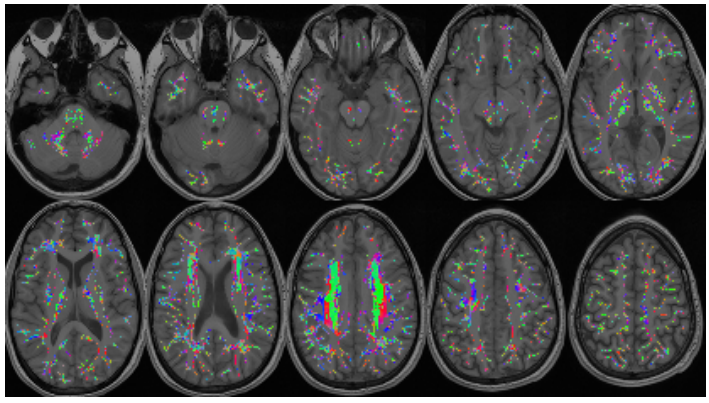

(c) tertiary fiber orientation

Fig. 7.7: The primary (a), secondary (b) and tertiary (c) fiber orientations (in order of decreasing fODF amplitude) extracted for subject 1 with CSD, shown as RGB color maps (red: left-right, green: anterior-posterior, blue: inferior-superior).

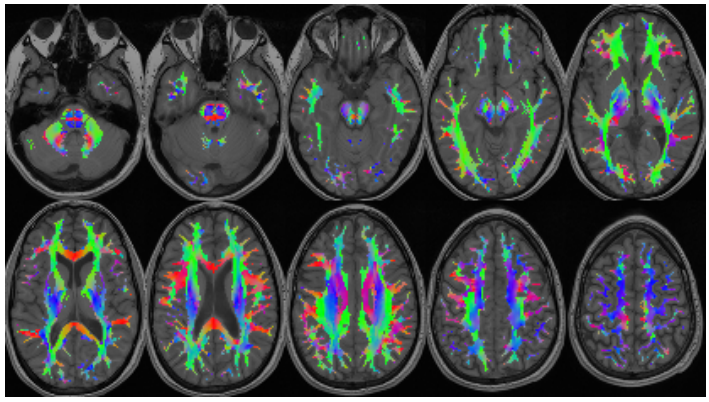

(a) primary fiber orientation

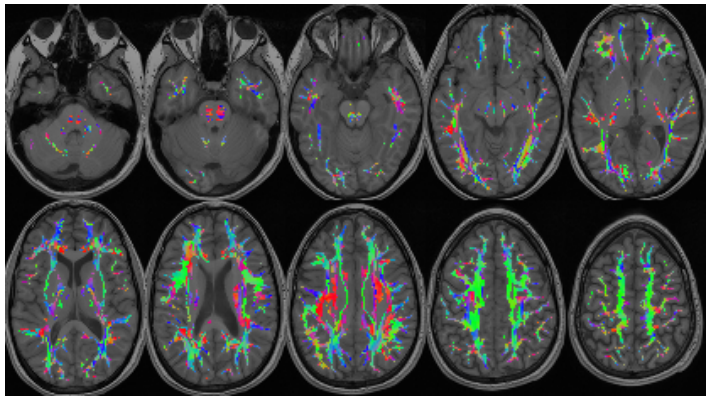

(b) secondary fiber orientation

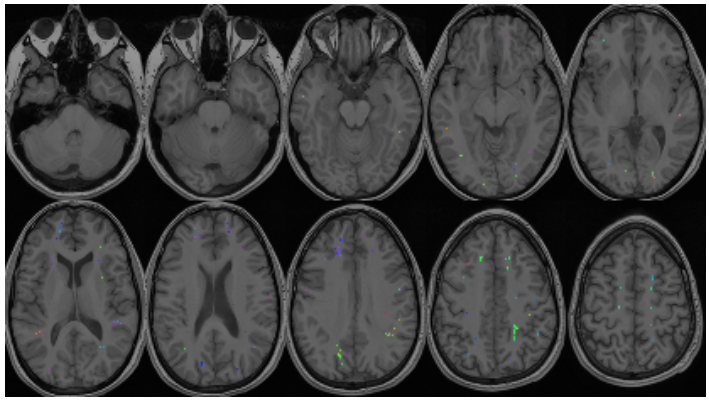

(c) tertiary fiber orientation

Fig. 7.8: The primary (a), secondary (b) and tertiary (c) fiber orientations (in order of decreasing volume fraction) extracted for subject 1 with bedpostx, shown as RGB color maps (red: left-right, green: anterior-posterior, blue: inferior-superior).

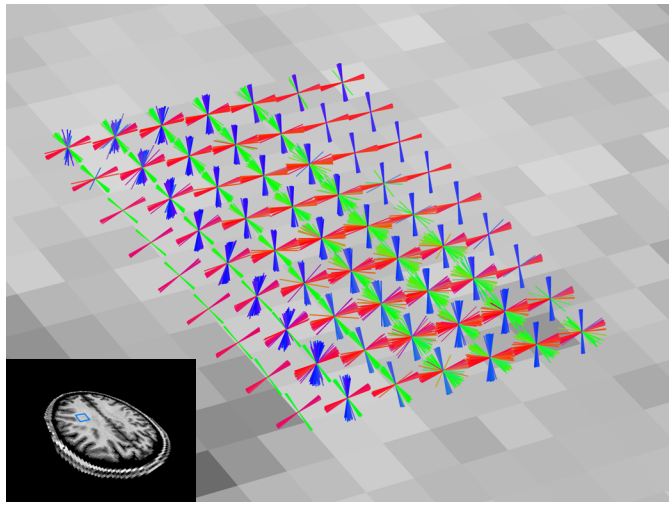

Fig. 7.9: Consistency of the orientations across residual bootstrap realizations, for the same region as Fig. 7.5d. To aid visualization, only 30 realizations are shown.

and result in anatomically plausible fiber bundles. Commissural fibers from the CC are shown in red, association fibers form the arcuate fasciculus are colored green and projection fibers from the corticospinal tract are shown in blue.

Using the residual bootstrap approach we were also able to estimate the uncertainty in the percentages reported in Table I for the CSD case. The 95% confidence intervals for the percentage of 1, 2 and $\geq$3 fiber voxels were $\pm$0.3%, $\pm$0.5% and $\pm$0.7%, respectively, for subject 1, and $\pm$0.6%, $\pm$1.3% and $\pm$1.7%, respectively, for subject 2. These small confidence intervals demonstrate the reproducibility of our CSD results with these data sets.

The effect of the fODF threshold (for CSD) or the partial volume threshold (for bedpostx) is shown in Fig. 7.11. As expected, an increase in the thresholds results in a reduction of the proportion of multi-fiber voxels for both approaches. For bedpostx, the results are relatively stable for partial volume thresholds between approximately 0.01 and 0.1 (the actual value used was 0.05). By contrast, the CSD results do not show a region that is stable with respect to the fODF threshold. Initially, the proportion of $\geq$3 fiber voxels reduces while the proportion of 2 fiber voxels increases, as would be expected. At an fODF threshold of approximately 0.2, the proportion of both 2 and $\geq$3 fiber voxels reduces while that of single fiber voxels increases. Importantly, even with a doubling of the fODF threshold to a value of 0.2 (actual value used was 0.1), the proportion of multi-fiber voxels is still very high at approximately 78%.

The performance of both methods with respect to inter-fiber angle can be appreciated from the histograms shown in Fig. 7.12. With CSD, a much higher number of 90° crossings was detected, presumably due to its better performance in 3-fiber cases, as previously shown in Figs. 7.4 and 7.5. CSD also detects a higher proportion of small inter-fiber angles, again in line with the simulation results in Fig. 7.4. In both cases, almost all inter-fiber angles detected are larger than

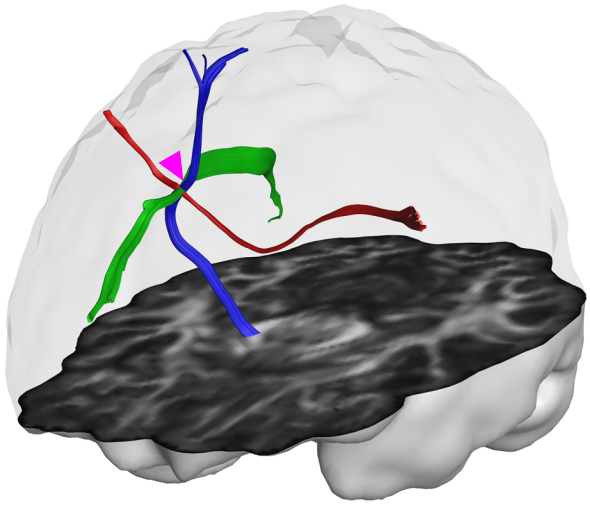

Fig. 7.10: Tractography in a 3-fiber region reveals global consistency of 3-fiber orientations. Seed region is indicated by a magenta arrowhead. Commissural fibers are colored red, association fibers green and projection fibers blue. All three pathways identified using CSD tracking are anatomically plausible.

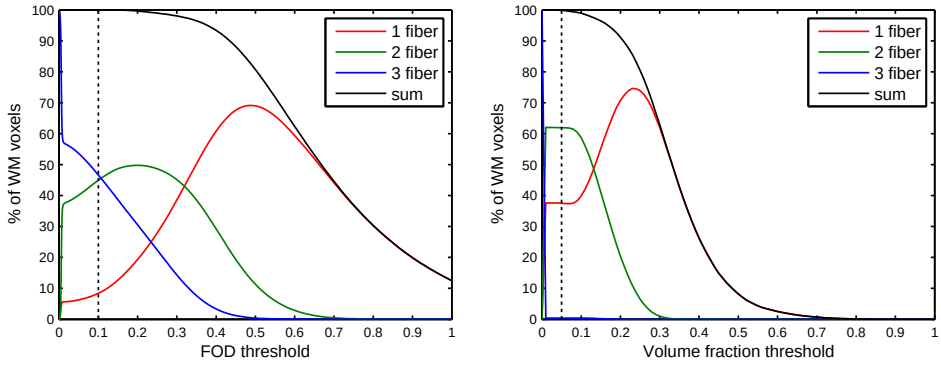

(a) CSD (b) bedpostx

Fig. 7.11: Percentages of single- and multi-fiber voxels throughout the WM for different CSD fODF thresholds (a)-(b) and bedpostx volume fraction thresholds (c)-(d). The actual threshold values used in this study are shown as a dashed line.

approximately 40°, the minimum angle that could be resolved by both methods in the simulations. It is likely that smaller crossing angles do exist in the data, but cannot be resolved with the methods used. Since these would be labeled as single-fiber voxels, it is likely that the present results underestimate both the extent and the impact of the problem.

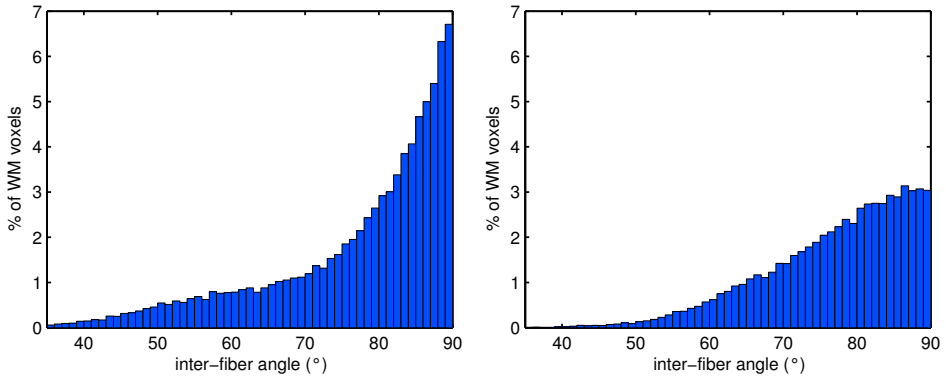

(a) CSD (b) bedpostx

Fig. 7.12: Histogram of the average inter-fiber angle for all voxels with ≥2 fiber populations for both CSD (a) and bedpostx (b).

7.3.3 Assessment of impact on DTI

The practical implications of these findings for tractography can be appreciated from Fig. 7.13. The fiber orientations estimated using the tensor model and the nearest CSD peak are consistent only in single fiber regions (e.g. CC). In multi-fiber regions, the average angular error is approximately 11°. In half of all WM voxels, the angular error is greater than 8° (Fig. 7.13b,c).

The practical impact of these findings for anisotropy analyses can be appreciated from Fig. 7.14. Most WM voxels contain contributions from non-dominant fiber orientations that would be sufficiently large to affect tensor-derived measures of anisotropy (as well as radial and axial diffusivities [Wheeler-Kingshott and Cercignani, 2009]). For example, assuming a non-dominant partial volume fraction greater than 25% is sufficient to influence anisotropy measures significantly, approximately 75% of all WM voxels would be affected (Fig. 7.14b,c). Conversely, it can be seen that half of all WM voxels contain more than 40% contamination from crossing fibers.

7.4 Discussion

The aim of this study was to provide a more accurate estimate of the extent and impact of the crossing fiber problem in DW-MRI. Using CSD, we observed multiple fiber orientations in approximately 90% of all WM voxels, a much higher proportion

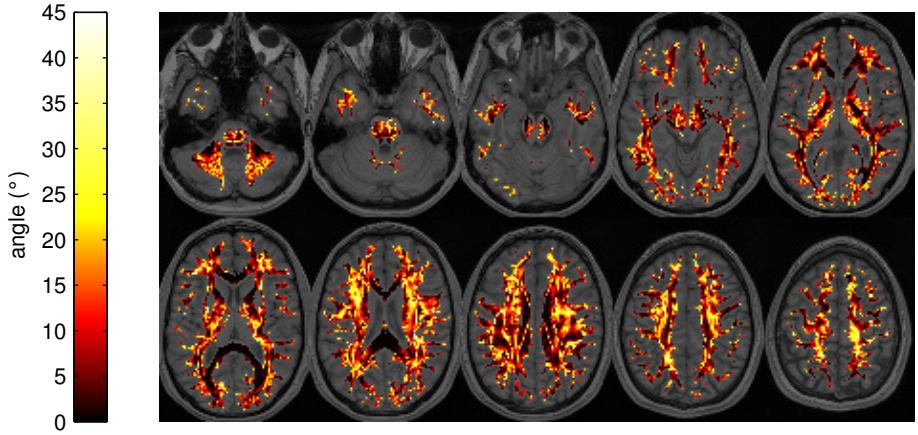

(a) Spatial distribution

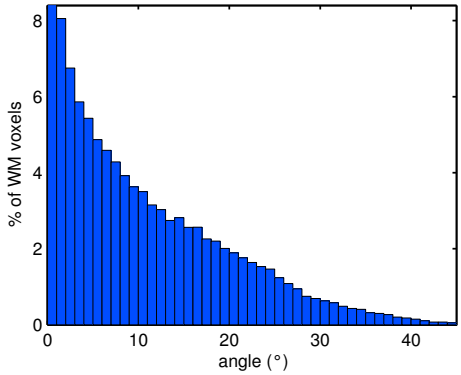

(b) Histogram

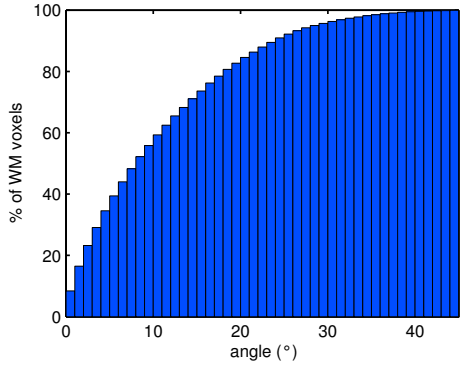

(c) Cumulative histogram

Fig. 7.13: The angle between the fiber orientation estimated by the primary eigenvector from DTI and the nearest CSD fiber orientation, (a) displayed overlaid on an anatomical reference image, (b) as a histogram over all WM voxels, and (c) as the corresponding cumulative histogram.

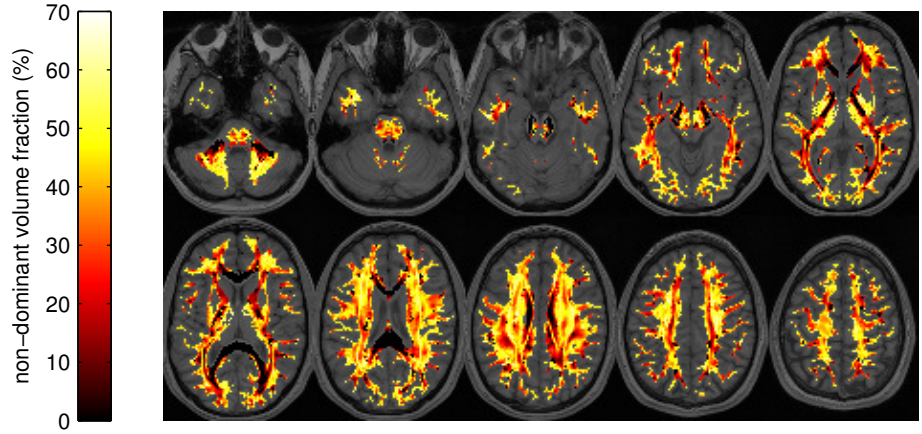

(a) Spatial distribution

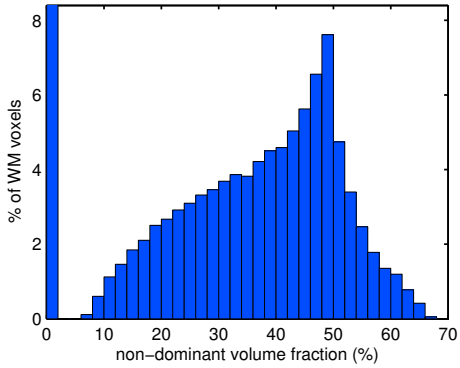

(b) Histogram

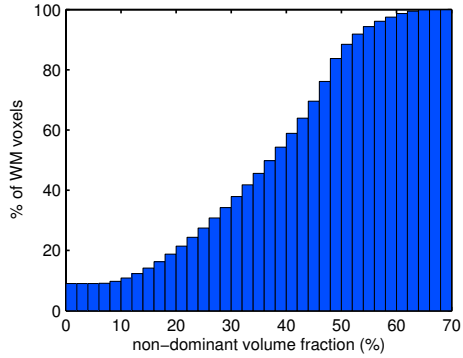

(c) Cumulative histogram

Fig. 7.14: The non-dominant volume fraction measured by CSD, (a) displayed overlaid on an anatomical reference image, (b) as a histogram over all WM voxels, and (c) as the corresponding cumulative histogram.

than previously reported. With bedpostx, multiple fiber orientations were detected in approximately 63% of all WM voxels, again a much higher proportion than the value of 33% previously reported using the same algorithm, as discussed below [Behrens et al., 2007].

7.4.1 Implications for DTI

The impact of these findings for diffusion tensor imaging is profound, particularly for tensor-based tractography, but also for tensor-derived scalar measures. It is widely acknowledged that the fiber orientation estimated using the primary eigenvector of the diffusion tensor will be erroneous in crossing fiber voxels, and that these errors will introduce some degree of corruption in the estimated WM pathways [Jones, 2010]. However, until now the proportion of WM voxels affected by crossing fiber effects was often assumed to be relatively small. Our results clearly indicate that this assumption is not valid. With such a high proportion of WM voxels containing multiple fiber orientations, it is very unlikely that any WM tract will remain entirely within single fiber voxels over its entire path. Indeed, as shown in Fig. 7.13, errors in the estimated fiber orientations are widespread throughout the WM: in over half the WM, these errors are larger than 8°. It follows that these errors will adversely and significantly affect the delineation of WM tracts, and lead to large numbers of both false positive and negative results as the tracking algorithm veers off-course, away from the true end-point of the WM tract (false negatives [Behrens et al., 2007, **Jeurissen** et al., 2011]), and/or into adjacent yet unrelated WM tracts (false positives [**Jeurissen** et al., 2011, Pierpaoli et al., 2001]). Moreover, it should be emphasized that these errors are provided with respect to the nearest fiber orientation; errors with respect to other fiber orientations that might be present will obviously be considerably greater.

In addition, it is well known that tensor-derived measures of so-called 'WM integrity', such as fractional anisotropy (FA), as well of other indices such as axial and radial diffusivity, all of which are currently widely used, become ambiguous in these regions [Wheeler-Kingshott and Cercignani, 2009, Jones and Cercignani, 2010]. In Pierpaoli et al. [2001], it was shown that Wallerian degeneration can lead to *increased* diffusion anisotropy in the rostral pons, where transverse pontine fibers are crossing the descending motor pathways. Wallerian degeneration of the motor pathways causes the transverse pontine fibers to become the dominant pathway and, paradoxically, the measured diffusion anisotropy can increase because fibers are now more coherently oriented within the voxel. In another study, choice reaction time of healthy volunteers was found to be *positively* correlated with FA [Tuch et al., 2005]. The myelin hypothesis would predict a negative correlation between reaction time and FA because increased myelin thickness would cause increased FA and faster nerve conduction velocity, which would in turn result in a shorter reaction time. However, in regions containing multiple fiber orientations, increased FA of an individual fiber population can result in a decrease in the overall FA. Although this observation could be explained by increased axonal diameters [Alexander et al., 2010], crossing-fiber effects offer a much more simple and likely explanation, especially given that crossing fibers can readily be observed in the region identified. In yet another study, *increased* diffusion anisotropy was

measured in the centrum semiovale of patients with mild cognitive impairment and mild Alzheimer's disease [Douaud et al., 2011]. This was explained by a relative preservation of motor-related projection fibers crossing with the association fibers of the SLF. These examples show that while tensor-derived indices are highly *sensitive* to changes in the underlying tissue diffusion, their *specificity* in terms of biological interpretation is very ambiguous as any observed changes can also be explained by fiber crossings.

Note that this does not imply that DTI analyses are "wrong" in themselves. Assuming that the DTI analysis was performed well, avoiding all the known pitfalls [Jones and Cercignani, 2010], an observed change in FA is highly likely to correspond to a true underlying biophysical phenomenon. The issue arises from the usual practice of interpreting FA a marker of WM integrity. As illustrated by the examples, in the presence of crossing fibers, the interpretation of increases (or decreases) in FA become highly ambiguous, as they can correspond to either increased or decreased WM integrity, or indeed to changes in the relative volume fractions of the various fiber populations. As shown in Fig. 7.14, the proportion of WM voxels where these measures are expected to be significantly confounded is of the order of 75%; given that the interpretation commonly ascribed to these measures is only valid in single fiber regions, this implies that there are very few regions of brain WM where these measures (including FA and radial/axial diffusivities) can reliably be interpreted as markers of 'WM integrity'.

While the data used in this study are of much higher quality than would typically be acquired, it is important to emphasize that these 'crossing fiber' issues will still be present to the same extent in any DW-MRI data set. With lower quality data, the power to detect WM voxels containing complex configurations would undeniably be lower, and the estimated proportion of affected voxels would most likely be lower than that reported here. However, while the statistical power to detect multiple fiber orientations would be lower, these multi-fiber voxels are nonetheless present in the data. Clearly, the impact on tensor-derived estimates of orientation, anisotropy or radial/axial diffusivity would be identical, with the only difference being noisier estimates.

7.4.2 Robustness of approach

Given the importance of these findings, great care was taken to ensure the robustness of our results, and particularly to avoid any overestimation of the number of fiber orientations. In particular:

- For each subject we collected 720 DW images, 12 times the amount of data collected in Behrens et al. [2007]. With such a large data set, a higher reliability can be achieved for any subsequent analysis than with a traditional scan consisting of approximately 60 DW images [Jones, 2004].

- Cardiac motion causes local misregistrations of the DW images [Skare and Andersson, 2001, Pierpaoli et al., 2003, Jones and Pierpaoli, 2005], and local signal attenuation in voxels affected by pulsatile motion [Atkinson et al., 2006, Walker et al., 2011]. Both effects could potentially lead to artifactual

fiber orientations being detected inside WM voxels. To avoid such pulsation artifacts, cardiac gating was applied [Jones and Cercignani, 2010].

- Head motion and eddy currents cause global misregistration of the DW images which could also introduce artifactual multi-fiber voxels due to the mixing of fiber bundles with different orientations. We therefore corrected for subject motion and eddy-current distortions, including the required B-matrix adjustments [Leemans and Jones, 2009] and appropriate modulation of the DW images with the Jacobian of the transformation matrix [Jones and Cercignani, 2010].

- Previous studies have employed an FA threshold to select WM voxels [Behrens et al., 2007], a method very likely to include both false positives (some GM voxels may have FA > 0.1) and false negatives (3-fiber WM voxels may have FA < 0.1). To avoid such issues, an objective WM selection method was used based on the corresponding T_1-weighted images (Fig. 7.2).

- Extensive simulations were performed using parameters *derived from the real data* to carefully tune the fODF threshold and the ARD weight (Fig. 7.3). Note that we opted for specificity over sensitivity and selected very conservative thresholds.

In this study we used a b-value of $b = 1200\,\mathrm{s/mm^2}$. While this can be considered relatively low for HARDI reconstruction methods, this b-value corresponds to what most diffusion MRI studies are currently using [Jones et al., 1999], and our findings are therefore relevant for the vast majority of current DW-MRI studies. However, a consequence of this relatively low b-value is that the minimum angle that can resolved reliably is limited to approximately 55° using our method (Fig. 7.4). The practical consequence is that fiber orientations with an inter-fiber angle smaller than 55° will tend to merge into one (average) fiber orientation, making overestimation of the number of fiber orientations very unlikely. Additionally, it shows that even at b-values employed in common practice, multi-fiber voxels can be detected in a large extent of the WM. In the absence of noise and artifacts, performing the same experiment with increased b-values would likely increase the ability of both CSD and bedpostx to resolve smaller inter-fiber angles [Tournier et al., 2007, Behrens et al., 2007, Alexander and Barker, 2005]. However, at high b-values, the reduced SNR of the DW images makes it difficult to use registration-based motion and eddy-current correction techniques. Given the long scan time used in this study, robust motion correction was deemed imperative, and a more moderate b-value was therefore chosen

In this study, we did not specifically investigate voxels with more than three fiber orientations, as the volume fractions of the constituent fiber bundles would become very small and result in small corresponding fODF peak amplitudes in the CSD case (this is not an issue for bedpostx since it rarely reported more than 2 fiber orientations). A very small fODF threshold would be required to detect such small fODF peaks, increasing the risk of introducing false positives (Fig. 7.3a). Furthermore, as the number of fiber orientations increases, the angle between them will tend to decrease. This will cause many of these fiber orientations to merge (Fig. 7.4). Nonetheless, we emphasize that this maximum of 3 fiber orientations

per voxel does not influence the results for the lower orientation counts, since the fODF estimated by CSD is independent of this parameter; it is only used in the subsequent step, to select the 3 largest peaks in the fODF.

A further issue relates to the fact that 'bending' and 'fanning' configurations contain a range of fiber orientations, which cannot be adequately described using a single discrete number. Nonetheless, while these configurations do not contain 'crossing fibers' as such, it is clear that they can only be labeled as containing multiple fiber *orientations*. In this study, the fODF estimated for such configurations will tend to contain a single peak when the curvature remains relatively small, or multiple distinct peaks when the curvature is sufficiently large. From this point of view, it is clear that our approach remains conservative.

The voxel size used in this study was $2.4 \times 2.4 \times 2.4\,\mathrm{mm}^3$, a value typical of the DTI literature. This value was chosen since the primary focus of this study was to estimate the extent and impact of the crossing fiber problem given currently established data acquisition parameters. From a theoretical perspective, increasing spatial resolution has the potential to resolve a proportion of voxels where multiple coherent fiber bundles 'brush', i.e. at the interface between coherent fiber bundles. However, it should be noted that some voxels will always be located at the interface between bundles, and will therefore still contain crossing fibers. Furthermore, increasing the resolution will not resolve cases where individual axons of multiple fiber bundles 'interdigitate', unless the resolution is increased to the level of the axonal diameter (i.e. of the order of 1 µm), which is clearly impossible with current technology. Consequently, while increasing the resolution may reduce the incidence of multi-fiber voxels to some extent, it will not remove the problem altogether. From a practical perspective, increasing the spatial resolution is a challenging task. For example: simply reducing the voxel size from $2.4 \times 2.4 \times 2.4\,\mathrm{mm}^3$ to $2 \times 2 \times 2\,\mathrm{mm}^3$ would almost halve the SNR, which can only be recovered by acquiring 4 signal averages, whilst requiring an increased number of slices to achieve the same spatial coverage. The corresponding increase in scan time required by such an approach is clearly not practical for the vast majority of diffusion studies.

As shown in Fig. 7.5, the fiber orientations extracted using CSD are very consistent with the surrounding orientations, supporting genuine anatomical structures. The same can be deduced from the highly clustered and smoothly transitioning color encoded orientation maps in Figs. 7.7 and 7.8 and from the anatomically plausible fiber tracking results in Fig. 7.10. Moreover, by repeating the experiment on a large collection of residual bootstrap realizations and on a different subject, we have shown that our results are consistent both across noise realizations of the same data set (Fig. 7.9) and across subjects (Table I).

The full course of the relationship between the fODF threshold and the number of WM voxels with multiple fiber orientations can be seen in Fig. 7.11a. Even using an extremely conservative threshold of 0.2, multiple fiber orientations are still found in approximately 78% of all WM voxels. Further increasing the threshold will result in many small fiber populations being discarded and the introduction of WM voxels without any fiber orientation. Fig. 7.11b shows the relationship between the bedpostx volume fraction threshold and the number of WM voxels with multiple fiber orientations. In the range of [0.01 0.1], the number of fiber orientations reported by the bedpostx method is stable, indicating that the ARD has indeed

forced compartments to zero, for which it believed evidence was not sufficiently strong. Starting from a threshold of 0.1, small secondary volume fractions are being discarded, increasing the number of single fiber voxels and introducing WM voxels without any fiber orientation.

7.4.3 Differences between CSD and bedpostx

The two methods used in this study, CSD and bedpostx, provided very different results. These differences can be explained by the simulation results shown in Fig. 7.4, and the *in vivo* results in Fig. 7.5: in voxels containing $\geq$3 fiber orientations, bedpostx will instead report 1 or 2 fiber orientations. Note that the original authors of the ARD method also reported similar limitations [Behrens et al., 2007]. This explains both the increase in 1 and 2 fiber voxels and the relative absence of $\geq$3 fiber voxels in the bedpostx results, ultimately resulting in a lower percentage of multi-fiber voxels.

The large difference between the bedpostx results in this study (63% multi-fiber voxels) and the bedpostx results from the original study conducted by Behrens et al. [2007] (33% multi-fiber voxels), can be attributed mostly to the use of a much larger number of DW images, increasing the effective SNR of our data sets: improving SNR will increase the model evidence for smaller fiber volume fractions, resulting in a larger number of significant fiber orientations. In addition, in this study the ARD weight was tuned specifically to our data, and a longer 'burn-in' (a tunable parameter in bedpostx) was used to ensure convergence. Additionally, Behrens et al. [2007] used an FA threshold to select WM voxels, implicitly assuming that all voxels with FA > 0.1 are considered WM, possibly excluding multi-fiber voxels on account of being too isotropic, introducing a bias towards low orientation counts. In addition, low FA values can become unreliable in the presence of noise [Jones and Cercignani, 2010]. To avoid such issues in our study, an objective WM selection method was used based on the corresponding T_1-weighted images (Fig. 7.1).

7.4.4 Towards new measures of WM 'integrity'

An interesting alternative approach to tensor-based scalar metrics is to use the volume fractions as identified by mixture model approaches (such as, for instance, bedpostx and CSD) as a quantitative index. Jbabdi et al. [2010] make tract-wise comparisons directly on the volume fractions as obtained with bedpostx, assuming that increased volume fractions correspond to an increased axonal density along the corresponding fiber orientation. Raffelt et al. [2012] use the fODF derived with spherical deconvolution and make voxel-wise comparisons directly on the full fODF. Their measure, dubbed 'apparent fiber density' (AFD) assumes that any differences in the fODF amplitude along a given orientation can be attributed to differences in the relative amount of underlying axons thought to be aligned with this orientation. Recent advances allow non-linear registration of fODF images [Raffelt et al., 2011], including appropriate reorientation and modulation, thus enabling group comparisons of AFD between patients and controls. While DTI offers an ambiguous average scalar metric for the entire voxel, these new methods provide directionally dependent metrics, which can be associated with individual

fiber tracts, providing more specific and more readily interpretable results.

7.5 Conclusion

In this chapter, we investigated the prevalence of complex fiber configurations in WM tissue with diffusion MRI. Our results indicate that multiple fiber orientations can be found in a much higher percentage of WM voxels (approximately 90%) than previously reported, with CSD providing much higher estimates than bedpostx. These findings have obvious and profound implications for both tractography and anisotropy analyses, and strengthen the growing awareness that fiber tractography and 'WM integrity' metrics derived from DTI need to be interpreted with extreme caution.

Bibliography

A. L. Alexander, K. M. Hasan, M. Lazar, J. S. Tsuruda, and D. L. Parker. Analysis of partial volume effects in diffusion-tensor MRI. *Magnetic Resonance in Medicine*, 45(5):770–780, 2001.

D. C. Alexander. Multiple-fiber reconstruction algorithms for diffusion MRI. *Annals of the New York Academy of Sciences*, 1064:113–133, 2006.

D. C. Alexander and G. J. Barker. Optimal imaging parameters for fiber-orientation estimation in diffusion MRI. *NeuroImage*, 27(2):357–367, 2005.

D. C. Alexander, G. J. Barker, and S. R. Arridge. Detection and modeling of non-Gaussian apparent diffusion coefficient profiles in human brain data. *Magnetic Resonance in Medicine*, 48(2):331–340, 2002.

D. C. Alexander, P. L. Hubbard, M. G. Hall, E. A. Moore, M. Ptito, G. J. M. Parker, and T. B. Dyrby. Orientationally invariant indices of axon diameter and density from diffusion MRI. *NeuroImage*, 52(4):1374–1389, 2010.

J. Ashburner and K. J. Friston. Unified segmentation. *NeuroImage*, 26(3):839–851, 2005.

Y. Assaf and O. Pasternak. Diffusion tensor imaging (DTI)-based white matter mapping in brain research: a review. *Journal of Molecular Neuroscience*, 34(1): 51–61, 2008.

D. Atkinson, S. Counsell, J. V. Hajnal, P. G. Batchelor, D. L. G. Hill, and D. J. Larkman. Nonlinear phase correction of navigated multi-coil diffusion images. *Magnetic Resonance in Medicine*, 56(5):1135–1139, 2006.

P. J. Basser, J. Mattiello, and D. LeBihan. Estimation of the effective self-diffusion tensor from the NMR spin echo. *Journal of Magnetic Resonance Series B*, 103: 247–247, 1994a.

P. J. Basser, J. Mattiello, and D. LeBihan. MR diffusion tensor spectroscopy and imaging. *Biophysical Journal*, 66(1):259–267, 1994b.

T. E. J. Behrens, H. Johansen-Berg, S. Jbabdi, M. F. S. Rushworth, and M. W. Woolrich. Probabilistic diffusion tractography with multiple fibre orientations: what can we gain? *NeuroImage*, 34(1):144–155, 2007.

O. Ciccarelli, M. Catani, H. Johansen-Berg, C. Clark, and A. Thompson. Diffusion-based tractography in neurological disorders: concepts, applications, and future developments. *The Lancet Neurology*, 7(8):715–727, 2008.

M. Descoteaux, R. Deriche, TR Knösche, and A. Anwander. Deterministic and probabilistic tractography based on complex fibre orientation distributions. *IEEE Transactions on Medical Imaging*, 28(2):269–286, 2009.

O. Dietrich, J. G. Raya, S. B. Reeder, M. F. Reiser, and S. O. Schoenberg. Measurement of signal-to-noise ratios in MR images: influence of multichannel coils, parallel imaging, and reconstruction filters. *Journal of Magnetic Resonance Imaging*, 26(2):375–385, 2007.

G. Douaud, S. Jbabdi, T. E. J. Behrens, R. A. Menke, A. Gass, A. U. Monsch, A. Rao, B. Whitcher, G. Kindlmann, P. M. Matthews, and S. M. Smith. DTI measures in crossing-fibre areas: increased diffusion anisotropy reveals early white matter alteration in MCI and mild Alzheimer's disease. *NeuroImage*, 55 (3):880–890, 2011.

P. Fillard, M. Descoteaux, A. Goh, S. Gouttard, **B. Jeurissen**, J. G. Malcolm, A. Ramirez-Manzanares, M. Reisert, K. Sakaie, F. Tensaouti, T. Yo, J. F. Mangin, and C. Poupon. Quantitative evaluation of 10 tractography algorithms on a realistic diffusion MR phantom. *NeuroImage*, 56(1):220–234, 2011.

L. R. Frank. Anisotropy in high angular resolution diffusion-weighted MRI. *Magnetic Resonance in Medicine*, 45(6):935–939, 2001.

L. R. Frank. Characterization of anisotropy in high angular resolution diffusion-weighted MRI. *Magnetic Resonance in Medicine*, 47:1083–1099, 2002.

H. A. Haroon, D. M. Morris, K. V. Embleton, D. C. Alexander, and G. Parker. Using the model-based residual bootstrap to quantify uncertainty in fiber orientations from Q-ball analysis. *IEEE Transactions on Medical Imaging*, 28(4):535–550, 2009.

S. Jbabdi, T. E. J. Behrens, and S. M. Smith. Crossing fibres in tract-based spatial statistics. *NeuroImage*, 49(1):249–256, 2010.

B. Jeurissen, A. Leemans, J. D. Tournier, and J. Sijbers. Fiber tracking on the 'Fiber Cup phantom' using constrained spherical deconvolution. In *Proceedings of the MICCAI'09 Workshop on Diffusion Modelling and the Fiber Cup*, pages 232–235, London, United Kingdom, 2009.

B. Jeurissen, A. Leemans, D. K. Jones, J. D. Tournier, and J. Sijbers. Counting the number of fiber orientations in diffusion MRI voxels using constrained spherical deconvolution. In *Proceedings of the ISMRM Benelux Chapter*, volume 2, page 18, Utrecht, The Netherlands, 2010a.

B. Jeurissen, A. Leemans, D. K. Jones, J. D. Tournier, and J. Sijbers. Estimating the number of fiber orientations in diffusion MRI voxels: a constrained spherical deconvolution study. In *Proceedings of the International Society for Magnetic Resonance in Medicine*, volume 18, page 573, Stockholm, Sweden, 2010b.

B. Jeurissen, A. Leemans, D. K. Jones, J. D. Tournier, and J. Sijbers. Probabilistic fiber tracking using the residual bootstrap with constrained spherical deconvolution. *Human Brain Mapping*, 32:461–479, 2011.

B. Jeurissen, A. Leemans, J. D. Tournier, D. K. Jones, and J. Sijbers. Assessing the implications of complex fiber configurations for DTI metrics in real data sets. In *Proceedings of the International Society for Magnetic Resonance in Medicine*, volume 20, Melbourne, Australia, 2012.

B. Jeurissen, A. Leemans, J. D. Tournier, D. K. Jones, and J. Sijbers. Investigating the prevalence of complex fiber configurations. *Human Brain Mapping*, in press.

H. Johansen-Berg and T. E. J. Behrens. Just pretty pictures? What diffusion tractography can add in clinical neuroscience. *Current Opinion in Neurology*, 19: 379–385, 2006.

D. K. Jones. The effect of gradient sampling schemes on measures derived from diffusion tensor MRI: a Monte Carlo study. *Magnetic Resonance in Medicine*, 51 (4):807–815, 2004.

D. K. Jones. Studying connections in the living human brain with diffusion MRI. *Cortex*, 44(8):936–952, 2008.

D. K. Jones. Challenges and limitations of quantifying brain connectivity in vivo with diffusion MRI. *Imaging in Medicine*, 2(3):341–355, 2010.

D. K. Jones and M. Cercignani. Twenty-five pitfalls in the analysis of diffusion MRI data. *NMR in Biomedicine*, 23(7):803–820, 2010.

D. K. Jones and C. Pierpaoli. Contribution of cardiac pulsation to variability of tractography results. In *Proceedings of the International Society for Magnetic Resonance in Medicine*, volume 13, page 222, Miami, USA, 2005.

D. K. Jones, M. A. Horsfield, and A. Simmons. Optimal strategies for measuring diffusion in anisotropic systems by magnetic resonance imaging. *Magnetic Resonance in Medicine*, 42(3):515–525, 1999.

S. Klein, M. Staring, K. Murphy, M.A. Viergever, and J. P. W. Pluim. elastix: a toolbox for intensity based medical image registration. *IEEE Transactions on Medical Imaging*, 29(1):196–205, 2010.

C. G. Koay, L. C. Chang, J. D. Carew, C. Pierpaoli, and P. J. Basser. A unifying theoretical and algorithmic framework for least squares methods of estimation in diffusion tensor imaging. *Journal of Magnetic Resonance*, 182(1):115–125, 2006.

A. Leemans and D. K. Jones. The B-matrix must be rotated when correcting for subject motion in DTI data. *Magnetic Resonance in Medicine*, 61(6):1336–1349, 2009.

A. Leemans, J. Sijbers, M. Verhoye, A. Van der Linden, and D. Van Dyck. Mathematical framework for simulating diffusion tensor MR neural fiber bundles. *Magnetic Resonance in Medicine*, 53(4):944–953, 2005.

A. Leemans, **B. Jeurissen**, J. Sijbers, and D. K. Jones. ExploreDTI: a graphical toolbox for processing, analyzing, and visualizing diffusion MR data. In *Proceedings of the International Society for Magnetic Resonance in Medicine*, volume 17, page 3537, Honolulu, USA, 2009.

D. Mattes, D. R. Haynor, H. Vesselle, T. K. Lewellyn, and W. Eubank. Nonrigid multimodality image registration. In *Proceedings of SPIE*, volume 4322, page 1609, 2001.

K. L. Miller, C. J. Stagg, G. Douaud, S. Jbabdi, and S. M. Smith. Diffusion imaging of whole, post-mortem human brains on a clinical MRI scanner. *NeuroImage*, 57 (1-4):167–181, 2011.

S. Mori and P. C. M. Van Zijl. Fiber tracking: principles and strategies-a technical review. *NMR in Biomedicine*, 15(7-8):468–480, 2002.

S. Mori and J. Zhang. Principles of diffusion tensor imaging and its applications to basic neuroscience research. *Neuron*, 51(5):527–539, 2006.

J. O'Muircheartaigh, C. Vollmar, C. Traynor, G. J. Barker, V. Kumari, M. R. Symms, P. Thompson, J. S. Duncan, M. J. Koepp, and M. P. Richardson. Clustering probabilistic tractograms using independent component analysis applied to the thalamus. *NeuroImage*, 54(3):2020–2032, 2011.

C. Pierpaoli, A. Barnett, S. Pajevic, R. Chen, L. R. Penix, A. Virta, and P. J. Basser. Water diffusion changes in Wallerian degeneration and their dependence on white matter architecture. *NeuroImage*, 13(6):1174–1185, 2001.

C. Pierpaoli, S. Marenco, G. Rohde, D. K. Jones, and A. S. Barnett. Analyzing the contribution of cardiac pulsation to the variability of quantities derived from the diffusion tensor. In *Proceedings of the International Society for Magnetic Resonance In Medicine*, volume 11, page 70, Toronto, Canada, 2003.

D. Raffelt, J. D. Tournier, J. Fripp, S. Crozier, A. Connelly, and O. Salvado. Symmetric diffeomorphic registration of fibre orientation distributions. *NeuroImage*, 56:1171–1180, 2011.

D. Raffelt, J. D. Tournier, S. Rose, G. R. Ridgway, R. Henderson, S. Crozier, O. Salvado, and A. Connelly. Apparent fibre density: a novel measure for the analysis of diffusion-weighted magnetic resonance images. *NeuroImage*, 59: 3976–3994, 2012.

S. Skare and J. L. R. Andersson. On the effects of gating in diffusion imaging of the brain using single shot EPI. *Magnetic Resonance Imaging*, 19(8):1125–1128, 2001.

E. O. Stejskal and J. E. Tanner. Spin diffusion measurements: spin echoes in the presence of a time-dependent field gradient. *The Journal of Chemical Physics*, 42(1):288, 1965.

J. D. Tournier, F. Calamante, D. G. Gadian, and A. Connelly. Direct estimation of the fiber orientation density function from diffusion-weighted MRI data using spherical deconvolution. *NeuroImage*, 23(3):1176–1185, 2004.

J. D. Tournier, F. Calamante, and A. Connelly. Robust determination of the fibre orientation distribution in diffusion MRI: non-negativity constrained super-resolved spherical deconvolution. *NeuroImage*, 35(4):1459–1472, 2007.

J. D. Tournier, C. H. Yeh, F. Calamante, K. H. Cho, A. Connelly, and C. P. Lin. Resolving crossing fibres using constrained spherical deconvolution: validation using diffusion-weighted imaging phantom data. *NeuroImage*, 42(2):617–625, 2008.

J. D. Tournier, S. Mori, and A. Leemans. Diffusion tensor imaging and beyond. *Magnetic Resonance in Medicine*, 65(6):1532–1556, 2011.

J. D. Tournier, F. Calamante, and A. Connelly. MRtrix: diffusion tractography in crossing fiber regions. *International Journal of Imaging Systems and Technology*, 22(1):53–66, 2012.

D. S. Tuch, T. G. Reese, M. R. Wiegell, N. Makris, J. W. Belliveau, and V. J. Wedeen. High angular resolution diffusion imaging reveals intravoxel white matter fiber heterogeneity. *Magnetic Resonance in Medicine*, 48(4):577–582, 2002.

D. S. Tuch, D. H. Salat, J. J. Wisco, A. K. Zaleta, N. D. Hevelone, and H. D. Rosas. Choice reaction time performance correlates with diffusion anisotropy in white matter pathways supporting visuospatial attention. *Proceedings of the National Academy of Sciences of the United States of America*, 102(34):12212–12217, 2005.

S. B. Vos, D. K. Jones, M. A. Viergever, and A. Leemans. Partial volume effect as a hidden covariate in DTI analyses. *NeuroImage*, 55(4):1566–1576, 2011.

S. B. Vos, D. K. Jones, **B. Jeurissen**, M. A. Viergever, and A. Leemans. The influence of complex white matter architecture on the mean diffusivity in diffusion tensor MRI of the human brain. *NeuroImage*, 59(3):2208–2216, 2012.

L. Walker, L.C. Chang, C.G. Koay, N. Sharma, L. Cohen, R. Verma, and C. Pierpaoli. Effects of physiological noise in population analysis of diffusion tensor MRI data. *NeuroImage*, 54(2):1168–1177, 2011.

C. A. M. Wheeler-Kingshott and M. Cercignani. About axial and radial diffusivities. *Magnetic Resonance in Medicine*, 61(5):1255–1260, 2009.

M. W. Woolrich, S. Jbabdi, B. Patenaude, M. Chappell, S. Makni, T. E. J. Behrens, C. Beckmann, M. Jenkinson, and S. M. Smith. Bayesian analysis of neuroimaging data in FSL. *NeuroImage*, 45(1):173–186, 2009.

Conclusion

In this dissertation we developed a **new deterministic tractography algorithm based on CSD** which is able to track through regions of complex fiber architecture, enabling a more accurate delineation of many of the WM pathways of the brain. These improved delineations are not only of interest for the purpose of visualization and exploratory anatomical research, but can also be used as ROIs for the quantitative analysis of popular scalar diffusion indices. In a recent study on Alzheimer's disease, it was shown that improved delineation of the superior longitudinal fasciculus using CSD tractography, significantly increased the sensitivity to detect WM abnormalities as opposed to results obtained with conventional DTI based tractography.

While deterministic CSD tractography in itself is able to produce impressive results, it assumes a unique fiber orientation estimate in each voxel, neglecting the uncertainty associated with each step. As diffusion MRI is known to be a noisy imaging technique and errors are known to propagate during tractography, different noise realizations of the same data set can produce substantially different tractography results. Even a small error at one point in the trajectory can cause the algorithm to enter and follow a different WM tract, leading to erroneous statements about the WM 'connectivity'. To characterize this uncertainty, we developed a **new probabilistic tractography algorithm based on CSD** which generates a large collection or *distribution* of possible trajectories from each seed point. Brain regions that contain higher densities of the resulting trajectories are then deemed to have a higher probability of 'connection' with the seed point. To create such a distribution we made use of a statistical technique called bootstrapping. Using simulations we have benchmarked different variations of the bootstrap. Our results showed that the 'classic bootstrap' significantly underestimates the uncertainty when only a few repeated acquisitions are available, which is typically the case. This large downward bias can be removed by using the bootknife approach, allowing accurate CSD fiber orientation uncertainty estimates with only a limited set of repeated measurements and without making assumptions about the sources of uncertainty in the data. However, in a clinical setting, even a few repeated measurements can render acquisition time unacceptably long. This limitation can be overcome using model-based residual bootstrapping techniques, that require only a single acquisition. Simulations showed that the combination of the residual bootstrap with the modified spherical harmonics model allows accurate estimates of the CSD fiber trajectory uncertainty, bringing it into the clinical realm. Using real data from a healthy volunteer we have shown that probabilistic CSD tractography produces much more plausible trajectories than its DTI counterpart, even in large WM structures such as the corpus callosum, superior longitudinal fasciculus and

corticospinal tract, with probabilistic DTI tractography producing many false positives and false negatives in regions of complex fiber architecture.

To underline the importance of this work, we set out to assess the **prevalence of voxels containing multiple fiber orientations**, as these are the voxels where multi-fiber reconstruction algorithm would result in improved tractography results. For this purpose, we acquired large, high quality DW data sets and extracted the fiber orientations using both CSD and the bedpostx algorithm. Our results indicated that multiple fiber orientations can be found in a much higher percentage of WM voxels than previously reported, with CSD providing much higher estimates than bedpostx. These findings have obvious and profound implications for both tractography and integrity analyses, and strengthen the growing awareness that fiber tractography and 'WM integrity' metrics derived from DTI need to be interpreted with extreme caution.

Note that in the above text, we systematically wrote 'connectivity' between quotation marks. Indeed, there is still a significant gap between connectivity in the diffusion MRI data and actual anatomical connectivity in the WM. In the introductory chapters we provided an overview of the major limitations of diffusion MRI at the level of the acquisition (low spatial resolution, low SNR, motion and eddy current distortions), together with the major limitations of fiber tractography (noise and artifacts induced errors, modeling errors and integration errors). All these factors will influence the accuracy and precision of the reconstructed fiber pathways. Probabilistic tractography is already an important step forward, in that it gives us an indication of the precision of the results. Unfortunately it says nothing about the accuracy. Probabilistic tractography algorithms are as susceptible to systematic errors in the data acquisition and analysis pipeline as deterministic algorithms. Even without systematic errors, the interpretation of probabilistic tractography results remains a challenging task. For example, it can be shown in a set of pathways comprising identical microstructure, that the path deemed to mediate the highest connectivity by probabilistic tractography, will be the shortest, simplest and straightest path. The popular interpretation of tractography in terms of 'connectivity' thus remains questionable and one should always be aware of the underlying limitations, pitfalls and confounds when using these methods for neuroscientific research.

List of abbreviations

3D three dimensional

AD axial diffusivity

ADC apparent diffusion coefficient

AFD apparent fiber density

ARD automatic relevance determination

ASSET array spatial sensitivity encoding technique

bedpostx Bayesian estimation of diffusion parameters obtained using sampling techniques with modeling of crossing fibers

CC corpus callosum

CHARMED composite hindered and restricted model of diffusion

CI confidence interval

CL coefficient of linearity

CP coefficient of planarity

CS coefficient of sphericity

CSD constrained spherical deconvolution

CSF cerebrospinal fluid

CST corticospinal tract

dODF diffusion orientation distribution function

DSI diffusion spectrum imaging

DT diffusion tensor

DTI diffusion tensor imaging

DW diffusion-weighted

DWI diffusion-weighted imaging

EPI echo-planar imaging

FA fractional anisotropy

FC Fiber Cup

FE first eigenvector

FEFA first eigenvector fractional anisotropy

FFT fast Fourier transform

fODF fiber orientation distribution function

FOV field of view

fMRI functional magnetic resonance imaging

FRT Funk-Radon transform

FSL FMRIB Software Library

GFA generalized fractional anisotropy

GM gray matter

GRAPPA generalized autocalibrating partially parallel acquisition

HARD high angular resolution diffusion

HARDI high angular resolution diffusion imaging

IFFT inverse fast Fourier transform

IQR interquartile range

MCMC Markov chain Monte Carlo

MD mean diffusivity

MICCAI Medical Image Computing and Computer Assisted Intervention

MR magnetic resonance

MRI magnetic resonance imaging

NEX number of excitations

NMR nuclear magnetic resonance

ODF orientation distribution function

PAS persistent angular structure

PDF probability density function

PDV principal diffusion vector

PGSE pulsed gradient spin-echo

QBI q-ball imaging

RBW receiver bandwidth

RD radial diffusivity

RF radio frequency

RGB red green blue

RK2 second order Runge-Kutta integration

RK4 fourth order Runge-Kutta integration

RMSE root mean squared error

ROI region of interest

SD spherical deconvolution

SE spin-echo

SH spherical harmonics

SLF superior longitudinal fasciculus

SNR signal-to-noise ratio

SPM Statistical Parametric Mapping

sRMSE symmetrized root mean squared error

TE echo time

TH thickness

TI inversion time

TR repetition time

uODF uncertainty orientation distribution function

VC visitation count

WM white matter

Academic overview

Journal papers

1. W. Van Hecke, A. Leemans, S. De Backer, **B. Jeurissen**, P. M. Parizel, and J. Sijbers. Comparing isotropic and anisotropic smoothing for voxel-based DTI analyses: a simulation study. *Human Brain Mapping*, 31(1):98–114, 2010

2. **B. Jeurissen**, A. Leemans, D. K. Jones, J. D. Tournier, and J. Sijbers. Probabilistic fiber tracking using the residual bootstrap with constrained spherical deconvolution. *Human Brain Mapping*, 32:461–479, 2011a

3. P. Fillard, M. Descoteaux, A. Goh, S. Gouttard, **B. Jeurissen**, J. G. Malcolm, A. Ramirez-Manzanares, M. Reisert, K. Sakaie, F. Tensaouti, T. Yo, J. F. Mangin, and C. Poupon. Quantitative evaluation of 10 tractography algorithms on a realistic diffusion MR phantom. *NeuroImage*, 56(1):220–234, 2011

4. J. Veraart, T. B. Leergaard, B. T. Antonsen, W. Van Hecke, I. Blockx, **B. Jeurissen**, Y. Jiang, A. Van der Linden, G. A. Johnson, M. Verhoye, and J. Sijbers. Population-averaged diffusion tensor imaging atlas of the Sprague Dawley rat brain. *NeuroImage*, 58(4):975–983, 2011

5. J. Rajan, **B. Jeurissen**, M. Verhoye, J. Van Audekerke, and J. Sijbers. Maximum likelihood estimation-based denoising of magnetic resonance images using restricted local neighborhoods. *Physics in Medicine and Biology*, 56: 5221–5234, 2011

6. S. B. Vos, D. K. Jones, **B. Jeurissen**, M. A. Viergever, and A. Leemans. The influence of complex white matter architecture on the mean diffusivity in diffusion tensor MRI of the human brain. *NeuroImage*, 59(3):2208–2216, 2012

7. D. Poot, **B. Jeurissen**, Y. Bastiaensen, J. Veraart, W. Van Hecke, P.M. Parizel, and J. Sijbers. Super-resolution for multislice diffusion tensor imaging. *Magnetic Resonance in Medicine*, in press

8. **B. Jeurissen**, A. Leemans, J. D. Tournier, D. K. Jones, and J. Sijbers. Investigating the prevalence of complex fiber configurations. *Human Brain Mapping*, in press

9. I. Blockx, M. Verhoye, J. Van Audekerke, I. Bergwerf, J. X. Kane, R. Delgado y Palacios, **B. Jeurissen**, J. Veraart, K. Raber, S. von Hörsten, P. Ponsaerts,

J. Sijbers, T. B. Leergaard, and A. Van der Linden. Identification and characterization of Huntington related pathology: a DKI imaging study. *Neurobiology of Aging*, submitted

Conference papers

1. **B. Jeurissen**, A. Leemans, J. D. Tournier, and J. Sijbers. Estimation of uncertainty in constrained spherical deconvolution fiber orientations. In *Proceedings of the IEEE International Symposium on Biomedical Imaging: From nano to macro*, pages 907–910, Paris, France, 2008d

2. **B. Jeurissen**, A. Leemans, J. D. Tournier, and J. Sijbers. Fiber tracking on the 'Fiber Cup phantom' using constrained spherical deconvolution. In *Proceedings of the MICCAI'09 Workshop on Diffusion Modelling and the Fiber Cup*, pages 232–235, London, United Kingdom, 2009a

3. J. Rajan, **B. Jeurissen**, J. Sijbers, and K. Kannan. Denoising magnetic resonance images using fourth order complex diffusion. In *Proceedings of the International Machine Vision and Image Processing Conference*, pages 123–127, Dublin, Ireland, 2009

Conference abstracts

1. **B. Jeurissen**, A. Leemans, E. Fieremans, and J. Sijbers. Fiber tractography on a crossing fiber phantom using constrained spherical deconvolution MRI. In *Proceedings of Liège Image Days*, Liège, Belgium, 2008a

2. **B. Jeurissen**, A. Leemans, J. D. Tournier, and J. Sijbers. Bootstrap methods for estimating uncertainty in Constrained Spherical Deconvolution fiber orientations. In *Proceedings of the International Society for Magnetic Resonance in Medicine*, volume 16, page 3324, Toronto, Canada, 2008b

3. **B. Jeurissen**, A. Leemans, J. D. Tournier, and J. Sijbers. Can residual bootstrap reliably estimate uncertainty in fiber orientation obtained by spherical deconvolution from diffusion-weighted MRI? In *Proceedings of the Organization for Human Brain Mapping*, volume 14, Melbourne, Australia, 2008c

4. **B. Jeurissen**, A. Leemans, J. D. Tournier, and J. Sijbers. Probabilistic Fiber Tracking using the Residual Bootstrap with Constrained Spherical Deconvolution MRI. In *Proceedings of the International Society for Magnetic Resonance in Medicine*, volume 17, page 1438, Honolulu, USA, 2009b

5. A. Leemans, **B. Jeurissen**, J. Sijbers, and D. K. Jones. ExploreDTI: a graphical toolbox for processing, analyzing, and visualizing diffusion MR data. In *Proceedings of the International Society for Magnetic Resonance in Medicine*, volume 17, page 3537, Honolulu, USA, 2009

6. **B. Jeurissen**, A. Leemans, D. K. Jones, J. D. Tournier, and J. Sijbers. Counting the number of fiber orientations in diffusion MRI voxels using constrained spherical deconvolution. In *Proceedings of the ISMRM Benelux Chapter*, volume 2, page 18, Utrecht, The Netherlands, 2010a

7. **B. Jeurissen**, A. Leemans, D. K. Jones, J. D. Tournier, and J. Sijbers. Estimating the number of fiber orientations in diffusion MRI voxels: a constrained spherical deconvolution study. In *Proceedings of the International Society for Magnetic Resonance in Medicine*, volume 18, page 573, Stockholm, Sweden, 2010b

8. **B. Jeurissen**, M. Naeyaert, A. Leemans, and J. Sijbers. Correction of DWI gradient orientations using registration techniques. In *Proceedings of the ISMRM Benelux Chapter*, volume 3, page 108, Hoeven, The Netherlands, 2011b

9. **B. Jeurissen**, M. Naeyaert, A. Leemans, and J. Sijbers. Registration based correction of DWI gradient orientations. In *Proceedings of the International Society for Magnetic Resonance in Medicine*, volume 19, page 1944, Montréal, Canada, 2011c

10. M. Froeling, G. J. Strijkers, **B. Jeurissen**, M. P. van der Paardt, J. Stoker, Nicolay K., A. J. Nederveen, and A. Leemans. Fiber architecture of the female pelvic floor: an exploratory investigation using different diffusion MRI tractography algorithms. In *Proceedings of the International Society for Magnetic Resonance in Medicine*, volume 19, page 3260, Montréal, Canada, 2011

11. Y. D. Reijmer, A. Leemans, S. M. Heringa, I. Wielaard, **B. Jeurissen**, H. L. Koek, and G. J. Biessels. Constrained spherical deconvolution based tractography and cognition in Alzheimer's disease. In *Proceedings of the Organization for Human Brain Mapping*, Québec, Canada, 2011a

12. Y. D. Reijmer, A. Leemans, S. M. Heringa, I. Wielaard, **B. Jeurissen**, H. L. Koek, and G. J. Biessels. Constrained spherical deconvolution based tractography and cognition in Alzheimer's disease. In *Proceedings of the International Conference on Alzheimer's Disease*, Paris, France, 2011b

13. **B. Jeurissen**, A. Leemans, J. D. Tournier, and J. Sijbers. HARDI-based methods for fiber orientation estimation. In *Proceedings of the International Society for Magnetic Resonance in Medicine*, volume 20, Melbourne, Australia, 2012b

14. **B. Jeurissen**, A. Leemans, J. D. Tournier, D. K. Jones, and J. Sijbers. Assessing the implications of complex fiber configurations for DTI metrics in real data sets. In *Proceedings of the International Society for Magnetic Resonance in Medicine*, volume 20, Melbourne, Australia, 2012a

Moderator

1. 'MR methods' session, 4th Annual Meeting of The Benelux Chapter of the International Society for Magnetic Resonance in Medicine (ISMRM), Leuven, January 16, 2012

Reviewer for the following journals

1. Brain Connectivity
2. IEEE Transactions on Medical Imaging
3. International Journal of Biomedical Imaging
4. Magnetic Resonance in Medicine
5. Medical Image Analysis
6. NeuroImage

Awards

1. *Educational Stipend Award* for the work: **B. Jeurissen**, A. Leemans, J. D. Tournier, and J. Sijbers. Bootstrap methods for estimating uncertainty in Constrained Spherical Deconvolution fiber orientations. In *Proceedings of the International Society for Magnetic Resonance in Medicine*, volume 16, page 3324, Toronto, Canada, 2008b

2. *Educational Stipend Award* for the work: **B. Jeurissen**, A. Leemans, J. D. Tournier, and J. Sijbers. Probabilistic Fiber Tracking using the Residual Bootstrap with Constrained Spherical Deconvolution MRI. In *Proceedings of the International Society for Magnetic Resonance in Medicine*, volume 17, page 1438, Honolulu, USA, 2009b

3. *Best Diffusion MRI Modeling and Tractography Algorithm, Second Place* for the work: **B. Jeurissen**, A. Leemans, J. D. Tournier, and J. Sijbers. Fiber tracking on the 'Fiber Cup phantom' using constrained spherical deconvolution. In *Proceedings of the MICCAI'09 Workshop on Diffusion Modelling and the Fiber Cup*, pages 232–235, London, United Kingdom, 2009a

4. *Educational Stipend Award* for the work: **B. Jeurissen**, A. Leemans, D. K. Jones, J. D. Tournier, and J. Sijbers. Estimating the number of fiber orientations in diffusion MRI voxels: a constrained spherical deconvolution study. In *Proceedings of the International Society for Magnetic Resonance in Medicine*, volume 18, page 573, Stockholm, Sweden, 2010b

Involvement in diffusion MRI software

1. Co-developer of *ExploreDTI*: a graphical toolbox for processing, analyzing, and visualizing diffusion MR data (`http://www.exploredti.com/`). Main contributions include HARDI data processing and tractography.

2. Maintainer of the Windows port of *MRtrix*: tools to perform diffusion-weighted MRI white matter tractography in the presence of crossing fibers, using CSD (`http://www.nitrc.org/projects/mrtrix/`).

Teaching and supervision

1. **2008-2009**: Tutor 'Mathematical methods for Physics I' (1st year B. Sc. in Physics), supervising lecturer: Prof. Dr. David Eelbode

2. **2009-2010**: Co-supervisor of Bert Cuypers (thesis B. Sc. in Physics, University of Antwerp): 'Estimating the gradient orientations in diffusion MRI' (Supervisor: Prof. Dr. Jan Sijbers)

3. **2010-2011**: Co-supervisor of Maarten Naeyaert (thesis M. Sc. in Physics, University of Antwerp): 'Automatic correction of the gradient table for diffusion tensor MRI' (Supervisor: Prof. Dr. Jan Sijbers)

4. **2010-2011**: Co-supervisor of Toon Van Craenendonck (thesis B. Sc. in Computer Sciences, University of Antwerp): 'A graphical toolbox for the visualization of diffusion MRI images' (Supervisor: Prof. Dr. Jan Sijbers)

Relevant courses

1. 'Diffusion Imaging and Tractography', Educational Course organized by the Organization for Human Brain Mapping, Melbourne, Australia, June 15, 2008

2. 'Diffusion: from Basic Physics to Exploration of Microscopic Structure', Lectures on MR organized by the European Society for Magnetic Resonance in Medicine and Biology, Cardiff, United Kingdom, September 17-19, 2008

3. Weekend Educational Program organized by the International Society for Magnetic Resonance in Medicine, several locations, 2008-2012

Nederlandstalige samenvatting

Achtergrond

Magnetische resonantie beeldvorming (MRI) combineert een krachtige magneet, radiogolven en geavanceerde computers om gedetailleerde informatie te verschaffen over de plaats, omvang en samenstelling van zachte lichaamsweefsels. MRI gebruikt geen röntgenstraling maar maakt gebruik van de magnetische eigenschappen van de waterstofkernen in ons lichaam. Door een heel sterk magnetisch veld worden de moleculen een kant op gericht. Door vervolgens een kort radiosignaal in te sturen worden deze moleculen even uit hun positie geduwd. Bij het teruggaan naar hun oorspronkelijke situatie geven ze een heel klein elektromagnetisch signaal af dat kan worden waargenomen in de scanner. Doordat waterstofkernen in verschillende weefsels verschillend reageren, is het mogelijk mooie contrastbeelden te maken. Zo is MRI onmisbaar geworden om de hersenen op een niet-invasieve manier in al hun anatomische details te visualiseren.

Diffusie MRI (DW-MRI) is een gespecialiseerde vorm van MRI die toelaat om de willekeurige bewegingen (of diffusie) van de waterstofkernen in biologische weefsels te meten. In een omgeving zonder obstakels, bijvoorbeeld in een glas water, zal de bewegelijkheid van de waterstofkernen in alle richtingen hetzelfde zijn. In weefsels met een sterke vezelstructuur daarentegen, zoals bijvoorbeeld in de witte stof van de hersenen, zullen de waterstofkernen meer bewegen langsheen de vezels dan loodrecht daarop. Op basis van dit principe kan op een indirecte manier informatie verkregen worden over de oriëntatie van de onderliggende microstructuur. Met behulp van vezeltractografie kan de lokale oriëntatie-informatie geïntegreerd worden tot globale vezelbundels. Op deze manier kunnen verbindingen in de gehele witte stof van de hersenen worden gereconstrueerd. Dergelijk onderzoek naar de "neurale bekabeling" van de hersenen is erg belangrijk bij het plannen van hersenoperaties en bij het bestuderen van neurodegeneratieve aandoeningen zoals multiple sclerose en de ziekte van Alzheimer.

Het meeste gebruikte model om diffusie informatie voor te stellen is de diffusie tensor. Diffusie tensor beeldvorming (DTI) vereist slechts een beperkt aantal DW-MRI scans, waardoor het erg populair is voor klinische toepassingen. DTI is echter niet in staat om complexe vezelconfiguraties, bv. kruisende vezelbundels binnen één voxel, te beschrijven. In zulke voxels is de oriëntatie-informatie onbetrouwbaar. Recente acquisitie methoden die diffusie opmeten met hoge hoek resolutie en sterke diffusiegevoeligheid (zogenaamde HARDI-acquisities) en nieuwe reconstructietechnieken maken het echter mogelijk om verschillende vezeloriëntaties te onderscheiden in één enkele voxel.

Bijdrage

In dit proefschrift worden nieuwe methoden voor vezeltractografie voorgesteld die gebruik maken van HARDI data en die in staat zijn de vezelbundels te reconstrueren in regio's met complexe vezeloriëntaties.

De lokale vezeloriëntaties worden uit de DW-MRI data bepaald met behulp van sferische deconvolutie. Sferische deconvolutie laat toe in elke voxel de volledige vezeloriëntatie distributie functie (fODF) te bepalen, gebruik makende van het principe van deconvolutie. Door te eisen dat de fODF geen negatieve waarden mag aannemen, is het mogelijk om op een betrouwbare manier verschillende vezeloriëntaties te onderscheiden op basis van relatief bescheiden acquisities. Vervolgens wordt de richtinginformatie van de lokale fODFs geïntegreerd tot globale hersenvezelbundels d.m.v. deterministische vezeltractografie. Experimenten op fantoomdata en reële data tonen aan dat de vezelbanen die op deze manier verkregen worden beter overeenstemmen met de onderliggende microstructuur dan de vezelbanen verkregen met de gangbare DTI vezeltractografie. Er werd ook aangetoond dat de verbeterde aflijning van bepaalde hersenstructuren op basis van tractografie met sferische deconvolutie kan leiden tot verhoogde sensitiviteit in het detecteren van neurodegeneratieve aandoeningen.

Aangezien DW-MRI beelden typisch erg ruizig zijn, gaan de gereconstrueerde vezelbanen gepaard met betrekkelijk hoge onzekerheid. Verschillende opnamen kunnen bijvoorbeeld aanleiding geven tot substantieel verschillende tractografie resultaten. Om de onzekerheid van de gereconstrueerde vezelbanen in kaart te brengen werd er ook een probabilistische tractografie methode ontwikkelde op basis van sferische deconvolutie. In tegenstelling tot deterministische tractografie, waarbij voor elk startpunt één vezeltraject wordt bepaald, wordt bij probabilistische tractografie voor elke startpunt een distributie van trajecten bepaald. Regio's met een hogere dichtheid aan verbindingen zijn dan met een hogere waarschijnlijkheid verbonden met het startpunt. De lokale vezeloriëntatie-onzekerheid wordt bepaald met behulp van de residual bootstrap methode, een statistische procedure gebaseerd op resampling. Experimenten op fantoomdata tonen aan dat deze methode een nauwkeurig beeld geeft van de onzekerheid van de gereconstrueerde vezelbanen, zonder herhaalde DW-MRI scans te vereisen. Op basis van reële data kon bovendien worden aangetoond dat probabilistische tractografie met sferische deconvolutie aanleiding geeft tot een meer plausibele aflijning van diverse hersenvezelbundels.

Tot slot werd er onderzoek gedaan naar de prevalentie van voxels met meerdere vezeloriëntaties, aangezien dit de voxels zijn waar de ontwikkelde tractografie algoritmen tot verbeterde resultaten leiden. Dit onderzoek toont aan dat complexe vezeloriëntaties terug te vinden zijn in ongeveer 90% van de voxels in de witte stof, een veel groter percentage dan tot nu toe werd aangenomen. Dit toont aan dat tractografie op basis van DTI erg onbetrouwbaar is en onderstreept nog eens het belang van de methoden ontwikkeld in dit werk.